UNIVERSITY OF BIRMINGHAM

COLLEGE OF ENGINEERING AND PHYSICAL SCIENCES

SCHOOL OF METALLURGY AND MATERIALS

Effect of chemistry and temperature on planar defects in superalloys

Author
Joshua D. T. ALLEN

Supervisor
Prof. Alessandro MOTTURA

Thesis submitted for
the degree of
Doctor of Philosophy

April 2019

Abstract

Fault energies are exceptionally important, determining the activation of deformation processes in metals. This is especially true in the case of two phase γ/γ' superalloys. However there is currently no model for how the fault energies in these alloys vary with composition. This is a large issue due to the complex nature of superalloys, which typically feature more than 10 alloying elements. The main aim of this thesis is to design a model to predict fault energies for arbitrary alloying compositions of superalloys. This would provide a tool for alloy designers, allowing the choice of alloy compositions to make the alloys resist deformation, facilitating higher operational temperatures and efficiency.

In this research, first-principles calculations are undertaken using the projector augmented wave basis set in conjunction with the generalised-gradient approximation, as implemented in the Vienna ab initio simulation package. This allows the generation of input parameters for axial interaction models. Calculations are made for a large number of compounds and alloys to allow the assessment of how changing the alloy chemistry impacts the intrinsic stacking fault and superlattice intrinsic stacking fault energy. Using interpolation and fitting of these results it is possible to produce a model for arbitrary alloying compositions. Due to the high operational temperatures of superalloys the change in these fault energies with temperature was calculated (as first-principles calculations are traditionally only possible at 0 K). This was done using the quasiharmonic Debye model as implemented in the GIBBS package. The effects of temperature were found, in general, to be significantly less than the effects of alloying, providing validation for the

usage of first-principles calculations for high temperature alloys.

Publications

1. A. Breidi, J. Allen, and A. Mottura. First-principles calculations of thermodynamic properties and planar fault energies in Co_3X and Ni_3X $L1_2$ compounds. *Physica Status Solidi B*, 254:1–12, 2017. doi: 10.1002/pssb.201600839

2. A. Breidi, J. Allen, and A. Mottura. First-principles modeling of superlattice intrinsic stacking fault energies in Ni_3Al based alloys. *Acta Materialia*, 145:97 – 108, 2018. doi: https://doi.org/10.1016/j.actamat.2017.11.042

3. J. D. T. Allen, A. Mottura, and A. Breidi. First-Principles Modeling of the Temperature Dependence for the Superlattice Intrinsic Stacking Fault Energies in $L1_2$ $Ni_{75-x}X_xAl_{25}$. *Metallurgical and Materials Transactions A*, 49(9):4167–4172, 2018. doi: 10.1007/s11661-018-4763-4

With regard to the contribution of the author of this thesis to the papers 1) all calculations of Co_3X compounds at 0 K and a sizable contribution to the 0 K Ni_3X calculations, no contribution to the temperature decay calculations (note all results were retaken and refined for this thesis) 2) all calculations concerning temperature change 3) all of the calculations. Note also there is a fourth paper concerning the data for chapter 6 that is in the final stages of editing as of the date of publication of this thesis. Chapter 7 relates strongly to 1) chapter 8 relates strongly to 2) and 3), and chapter 6 relates strongly to the fourth paper currently in production.

Contents

List of Figures

List of Tables

Chapter 1

Introduction

Increasing the efficiency of jet engines and industrial gas turbines requires an increase in the temperature difference in the following equation $E_f = 1 - T_c/T_h$, where E_f is efficiency, T_c and T_h are the temperatures of the air and the air/fuel mixture at combustion respectively. The former is unable to be engineered, the latter is able, provided that the turbine blades can sustain the high temperatures ($\approx$1900 K environment temperature and $\approx$1350 K metal operating temperature[1]) for long periods without succumbing to oxidation, hot corrosion, low or high cycle fatigue or creep deformation. However in the first stage of the turbine it is creep that is the primary concern. One of the ways with which turbine blade alloys can be made more resilient to creep and hence be operable at higher temperatures, resulting in more efficient engines and gas turbines is by planar fault engineering. This means tweaking the alloy composition for the purpose of modifying the energies of different types of planar faults in the 2 main phases of a superalloy γ and γ'. In this research 2 fault types are investigated, the intrinsic stacking fault in

the γ phase and the superlattice intrinsic stacking fault in the γ' phase. The first way in which planar fault engineering can be used to make alloys more resistant to creep, is by enhancing the energy required (and hence the difficulty) for dislocations to shear the γ' precipitates, delaying a key part of the creep process. The second way is the manipulation of fault energies in the γ phase to make dislocation motion more difficult in the early stages of high temperature creep.

This project uses first-principles density functional theory (as implemented in the Vienna ab initio simulation package) to determine free energies and relevant volumes that can then be inserted into Axial Interaction Models to determine these fault energies in an array of binary and pseudo-binary alloys and compounds, which have relevance to superalloys (but do not constitute superalloys themselves). The reason for the usage of density functional theory over experiments is that whilst experimental determinations of fault energies are possible they typically are subject to a large array of difficulties and inaccuracies. For example the intrinsic stacking fault energies in pure nickel determined by experiment have a very large range of 79-450 mJ/m^2. A further reason in favour of the usage of this technique is that it can model situations that cannot be created experimentally such as compounds that are purely hypothetical but have relevance to a certain alloy system. Also it is known for its high calibre of accuracy. The reasons behind the usage of axial interaction models is that they require less computational expense than the supercell approach as they do not require an explicit calculation of the planar fault and operate on series approximation, produced from a series of different unfaulted structures. Despite the lack of an explicit fault calculation, the axial interaction models

were found to provide accurate planar fault energies in a large array of circumstances.

Also of importance is the fact that density functional theory calculations are only able to be performed at 0 K, due to the fact that the temperature the alloy operates at is 800-1000°C (environment temperature 1200-1400°C). It becomes necessary to validate the results at operational temperatures. To do this the quasiharmonic Debye model (as implemented in the GIBBS package) is employed in addition to the quasistatic approach (the changes in lattice parameter are the only finite temperature effect to impact the planar fault energy) which may initially appear to be crude but has produced accurate results in a wide array of circumstances. Ultimately it is hoped that the fault energies calculated in this thesis can inform the creation of superalloys which exhibit greater creep resistance.

Chapter 2

Theoretical Basis: Metallurgy of Superalloys

2.1 Ni-Based Superalloys

2.1.1 Introduction and History

Ni-based Superalloys have been, since conception, tightly linked to the development of jet engines for aircraft. Ni-based superalloys were first developed in 1929 independently by the three researchers Pilling, Bedford and Merica[2]. At this time the main thesis between researchers was that creating more robust ferritic steels was the way forward with regards to turbine development[2]. The first superalloys were created when small additions of Ti and Al were added to the "80/20" Ni-Cr alloy, resulting in vast improvements to the alloy's creep resistance[2, 3]. It was yet unknown to these researchers the cause for this improvement, this discovery was made shortly after the outbreak of World War II in

1940 by Bradley and Taylor[2, 4]. The cause was the introduction of a new phase, the γ' phase, of composition Ni_3Al, in the form of coherent precipitates (see figure 2.1) to the γ Ni matrix[2, 5]. The γ and γ' phases are both based off the Face Centred Cubic (FCC) structure however in the case of γ' the positions of the Ni and Al atoms are ordered, while there is no such ordering between Ni and any present alloying elements in the γ phase (see figure 2.2)[5].

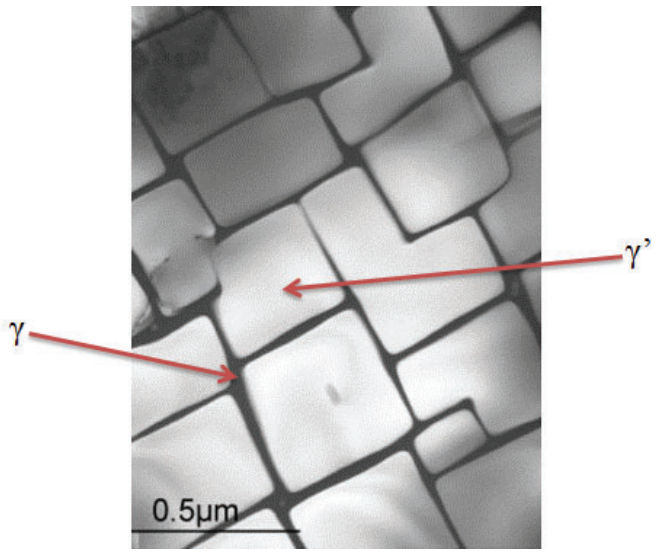

Figure 2.1: A micrograph depicting the microstructure of a Ni-based superalloy (adapted from [6]).

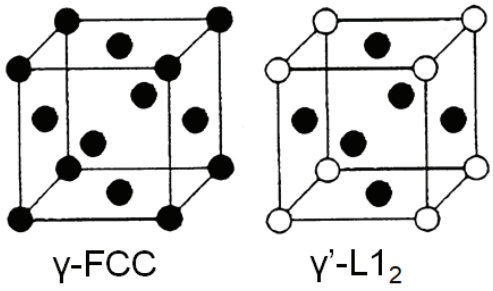

Figure 2.2: Diagram depicting the structure and element distribution of the γ and γ' phases, where black atoms are Ni atoms and white atoms are Al atoms (adapted from [7]).

Ni-based superalloys have gained in complexity over the years with a plethora of different alloying additions being added for various reasons[2]. Examples of additions include Co to raise the γ' solvus temperature[8, 9] and Cr for oxidation and corrosion resistance[8, 10, 11]. Because of this superalloys stand today as some of the most complex materials known to man[5]. Delicate control of these alloying elements has been required however as for example an over-abundance of Nb, Ta and Ti (added mainly to produce more γ') can result in the formation of the deleterious η phase, a topologically close packed (TCP) phase[5], which degrades the mechanical properties[2, 11, 12]. Ni-based superalloy development is split into 6 generations; a summary of the broad advances is as follows. The first generation of superalloys were relatively primitive and contained no Rhenium[8, 13]. Rhenium is exceptionally important in superalloy metallurgy due to the extreme increases in creep life that it offers; for example assuming operating conditions of 1173 K and 400 MPa creep life can be increased 10 fold by the addition of rhenium[5, 14]. Whilst this was originally thought to be due to the effects of rhenium clustering in

the γ phase, later works proved that this was due to the significant hindrance of the mass transport necessary for climb at the γ/γ' interfaces[14–16]. Hence the inclusion of rhenium in all later generations[13]. Generation 2 superalloys contain in the realm of 3 weight percent rhenium, with 3rd generation alloys increasing increasing contents to the excess of 5.5 weight percent, these alloys may also include hafnium (improves castability and environmental resistance[17])[8, 13]. In fourth generation superalloys the alloying addition ruthenium was introduced (in amounts of 3 weight percent in the case of EPM 102[18]). Ruthenium was found to modify the partitioning behavior of a number of refractory additions, causing them to partition more readily to the γ' phase, allowing for greater alloying content for the purpose of improving high temperature strength, as well as improved microstructure stability and creep rupture life (with fourth generation alloys having on average a 30 K higher operational temperature capacity then third generation alloys[18, 19]). Fifth generation superalloys further expanded the Ruthenium content to between approximately 5-6 weight percent as this chiefly facilitates higher rhenium additions (up to 6.9 weight percent)[13, 20, 21]. Fifth generation superalloys are characterized by superior creep resistance to previous generations[19, 20] with the alloy TMS-162 being the first alloy to exhibit a creep rupture life of 1000 hours at conditions of 1373 K and 137 MPa[13, 20, 21].

These improvements of the fourth and fifth generations have not been without drawbacks however as the increased presence of refractory elements degrades the resistance to oxidation of the alloys relative to previous generations[19]. The creation of the sixth generation alloy TMS-238 involved tuning the composition of TMS-196 (fifth generation)

for example reducing Mo content to the end of improving oxidation[19]. This alloy was found to have superior oxidation and corrosion properties to several alloys from previous generations[19]. In addition it possesses great creep properties exhibiting a creep rupture life of approaching 2000 h at 1373 K and 137 MPa[19].

The timeline of the development of the generations of superalloys is as follows. First generation alloys were first created in the mid 70s[5]. Second generation superalloys were then developed first appearing in the mid 80s[5]. Third generation alloys made their first appearance the the mid 90s, with fourth generation alloys first being developed around the year 2000[5]. The first appearance of fifth generation alloys in the literature was in 2004[20, 21]. Finally, to the authors knowledge the first sixth generation superalloy was TMS-238 which was first developed in 2012[19].

Superalloys were assigned the prefix super due to several reasons including the fact they have excellent creep resistance and oxidation resistance, fatigue resistance, ductility and resistance to hot corrosion as well as impacts[11, 22, 23]. The main reason however is due to a phenomenon called the yield stress anomaly (YSA hereafter) (see figure 2.3). The YSA is that for a set temperature range depending on the specific alloy in question, the yield stress is in defiance of the usual expectation to decline with increasing temperature (region I figure 2.3).

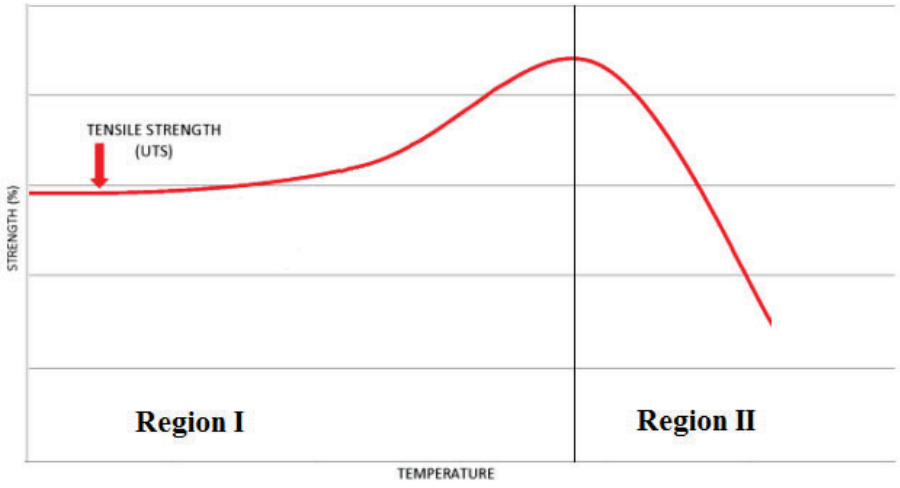

Figure 2.3: A graph depicting the yield stress anomaly, in region I the anomalous increase in yield stress occurs and in region II the yield stress anomaly is passed and the yield stress declines (adapted from [24]).

The exact details behind the causes of this phenomenon will be detailed in section 2.2.3. The final item brought in at this stage will be the introduction to single-crystal and polycrystalline alloys. The alloying additions added to both types of these alloys are in general different, for example B is added to polycrystalline alloys for the purpose of grain boundary strengthening, but this is a non factor in single-crystal alloys[25–27]. Single-crystal alloys for turbine blade applications were introduced in the 1980's and are known for superior properties in creep due to the fact that, in polycrystalline alloys, failure occurs at grain boundaries due to the process of cavitation[5, 28].

2.1.2 Applications of Ni-Based Superalloys

The main application of superalloys, as alluded to previously, is the use in jet engines for aircraft[2]. Where superalloys are employed in a jet engine (Trent 800 specifically, designed for use in the Boeing 777 series of planes, as of 2014 the second most purchased commercial airliner[29], and engine seen as largely typical of the industry) can be seen in Figure 2.4.

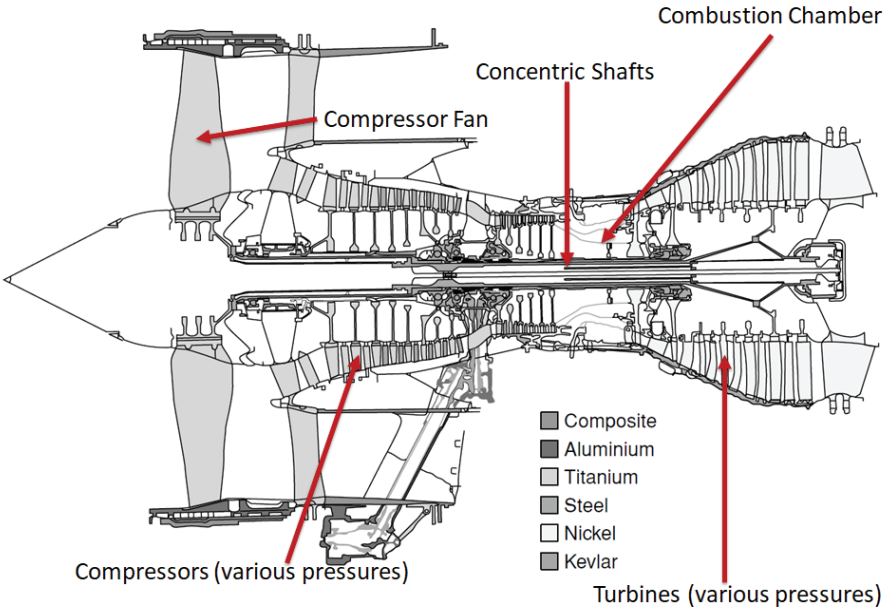

Figure 2.4: Diagram of a Trent 800 Engine with main components and the broad types of alloys employed in said components (courtesy of Rolls-Royce).

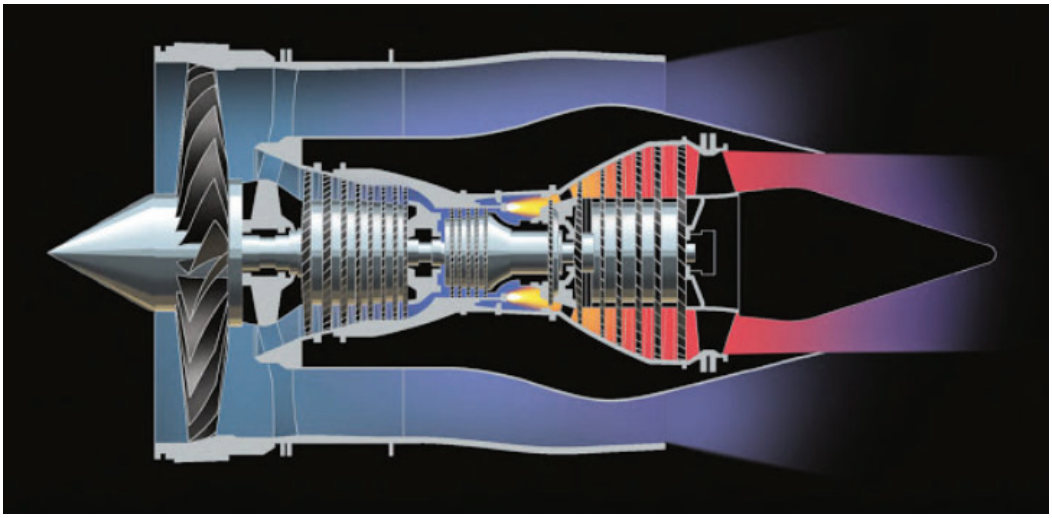

Figure 2.5: Diagram of a high-bypass turbofan engine demonstrating the air flow (taken from [30]).

The basic operation of said engine is as follows, a large quantity of air (in the realm of a tonne during takeoff[30]) is sucked in by the compressor fan, this air is utilized in one of 2 ways[5, 30]. Either passing through the core of the engine or through a bypass duct (see figure 2.5)[5, 30]. The relative quantities of air determine the bypass ratio 6.4:1 in the case of the Trent 800 meaning that ≈86% of the air passes through the bypass duct, with the remaining ≈14% passing through the core of the engine[31].

The air which passes through the core is compressed to high pressure by multiple compressors which compress the air to set pressures[5, 30]. This air is then mixed together with fuel in the combustion chamber and ignited[5, 30]. The high temperature gases expand in the combustion chamber and through a series of turbines operable, similarly to the compressors at set pressures[5, 30]. The result is two-fold, gases leave the right side of Figure 2.4 at significantly higher velocities to which they enter resulting

in a large degree of thrust (approximately 25% of total engine thrust, and the spinning turbines are connected to a series of shafts which facilitate the running of the compressor fan in addition to the compressors[5, 30]. The bypassed air contributes around 75% of the thrust due to a large quantity of air being accelerated to a modest velocity (only slightly greater than the speed of the plane itself)[30].

Upon observation of figure 2.4 it can be seen that the Ni-based alloys are used extensively in the turbines, high pressure compressors and combustion chamber (details behind the selection of the other alloys as well as operation are detailed in [30] and [32]). There is a major incentive to increase the temperatures which these alloys can sustain for the purposes of driving efficiency and fuel economy by increasing the turbine entry temperatures (TET's hereafter) of these engines. Even small increases in the TET could reap massive fuel savings in the grand scheme of things[3, 33].

It is a worthwhile aside at this point to mention that improvements to the compositions of Ni-based superalloys are not the only factor in improving operational temperatures and service lives, one of the key innovations in superalloy turbine blades was the introduction of cooling passages in the blades (see figure 2.6)[34–36]. A second major innovation was the introduction of thermal barrier coatings in addition to bond coats, these two innovations restrict the temperature the superalloy can reach during operation[33, 34, 36].

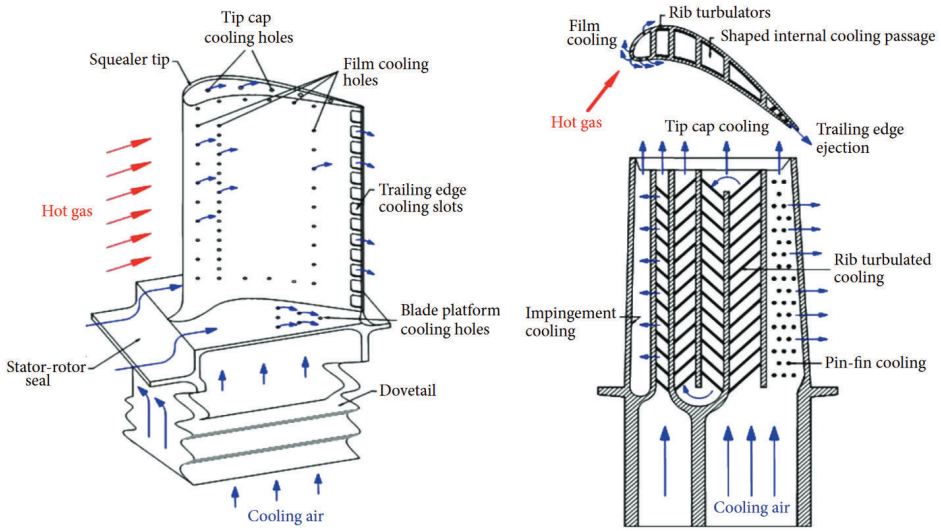

Figure 2.6: Schematic diagram of a superalloy turbine blade with cooling passages (taken from [35]).

Superalloys are utilised in a somewhat similar vein in the fossil fuel industry, as turbine blades in the gas turbines used to generate power[34]. Here similar concerns about improving fuel economy by increasing the operational temperatures, the magnitude of this concern is emphasised by the fact there are large efforts in Japan, Europe and the USA to accomplish this[37]. This is with good reason as enhancing the TET by 30 K can lead to a 1 percent increase in efficiency and 15 million USD in savings over the operational lifetime of the turbine[34, 38].

2.2 Planar Faults

2.2.1 Introduction

Planar faults on the {111} planes in both the γ and γ' phases are highly important in Ni-based superalloys as they, and the interplay between the various energies, inform significantly the metallurgy including heavy influence on the creep mechanism and properties (they are also very significant to the aforementioned yield stress anomaly). In both phases (γ and γ') there are multiple different types of planar faults that will be detailed in this section.

2.2.2 Different Types of Planar Fault

γ phase

In the γ phase there exist 2 types of planar fault the first is the intrinsic stacking fault (ISF hereafter) and the second is the extrinsic stacking fault (ESF hereafter). An ISF can be created by either the removal of a plane or a shift of $\frac{1}{6} < 21\bar{1} >$ (for example taking the stacking sequence from ABCABCABC to ABCA|CABC where | denotes the shift) this makes the second A and C planes locally exhibit a HCP structure[5, 39, 40]. An ESF can be created by the addition of a plane or 2 shifts of $\frac{1}{6} < 21\bar{1} >$ on neighboring planes (for example making the stacking sequence ABCA|C|BCABC) and again the second A and C exhibit a HCP structure[39]. Hence an ESF can be thought of as a combination of 2 ISFs. It is important to note that stacking faults do not break any bonds in the process of formation[39]. The reason that these faults exist is due to free energy concerns. The

energy of a dislocation is proportional $|\hat{b}|^2$ where $\hat{b}$ is the Burgers vector, this means that if a dislocation can dissociate whilst remaining stable it can increase slightly its total dislocation length overall but decrease its total energy. The fact that stable stacking faults exist on the $\{111\}$ planes in FCC means that there is a preference relative to other planes for glide to occur on these planes, contrast this with BCC (where no stable stacking faults exist) where there is not a strong preference for glide on any single set of planes[41]. In the majority of cases the energies of ISFs are between 10-200 mJ/m^2[41]. An ISF is created by the following reaction[41]

$$\frac{1}{2}[110] \rightarrow \frac{1}{6}[21\bar{1}] + ISF + \frac{1}{6}[121] \tag{2.1}$$

note that in $\{111\}$ in FCC $\frac{1}{2} < 110 >$ is a perfect dislocation (it can move without creating a stacking fault).

γ' phase

There are analagous stacking faults to the ISF and ESF in the γ' phase, they are labelled the Superlattice intrinsic stacking fault (SISF hereafter) and the superlattice extrinsic stacking fault (SESF hereafter). A SISF can be formed by removing a $\{111\}$ plane or by shifting said plane by $\frac{1}{3} < \bar{2}11 >$[5]. A SESF likewise is produced by 2 shifts of $\frac{1}{3} < \bar{2}11 >$ on neighboring planes and hence can be created by the combination of 2 SISFs[34]. In addition to these a complex stacking fault (CSF hereafter) can be produced by a shift of $\frac{1}{6} < \overline{11}2 >$. There is another type of stacking fault the complex extrinsic stacking

fault (CESF hereafter) which is created when on a neighbouring plane to a SESF a CSF is created[42]. The CESF has yet to be observed experimentally but is at this stage theoretically predicted to be stable[42]. The final fault type introduced here is the anti-phase boundary (APB hereafter) which can be produced by a shift of $\frac{1}{2} < 110 >$. APBs can exist in many planes, all of which have different energies mainly due to the reasoning present in the proceeding paragraph[5, 43].

An important concern which arises only when dealing with ordered substances is at which level the creation of the fault changes the nearest neighbours and how this plays into the energy[5, 44]. For example the CSF and APB{111} and APB{110} change the first nearest neighbours creating forbidden Al-Al and Ni-Ni bonds whereas SISF, SESF and APB{100} modify higher order nearest neighbours (second order in the case of APB{100}[43] and beyond second order in the case of SISF[45, 46]). Note the stacking sequences for all of the faults discussed in this section are depicted in figure 2.7.

2.2.3 Yield Stress Anomaly

It is time for elaboration on the YSA which was introduced in section 2.1.1. It is important to first note that the shift required to create the APB is the same as that caused by the perfect dislocation in the γ phase $\frac{1}{2} < 110 > \{111\}$. This dislocation in the γ' phase however is not a perfect dislocation; the reason for this is that whilst the γ and γ' phases share the same close packed planes $\{111\}$, in the case of the γ' phase the shortest lattice vectors are different, $< 100 >$ instead of $\frac{1}{2} < 1\bar{1}0 >$. Additionally in the case of the γ' phase these vectors do not lie in the close packed planes. The result

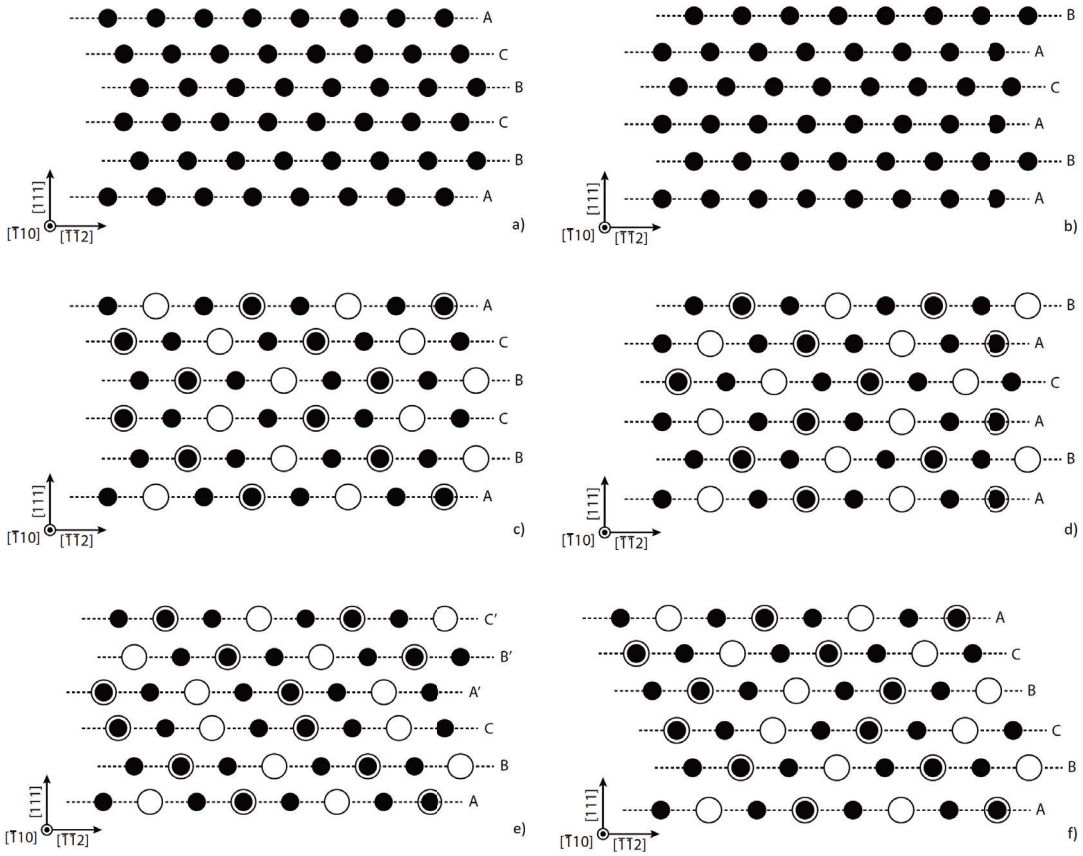

Figure 2.7: The stacking sequences for each of the fault types discussed in section 2.2.2. Figure 2.7a-2.7f are the ISF, ESF, SISF, SESF, APB and CSF respectively. Black atoms are nickel atoms, white atoms are aluminium atoms, hence a white ring around a black atom refers to an aluminium atom behind a nickel atom.

of this is that in order for the $\frac{1}{2} < 110 > \{111\}$ dislocations to gain entry into the γ' precipitates they must travel in some form of paired configuration after the precipitate has been sheared, an example of which depicted in figure 2.8[5].

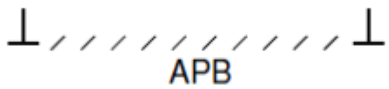

Figure 2.8: Diagram of two-fold superdislocation dissociation; a mechanism for $\frac{1}{2} < 110 > \{111\}$ dislocations to travel through the γ' phase (adapted from [5]).

It is necessary to introduce two terms in the metallurgical nomenclature at this point, whilst in the γ' phase a $\frac{1}{2} < 110 > \{111\}$ dislocation is referred to as a superpartial and the combination of two of these is dubbed a superdislocation[5, 47]. Further energetic stability can be gained by the dissociation of the superpartials in figure 2.8 each dissociating into two Shockely partials $\frac{1}{6} < 211 > \{111\}$ resulting in the configuration displayed in figure 2.9[48].

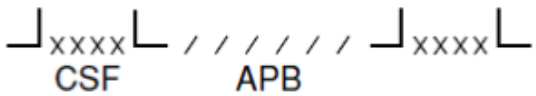

Figure 2.9: Diagram of four-fold superdislocation dissociation; a mechanism for $\frac{1}{2} < 110 > \{111\}$ dislocations to travel through the γ' phase (adapted from [5]).

Recall from the previous subsection that the APB{111} is much higher energy than the APB{100}, the desire of any system is to minimise its free energy, hence the APB transferring crystallographic by the process of cross-slip is beneficial to this end[5, 49]. It is important to remember that the difference between the APB on these 2 planes is not the only factor resulting in the promotion of cross-slip and that elastic anisotropy also plays an equal role[5, 50]. In order for this cross-slip to occur however the recombina-

tion of Shockely partials to form a superpartial is necessary beforehand and is achieved through a thermally activated process called constriction[49]. Once this has happened the superpartial cross-slips onto the {100} plane, when the entire length of the APB is present on the {100} plane the superpartial is at liberty to reduce its energy by dissociating into Shockely partials separated by a CSF on another {111} plane[34]. This configuration is named a Kear-Wilsdorf lock and it severely hinders dislocation motion in the γ' phase (The process of production of this lock is displayed in figure 2.10)[34, 49]. Due to the thermal activation of constriction the higher the temperature the more locks can be formed[43, 49]. However as implied by figure 2.3 this does not carry on forever, the resistance to deformation the γ' precipitates provide at temperatures above the peak is undermined by the fact that unaccompanied $\frac{1}{2} < 110 > \{111\}$ dislocations simply are able to bypass the γ' precipitates without much shearing, negating the majority of their strengthening effect[3].

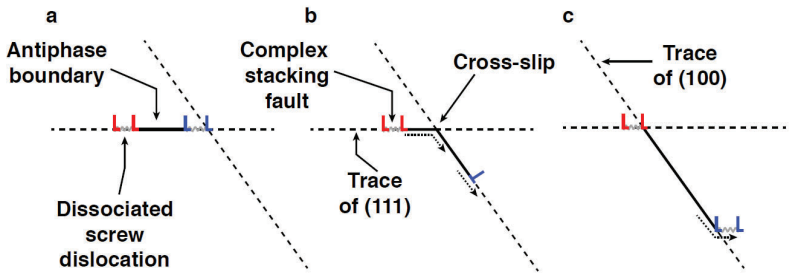

Figure 2.10: Diagram of the process governing the creation of a Kear-Wilsdorf lock (taken from[34]).

Note that there exists a transition between these two deformation mechanisms, a short temperature range where the deformation is caused by γ' precipitate shearing by a

$\frac{1}{3} < \bar{1}12 >$ dislocation (note can be refereed to as a super-Shockely partial[25]) according to the following reaction at the γ/γ' interface[3, 51].

$$\frac{1}{2} < 011 > + \frac{1}{2} < \bar{1}01 > \rightarrow \frac{1}{3} < \bar{1}12 > + SISF + \frac{1}{6} < \bar{1}12 > \tag{2.2}$$

where the Shockely partial is left at the γ/γ' interface[3, 51, 52]. Alternatively SISFs can be formed by the following dissociation mechanism at the γ/γ' interface[53, 54].

$$\frac{1}{2} < \bar{1}01 > \rightarrow \frac{1}{3} < \bar{2}11 > + SISF + \frac{1}{6} < 1\bar{2}1 > \tag{2.3}$$

2.2.4 Effects of Alloying Elements

This project focuses extensively on the effects of alloying additions in Ni-based superalloys and how they impact upon fault energies. It is necessary to also include a discussion of the many changes alloying additions cause external to fault energy modification. Any element added is certain to have other effects beyond its fault energy changes alone. This subsection contains a list of alloying elements and their various advantages and drawbacks in Ni-based superalloys (note this list makes no claim to be exhaustive due to the complex nature of Ni-based superalloys).

Cu, Si, Mn and Sb segregate to grain boundaries resulting in inferior creep ductility and hot malleability as grain boundaries are weakened (note Mn can counteract the negative effects of S but compositions must be low as it degrades grain boundaries)[11]. Si has the secondary effect of reducing hot ductility as inclusions become more commonplace[11].

Sn can also result in degradation of creep ductility due to segregation[11], Sn is a double-edged sword however as it can result in large increases in stress rupture life[11]. Nb, W, Ta, Mo and Ti are effective at reducing misfit stresses, Cr, Co and Fe are still, but somewhat less effective[5, 11, 23, 55](note however that Ti degrades oxidation resistance and can lead to inter-granular corrosion, whilst increasing somewhat hot corrosion resistance)(also note Re increases misfit[10, 11]). There exist multiple elements which are added for the purpose of solid solution strengthening including Cr, Fe, Mo, Re (note has strong influence on liquidus temperature[5]), Ta, W, Co (note mild) and Nb, where Nb and Ta solidus and melting temperatures, and Co increases the γ' solvus temperature, W increases the solidus temperature as well[8, 10, 56]. Cr can however if present in excessive quantities (above 30%) result in the destabilisation of the γ and the promotion of TCP phases[10, 11]. Si is known for promoting the nucleation of the β phase, whilst Al, Mo and Ta discourage β formation, note Fe can also promote η formation (Ta can also have the added benefit of reducing the likelihood of freckling during solidification[56]).

Cr, Co, Mo and W can reduce the rate at which the γ' precipitates coarsen in service[5, 11] Ta, Ti, Nb, Va and Mo are known for the stabilisation of MC (note C must be present in quantities above around 0.2wt% for MC carbide to form[5]) type carbides which can improve creep properties in polycrystalline alloys[11, 56](it is also of note that Nb promotes the formation of γ'' which can result in strengthening (note in nickel-iron alloys this is used as the main strengthening phase), but can also promote the production of the δ phase which degrades mechanical properties (Co may potentially offset this however, Cr, Mo and W can also contribute to deleterious phase formation at high

compositions)[5, 10, 23, 56]). B is known for strengthening grain boundaries by resulting in the propensity for carbides in the cellular morphology being reduced in addition to improving hot ductility and rupture life (if present in large quantities)[8, 11]. Mo and W in high abundances result in the presence of M_6C type carbides, which depending on morphology can be beneficial or negative (note that high Si content causes these carbides to preferentially form at grain boundaries)[11]. Cr is known for the formation of the Cr_2O_3 compound (note that this can break down at very high temperatures) which is known to defend against hot corrosion and oxidation (note Ce can also be added for the purpose of improving oxidation resistance[8])[23]. Co is known for the improvement of hot corrosion resistance due to modifications in diffusivity (Th and La are also added for the purpose of hot corrosion resistance)[8, 11].

Al in addition to being critical for Ni_3Al formation improves resistance to oxide spalling and oxidation[11]. Si and Mn when present in small amounts can also improve oxidation resistance, but Si can in some instances make oxide spalling easier[11]. Note at this stage that if an element is insoluble in Ni then it will have embrittling effects for example Bi, Th, TI[11]. P is infamous for causing cracking and is one of a group called tramp elements which include Si, S, Pb, Bi, Te, Se and Ag all of which if present cause degradation of mechanical properties[8, 11]. Zr can offset the harmful effects of S by reducing the presence of $M_{23}C_6$ oxides, in addition to improving ductility and grain boundary strength[10]. Mn also improves the stress rupture life by offsetting the effects of S and Hf also offsets S in a similar vein and improves ductility and in a similar vein improves ductility and strength[8, 11, 57]. Y has in some alloys been added for the

purpose of improving the longevity of coatings[8]. Oxidation resistance can be improved in some alloys by the addition of La[8]. There is another group of elements known as γ' stabilisers which promote ordered phases.

2.3 High-Temperature Creep Mechanisms

As mentioned in section 2.1.1 creep properties are highly important to superalloys. One reason emphasising their importance is the fact that the definition of failure for a superalloy turbine blade is when it has extended slightly due to creep and no longer has dimensions suitable to the task at hand[5]. As one may assume the creep properties and mechanisms of single-crystal and polycrystalline alloys differ[5]. The details surrounding this will be covered in the proceeding subsections.

2.3.1 Polycrystalline Alloys

Creep in polycrystalline alloys typically takes place in 3 phases in analogy to pure metals (the primary, secondary and tertiary phases), consult figure 2.11[5, 58].

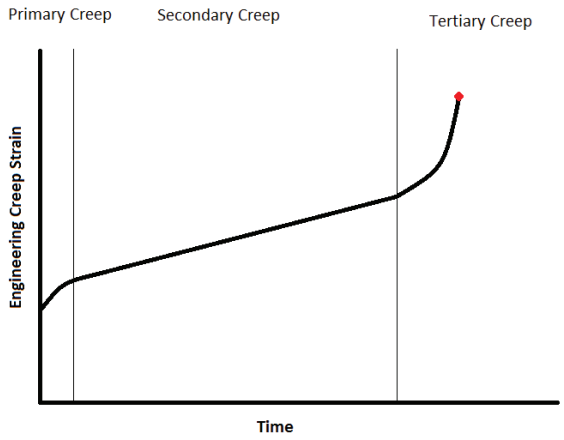

Figure 2.11: The 3 phases of creep in a polycrystalline alloy, the red diamond represents where the alloy fails (note diagram is simply illustrative and is not derived from real data).

The reason for the existence of these 3 phases is as follows, the primary phase occurs as the mechanisms for dislocation multiplication are more active then those of dislocation annihilation resulting in an initial transient[5, 58]. In the secondary phase the aforementioned mechanisms are equally prominent resulting in a straight line (note the secondary phase can also be called steady state creep)[5, 58]. In the tertiary phase the line on figure 2.11 rapidly increases as the alloy accelerates toward failure, this is due to the activation of further mechanisms, most prominently grain boundary cavitation; although crack formation (typically not very prominent in Ni-based superalloys) and rafting and associated weaknesses could also be activated[5, 58].

The creep of these alloys is well described in the secondary phase by the equation of

power law creep[5, 58, 59].

$$\frac{d\epsilon}{dt} = A\left(\frac{\gamma}{G\hat{b}}\right)^3 \left(\frac{\sigma}{G}\right)^n e^{\frac{-Q}{TR}} \tag{2.4}$$

Where ϵ is the creep strain, Q is the activation energy for creep (typically related strongly to the energy of self diffusion), T is the temperature, R is the gas constant, σ is the applied stress, G is the shear modulus, $\hat{b}$ is the burgers vector, γ is the fault energy and n is described as the stress exponent[5, 58]. A is represented as follows

$$A = \frac{2KD_0}{3M\hat{b}^5} \tag{2.5}$$

where K is the kinetic constant, M is the dislocation multiplication constant and D_0 is called the pre-exponential term[5, 58]. Returning to n, the value is typically between 4.5 and 5 but can be in some alloys around 3 (these are called class I alloys, the others named class II)[5, 58]. Class I behaviour is typically motivated by a large difference in the radii of solute and solvent[5, 60]. Class II alloys are known for creep being affected significantly by the stacking fault energy and a significant degree of primary creep. Note also that n typically increases with time[5, 60].

Creep resistance in polycrystalline alloys can be increased by alloying (consult section 2.2.4) increasing the size of the grains (fewer grain boundaries means less prominent cavitation effects) and smaller but more numerous γ' precipitates (due to the change in deformation mechanism from shearing to Orawan looping which occurs above a γ channel width of 0.5μm) and tertiary γ' precipitates[58].

2.3.2 Single-Crystal Alloys

In contrast to polycrystalline alloys, there are multiple regimes that can be observed dependant on the applied stress and temperature[5, 61].

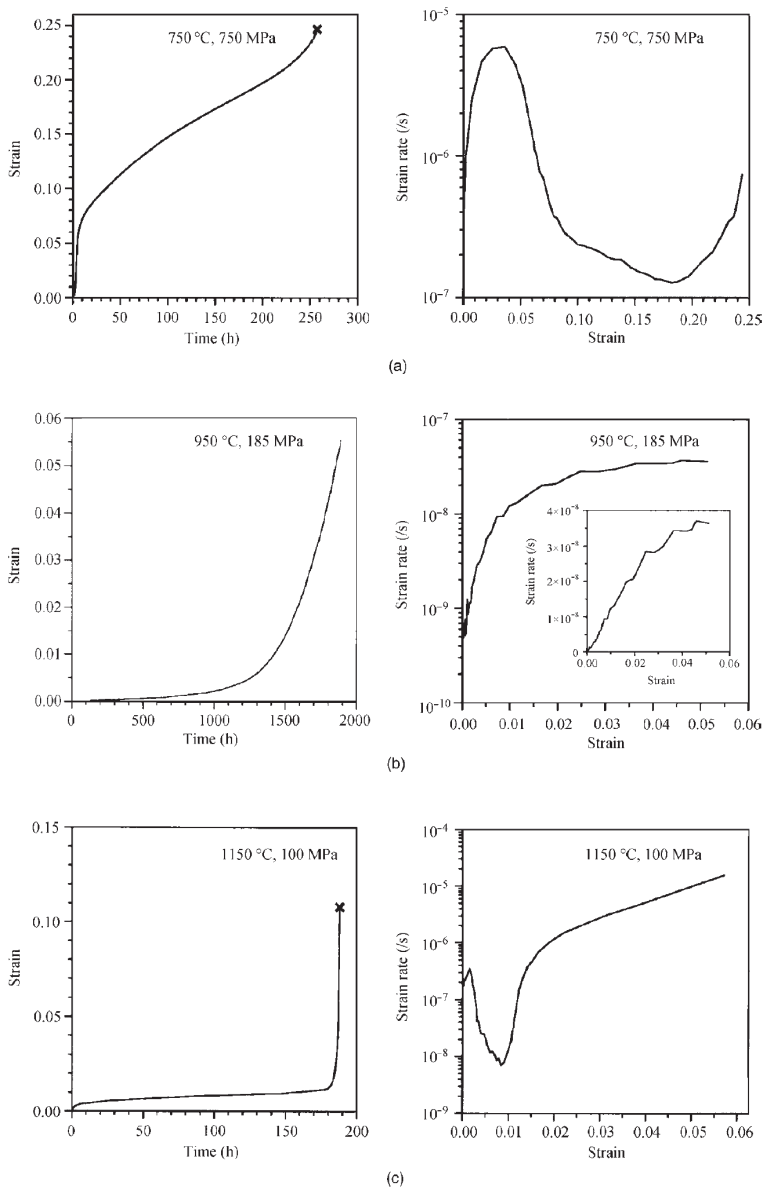

Figure 2.12: Creep data for the CMSX-4 alloy a) showcases what happens under lower operating temperatures and high stresses, b) shows what occurs under low stress and higher temperature c) shows what occurs under very high temperatures and low stresses (Whilst this data is specific to CMSX-4 note that similar curves have been observed in other single-crystal alloys but specific temperatures and stresses transitioning between them will be different)[5] (taken from [61]).

In Figure 2.12b the system of tertiary creep is in effect, the curve on the left can be modelled to a high accuracy as an exponential, note this disregards the incubation period where the dislocations are first created[5, 62]. In the incubation period dislocation multiplication is heavily favoured to occur in channels that are perpendicular to the applied stress due to the effect of enhancement by the γ/γ' misfit[5, 62]. In this system $\frac{1}{2} < 110 > \{111\}$ dislocations are rarely observed to shear the γ' precipitates, coarsening of the γ' precipitates is absent in this system. The leading sections of the extended dislocations are found to be screw, but mixed character dislocations are found to be deposited at γ/γ' boundaries, also typically only a few slip systems are active[5, 34, 62].

In the latter stages of ternary creep shearing of the γ' precipitates begins to occur. At these heightened temperatures shearing will occur as detailed by figure 2.13 (The transition between shearing mechanisms occurs near 1123 K [34, 63]), by pairs of $\frac{1}{2} < 011 > \{111\}$ superpartials separated by an APB[34, 63]. These shearing events occur as the lattice misfit and applied misfit stresses rise high enough levels such that shearing can occur[34, 63].

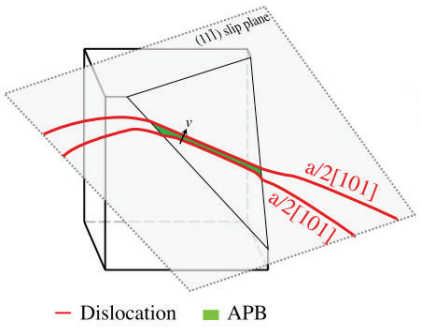

Figure 2.13: The high temperature (above 1123 K) shearing mechanism in the latter stages of tertiary creep in Ni-based superalloys (adapted from [63]).

In figure 2.12a there appears a prominent initial transient known similarly in polycrystalline alloys as primary creep[5]. Primary creep is only activated when a certain stress level is reached (in the case of CMSX-4 it is 500 MPa[5]) the further above this limit the greater amount of deformation will occur in primary creep[5, 61, 64]. In contrast to the tertiary creep system significant anisotropy in the deformation occurs resulting in stretching of the component in a specific axis[5]. Primary creep occurs due to the $< 112 > \{111\}$ slip system[5, 64, 65]. Unlike in tertiary creep this time γ' precipitates are sheared. The way the relevant dislocations in the $< 112 > \{111\}$ slip system are created is by the reaction in (2.3)[5, 64, 65]. The next reaction that occurs is between the right hand side of (2.3) and two more $\frac{1}{2} < 110 > \{111\}$ dislocations[5, 64],

$$\frac{1}{3} < \bar{1}12 > + SISF + \frac{1}{6} < \bar{1}12 > + \frac{1}{2} < 011 > + \frac{1}{2} < 011 > \rightarrow \frac{1}{3} < \bar{1}12 > + ...$$
$$SESF + \frac{1}{6} < \bar{1}12 > + APB + \frac{1}{6} < \bar{1}12 > + SISF + \frac{1}{3} < \bar{1}12 > \quad (2.6)$$

The equations (2.3) and (2.6) are represented diagrammatically in figure 2.14[5, 64].

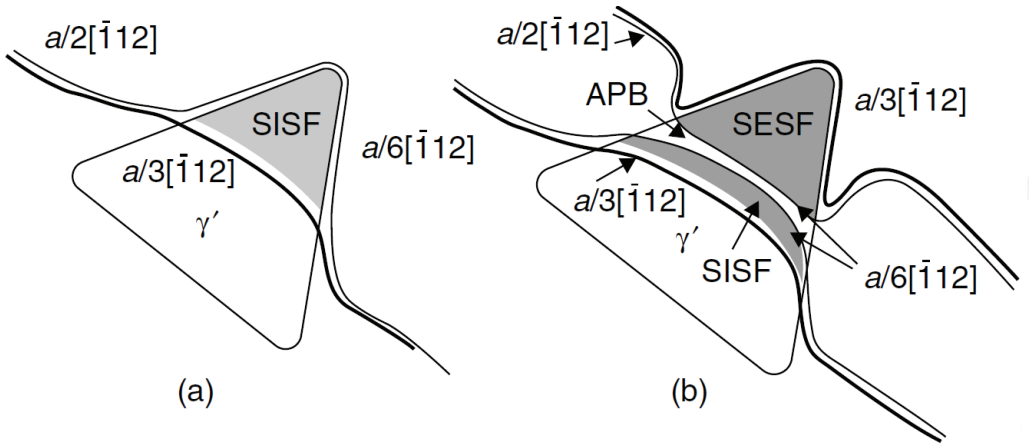

Figure 2.14: Diagrams of the the shearing mechanism of primary creep a) represents equation (2.3) and b) represents equation (2.6)(taken from [5]).

The formation in Figure 2.14(b) is free to move in a glissile fashion until it encounters an additional $\frac{1}{2} < 110 > \{111\}$ dislocation at a γ/γ' interface, this process is what results in the transition between primary and secondary creep[5]. This transition typically also corresponds to the relevant channels depending on misfit becoming full of dislocations[33] resulting in an equilibrium established with stable dislocation structures in the γ channels. Secondary creep and the mechanisms behind how it operates have scarcely been investigated[33]. It was the conclusion of Rae[33] that the core mechanisms behind primary and secondary creep are the same. However now due to the stable dislocation structures the rate determining process changes from dislocation propagation (short as the distance dissociated $a < \bar{1}12 >$ can travel before encountering another dislocation or a network thereof[33, 65] is of the order of precipitate size) to generation via equations (2.3 and 2.6). Notice in general an alloy with high primary creep rate will have high secondary creep rate[33]. Primary creep can be reduced by either narrowing the γ

channels or reducing fault energies but too much of these effects can be detrimental[33].

There is also another regime represented in figure 2.12(c) called the rafting system; which initiates by the formation of equilibrium dislocation networks (of mostly edge character) at γ/γ' interfaces and the rafting of γ' precipitates (the combination of the precipitates along a specific direction to form a layered morphology[5, 28, 66]. These networks reduce the misfit stresses at the γ/γ' interfaces[5, 66].

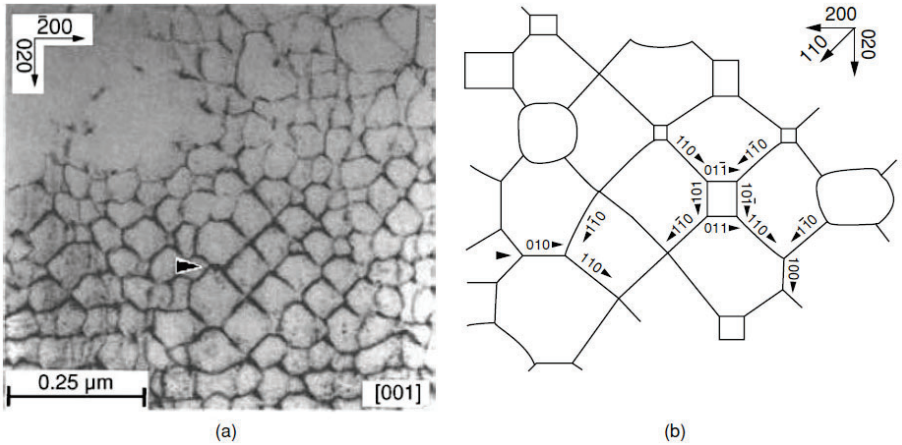

Figure 2.15: (a) A micrograph depicting a dislocation network at a γ/γ' interface, (b) a schematic diagram of said network (note the arrows in (a) and (b) correspond to the same position) (taken from [5]).

These networks require the presence of $\frac{1}{2} < 110 > \{111\}$ type dislocations on all of the $\{111\}$ planes, where a strong creep strengthening effect is observed when dislocation spacing is small, due to the hindrance afforded by these networks of dislocation shearing and the enhancement of rafting[5, 20, 67]. Once these networks are developed and the misfit stresses relaxed; mass transfer of γ and γ' forming elements into the relevant channels (depending on applied stress direction and misfit[28]) can occur facilitating

rafting, which then reduces the prevalence of $\frac{1}{2} < 110 > \{111\}$ dislocations[5, 61]. The development of fully-fledged rafts corresponds with the cessation of the initial transient and the start of the flat region in figure 2.12(c)[5]. The rapid acceleration to failure is caused in inconsistent time-frames even in the same alloys, as it is caused by either cavitation in the interdendritic regions at porous areas formed during casting[5, 61], or alternatively the pores can be produced by the formation of TCP phases[5, 61]. Hot isostatic pressing on average delays the occurrence of this rapid increase[5].

2.4 Other Metallurgical Features that Impact Mechanical Properties

2.4.1 Precipitate Morphology

Precipitate Morphology impacts largely the mechanical and creep properties[68]. Precipitates can exhibit many forms ranging from spherical all the way to solid state dendrites[5, 69] (see figure 2.16).

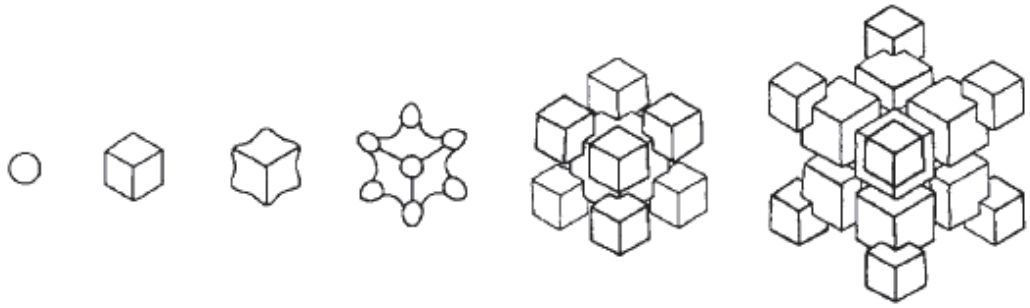

Figure 2.16: A series of diagrams depicting the different morphologies that γ' precipitates can exhibit (adapted from ref.[69]).

Here the concept of the lattice misfit σ_{misfit} enters the field of play. It can be represented as follows

$$\sigma_{misfit} = 2 \cdot \left(\frac{a_{\gamma'} - a_{\gamma}}{a_{\gamma'} + a_{\gamma}} \right) \tag{2.7}$$

where $a_{\gamma'}$ and a_{γ} are the lattice parameters of their respective structures[5, 34, 68]. σ_{misfit} can be either positive or negative but generally speaking for Ni-based superalloys it is negative[34]. Due to how close the lattice parameters of the γ and γ' interfaces are misfit is small in these alloys[5]. This has multiple effects the first one is to promote low

interfacial energy and hence coherency of the γ/γ' interface[5]. Due to this coherency a cube-cube orientation occurs between the matrix and the precipitates[5]. σ_{misfit} can be altered strongly by adding specific alloying elements (by extension altering morphology) with significantly different atomic radii (note that $a_{\gamma'}$ is less sensitive to this effect then a_{γ})[5, 23]. Note that σ_{misfit} varies with temperature due to the differential thermal expansion of the two phases[23, 28]. The misfit chiefly informs the timing during ageing of the first transition spherical to cuboidal, for low $|\sigma_{misfit}|$ alloys precipitates grow larger before the transition than for high $|\sigma_{misfit}|$ alloys[5, 69]. The more ageing is done to an alloy the further to the right of figure 2.16 the precipitates will progress[5, 69].

Other features of precipitate morphology include tertiary γ' precipitates (less than 50nm in diameter[70]) which are known to result in strengthening in creep [58, 71]. The formation of tertiary γ' precipitates is dependant on the cooling rate with fast rates suppressing their formation and slow rates resulting in formation near the end of the cooling process[70].

Another metallurgical feature which was mentioned in previously was rafting (note the direction of rafting depends on the misfit). The use of a rafted microstructure in single-crystal superalloys was found to improve creep properties in some but not all cases[28, 72, 73]. Note the extraordinary temperature dependence of rafting where an increase of 50 K can result in rafting of single-crystal Ni_3Al accelerating by a factor of 5[74].

2.5 Co and CoNi-Based Superalloys

It important for the reader to note that this section will only draw attention to parts of the discussion where these types of alloys differ from those of the previous sections of this chapter (Ni-based superalloys). It is important to note however; that there has been much less experimentation in these two types of alloys, hence certain behaviours and mechanisms are not known in as much depth if any.

2.5.1 Introduction and History

Co-based superalloys existed for many decades but traditionally relied on carbides for strengthening meaning their usage was fraught with difficulty at high temperatures due to a range of factors including propensity for fatigue cracking[75, 76]. Co-based alloys have made a resurgence since 2006 when the ordered $L1_2$ phase $Co_3(W_xAl_{1-x})$ was discovered by Sato et.al[77] (Co-based superalloys will be used to refer from this point forward as the γ' strengthened type only with the carbide strengthened type playing no further role in the discussion)[23]. This discovery was of great interest as Co-based alloys have a higher melting temperature typically by 50-150 K then their Ni-based counterparts meaning the potential for higher TET's[25, 34, 78]. It was discovered however that a new issue arises; the solvus temperature is lower by 100-300 K than the melting temperature of most Ni-based superalloys (note that melting and γ' solvus temperatures are close in Ni-based alloys, hence the melting temperature can be thought of as the limiting temperature); meaning that dissolution of the γ' phase occurs significantly before melting, hence the advantage of higher melting temperature is yet unexploited[25, 34, 63]. Note whether

$L1_2$-$Co_3(W_xAl_{1-x})$ is stable or metastable is heavily dependent on temperature, for example it was found to be stable at 1173 K and metastable at 1273 K by Sato et.al[77]. DFT computer simulations have confirmed metastability at 0 K[79], meaning that the observed stability must be a result of finite temperature effects such as vibrational entropy, thermal electronic excitations and configurational entropy[79, 80]. The topic of stability of γ' in Co-based alloys has been subject to much research interest[77, 79, 80]. Rhein produced a figure using first-principles simulation, of the stability energy vs composition at various temperatures (figure 2.17)[80]. Where the stability energy is defined as the difference in gibbs free energy between the $L1_2$ structure and the three phase mixture of; pure Co (HCP transforms to FCC above 723 K), Co_3W ($D0_{19}$) and CoAl (B2)[80].

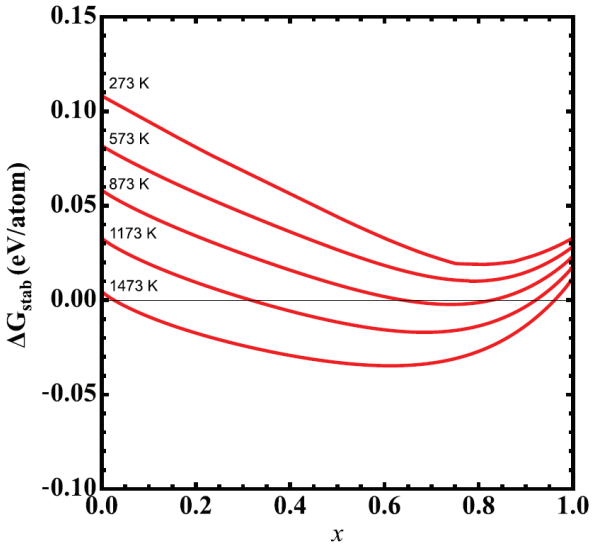

Figure 2.17: The stability energy of $L1_2$-$Co_3(W_xAl_{1-x})$ vs composition x at a series of temperatures (taken from [80]).

There has been a drive to, through alloying, increase the solvus temperature and γ'

percentage in these alloys[25, 75]. Co-based alloys are showing promise as despite their early stage of development (particularly compositional development) relative to Ni-based superalloys they already have been shown to possess similar creep properties and have the potential for higher fatigue resistance[25, 81].

During this time experimentation with CoNi-based superalloys (superalloys with significant compositions of both Co and Ni) has also been taking place. The reasoning for this is that Ni will lead to an increase in the magnitude of the γ' phase field and that some degree of substitution of Co for Ni in the γ' phase should result in the increased stability of γ'[82, 83]. It is not yet known whether alloys of these two types that are vastly superior to traditional Ni-based superalloys will materialise[82]. However if only similar properties end up being realised, significantly more flexibility will be afforded to alloy designers[82].

2.5.2 High Temperature Creep Mechanisms

Titus et.al used experimental data to derive figure 2.18 which is a speculative diagram as to how the energies of the SISF and APB vary as the Ni content is increased[34, 63].

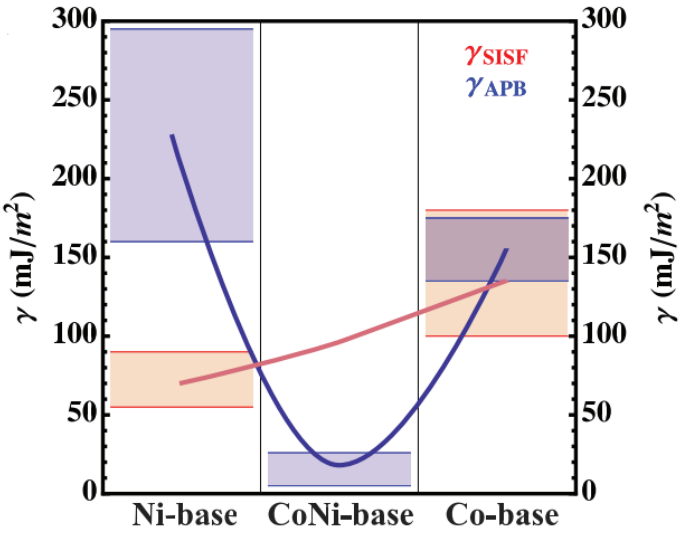

Figure 2.18: How the energies of the SISF and APB are projected to vary with Ni content in superalloys (note this diagram is mostly based on the observations of shearing systems in different alloys not direct measurement) (taken form [63]).

This diagram was produced by the observation of the following shearing mechanisms in the 3 types of alloys at temperatures in excess of 1123 K (see figures 2.13 and 2.19).

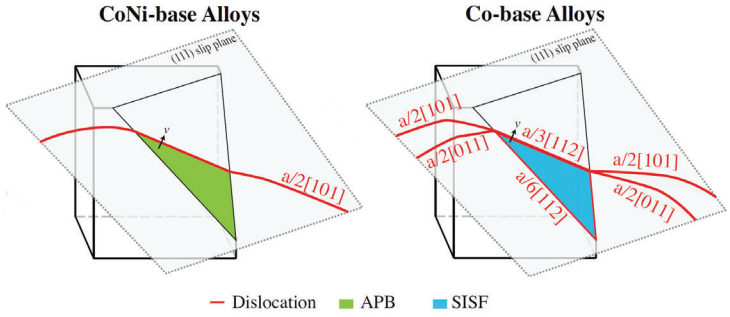

Figure 2.19: High temperature (excess of 1123 K) predominant shearing mechanisms in CoNi and Co-based superalloys. (adapted from [63]).

Note that fault energies are not the sole factor in the determination of which of shearing mechanism will be prominent and that misfit and interdiffusion rates as well as

other properties are likely to have some role[34, 81]. It initially seems paradoxical that despite the significantly lower energy of the SISF relative to the APB that in Ni-based alloys the shearing occurs by APB[34, 63]. The reasoning behind this is that despite the lower SISF energy the arrangement of two superpartials and an APB is lower energy then any SISF shearing configuration[34, 63].

In an experiment at 1123 K Co-based alloys were found to spend most of their creep life in the tertiary regime but exhibit a very small amount of primary creep, broadly the same can be said for CoNi-based superalloys[34]. It is important to mention that the shearing mechanisms are scarcely affected by the precipitate morphology, volume fraction or size[34, 63].

Similarly to Ni-based superalloys the initial step in creep is the rapid filling of the γ channels with dislocations [5, 34, 63]. In this phase some dislocations climb to become edge character in addition to reducing their width[34]. After this phase shearing events can now occur creating planar faults, as outlined above these faults are most likely SISFs, but SESFs (can be formed by the interactions of two SISFs) and APBs (formed by a superpartial shearing the γ' precipitate) were also observed by Titus[34, 81]. These were created by the shearing mechanism depicted on the left hand side of figure 2.19, however this was much rarer[34, 81]. There exists a key difference in shearing characteristics to Ni-based superalloys. Whereas faults are created on all {111} planes and generally are restricted to one precipitate, in Co-Based superalloys faults are typically only found on one or two of the {111} planes and pass through multiple precipitates[81].

In CoNi-based alloys bowing of the γ' precipitates can occur by $\frac{1}{2} < \bar{1}01 >$ dislo-

cations (note becomes more prevalent at temperatures significant enough to reduce the γ' volume fraction)[34]. APBs were observed transitioning between {111} and {100} planes throughout the width of the APB, demonstrating cross-slip[34].

There is not, to the author knowledge a paper on Co and CoNi-based alloys which is as comprehensive as [61] when it comes to assessing how these alloys will behave in a vast array of temperature and stress conditions. Co and CoNi-based alloys are subject to some degree of primary creep but this is typically small (>0.3% in the case of Co-based) in which dislocation networks are established in the γ channels. Creep curves in these alloys typically resemble the creep curves of the Ni-based superalloys in the tertiary regime (see figure 2.20).

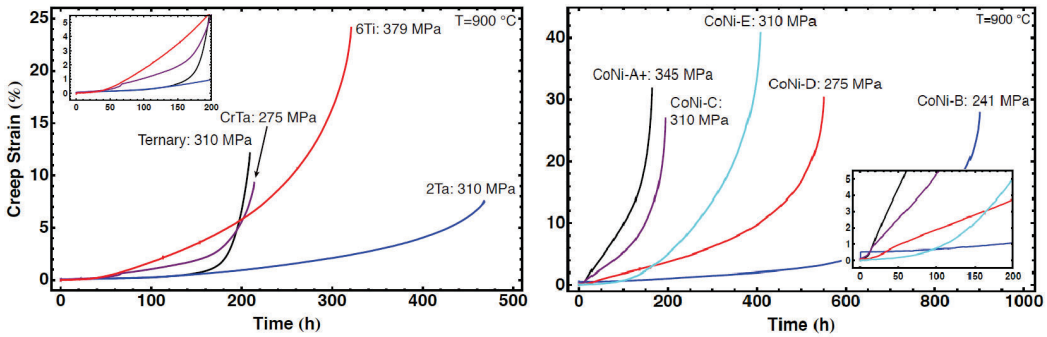

Figure 2.20: High temperature creep curves of Co (a) and CoNi-based alloys (b) insets display first 200h of the creep tests, applied stresses are next to alloy names (note the sign of misfit is negative in CoNi-E)(taken from [34]).

The creep rupture lives of many the Co and CoNi-based alloys are comparable to the creep rupture lives of typical first generation Ni-based alloys, 6Ti and CoNi-E are even comparable to 2nd generation alloys[34]. To this date there has been no major investigations into polycrystaline Co and CoNi-based alloys that the author is aware of;

there appears a preliminary investigation of the A9 alloy and shearing mechanisms in [34] but no creep curves were produced.

2.5.3 Yield Stress Anomaly

Similarly to their Ni-based counterparts, Co and CoNi-based superalloys are subject to yield stress anomaly as well[3, 25, 26]. In general, the two deformation mechanisms separated by a transition period found in Ni-based alloys are found here[51](see section 2.2.3). The first big difference between the types of alloys is the general shape of the curves (see figure 2.21)[3, 25].

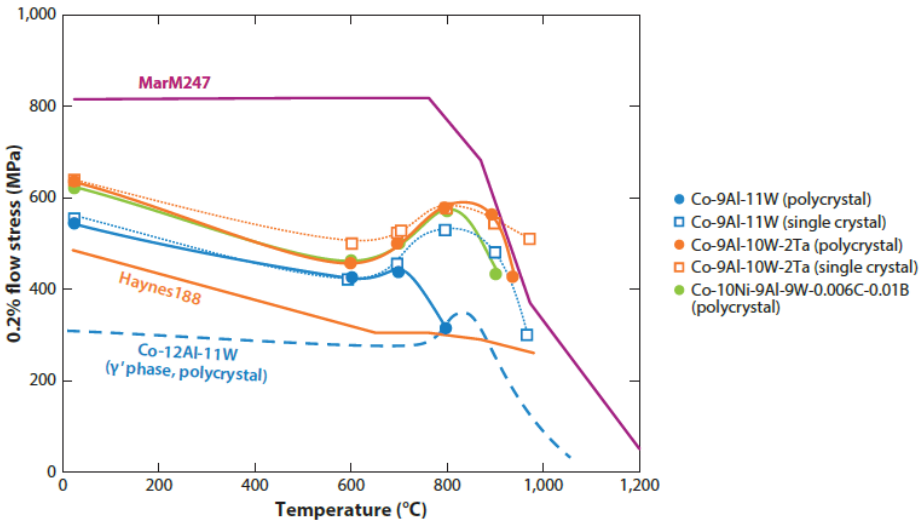

Figure 2.21: The yield stress anomaly curves for a series of alloys MarM247 being an Ni-based superalloy and Haynes188 being a conventional Co-based superalloy for comparison (taken from [25]).

In Ni-based superalloys the increase starts from much lower temperatures and over a much larger range, whilst in Co and CoNi-based alloys the anomalous increase occurs

over a much smaller temperature range and is preceded by a decline[3, 25]. The reasoning behind this is the low CSF energy relative to Ni-based superalloys making constriction harder, as it has to occur over a larger distance[25]. Notice how also the typical Ni-based superalloy MarM247 exhibits higher strength then the Co and CoNi-based superalloys, this is believed to only be an artefact of the infancy of these types of alloys resulting in crude optimisation[25]. The reason for the rapidity of the decline in many alloys is contributed to by the dissolution of γ' at such high temperatures[25]. Note that of all the alloys, Co-9Al-10W-2Ta actually exceed the strength of MarM247 at high temperatures[3, 25, 52]. This was found by Suzuki in 2006 to be caused by the activation of slip via the reaction of (2.3) at the interfaces; dislocations that shear the precipitates above the peak temperature (as opposed to bypass) meaning that the strengthening effect of the γ' precipitates is better retained[3, 52, 84]. It is clear that more research needs to be done in these alloys to understand what initiates this change.

2.5.4 Effects of Alloying Elements

Due to the infancy of Co and CoNi-based superalloys data is scant relative to their Ni-based counterparts. Again these lists may not be exhaustive and be subject to the weakness that some elements have unique effects active when only certain combinations are present[85].

Co-Based Alloys

The γ' solvus temperature was found to increase with additions of Ta and Ti, whilst Cr has the opposite effect[34, 75]. In addition to Cr, Si and Mo also cause a decrease in the γ' solvus temperature[75]. Thus far the most effective element to this end has been Ir; also important is the possible formation of $(Co,Ir)_3(Al,W)$ which retains hardness at high temperatures[75, 77]. Of key importance in both Co and CoNi-based superalloys is having sufficient Al content, else deleterious phase Co_3W-$D0_{19}$ will form[34]. Ta, Ti, Nb, W and Hf and to a lesser extent V and Ni have been experimentally proven to stabilise the γ' phase, whilst Cr, Mn, and Fe destabilise it[25, 63, 75, 81, 86]. An important feature of W is that large amounts result in a high density for the alloy[85]. Hf, Nb, and especially Mo were found to be detrimental to oxidation resistance despite somewhat enhancing the strength at room and elevated temperatures[87]. V had a strong negative influence on the oxidation resistance due to poor adherence of the oxide scale[76]; a benefit of V however is its low density which can be used to reduce alloy weight[88]. Cr and Si are found to enhance the oxidation resistance however, as they promote the formation of the protective scales Cr_2O_3 and Al_2O_3 in the former case[86] and just Al_2O_3 in the latter case due to selective oxidation[89]. B also led to the enhancement of Al_2O_3 at high temperatures[86]. In addition B had the effect of increasing the ductility in polycrystaline alloys by suppressing intergranular fractures[26]. The appearance of W in γ is beneficial for the delaying of coarsening to the precipitates[82], the same can be said here for CoNi-based superalloys.

CoNi-Based Alloys

The increases in Ni content in these alloys was also found to increase the γ' solvus temperature[34, 83, 90]. Zr, B and C were found to be grain boundary strengtheners in CoNi-based alloys[23, 91]. Cr retains its role of improving the oxidation resistance despite destabilising the γ' phase[34, 91], but there is an additional detail specific to these alloys, that is they are more resistant to the said detrimental effects of Cr[82]. The addition of Ni has the advantage of reducing the density of the alloy relative to purely Co-Based superalloys[82]. Ti reprises its role in these alloys as a strong γ' stabiliser[82]. In addition to Ti, Ta, Nb and W also retain their roles and γ' stabilisers[82].

Chapter 3

Theoretical Basis: Fault Energy Modelling and Computational Techniques

3.1 Modelling Planar Faults

The 2 main ways to generate planar faults computationally are to use either the supercell approach or an AIM (Axial Interaction Model)[92]. If there is randomness in the distribution of the various alloy components in the cell (for example in pure γ' this is not a concern, but in $Ni_3(Al_xFe_{1-x})$ the Fe could substitute for any selection of Al atoms, same applies if more elements are present on a sublattice) it is also necessary to account for this in one of 4 ways[93, 94]. Either use a very large supercell, select a series of arrangements which properties are then averaged (the Monte-Carlo Approach) or use an SPCM or a Special Quasirandom Structure (SQS)[93]. SPCM and SQS operate on the principle that certain selective arrangements of atoms on a cell simulate randomness[93].

One of the main arguments in favour of either SQS or SPCM is that in order to reach statistical significance in the other 2 approaches; even when simple alloys are analysed, either a supercell of the size 10^3 atoms or 10^6 configurations (both highly impractical) can be required; whilst a SQS and SPCM can have a much lower number of atoms and yield highly accurate results[93].

As outlined in the previous paragraph, in order for full statistical rigour use of the Monte-Carlo method would require very large computational expense; however in practical circumstances confidence in the result can be reasonably achieved with significantly less calculations performed. For example Chandran[92] did such calculations for a series of different atomic arrangements in $Ni_{90}Co_{10}$ and $Ni_{50}Co_{50}$ and found that if 4 calculations were included, the difference in ISF energy was expected to only be 20-30 mJ/m^2. Even with this said AIM models with either SQS or SPCM would still have 4 times less computational expense.

As for the supercell approach what degrees of freedom are allowed to relax in a fault energy calculation varies between the literature and what the scenario is being modelled. In [92] there were also supercell calculations conducted which utilised full relaxation. However, when the same author modelled the APB in superalloys only volume relaxation was allowed, as any departure from cubic symmetry was deemed to be energetically unfavourable. Vamsi[95] conducted supercell calculations of the SISF for $Ni_3Al_xX_{1-x}$ alloys in the γ' phase and allowed atomic relaxation but not volume relaxation (where volume was set to be consistent with the equilibrium lattice parameter for the specific composition). Limmer[96] carried out supercell calculations for the effects

of alloying on the ISF of iron, where relaxation was allowed in the direction normal to the stacking fault plane. Shao[97] performed high throughput ISF calculations on a large number of copper alloys. Shao concluded the most accurate results could be obtained by allowing full structure relaxation with all atoms relaxed in three directions.

3.1.1 Supercell Approach

In this approach two supercells are created; one is simply of the relevant substance (with randomness accounted for if necessary) in its unfaulted state. The next supercell is identical except for the fact that it is now faulted; both are relaxed using ab initio techniques[92, 98]. The energy of the fault $\gamma_{supercell}$ can then be computed using the following equation[92].

$$\gamma_{supercell} = \frac{E_{faulted} - E_{unfaulted}}{A \cdot n} \tag{3.1}$$

where $E_{faulted}$ and $E_{unfaulted}$ are the energies of the faulted and unfaulted cells respectively and A is the area of the planar fault[92]. Note there exists multiple factors that can frustrate the use of the supercell approach: the first is the fact that the relaxation of a faulted structure is a lot more computationally intensive as swift computation is dependant on symmetry[99]. Also is the fact that in the scenario where the fault analysed is not perfect, boundary conditions will be violated; hence it is necessary to use multiple faults where their combined shift vectors add up to a perfect fault (n is the number of faults in (3.1)) this induces a problem however as faults have strong influence outside of

the planes they are present on this leads to larger supercells being necessary to reduce significantly the interaction between faults[92, 100].

3.1.2 Axial Interaction Models (AIM)

AIM for γ Phase Calculations

AIM is a broad term for a potentially infinite group of techniques each one requiring more configurations to be utilised, and taking into account further sets of neighbours. The ones which are the most important are the ANNI (axial nearest neighbour ising) and the ANNNI (Axial next nearest neighbour ising)[101]. The way these techniques operate is to construct a number of supercells of the relevant compound (again with randomness taken into account where relevant), but this time in different structures; the energy per atom differentials can then be used to deduce the fault energy[39, 92, 94]. AIM models were first applied to stacking faults by Denteneer in 1987[39, 92]. AIM models exploit the fact that stacking faults are limiting structures of polytypes[39]. These models gain the word Ising in their acronyms as they use the analogy as to whether a layer agrees with the stacking sequence of the structure to that of Ising spin[39]. In these models if a layer follows the stacking sequence of the structure it is assigned a spin value S_i (where i is the index of the layer) of 1 and if it violates it a S_i value of -1 is assigned[39, 92, 94]. This allows the energy of the system to be defined as follows[39, 92, 101].

$$E = J_0 - J_1 \sum_i S_i S_{i+1} - J_2 \sum_i S_i S_{i+2} - J_3 \sum_i S_i S_{i+3} ... \tag{3.2}$$

The $J's$ are termed expansion coefficients and represent interaction energies between different sets of neighbours (J_1 is the interaction energy between the first set of nearest neighbours, J_2 the second nearest neighbours etc) J_0 is the energy of the substance when interactions between layers are completely disregarded[39, 94]. The energies of substances with perfect stacking sequences can be expressed in terms of $J's$ by utilizing (3.2)[39, 92, 94].

$$E_{FCC} = J_0 - N(J_1 + J_2 + J_3 + J_4...) \tag{3.3}$$

$$E_{HCP} = J_0 + N(J_1 - J_2 + J_3 - J_4...) \tag{3.4}$$

$$E_{DHCP} = J_0 + N(J_2 - J_4...) \tag{3.5}$$

where N is the number of planes. In addition to this, substances with stacking faults can be accounted for such as an FCC structure with an ISF or ESF present[39, 94].

$$E_{FCC-ISF} = J_0 + \left(\frac{4-N}{N}\right)(J_1 + J_2 + J_3 + J_4...) \tag{3.6}$$

$$E_{FCC-ESF} = J_0 + \frac{4-N}{N}J_1 + \left(\frac{8-N}{N}\right)(J_2 + J_3 + J_4...) \tag{3.7}$$

Equation (3.1) can now be adapted to this model as follows[39, 94].

$$\gamma_{AIM} = \frac{4(J_1 + J_2 + J_3 + J_4...)}{A} \tag{3.8}$$

This is where the distinction between the ANNI and ANNNI models first appears. The ANNI model includes the expansion coefficients up to J_1 and the ANNNI includes ex-

pansion coefficients up to J_4[101]. This allows (3.8) to be rewritten in the following 2 ways utilising (3.3-5)[94, 101, 102].

$$\gamma_{ANNI}^{ISF} = \frac{2(E_{HCP} - E_{FCC})}{A} \tag{3.9}$$

$$\gamma_{ANNNI}^{ISF} = \frac{E_{HCP} - 3E_{FCC} + 2E_{DHCP}}{A} \tag{3.10}$$

Note that magnitude of the expansion coefficients decline with their index as higher indexed coefficients correspond to further away neighbours[39, 94]. This effect is even more prominent in metals as interactions are very short range so in many cases simply ANNI will produce accurate results[94, 103]. The crystal structures used in the ANNI and ANNNI models in the γ are displayed in figure 3.1.

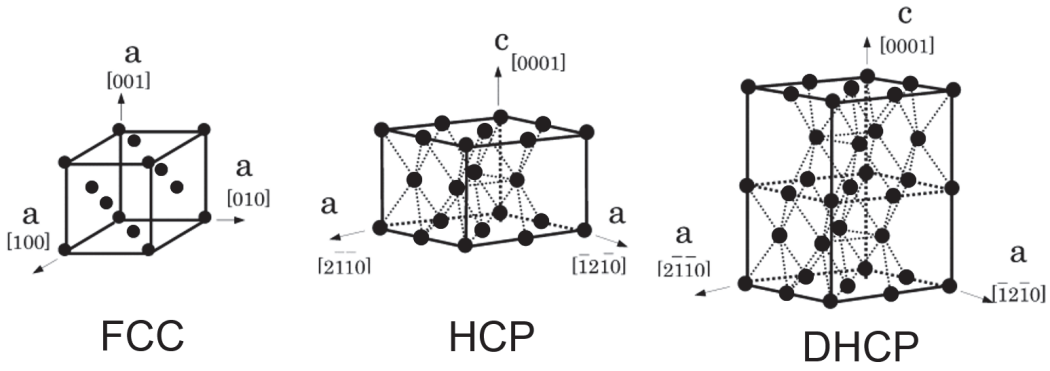

Figure 3.1: Diagram of the crystal structures used in the ANNI and ANNNI models in the γ phase (adapted from [104]).

It is worthwhile to note that in the case of the ANNI model the ISF and ESF are equivalent which is reasonable as energies between them typically differ by very small amounts[94]. Due to the approximations made in the AIM models they do not

replicate the supercell approach entirely[92, 102]. For instance they fail to take into account changes to local magnetic order, atomic arrangement around the fault and segregation of impurities[105–107]. Still they are known to produce in general very similar results[92, 102].

AIM for γ' Phase Calculations

Due to the similarities the FCC and $L1_2$, HCP and $D0_{19}$ and DHCP and $D0_{24}$, the latter being of the same stacking sequences but possessing order; it is possible to adapt (3.9) and (3.10) to the γ' phase[101].

$$\gamma_{ANNI}^{SISF} = \frac{8(E_{D019} - E_{L12})}{V_{L12}^{2/3} \cdot \sqrt{3}} \tag{3.11}$$

$$\gamma_{ANNNI}^{SISF} = \frac{4(E_{D019} - 3E_{L12} + 2E_{D024})}{V_{L12}^{2/3} \cdot \sqrt{3}} \tag{3.12}$$

Where E_{L12}, E_{D019} and E_{D024} are the energies per atom in the $L1_2$, $D0_{19}$ and $D0_{24}$ structures respectively and V_{L12} is the volume of 4 atoms in the $L1_2$ configuration, making the denominator the area of 4 atoms on the $L1_2$-$\{111\}$ plane[101]. The crystal structures used in the ANNI and ANNNI models in the γ' are displayed in figure 3.2.

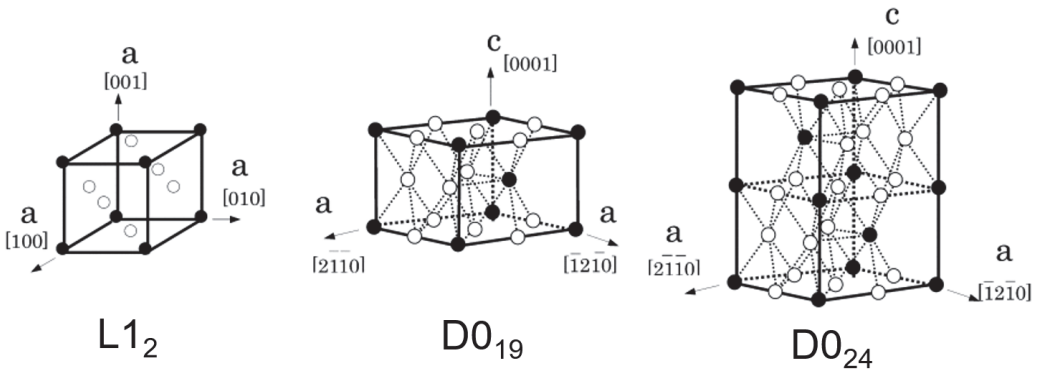

Figure 3.2: Diagram of the crystal structures used in the ANNI and ANNNI models in the γ' phase. White atoms represent the majority element and black atoms represent the minority element (adapted from [104]).

3.1.3 Special Quasirandom Structures (SQS)

The main goal of the production of an SQS is to judiciously place atoms in a structure to approximate the multisite correlation functions of a truly random structure[93, 94]. An SQS is designed by breaking configurations of atoms (denoted by σ) down into a series of figures (denoted by f) where the two items which constitute a figure are k values (for example a pair of atoms would be assigned $k = 2$ and a triangular configuration of atoms would be assigned $k = 3$) and m which is the distance between the atoms of that figure[93, 94]. In the example of a binary alloy, in order to distinguish between the two different atoms a spin value (denoted by S) is assigned to each atomic position where $S = 1$ for A and $S = -1$ for B (note the similarity in convention to the AIM models)[93, 94]. The product of these spin variables is then taken for each figure and averaged over the whole of the lattice in question to arrive at the following equation for the lattice averaged spin over all locations (denoted by l) (which also accounts for

orientation) of symmetry-related figures of type f gives[93]

$$\overline{\Pi}_f(\sigma) = \frac{1}{ND_f}\Sigma_l \Pi_f(\sigma, l) \tag{3.13}$$

where D_f is the amount of figures in a site, N is the total number of atoms and $\Pi_f(\sigma, l)$ an alternate representation for the product of the spin variables[93, 94]. SQS's are very successful as proven by the calculations of Zunger with SQS's with 8 or less atoms providing results of many properties which are highly accurate to fully random alloys[93]. SQSs do suffer from one main drawback and that is that such judicious placing of solute atoms will result in correlations in the results being present which do not exist in reality[93]. However these false correlations typically involve distant sets of neighbours which have little impact on the results (this also applies to SPCM)[93]. SQS's have a long and successful history of use in a large array of applications (the original paper the technique was proposed in [93] has over 1500 citations). Examples of this research include calculations of lattice parameter and enthalpy of mixing (which correspond well to experimental values) of a series of binary random solutions in the HCP structure[108]. An analysis of equilibrium lattice parameters, formation enthalpies, bulk and shear modulus of non-stoichiometric B2-NiAl with various constitutional point defects (again agreeing with experiment)[109]. Calculation of alloy bowing coefficients for a series of three mixed-cation and three mixed-anion chalcopyrite alloys[110]. With specific regard to fault energies in relevant compounds to superalloys, calculation of fault energies in the γ' phase of Co-based superalloys and how this varies with the addition of

Ta[81, 94]. The APB energies were calculated using SQS for a series of $L1_2Ni_3(Al_{1-x},X_x)$ alloys for the purpose of validation of the CALPHAD (CALculation of PHAse Diagrams) method with agreement between the methods found in most cases but large discrepancies in some[111].

3.1.4 SPCM

In this work the SPCM is used to simulate randomness. The main aim of the SPCM is to selectively place atoms on a cell for the purpose of manipulation of the Warren-Cowley short range order parameters (WC-SROP)[112–114]. The WC-SROP were originally derived from a three dimensional Fourier analysis of the scattering of x-rays from a sample[112, 115]. In a binary material the WC-SROP Γ are defined as follows[112–116].

$$\Gamma_{AB}^{(i)} = 1 - \frac{P_{AB}^{i}}{m_b} \tag{3.14}$$

$$\Gamma_{BA}^{(i)} = 1 - \frac{P_{BA}^{i}}{m_a} \tag{3.15}$$

Where A and B are two elements in the binary, i is an index representing the crystallographic shells (the higher the number the further away the shell atom in question), P_{AB}^{i} is the probability of finding an atom of B in the ith shell around an A atom, P_{BA}^{i} is the probability of finding an atom of A in the ith shell around an B atom and m_A and m_B are the concentration of one of the elements A and B respectively[112–116](note that (3.14) and (3.15) are equivalent[116]). These parameters have the following characteristics; a value of 0 for a completely random distribution[112, 116, 117] and have

a maximum value (note is absolute) for perfect order[112, 113]. Hence minimization of these parameters is the goal of the selective placement of atoms. SPCMs have been used to analyse element resolved local-distortions and how they impact upon magnetism and the relation to solid solution strengthening in the high entropy equi-atomic FCC FeCoNiCrMn alloy[118]. It is to be noted that there is no literature to the author knowledge that compares the results from SPCM and SQS however they are expected to yield similar results due to their methodological similarities. The main difference between the two methodologies is that SQS are more complicated and hence need in many cases to be larger, but they also would be expected to yield slightly more accurate results, because they include figures which have more than 2 atoms.

3.2 Basics of Density Functional Theory (DFT)

3.2.1 Quantum Many-Body Problem

The main theme running through DFT calculations in this research is the finding of the ground state of a continuous solid substance (note this can also apply to molecules and surfaces)[99, 119]. In order to find this ground state, N nuclei and ZN electrons, and the Coulomb forces between them must be considered[99, 119, 120]. A major feature of these particles is that they are small enough to be subject to significant quantum mechanical effects. Hence it is necessary to introduce the Schrödinger equation[99, 119].

$$\underline{H}\Psi = \lambda\Psi \tag{3.16}$$

Where $\underline{H}$ is the Hamiltonian operator, Ψ and λ represent a series of eigenvectors and eigenvalues respectively[99, 119]. The problem necessary to solve to find the ground state is named the quantum many-body problem and is subject to the following $\underline{H}$[119].

$$\underline{H} = -\frac{\hbar^2}{2}\sum_i \frac{\nabla^2_{\hat{R}_i}}{M_i} - \frac{\hbar^2}{2}\sum_i \frac{\nabla^2_{\hat{r}_i}}{m_e} - \frac{1}{4\pi\epsilon_0}\sum_{i,j}\frac{e^2 Z_i}{|\hat{R}_i - \hat{r}_j|} + ... \\ \frac{1}{8\pi\epsilon_0}\sum_{i\neq j}\frac{e^2}{|\hat{r}_i - \hat{r}_j|} + \frac{1}{8\pi\epsilon_0}\sum_{i\neq j}\frac{e^2 Z_i Z_j}{|\hat{R}_i - \hat{R}_j|} \tag{3.17}$$

Where the terms from left to right are kinetic energy of the nuclei, kinetic energy of the electrons, Coulomb force between nuclei and electrons, electrons and electrons, and finally between nuclei and other nuclei[119]. Where i and j are indexes to represent the number of electrons and nuclei[119]. M_i and m_e represent the mass of nuclei and electrons respectively, $\hat{R}$ and $\hat{r}$ are positions of electrons and nuclei respectively and Z represents the charge of a nucleus[119]. There are certain select cases for which the Schrödinger equation could be solved exactly however in any realistic system it will be practically speaking impossible to solve exactly and hence it is necessary to introduce approximations[99, 120].

3.2.2 The Born-Oppenheimer Approximation

The Born-Oppenheimer approximation is based off the following observation. Electrons are $\approx$ 1800 times less massive than protons, hence in a case of equal momentum electrons will move much faster and be significantly more responsive to changes in there environment then nuclei[99, 120]. It can be thought of that each electron whilst in mo-

tion "*sees*" the nuclei as stationary in a given short time frame[120]. Separation of the behaviour of nuclei and electrons into separate mathematical problems means that $\underline{H}$ can be reduced to the following[99, 119].

$$\underline{H} = -\frac{\hbar^2}{2}\sum_i \frac{\nabla^2_{\hat{r}_i}}{m_e} - \frac{1}{4\pi\epsilon_0}\sum_{i,j}\frac{e^2 Z_i}{|\hat{R}_i - \hat{r}_j|} + \frac{1}{8\pi\epsilon_0}\sum_{i\neq j}\frac{e^2}{|\hat{r}_i - \hat{r}_j|} + V_{nuc} \tag{3.18}$$

Where as nuclei are modelled not to move the first term (kinetic energy of nuclei) disappears and the last term (nuclei-nuclei Coulomb interaction) is reduced to a constant V_{nuc}[119].

3.2.3 Key Concepts of Density Functional Theory

For the Hamiltonian in (3.18) Ψ is given as the electronic wave function and λ as the ground state energy[99, 120]. The electronic wave function has $4ZN$ dimensions (N being the number of atoms and the 4 originating from the fact that each electron exists in 3 dimensional space and has spin properties, note that time is not included as a dimension as the ground state simply does not depend on it)[99]. This is where the major difficulty with solving the Schrödinger equation is revealed, in realistic supercells there will be for example 50 atoms, if they are nickel atoms there is $28 \times 50 \times 4 = 5600$ dimensions which need to be considered[99]. DFT enters at this juncture, using the electron density $n(\hat{r})$ as opposed to the wavefunction to solve this problem[99, 120]. $n(\hat{r})$ is expressed as

follows

$$n(\hat{r}) = 2\sum_{i} \psi_i^*(r)\psi_i(r) \tag{3.19}$$

where ψ_i are single electron wavefunctions (these are derived by approximating Ψ as a Hartree product $\Psi = \prod_{i=1}^{Q} \psi_i$ where Q is the number of electrons) and the 2 is a feature of the Pauli exclusion principle, and that is that an electron can occupy the same state as another electron provided that it has opposite spin[99]. This is critical as the problem can be reduced from one of thousands or in some cases tens of thousands of dimensions down to one of just 3[99]. DFT stands on two main pillars the two Honenberg-Kohn theorems and the Kohn-Sham equations[99, 119, 120].

Hohenberg-Kohn Theorems

The Hohenberg-Kohn theorems are expressed in words as follows.

1) The ground-state energy from the Schrödinger equation is a unique functional of the electron density $E[n(\hat{r})]$[99].

2) The electron density that minimizes the energy of the overall functional is the true electron density corresponding to the full solution of the Schrödinger equation[99].

There is a second observation to be made which is pertinent to 1) which is that the expectation values of all properties are determined uniquely by the ground state electron density e.g. wavefunction[99, 119]. Another point of note is that value of energy from $E[n(\hat{r})]$ is only of physical relevance when evaluated at the ground state electron density

at all other densities the value is meaningless[119]. It has now been determined that a functional exists and can be used to calculate ground state properties in any system[99]. The problem that is now encountered is that only some terms of this functional are known[99].

$E[n(\hat{r})]$ can be expressed as follows

$$E[n(\hat{r})] = E_{known}[n(\hat{r})] + E_{unknown}[n(\hat{r})] \tag{3.20}$$

$E_{known}[n(\hat{r})]$ are all of the terms that are involved in the classical version of the problem which can be expressed in terms of the single electron wavefunctions as follows.

$$E_{known}[\psi_i] = \frac{h^2}{m_e}\sum_i \int \psi_i^* \nabla^2 \psi_i d^3r + \int V_{out}(\hat{r}) n(\hat{r}) d^3r + ... \\ \frac{e^2}{m_e}\int\int \frac{n(\hat{r})n(\hat{r}')}{|\hat{r}-\hat{r}'|} d^3r d^3r' + V_{nuc} \tag{3.21}$$

Where the terms from left to right are electron kinetic energy, Coulomb interaction between electrons and nuclei, Coulomb interaction between electrons, and Coulomb interaction between nuclei (note that $V_{out}(\hat{r})$ is the potential that the electrons exist in due to the nuclei, a consequence of the Born-Oppenheimer approximation)[99, 119]. $E_{unknown}[n(\hat{r})]$ contains the quantum mechanical effects of exchange and correlation ($E_{unknown}[n(\hat{r})]$ will be referred to as the exchange-correlation functional from now on $E_{XC}[n(\hat{r})]$)[99]. Exchange is caused by a repulsion of electrons of the same spin-state. Taking account of exchange is necessary as if two electrons have their positions switched

the wavefunction should change sign. Correlation exists as the motion of electrons is influenced by those of the same spin state. We will return to $E_{XC}[n(\hat{r})]$ at a later point just assume for now that his term can be reasonably approximated.

Kohn-Sham Equations

The Hohenberg-Kohn theorems were a significant discovery but it was not until the derivation of the Kohn-Sham equations in 1965 that DFT was able to be used in a practical manner[99, 119, 120]. This is because solving equation (3.20) would be seldom less complicated then solving the Schrödinger equation with the Hamiltonian in (3.18)[99]. The Kohn-Sham equations are a series of equations that only depend on ψ_i[99, 120]. Consider first three functionals, one which is perfect $G_{perf}[n(\hat{r})]$ one which neglects correlation $G_{no-c}[n(\hat{r})]$ and one which neglects both exchange and correlation $G_{no-xc}[n(\hat{r})]$ (note these functionals neglect the effects of $V_{out}(\hat{r})$ on the electrons, hence are denoted by a G not an E)[119]. As a consequence of the Hohenberg-Kohn theorems, each one of these 3 functionals can be broken down into two parts, one concerning kinetic energy and the other concerning potential energy (note that for ease of reading the $[n(\hat{r})]$ that suffixes the terms on the right hand side of equations (3.22-30) have been removed)[119].

$$G_{perf}[n(\hat{r})] = T + V \tag{3.22}$$

$$G_{no-c}[n(\hat{r})] = T_0 + V \tag{3.23}$$

$$G_{no-cx}[n(\hat{r})] = T_0 + V_H \tag{3.24}$$

where T is the kinetic energy of the electrons, T_0 is the kinetic energy of a non-interacting electron gas, V is the exact potential energy (caused by interactions of electrons) and V_H is the Hartree potential given by[99, 119],

$$V_H = e^2 \int \frac{n(\hat{r})'}{|\hat{r} - \hat{r}'|} d^3r' \tag{3.25}$$

(3.22)-(3.23) gives the following

$$T - T_0 = E_C \tag{3.26}$$

where E_C is the potential energy contribution from correlation and (3.23)-(3.24) gives

$$V - V_H = E_X \tag{3.27}$$

where E_X is the potential energy contribution from exchange. Now $G[n(\hat{r})]$ (defined as $E[n(\hat{r})]$ with out the contribution from $V_{out}(\hat{r})$) can now be written as follows[119].

$$G[n(\hat{r})] = T + V + (T_0 - T_0) = T_0 + V + (T - T_0) \tag{3.28}$$

substituting (3.26) into (3.28) and adding $(V_H - V_H)$,

$$G[n(\hat{r})] = T_0 + V + E_C + (V_H - V_H) = T_0 + V_H + E_C + V - V_H \tag{3.29}$$

substituting (3.27) into (3.29) and combing exchange and correlation into one term $E_C + E_X = E_{XC}$

$$G[n(\hat{r})] = T_0 + V_H + E_{XC} \tag{3.30}$$

Note that $E[n(\hat{r})]$ can be expressed

$$E[n(\hat{r})] = G[n(\hat{r})] + \int V_{out}(\hat{r})n(\hat{r})d^3r + V_{nuc} \tag{3.31}$$

This allows the construction of a new Hamiltonian H_{KS}[119].

$$\begin{aligned} \underline{H_{KS}} = \underline{T_0} + \underline{V_H} + \underline{E_{XC}} + \underline{V_{out}} = -\frac{\hbar^2}{2m_e}\nabla_i^2 + ... \\ \frac{e^2}{4\pi\epsilon_0}\int \frac{n(\hat{r})'}{|\hat{r} - \hat{r}'|}d^3r' + \frac{\delta E_{XC}[n(\hat{r})]}{\delta n(\hat{r})} + \underline{V_{out}} \end{aligned} \tag{3.32}$$

where the third term is defined as the functional derivative[99, 119]. This new Hamiltonian can be used in the following set of equations[99, 119, 120].

$$\underline{H_{KS}}\psi_i = \lambda_i\psi_i \tag{3.33}$$

Each equation depends on only single electron and on 3 dimensions (note λ_i in this context corresponds to the energy of the orbital i)[99, 119]. It is important to note that the use of the Hartree potential computes the Coulomb interaction between the electron which is the subject of the current (3.33) and the total electron density of which it is a

part of[99]. Hence it includes a self-interaction which does not exist in reality[99]. E_{XC} is not known exactly, but it can be expressed in many useful ways, according to a series of different approximations: for example as depending on only the density locally at each point (the local density approximation) or as on depending on the local density and the gradient of said density (the generalised -gradient approximation), as will be covered in later sections of this chapter[99, 119, 120].

3.2.4 Iterative Solving

Iterative solving of the equations laid out in (3.33) is necessary as V_H is dependent on $n(\hat{r})$, but in order to deduce $n(\hat{r})$ it is necessary to know ψ_i, but ψ_i can only be known by finding the solutions to (3.33)[99, 119, 120]. The procedure for solving the problem iteratively can be carried out as follows[99].

1. Propose a reasonable guess to the electron density $n_0(\hat{r})$ (note the index corresponds to the iteration number)
2. Insert $n_0(\hat{r})$ into V_H
3. Use the V_H in (3.33) to solve and deduce ψ_i
4. Use the values of ψ_i to calculate the $n_1(\hat{r})$ using (3.19)
5. Compare $n_1(\hat{r})$ with $n_0(\hat{r})$ and assess how close the values are, if they agree within a certain defined limit the calculation is concluded at that point

If this is not the case then an updating procedure is undertaken on the $n_0(\hat{r})$ and the process is restarted again from step 2 until it is the case[99]. The above statements are

true in a static calculation (where the aim of the calculation is to determine the ground state electron density and the corresponding energy, for a given set of atomic positions) in a calculation involving relaxation a further 2 steps need to be added.

6. If the condition of step 5 is met move the atoms to updated positions (the new positions determined by an algorithm designed to minimize the free energy) and restart from 1

7. When the condition of step 5 is met again compare the ground state energies of the two sets of atomic positions, if they are within a certain limit from each other the calculation is said to be converged, if not then a new set of positions must be selected

Specifics regarding the algorithms used to select $n_0(\hat{r})$ as well as converge the atomic positions and electron density will be covered in later sections of this chapter.

3.3 K-points

3.3.1 Introduction

In order to perform calculations of the ground state electron density, integration of very complex mathematical functions must be performed[99, 121]. With the state of computational technology it is not yet possible to evaluate such integrals in their entirety[99]. This is cause for the existence of the k-point, the necessary mathematical operations are undertaken at a series of discrete points and each point is assigned a relevant weighting to form a numerical approximation of the true result[99, 122, 123]. Where results with

superior convergence will be attained with higher numbers of k-points, however such calculations will be more computationally intensive[99, 124]. To compute such integrations it is significantly easier to utilise reciprocal space (k-space hereafter)[99]. K-space similarly has 3 unit vectors that can be defined from the unit vectors in real space see (3.34-36)[99, 125].

$$\hat{b}_1 = 2\pi \frac{\hat{a}_2 \times \hat{a}_3}{\hat{a}_1 \cdot (\hat{a}_2 \times \hat{a}_3)} \tag{3.34}$$

$$\hat{b}_2 = 2\pi \frac{\hat{a}_3 \times \hat{a}_1}{\hat{a}_2 \cdot (\hat{a}_3 \times \hat{a}_1)} \tag{3.35}$$

$$\hat{b}_3 = 2\pi \frac{\hat{a}_1 \times \hat{a}_2}{\hat{a}_3 \cdot (\hat{a}_1 \times \hat{a}_2)} \tag{3.36}$$

Where $\hat{a}_1$, $\hat{a}_2$ and $\hat{a}_3$ are the real space vectors and $\hat{b}_1$, $\hat{b}_2$ and $\hat{b}_3$ are the corresponding reciprocal lattice vectors. This naturally leads to the observation that the larger a unit vector is in real space the shorter its equivalent will be in k-space and vice-versa as is determined by the inverse relationship between the two[99]. It is important to note that the reciprocal lattice will always exist in the same crystal system as the real lattice but does not necessarily have to have the same Bravais structure, for example the reciprocal lattice of a BCC real lattice is FCC (the reverse also applies)[99, 125].

In real space there is the concept of the primitive cell (the cell containing the least amount of atoms yet from which all information about a periodic material can be determined) there exists an equivalent concept in k-space which is called the Brillouin zone (BZ hereafter)[99, 125]. The volume relationship between the primitive cell and the BZ

is given as follows[99].

$$V_{BZ} = \frac{(2\pi)^3}{V_{PC}} \tag{3.37}$$

There is one key difference in the definition of the BZ and the direct (real space) lattice, it is that lattice points are defined as being in the centre of the cell as opposed to at the corners of the cell[125]. This has the consequence that points at a wavevector $\hat{k}$ and $-\hat{k}$ are equivalent[125]. In a lot of cases there will exist a large degree of symmetry in the BZ, this can be exploited to form what is called an irreducible Brillouin zone (IBZ hereafter)[99]. The IBZ satisfies the condition that by reflecting or copying the IBZ it can be used to flawlessly produce the full BZ[99]. This can be used to good effect to reduce the amount of k-points that are necessary to actually perform the calculation[99]. Note the following, convergence is chiefly dictated by the number of k-points in the BZ, whereas computational time varies strongly with the number of k-points in the IBZ[99].

For many of the factors used in a first-principles calculation including the total energy[126], numbers of electrons in bands[126], electronic charge density[127] and bulk properties[127] usage of integration in the reciprocal space is incredibly important or possibly even totally necessary, rendering reciprocal space superior to assess these quantities. Real space however also has advantages such as that geometry is better assessed in it. K-points in first-principles are selected according to one of many algorithms the most common and widely used is the Monkhorst-Pack scheme which is used for the research in this thesis[121, 122], but the main alternative is the Chadi-Cohen scheme[123].

These Monkhorst-Pack scheme as well as older techniques for historical context will be discussed in the following subsections.

3.3.2 Historical Context

Whilst in fact an estimate of the aforementioned complex integrals could be built up by randomly selecting any points within the BZ this would be less practical computationally and yield inferior results. There exists in the BZ points of high symmetry known as the Γ, X and L points respectively[128]. The Γ point is defined as the point in k-space where $\hat{k} = 0$[99]. However it was discovered by Baldereschi[128] that averaging over these points alone was inadequate and that substantially more points are needed to be used to attain accurate values of the average electron energy in the valence free bands[128]. Baldereschi proposed the derivation of the mean-value point($\hat{k}^*$)[128]. With the goal of choosing a point such that the average over the BZ is approximately equal to the value at that point[128]. A typical complex integral over the BZ that needs evaluation is of the form[99, 122, 128].

$$I = \int_{BZ} f(\hat{k}) d^3k \tag{3.38}$$

where f is a periodic function of $\hat{k}$, where f can be selected such that its integration will result in the calculation of a property[128]. This integral can be expressed in the

following way[128].

$$I = \frac{(2\pi)^3}{V_{PC}} \bar{f} \tag{3.39}$$

Where $\bar{f}$ is the average value of the function $f(\hat{k})$. By utilising the fact that $f(\hat{k})$ can be expressed as a completely irreducible representation of a crystal point group and exploiting the periodicity and symmetry the following expression can be formed[123, 128].

$$f(\hat{k}) = \sum_{m=0}^{\infty} a_m A_m(\hat{k}) \tag{3.40}$$

where

$$A_m(\hat{k}) = \sum_{|\hat{R}|=C_m} e^{i\hat{k}\cdot\hat{R}} \; m = 0, 1, ... \tag{3.41}$$

where the $\hat{R}$'s are a series of equivalent lattice vectors, where the set of vectors corresponding to a value of C_m is classified as a star[122, 123, 128]. A star is a set of k-points that can all be transformed into a single point by the employment of space group operations[121, 122]. The $A_m(\hat{k})$ are constructed to obey the following conditions

$$\frac{V_{PC}}{(2\pi)^3} \int_{BZ} A_m(\hat{k}) d^3k = 0 \; m = 0, 1, ... \tag{3.42}$$

$$\frac{V_{PC}}{(2\pi)^3} \int_{BZ} A_m(\hat{k}) A_n(\hat{k}) d^3k = N_n \delta_{mn} \tag{3.43}$$

$$A_m(\hat{k} + \hat{K}) = A_m(\hat{k}) \tag{3.44}$$

$$A_m(T\hat{k}) = A_m(\hat{k}) \tag{3.45}$$

$$A_m(\hat{k})A_n(\hat{k}) = \sum_j a_j(m,n)A_j(\hat{k}) \tag{3.46}$$

Where N_n is the number of lattice vectors in the shell n, T is any lattice point group operation, $\hat{K}$ is any reciprocal lattice vector and $a_j(m,n)$'s are integers determined by the choice of m and n[123]. If we initially ignore all of the terms except for the one corresponding to $m = 0$ then the following equation can be constructed from (3.39),(3.40) and (3.41)

$$I = \frac{(2\pi)^3}{V_{PC}} a_0, \tag{3.47}$$

as $A_0(\hat{k}) = 1$[123, 128]. This choice is somewhat justified as in fact the other terms contribution to $f(\hat{k})$ are significantly smaller and decline further with increasing m[123, 128]. The purpose of the $\hat{k}^*$ is to make judicious selection to satisfy the condition,

$$A_m(\hat{k}^*) = 0 \tag{3.48}$$

for as high an order as possible (note in reality only orders of up to 3 can be made to fit this condition)[123, 128]. This technique had some degree of success as it was able to produce similar results to the Kleinmann-Phillips technique which used upwards of 500 k-points[128]. It is only possible to satisfy (3.48) to higher orders if multiple points are introduced[99, 123]. The order to which (3.48) can be satisfied increases as the number of k-points does[123].

3.3.3 Monkhorst-Pack Scheme

The Monkhorst-Pack scheme was first proposed in 1976, 3 years after the Chadi-Cohen scheme[†]. It has been shown to produce identical sets of special k-points to the Chadi-Cohen scheme. The Monkhorst-Pack scheme starts with the definition of a series of integers.

$$u_x = \frac{(2r - q - 1)}{2q} \; r = 1, 2, ..., q \tag{3.49}$$

Where q spans the number of selected k-points in the set. The implication of this set of numbers is that the series of u_x's along with equivalent u_y's and u_z's defines the set of k-points.

$$\hat{K}_{xyz} = u_x\hat{b}_1 + u_y\hat{b}_2 + u_z\hat{b}_3 \tag{3.50}$$

Where said series of k-points span the BZ in addition to being equally spaced across it. The quantity $B_m(\hat{k})$ is then defined.

$$B_m(\hat{k}) = N_m^{-\frac{1}{2}} A_m(\hat{k}) \tag{3.51}$$

Where N_m is the number of members of the star corresponding to the value of m. Note that $B_m(\hat{k})$ retains the same lattice point group symmetry properties as $A_m(\hat{k})$[123].

[†]Other than if explicitly stated the source for the information in this subsection can be assumed to from reference[122].

Now the following quantities $S_{mn}(q)$ and $W_j^{ab}(q)$ can defined.

$$S_{mn}(q) = \frac{1}{q^3} \sum_{x,y,z=1}^{q} B_m^*(\hat{k}_{xyz}) B_n(\hat{k}_{xyz}) \tag{3.52}$$

$$W_j^{ab}(q) = \frac{1}{q} \sum_{x=1}^{q} e^{\frac{i\pi}{q}(2r-q-1)(R_j^b - R_j^a)} \tag{3.53}$$

Substituting $B_m(\hat{k})$ into (3.52) allows for $S_{m,n}(q)$ to be expressed as follows.

$$S_{mn}(q) = (N_m N_n)^{-\frac{1}{2}} \sum_{a=1}^{N_m} \sum_{b=1}^{N_n} \prod_{j=1}^{3} W_j^{ab}(q) \tag{3.54}$$

Where a and b are members of stars N and M respectively. The quantity $W_j^{ab}(q)$ is subject to the following conditions: It will equal 1 if $|R_j^b - R_j^a|$ is equal to an even number multiplied by q, it will equal $(-1)^{(q+1)}$ if $|R_j^b - R_j^a|$ is equal to an odd number multiplied by q, otherwise it will equal 0. A further set of conditions can now be imposed.

$$|R_j^a| < \frac{q}{2} \; j = 1, 2, 3 \tag{3.55}$$

$$|R_j^b| < \frac{q}{2} \; j = 1, 2, 3 \tag{3.56}$$

Now the following deduction can be made.

$$W_j^{ab}(q) = \delta(R_j^a, R_j^b) \tag{3.57}$$

Substituting (3.57) into (3.54) yields the following.

$$S_{mn}(q) = \delta_{mn} \tag{3.58}$$

The main consequence of this is that when the conditions laid out in (3.55) and (3.56) are adhered to, this corresponds to a function of $B_m(\hat{k})$ that is orthonormal on the k-points of the set $\hat{K}_{xyz}$. Significant simplification can be made by utilising the IBZ.

$$S_{mn}(q) = \frac{1}{q^3} \sum_{j=1}^{P(q)} \omega_j B_m(\hat{k}_j) B_n(\hat{k}_j) \tag{3.59}$$

Where $P(q)$ is the number of k-points present in the IBZ and ω_j is the weighting factor given by (3.60).

$$\omega_j = \frac{v_j}{q_j} \tag{3.60}$$

Where v_j is the order of the entire point group and q_j is the order of the group of the wavevector at $\hat{k}_j$.

3.3.4 Errors

It is important to again stress that the aforementioned methodologies present only approximations to integral (3.38)[†]. Following in this subsection is a calculation of the errors involved in employing the Monkhorst-Pack scheme. By exploiting the orthogonality of

[†]Other than if explicitly stated the source for the information in this subsection can be assumed to from reference[122].

the BZ, f_m can be expressed as follows.

$$f_m = \frac{V_{PC}}{(2\pi)^3} \int_{BZ} B_m^*(\hat{k}) f(\hat{k}) d^3k \tag{3.61}$$

By summing over a set of k-points it is possible to produce the following approximation $\tilde{f}_m$ of f_m.

$$\tilde{f}_m = \frac{1}{q^3} \sum_{j=1}^{P(q)} \omega_j f(\hat{k}_j) B_m(\hat{k}_j) \tag{3.62}$$

Note in the above equation that a term is included in this sum only if it obeys the conditions of (3.55) and (3.56). Hence a function which is totally symmetric and periodic in k-space can be expressed exactly (3.63) and approximately (3.64).

$$f(\hat{k}) = \sum_{m=1}^{\infty} f_m B_m(\hat{k}) \tag{3.63}$$

$$\tilde{f}(\hat{k}) = \sum_{m=1}^{\infty} \tilde{f}_m B_m(\hat{k}) \tag{3.64}$$

Note that (3.63) is the same function as in (3.40) just expressed differently for convenience. Now the error in the approximation ϵ_{BZ} can be represented by

$$\epsilon_{BZ} = \int_{BZ} [f(\hat{k}) - \tilde{f}(\hat{k})] = \sum_{m>1} f_m N_m^{\frac{1}{2}} S_{m1}(q) \tag{3.65}$$

where $S_{m1}(q)$ is equal to

$$S_{m1}(q) = (-1)^{(q+1)(R_1+R_2+R_3)/q} \tag{3.66}$$

in the condition where $R_3 - R_1$ are multiples of q and 0 in all other conditions. The errors depend very sensitively on the form of the function $f(\hat{k})$. Chadi and Cohen theorised that there is an inverse relationship between ϵ_{BZ} and C_m^{-3} however this was based on the analysis of a Taylor expansion of a smoothly varying function. This analysis downplays the major impact of the boundary of the BZ on the error.

In practice the quality of the mesh and hence numerical accuracy of the results, is assessed by using a convergence test. This is where a result or sample of results is run multiple times with a series of meshes with increasing k-points. Typically, there is an initial transient where the difference between the result with the highest k-points and those near the lower end of the spectrum being large. As the number of k-points is increased the difference between the results becomes smaller and levels off. This plateau is where the results can be said to be converged and from where the final number of k-points in the mesh should be chosen from. More information about this subject is detailed in section 5.1.2.

3.4 Partial Occupancies

In the case of metals a problem arises when evaluating integrals of the form (3.38) as the functions evaluated $f(\hat{k})$s are not continuous[99]. This leads to a unique characteristic

of the BZ where there are areas where electrons exist and areas where they don't[99] due to the partial filling of energy bands[124]. Separating these regions is a surface which is called the Fermi surface (FS hereafter)[99]. This fact makes evaluations of such integrals computationally more complex as exceptionally high numbers of k-points must be used to obtain good convergence[99, 124]. However there are techniques which can be employed to overcome this to a large degree. The two main types of technique are smearing methods and tetrahedron methods[99]. Smearing methods work in the following way, when a discontinuous function is encountered a smearing function is employed to smooth out the discontinuity[99].

$$U_{FD-smear}\left(\frac{\epsilon - E_F}{W}\right) = \left[e^{\frac{\epsilon - E_F}{W}} + 1\right]^{-1} \tag{3.67}$$

where E_F is the Fermi energy, ϵ represents energy and W is the characteristic broadening which reproduces the actual function perfectly when $W = 0$ and moves away from the step function as W increases (note this is called the Fermi-Dirac function)[99, 129]. The smearing method employed for calculations with relaxations in this research is however the superior Methfessel-Paxton smearing technique [99, 124]. Tetrahedron methods work by constructing a series of tetrahedra in k-space between the k-points and an approximation of the function can be constructed using interpolation[99, 121]. Various interpolation methods can be used including the simplest linear interpolation[99, 121]. The interpolation method used for static calculations in this thesis is the one derived by Blöchl which uses adjusted weights to reduce the errors[121]. Higher order interpolation

schemes such as that of MacDonald also can be used but these are subject to increased difficulties because of band crossings[121].

3.4.1 Methfessel-Paxton Technique

For a discontinuous function (3.38) can be rewritten as follows[†]

$$I = \int_{BZ} S(E(\hat{k}) - E_F) f(\hat{k}) d^3k \tag{3.68}$$

Where $E(\hat{k})$ is an energy band, E_F is the Fermi energy and $S(E(\hat{k}) - E_F)$ is a step function. The following quantity $F(\epsilon)$ can now be defined.

$$F(\epsilon) = \int_{BZ} f(\hat{k}) \delta(\epsilon - E(\hat{k})) d^3k \tag{3.69}$$

This allows (3.68) to be rewritten as

$$I = \int_{-\infty}^{\infty} S(\epsilon - E_F) F(\epsilon) d\epsilon \tag{3.70}$$

Note that by replacing the step function $S(E(\hat{k}) - E_F)$ by $U_{FD-smear}$ that the type of smearing described in section 3.4 is reproduced. Use of this type of smearing however induces a systematic error as the charge below E_f is calculated as

$$\int g(\epsilon) S_0(\epsilon - E_F) d\epsilon. \tag{3.71}$$

[†]Other than if explicitly stated the source for the information in this subsection can be assumed to from reference[124].

Where $g(\epsilon)$ is the density of states, note this does not apply in the select case where $F(\epsilon)$ is constant near E_F. S_N describes a series of successive approximations to the step function where N is a positive integer or 0. A dimensionless energy variable is now defined $x = (\epsilon - E_F)/W$ for convenience. Where W is defined as the characteristic broadening. The error in the following case is zero: where $F(\epsilon)$ is a polynomial of the order of S_N within the region of W. This allows the delta function to be expressed as the following sum.

$$\delta(x) = \sum_{n=0}^{\infty} A_n H_{2n}(x) e^{-x^2} \tag{3.72}$$

Where H_{2n} is a Hermite polynomial of the physicists definition of order $2n$

$$H_{2n} = (-1)^{2n} e^{x^2} \frac{d^{2n}}{dx^{2n}} e^{-x^2} \tag{3.73}$$

and A_n are a series of coefficients defined as follows.

$$A_n = \frac{H_{2n}(0)}{(2n)!\, 4^n \sqrt{\pi}} = \frac{(-1)^n}{n!\, 4^n \sqrt{\pi}} \tag{3.74}$$

The orthogonality of the Hermite polynomials can now be exploited.

$$\int_{-\infty}^{\infty} H_n(x) H_m(x) e^{-x^2} dx = n!\, 2^n \sqrt{\pi} \delta_{nm} \tag{3.75}$$

A sum $D_N(x)$ can now be defined as follows.

$$D_N(x) = \sum_{n=0}^{N} A_n H_{2n}(x) e^{-x^2} \tag{3.76}$$

Note that this will form an approximation to the delta function, the consequence of this is as follows when $P(x)$ is a polynomial of degree less than $2N + 2$.

$$\int_{-\infty}^{\infty} D_N(x) P(x) dx = \int_{-\infty}^{\infty} \delta(x) P(x) dx = P(0) \tag{3.77}$$

Now D_N is integrated with respect to arbitrary variable t to form an equation for $S_N(x)$.

$$S_N(x) = 1 - \int_{-\infty}^{x} D_N(t) dt \tag{3.78}$$

The following equations can now be utilised.

$$\left(\frac{d}{dx}\right) H_{2n}(x) e^{-x^2} = -H_{2n+1}(x) e^{-x^2} \tag{3.79}$$

$$erf(x) = \frac{2}{\sqrt{\pi}} \int_0^x e^{-t^2} dt \tag{3.80}$$

To produce the following result.

$$S_N(x) = S_0 + \sum_{n=1}^{N} A_N H_{2n-1}(x) \tag{3.81}$$

where

$$S_0 = \frac{1}{2}(1 - erf(x)) \tag{3.82}$$

A very important point to note is that (3.82) corresponds to the Fermi-Dirac smearing detailed previously. The use of higher terms as outlined in (3.81) removes the error which was previously induced by calculating the charge below E_F utilising (3.82). Finally the integral (3.68) for order N over a series of k-points can be written as

$$I = \sum_i \omega_i f(\hat{k}) S_N(x_i) \tag{3.83}$$

where i is a series of integers each one corresponding to a k-point and

$$x_i = \frac{E(\hat{k}_i - E_F)}{W} \tag{3.84}$$

There are two factors which require further evaluation W and N where better convergence is obtained as W is reduced and N is increased. In order to have high N however it demands that there is a fine k-point mesh. There is a lot of nuance in selecting these factors (including the shape of the energy bands) which is beyond the scope of this thesis but is detailed in [124]. This technique is clearly superior to Fermi-Dirac smearing and in the case of transition metals is about as effective as the linear tetrahedron method.

3.4.2 Blöchl Interpolation

There are two main issues concerning the linear tetrahedron method the first is called the mis-weighting problem of k-points and the second is the errors[†]. The main error is the linear tetrahedron method arises from the fact that if the curvature of the function is negative then the interpolation will result in an overestimation and vice-versa. An error is also contributed by the fact that the integration now being evaluated is different from the integration concerning the actual Fermi surface. The former error converges with respect to Z^2 and the latter error, is less significant converging with respect to Z^4, where Z is the spacing between the k-points. This error is not an issue in semi-conductors and insulators as a slight overestimation in one sector of the BZ will correspond to an equal underestimation in another of the tetrahedra and vice-versa. But in metals partially filled bands mean this does not apply. This method was found to be orders of magnitude more computationally efficient, for total energy calculations in metals then the standard linear tetrahedron method. Blöchl interpolation employs a formula to significantly reduce this error by modifying the weights in each of the tetrahedra. The corrections $d\omega_i$ are calculated respectively as

$$d\omega_i = \sum_T \frac{1}{40} D_T(E_f) \sum_{j=1}^{4} \epsilon_j - \epsilon_i \tag{3.85}$$

where $D_T(\epsilon_f)$ is the contribution of one of the tetrahedra to the density of states at the Fermi level, where the T's are indexes corresponding to each of the tetrahedra, ϵ_1

[†]Other than if explicitly stated the source for the information in this subsection can be assumed to from reference[121].

through ϵ_4 are the one particle energies at the 4 corners of the tetrahedron. The i's and j's are indexes corresponding to the four corners of a tetrahedron.

3.5 The Exchange-Correlation Functional

3.5.1 Introduction

As mentioned in section 3.2.3 the exact form of the exchange-correlation functional (XC hereafter) is unknown, hence it is necessary to use an approximate form. There exists a series of approximate forms each of which employ more physical information. A common way of visualising this is to use the analogy of Jacob's ladder as described in the biblical verse Genesis 28[99, 130]. In this analogy heaven is represented by a hypothetical perfect functional which employs zero approximations and the base of the ladder is represented by the simplest functional the local density approximation (LDA hereafter)[99, 130]. It is important to note that advancing to a higher rung on the ladder does not necessarily mean the results will better approximate physical reality, especially in the case where the functional on the higher rung is empirical and being applied to a scenario outside of where it was derived[99, 131].

3.5.2 Local Density Approximation

The LDA (note there are two versions spin averaged and spin-polarised (referred to as the LSD (local spin density)), this variant is evaluated in this subsection) is the simplest XC, it exploits the fact that the only scenario in which the Honenberg-Kohn theorems can

be solved exactly is that of a uniform electron gas[99]. The exchange-correlation energy is calculated for many densities using monte-carlo calculations, these values are fitted for the use of LDA[99, 130]. In the LDA the exchange-correlation energy is expressed as follows[132].

$$E_{XC}[n_\uparrow, n_\downarrow] = \int d^3r \epsilon_{XC}^{unif.}(n_\uparrow, n_\downarrow) n \tag{3.86}$$

Where $\epsilon_{XC}^{unif.}$ is the exchange-correlation energy for a uniform electron gas of the same electron density n as the electron density at that point, $n_\uparrow$ and $n_\downarrow$ are the densities of spin up and spin down electrons respectively where n is [132]

$$n = n_\uparrow + n_\downarrow \tag{3.87}$$

It is very important to note the existence of the uniform density limit of the Kohn-Sham functional and that it is in the scenario of a constant n that the exchange-correlation energy is equal to that of a uniform electron gas[99]. In a real substance however this will never be exactly the case, but in materials where the n is slowly varying the LDA induces very small errors[99, 132].

3.5.3 Generalised-Gradient Approximation

The next rung on the ladder above the LDA is the generalised-gradient approximation (GGA hereafter) which can be represented by the following equation[132].

$$E_{XC}[n_\uparrow, n_\downarrow] = \int d^3r f(n_\uparrow, n_\downarrow, \nabla n_\uparrow, \nabla n_\downarrow) \tag{3.88}$$

Whilst in theory there are many different schemes which can be used in the LDA they are all essentially the same, as whilst the formalisms may fit the values of $\epsilon_{XC}^{unif.}$ differently all will do so accurately; hence they can be considered essentially equivalent[99]. This is not true of the GGA as $\nabla n_\uparrow$ and $\nabla n_\downarrow$ can be implemented into the function $f(n_\uparrow, n_\downarrow, \nabla n_\uparrow, \nabla n_\downarrow)$ in a large number of ways leading to distinct GGA formalisms[99, 132]. For solid continuous substances the two most popular formalisms are the Perdew-Wang (PW-91 hereafter) formalism first proposed in 1991 and the Perdew-Berke-Ezerhof formalism (PBE hereafter) proposed 5 years later[99, 132, 133].

The formalism used for the research in this thesis is the PBE. The reasoning for this is that this research demands the higher accuracy and ability to function in scenarios of more rapidly varying n of utilising a GGA formalism over the LDA[99, 130, 132]; also PBE offers a large number of benefits over the PW-91[132]. Benefits include correct behaviour under uniform scaling in addition to a smoother potential, by only making very small sacrifices such as the correct behaviour under very specific limits[132].

It is necessary at this juncture to introduce the concept of the exchange-correlation hole; which arises due to the fact that in the quantum mechanical description of electrons

versus the solely classical description, the electrons are subject to the Pauli exclusion principle in addition to a non-classical Coulomb repulsion. This results in each electron generating a "hole" of density around itself[132, 133]. The PW-91 was generated by taking the second order density-gradient from this hole in a system of slowly varying electron density and removing spurious long range parts to satisfy various sum rules on the exact hole[132, 133]. This function is then fitted to satisfy as many other conditions as possible[132, 133]. This approach was successful but also has many flaws such as the over-parametrisation of $f(n_\uparrow, n_\downarrow, \nabla n_\uparrow, \nabla n_\downarrow)$, also said parameters do not flawlessly connect generating fluctuations in the functions[132]. It is to be noted that several properties of the hole are reproduced exactly in both PW-91 and PBE[99].

The PBE functional was generated in order to streamline the derivation and reduce the number of conditions to be followed to only those that will significantly impact the energy. First it is necessary to split E_{XC} into its two components[†][132].

$$E_{XC} = E_X + E_C \tag{3.89}$$

where E_X and E_C are the contributions from exchange and correlation respectively.

$$E_C[n_\uparrow, n_\downarrow] = \int d^3r n[\epsilon_C^{unif.}(r_s, \zeta) + H(r_s, \zeta, t)] \tag{3.90}$$

Where $H(r_s, \zeta, t)$ is called the gradient contribution, $\zeta = \frac{(n_\uparrow - n_\downarrow)}{n}$ is the relative spin-

[†]Other than if explicitly stated for the remainder of this subsection the source for the information in this subsection can be assumed to from reference[132].

polarisation, r_s is the local Seitz radius, k_s is the Thomas-Fermi screening wave number, and $t = \frac{|\nabla n|}{2\phi(\zeta)k_s n}$ is a dimensionless form of the density gradient where

$$\phi(\zeta) = \frac{[(1+\zeta)^{\frac{2}{3}} + (1-\zeta)^{\frac{2}{3}}]}{2} \tag{3.91}$$

Evaluating H in the following 2 limits and a condition i) $t \to 0$ where $H \to \frac{\phi^3 t^2 e^4 m_e \beta}{\hbar^2}$ (note β is a constant) ii) $t \to \infty$ where $H \to -\epsilon_c^{unif.}$ causing the effects of correlation to disappear iii) If $E_C[n_\uparrow, n_\downarrow]$ is assumed to scale linearly as density is increased all the way up to high density, (3.90) must scale to a constant and $H \to \frac{\phi^3 e^4 m_e \gamma \ln(t^2)}{\hbar^2}$ where $\gamma = \frac{1-\ln(2)}{\pi^2}$.

This allows $H(r_s, \zeta, t)$ to be expressed as follows.

$$H(r_s, \zeta, t) = \frac{e^4 m_e}{\hbar^2}\gamma\phi^3 \ln 1 + \frac{\beta}{\gamma}t^2[\frac{1+At^2}{1+At^2+A^2t^4}] \tag{3.92}$$

where

$$A = \frac{\beta}{\gamma}\left[exp\frac{-\epsilon_C^{unif.}\hbar^2}{\gamma\phi^3 e^4 m_e} - 1\right]^{-1} \tag{3.93}$$

E_X can now be expressed as follows,

$$E_X = \int d^3 r \epsilon_X^{unif.}(n) F_X(s) n \tag{3.94}$$

where

$$\epsilon_X^{unif.} = \frac{3e^2 k_F}{4\pi} \tag{3.95}$$

where $k_F = \frac{3^{1/2}\pi^{1/3}}{4^{1/3} r_s}$. Subjecting E_X the the following 4 conditions i) in order to recover the correct behaviour in a uniform electron gas $F_X(0) = 1$ ii) it must obey the spin scaling relationship iii) As $S \to 0$ $F_X(s) \to 1 + \frac{\beta\pi^2}{3}s^2$ iv) the Lieb-Oxford bound must be satisfied.

$$E_X[n_\uparrow, n_\downarrow] \geq E_{XC}[n_\uparrow, n_\downarrow] \geq -C_{LO} e^2 \int d^3 r n^{4/3} \tag{3.96}$$

The Lieb-Oxford bound concerns the repulsive Coulomb energy and the difference between it and the derivation assuming particle independence (no exchange and correlation), the right hand term is the lower bound for this difference[134, 135]. The constant C_{LO} is set at 1.679 in this case, this value is to 2 decimal places the same as proposed by Lieb[135] 1.68 (later improved to 1.6358 in by [136]) this value means the above equation will hold regardless of the number of electrons (note that further optimization can be achieved by specifying the number of electrons or applying the low density limit) whilst being tightly implemented (note lower value of C_{LO} results in tighter implementation)[135, 137]. $F_X(S)$ can be constructed to obey these conditions.

$$F_X(S) = 1 + \kappa - \frac{\kappa}{1 + s^2\mu/\kappa} \tag{3.97}$$

where $\kappa = 0.804$; finally this allows $E_{XC}[n_\uparrow, n_\downarrow]$ to be expressed as follows

$$E_{XC}[n_\uparrow, n_\downarrow] = \int d^3 r n \epsilon_X^{unif.}(n) F_{XC}(r_s, \zeta, s). \tag{3.98}$$

Where $F_{XC}(r_s, \zeta, s)$ is the enhancement factor, where the LDA is recovered when $s = 0$. It is also important to note that of the two effects, exchange and correlation; in most practical circumstances exchange is dominant and that correlation only begins to have an equal or greater effect than exchange at very low densities.

3.6 Iterative Algorithms

It was mentioned previously that the quantum many-body problem is in all practical cases solved iteratively not analytically. In order to do this with any computational efficiency, algorithms must be employed. In order to perform a static calculation only one algorithm is needed; one to find for a set of atomic positions, electron density and more importantly its corresponding free energy. However in calculations involving relaxation of atomic positions, after each determination of the free energy the atomic positions must be adjusted and the free energy determined again until satisfactory convergence is achieved. The algorithm used for atomic position relaxation is the conjugate-gradient algorithm (an alternative the quasi-Newton algorithm also exists, consult [99] for further details). There are two separate schemes used for determination of free energy the residual minimisation method-direct inversion in the iterative subspace (RMM-DIIS hereafter) scheme and the blocked davidson Scheme (BD hereafter).

3.6.1 Atomic Positions

Conjugate-Gradient Scheme

The conjugate-gradient scheme can be expressed in words in the following way. Initially relaxation of the ions is performed along the direction of the steepest descent which is the direction of the calculated forces and the stress tensor[129]. Following this the energy is recalculated at a position along the direction of steepest descent, this is called the trial step[129]. Utilising the following pieces of information the change of total energy and change in forces a minimum energy along this direction can be approximated by selecting a form of the curve (either quadratic or cubic)[129]. From here a corrector step is then carried out, this is then checked by re-evaluating the energy and forces and assessing whether there are significant force components parallel to the previous search direction, if so more corrector steps are carried out until this is no longer the case[129].

In order to express the conjugate-gradient method mathematically it is necessary to first define a set of linear algebraic equations[138].

$$a_{00}x_0 + a_{01}x_1 + a_{02}x_2 + ... + a_{0,N-1}x_{N-1} = b_0 \tag{3.99}$$

$$a_{10}x_0 + a_{11}x_1 + a_{12}x_2 + ... + a_{1,N-1}x_{N-1} = b_1 \tag{3.100}$$

.....

$$a_{M-1,0}x_0 + a_{M-1,1}x_1 + a_{M-1,2}x_2 + ... + a_{M-1,N-1}x_{N-1} = b_{M-1} \tag{3.101}$$

This series of equations can be expressed in matrix form as follows[138].

$$\boldsymbol{A} \cdot \boldsymbol{x} = \boldsymbol{b} \tag{3.102}$$

Considering for an N-dimensional point P that can be defined as the origin of the coordinate system with coordinates $\boldsymbol{x}$ any function can be approximated using a Taylor series[138].

$$f(\boldsymbol{x}) \approx c - \boldsymbol{b} \cdot \boldsymbol{x} + \frac{1}{2}\boldsymbol{x} \cdot \boldsymbol{A} \cdot \boldsymbol{x} \tag{3.103}$$

where $c = f(P)$. Now defining an arbitrary starting vector $\hat{g}_0$ and defining $\hat{h}_0 = \hat{g}_0$, two series of vectors can now be defined to satisfy the conjugacy and orthogonality conditions

$$\hat{g}_{i+1} = \hat{g}_i - \lambda_i \boldsymbol{A} \cdot \hat{h}_i \tag{3.104}$$

$$\hat{h}_{i+1} = \hat{g}_{i+1} - \Upsilon_i \hat{h}_i \tag{3.105}$$

where i is a positive integer or zero[138]: λ_i and Υ_i are defined as follows.

$$\lambda_i = \frac{\hat{g}_i \cdot \hat{h}_i}{\hat{h}_i \cdot \boldsymbol{A} \cdot \hat{h}_i} \tag{3.106}$$

$$\Upsilon_i = \frac{\hat{g}_{i+1} \cdot \hat{g}_{i+1}}{\hat{g}_i \cdot \hat{g}_i} \tag{3.107}$$

It initially appears that the matrix A is a key piece of information in order to produce the necessary conjugate directions $\hat{h}_i$, however this is not true as said directions can be

deduced without any knowledge of $\boldsymbol{A}$ by the following reasoning[138]. Providing we have the derivative of c at an arbitrary point i the following is true $\hat{g}_i = -\nabla f(P_i)$ assuming f is of the correct form (3.103)[138]. Moving in a direction h_i to the local minimum of f at a point defined as P_{i+1} and setting $\hat{g}_{i+1} = -\nabla f(P_{i+1})$ reproduces the correct vector from (3.104)[138]. One important nuance with regard to the conjugate-gradient method is the fact that there is only a limited amount of conjugate directions that can be calculated[99, 138]. When said calculation reaches $m \leq N$ steps there are no new conjugate directions to the vectors that already exist, because in an N-dimensional space we can only make a vector orthogonal to at most N-1 other vectors, hence the process will have to be restarted beyond this point[99, 138].

3.6.2 Electron Density

RMM-DIIS and BD have a significant amount in common but iterate slightly differently[†]. They are both techniques employed to approximate the relevant solutions to the general hermitian eigenproblem.

$$\boldsymbol{H} |a\rangle = \lambda \boldsymbol{S} |a\rangle \tag{3.108}$$

Where $\boldsymbol{H}$ is the Hermitian matrix, $\boldsymbol{S}$ is the overlap matrix, λ and $|a\rangle$ are an eigenvalue and eigenvector respectively. The need for iterative problem solving in electron density stems from the fact that in order to diagonalise $\boldsymbol{H}$ would require the computer to have

[†]Other than if explicitly stated the source for the information in this subsection can be assumed to from reference[139].

full random access to all matrix elements, and the computational effort necessary scales as N^3 (where iterative techniques scale as N^2) where N is the number of rows and columns. One such technique for full matrix diagonalisation is the Choleski-Householder technique.

In general only a small number of eigenvectors n, are necessary to calculate to determine ground state properties. All iterative techniques all utilize 3 sets of N dimensional vectors i) the basis set $|\theta_i\rangle$ where $i = 1, ..., N$ ii) the expansion set $|b_j\rangle$ where $j = 1, ..., N_b$ and iii) the complete set $|x_i\rangle$ where $j = 1, ..., N$. The basis set is a group of vectors used in the computation if the eigenstates, the expansion set is a set of vectors which exist inside a small section of the Hilbert space where all important eigenstates can be reproduced from: and the complete set, where any vector can be reproduced in terms of this set, and the full Hilbert space is spanned. Each iterative technique is noted for the different choice of complete and expansion sets.

The general outline of an iterative calculation is as follows a small section of the Hermitian matrix $\boldsymbol{H_0}$ of size $N_0 \times N_0$ which defines the zero order problem is selected. This matrix is then fully diagonalised (for example by using the Choleski-Householder technique). This provides a good starting point for later iterations. How iteration is done beyond this is to utilise a Newton-Nesbet step resulting in a residual vector $|\delta A\rangle$.

$$|\delta A\rangle = -\sum_i{}' \frac{\langle x_i|R\rangle\,|x_i\rangle}{\langle x_i|\,\boldsymbol{H} - E^{ap}\boldsymbol{S}\,|x_i\rangle} \tag{3.109}$$

where R is used to measure to what extent the approximate vector $|A^{ap}\rangle$ is incorrect

$$R = \left(\frac{\langle R|R\rangle}{\langle A^{ap}|\boldsymbol{S}|A^{ap}\rangle} \right)^{1/2} \tag{3.110}$$

Note the $'$ in (3.109) is used to denote the a cut-off δ which is typically $10ryd$ but results are scarcely sensitive of it. $|\delta A\rangle$ can now be added to the approximate eigenvector in question such that it more accurately reflects the true eigenvector. Note that this analysis requires use of the diagonal approximation which cancels a significant amount of terms. The two techniques in question are both basis expansion techniques, meaning that speed of convergence is improved, as after each iteration new vectors are added to the expansion set each iteration. Where the techniques differ is in there implementation of $|x_i\rangle$ and the way in which vectors are added to the expansion set.

Blocked Davidson

BD is an enhanced version of the Davidson algorithm with the main improvement being that many eigenvectors are derived at once. The BD utilises $|e_i\rangle$ to represent $|x_i\rangle$, where $|e_i\rangle$ is a row of vectors all zero except for the ith position which contains a 1. The $|b_j\rangle$ is defined in BD as follows. In each iteration the following vectors are added to $|b_j\rangle$

$$\left[|\delta A_k\rangle - \sum_{j=1}^{N_0+k-1} \langle b_j|\delta A_k|b_j\rangle \right]_{k=1,\ldots,m} \tag{3.111}$$

where m new vectors are added each iteration where the k's represent eigenvectors of $N_0 \times N_0$. The addition of these vectors allows convergence to be hastened significantly.

RMM-DIIS

The RMM-DIIS algorithm represents $|x_i\rangle$ as follows.

$$|x_i\rangle = [|a_j^0\rangle, j = 1, ..., N_0] + [|e_j\rangle \, j = N_0 + 1, ..., N], \tag{3.112}$$

Where p is the iteration number and $|a_j^0\rangle$ is the set of eigenvectors derived from diagonalisation of $\boldsymbol{H_0}$. The rationale behind this is that the aforementioned diagonal approximation, ceases to be an approximation if $|x_i\rangle$ contains the exact eigenvectors of $\boldsymbol{H_0}$. Noting the above it is possible to improve the selection of the complete set $|e_j\rangle$ by i) augmenting $|a_j^0\rangle$ with zeros to ensure that there are N dimensions and ii) adding unit vectors to make sure there are N vectors. Post to each iteration the following vector $|A_j^p\rangle$ are added to $|b_j\rangle$. This is important as it means that information from the entire iteration history is stored and utilised in $|b_j\rangle$. The RMM-DIIS technique performs a step in each iteration where 2 new matrices of dimensions $(p+1) \times (p+1)$ (note very small matrices) are defined and solved by Choleski-Householder. The addition of this step significantly improves the speed of convergence.

3.7 Basis Sets

There is an added issue which arises when attempting to solve the Kohn-Sham single electron wave functions ψ_i computationally, and that is that the Kohn-Sham orbitals associated with them ϕ_m (where m simply counts the number of orbitals) are in actuality arbitrary continuous functions which cannot be expressed on a computer[99]. This is

where basis sets become necessary. A basis set is a series of functions that when added together form an approximation of the true Kohn-Sham orbitals[119, 120]. There are in general 3 properties that are necessary for a useful basis set i) efficiency ii) no bias iii) simplicity[119, 120]. Efficiency in this context means that only a limited number of functions are needed to represent the ϕ_m[119, 120]. No bias means that there is no mechanism within the functions to drive the ϕ_m to a preconceived result (such as a basis set derived from a very specific problem)[119, 120]. Simplicity ensures that implementation within various programs will not be excessively difficult[119, 120]. The general form of expressing ϕ_m as a function of a basis set is as follows[119].

$$\phi_m = \sum_{q=1}^{Q} c_m^q \phi_q \tag{3.113}$$

where c_m^q are constants, ϕ_q are the waves of the basis set and Q is the limit to which the basis set is truncated (this could in principle be infinity corresponding to the exact solutions of ϕ_m, but obviously this is not computationally possible)[119]. The proceeding subsections will discuss the plane-wave, augmented plane-wave (APW hereafter) basis sets, the successors of the latter the linear augmented plane-wave (LAPW hereafter) and APW with local orbitals (APW+lo hereafter). Projector augmented wave (PAW hereafter) is the basis set used in this research and will also be outlined. Of course these are not the only possible basis sets that can be used in a DFT calculation, for example there exists the local atomic orbital basis set. This basis set has a prominent track record at modelling many situations including surfaces[140, 141] and molecules[142, 143] but

not for its use in materials calculations, hence will not be covered in further detail here.

3.7.1 Plane-Wave Basis Set

The plane-wave basis set fits the requirements of simplicity and no bias[119, 120, 144]. It is constructed by use of the Bloch theorem's solution for the wavefunction of an electron in a periodic potential[99, 119, 125].

$$\Psi_{\hat{k}}(\hat{r}) = u_{\hat{k}}(\hat{r})e^{i\hat{k}\cdot\hat{r}} \tag{3.114}$$

where $u_{\hat{k}}(\hat{r})$ is a function with the same periodicity as the lattice and $\hat{k}$ corresponds to any vector in reciprocal space[99, 120, 125]. Noting that any $\hat{k}$ can be rewritten as

$$\hat{k} = \hat{g} + \hat{K} \tag{3.115}$$

Where $\hat{g}$ is a vector in the first-BZ and $\hat{K}$ is a vector which moves between two reciprocal lattice points[119, 120]. This means (3.114) can be rewritten[119].

$$\Psi_{\hat{k}}(\hat{r}) = u_{\hat{k}}(\hat{r})e^{i\hat{K}\cdot\hat{r}}e^{i\hat{g}\cdot\hat{r}} \tag{3.116}$$

Note the second factor also has the periodicity of the lattice[119]. For convenience here an alternate labelling scheme will be introduced, n (the band index) will depict the number of the BZ [119]. It is noted that n and $\hat{g}$ contain the same information as $\hat{k}$[119].

This allows the expression of the basis set as follows[99, 119, 120].

$$\phi_{\hat{g}}^{n} = \sum_{\hat{K}} e^{i(\hat{K}+\hat{g})\cdot\hat{r}} c_{\hat{K}}^{n,\hat{g}} \tag{3.117}$$

As alluded to in the previous section summing over all possible $\hat{K}$ vectors would result in an infinite basis set[99, 119]. It is noted that the free electron energy has the following relationship with the magnitude of $\hat{K}$[99, 119].

$$E = \frac{\hbar^2 K^2}{2m_e} \tag{3.118}$$

Hence cut-off can be thought of in terms of energy($E_{cut-off}$)[99, 119]. Employing a plane-wave basis set has an issue, that in order to accurately account for the sharp gradient change in the core region a very high number of plane-waves would be necessary (up to K with a period of an order of magnitude smaller than the core region)[99, 119, 120]. This results in such a low efficiency, that calculations would be difficult or sometimes impossible to be performed even on a supercomputer[99, 119]. It is noted however that the core properties, due to shielding are seldom affected by the chemistry of the structure in which the atom exists[119]. Hence it can be assumed that they behave the same as in a free atom[99, 119, 120].

This enables the use of pseudopotentials where the potential in the core region is replaced such as to result in a smooth wavefunction in the core region[99, 119, 120](it is to be noted that it is impossible to assess the full wave function unlike linear methods mentioned in proceeding subsections[144]). When a pseudopotential is constructed it is

constructed as to obey the Pauli exclusion principle, meaning that the effective potential the electrons are subject to can be quite small due to cancelling of the crystal potential by the atomic functions[125]. The quality of pseudopotentials are determined by two metrics i) transferability and ii) softness[119]. Transferability means the ability to employ it in a series of different environments molecule, solid etc. whilst softness refers to how many plane-waves are required to utilise it[119]. It is noted that this technique struggles when dealing with certain transition metals and first row metals as pseudopotentials must be hardened in these cases and lose transferability[144]. Vanderbilt introduced what are known as ulutrasoft psedopotential which resolved many of these issues[144].

3.7.2 Augmented Plane-Wave (APW) Method

The APW method attempts to remedy the issue of low efficiency for plane-wave basis sets in an alternate way other than by the addition of a pseudopotential[119, 120]. The way it achieves this is by splitting each wave of the basis set into multiple parts[119, 120]. Inside an atomic core the wave is expressed as an atomic function and outside of an atomic core it is expressed as a standard plane-wave[119, 120]. To distinguish between these two regions a sphere is drawn around each atom and the inside is labelled the muffin-tin region, outside the sphere is called the interstitial region[119, 120]. Hence a generic APW can be defined as follows[119].

$$\phi_{\hat{K}}^{\hat{g}}(\hat{r}, E) = \frac{1}{V^{1/2}} e^{i(\hat{g}+\hat{K})\cdot\hat{r}} \text{ if } \hat{r} \,\epsilon\, I \tag{3.119}$$

$$\phi_{\hat{K}}^{\hat{g}}(\hat{r}, E) = \sum_{l,n,\hat{g}} A_{l,n,\hat{g}}^{\alpha(\hat{g}+\hat{K})} u_l^{\alpha}(r', E) Y_{n,\hat{g}}^{l}(\hat{r}') \text{ if } \hat{r} \,\epsilon\, R_{\alpha} \tag{3.120}$$

Where V is the unit cell volume, I corresponds to the interstitial region, R_α is the radius of the muffin-tin region, $\hat{r}' = \hat{r} - \hat{r}_\alpha$ is the position relative to the centre of a muffin-tin region[119]. The index α corresponds to a free atom, and E corresponds to a specific energy[119]. $Y^l_{n,\hat{g}}(\hat{r}')$ are a selection of spherical harmonics and $u^\alpha_l(r', E)$ are radial solutions to the Schrödinger equation at a series of fixed energies and orthogonalised to the core states[119]. It is important that $\phi^{\hat{g}}_{\hat{K}}(\hat{r}, E)$ is continuous hence it must be made that all across the surface of the muffin-tin region the two equations must be equal to each other (note gradient can be different)[119, 120]. $A^{\alpha(\hat{g}+\hat{K})}_{l,n,\hat{g}}$ is constructed for this purpose, however this condition cannot be adhered to exactly, as there are in theory an infinite number of terms $l = 0, ..., \infty$ and hence there needs to be a truncation[119]. l is typically truncated at $R_\alpha K_{cut-off} = l_{cut-off}$, exceeding this can however result in unstable behaviour at the surface of the muffin-tin zone[119]. The APW method requires significantly fewer waves than the standard plane-wave method[119]. However the calculation overall is much slower, due to the fact that only one eigenvalue is determined at a time (because E must be guessed as equal to the energy of an eigenstate) whereas in the plane-wave method multiple eigenstates are determined in each diagonalisation[119, 120, 144]. The APW basis set alone is not used in practical calculations any more due to this; either one of LAPW or APW+lo are used instead[119].

3.7.3 Augmented Plane-Wave with Local Orbitals (APW+lo) Method

The APW+lo removes the issue with the energy dependence of the basis set[119, 120]. The first step is to reproduce a series of APWs but this time E is set to a series of

fixed energies $E^{\alpha}_{1,l}$[119, 120]. The next step is to introduce local orbitals $\phi^{lm}_{\alpha,lo}$ which are defined as follows[119].

$$\phi^{lm}_{\alpha,lo}(\hat{r}) = 0 \text{ if } \hat{r} \,\epsilon\, I \text{ or } \hat{r} \,\epsilon\, R_{\alpha} \tag{3.121}$$

$$\phi^{lm}_{\alpha,lo}(\hat{r}) = A^{\alpha,lo}_{l,n,\hat{g}} u^{\alpha}_{l}(r', E^{\alpha}_{1,l}) + B^{\alpha,lo}_{l,n,\hat{g}} \dot{u}^{\alpha}_{l}(r', E^{\alpha}_{1,l}) \text{ if } \hat{r} \,\epsilon\, F_{\alpha} \tag{3.122}$$

Where F_{α} refers to the muffin-tin region of the atom which the lo corresponds[119]. The exact procedure for producing the coefficients $A^{\alpha,lo}_{l,n,\hat{g}}$, and $B^{\alpha,lo}_{l,n,\hat{g}}$ will not be detailed here but there exists a requirement that the lo is equal to zero at the surface of the muffin-tin sphere[119, 120]. If this is adhered to the value at the surface of the muffin-tin region for the lo and APW will be continuous but the values of their slopes will not be[119]. An APW+lo calculation requires a basis set size of around that of a pure APW calculation[119, 120]. But multiple eigenstates are recovered per diagonalisation so the calculation will be significantly faster[119].

3.7.4 Linear Augmented Plane-Wave (LAPW) Method

LAPW uses an alternate technique to eliminate energy dependence of the basis set by use of an additional quantity $B^{\alpha,\hat{g}+\hat{K}}_{l,n,g}$[119]. This is necessary due to the fact that a Taylor series is used to expand $u^{\alpha}_{l}(r', E_0)$ (where E_0 is the original guess of the eigenstate) to obtain values of $u^{\alpha}_{l}(r', \epsilon)$ at energies close to it, however the exact quantity $E_0 - \epsilon$ is not exactly known[119]. The process can be much improved by defining, instead of one E_0 a series of them $E^{\alpha}_{1,l}$ at the centres of relevant bands[119]. This leads to the final

expression of the LAPW[119].

$$\phi^{\hat{g}}_{\hat{K}}(\hat{r}, E) = \frac{1}{V^{1/2}} e^{i(\hat{g}+\hat{K})\cdot\hat{r}} \text{ if } \hat{r} \,\epsilon\, I \quad (3.123)$$

$$\phi^{\hat{g}}_{\hat{K}}(\hat{r}, E) = \sum_{l,n,\hat{g}} \left(A^{\alpha(\hat{g}+\hat{K})}_{l,n,\hat{g}} u^{\alpha}_{l}(r', E) + B^{\alpha(\hat{g}+\hat{K})}_{l,n,\hat{g}} \dot{u}^{\alpha}_{l}(r', E) \right) Y^{l}_{n,\hat{g}}(\hat{r}') \text{ if } \hat{r} \,\epsilon\, R_{\alpha} \quad (3.124)$$

LAPW has much higher efficiency than the plane-wave basis set but the calculation speed is slowed down by additional steps in the calculation, hence the speed is comparable[119]. The LAPW method is known for its ability to perform calculations efficiently for transition metals, it is also known for high accuracy, however it struggles in cases of broad valence bands[119, 120].

3.7.5 Linear Augmented Plane-Wave with local orbitals (LAPW+LO) Method

LAPW can also be aided by the use of local orbitals (LO) (note a different definition from the local orbitals in APW+lo) which are designed to account accurately for semi-core states[119, 120]. States which have some degree of influence outside the muffin-tin region, but do not have a strong presence there (valence states), or are contained entirely within the core (core states)[119, 120, 144]. It is for these states that local orbitals are defined as follows[119].

$$\phi^{lm}_{\alpha,LO}(\hat{r}) = 0 \text{ if } \hat{r} \,\epsilon\, I \text{ or } \hat{r} \,\epsilon\, R_{\alpha} \quad (3.125)$$

$$\phi^{lm}_{\alpha,LO}(\hat{r}) = \left(A^{\alpha,LO}_{l,n,\hat{g}} u^{\alpha}_{l}(r', E^{\alpha}_{1,l}) + B^{\alpha,LO}_{l,n,\hat{g}} \dot{u}^{\alpha}_{l}(r', E^{\alpha}_{1,l}) + ... \right.$$

$$C^{\alpha,LO}_{l,n,\hat{g}}\,\dot{u}^{\alpha}_{l}(r',E^{\alpha}_{1,l})\Big)Y^{l}_{n,\hat{g}}(\hat{r}')\text{ if }\hat{r}\,\epsilon\,F_{\alpha} \tag{3.126}$$

Again the specifics behind the 3 coefficients $A^{\alpha,LO}_{l,n,\hat{g}}$,$B^{\alpha,LO}_{l,n,\hat{g}}$ and $C^{\alpha,LO}_{l,n,\hat{g}}$ will not be detailed. A local orbital only has a non-zero value in the muffin-tin region of the atom in which it exists[119]. It is also important to note that there is no $\hat{g}$ or $\hat{K}$ in the LOs in other words they have no relation to the interstitial region[119, 120]. Employing LOs only results in an expansion of the basis set size by a few LAPWs but is in general worth the small addition in computational time for the increased accuracy that LOs provide[119, 120].

3.7.6 Projector Augmented Wave (PAW) method

The purpose of the PAW method was to form a hybrid of the LAPW and plane-wave with pseudopotential approaches[†]. The PAW basis set is recognised for its high efficiency and is unbiased[119, 144]. The first step in the generation of the PAW basis set is to take the states which are orthogonal to core states which exist in a Hilbert space and transform these states into a pseudo-Hilbert space (PS hereafter). The main point of this is convenience allowing complex Kohn-Sham (KS hereafter) wavefunctions to be transformed into computationally tractable PS wavefunctions. Utilizing these wavefunctions expectation values of certain properties can be deduced (note ˜ is used to reference the PS and wavefunctions thereof)

$$\langle A\rangle=\langle\tilde{\Psi}|\underline{\tilde{A}}|\tilde{\Psi}\rangle \tag{3.127}$$

[†]Other than if explicitly stated the source for the information in this subsection can be assumed to be from reference[144].

where Ψ is a KS wavefunction $\underline{A}$ is an operator which corresponds to a property, and

$$\tilde{\underline{A}} = T^{\dagger}\underline{A}T \tag{3.128}$$

where T transforms PS waves into KS waves. By analogy to the muffin-tin regions of APW type methods the PAW method used a similar concept called augmentation spheres (Ω_R) around each atom where the core region exists. In the PAW method outside of said augmentation regions KS and PS wavefunctions must be equal. It is now possible to express T as a sum of contributions from the augmentation regions of the atoms T_α.

$$T = 1 + \sum_{\alpha} T_\alpha \tag{3.129}$$

At this juncture a series of partial PS waves $|\phi_i\rangle$ must be defined such that the series of T_α can also be defined. A natural fit for these waves are the radial solutions to the Schrödinger equation for an isolated atom (these waves can if necessary be orthogonalised to the core states). A transformation between a PS and KS partial wave can now be expressed within Ω_R as follows (it should be noted that index i in this context represents angular momentum quantum numbers, α and n an index to label partial waves which are different but have the same α and angular momentum).

$$|\phi_i\rangle = (1 + T_\alpha)\,|\tilde{\phi}_i\rangle \tag{3.130}$$

Expressing $|\tilde{\phi}_i\rangle$ as a series of partial waves

$$|\tilde{\Psi}\rangle = \sum_i c_i \, |\tilde{\phi}_i\rangle \, \Omega_R \tag{3.131}$$

The following also holds true

$$T \, |\tilde{\Psi}\rangle = |\Psi\rangle = \sum_i c_i \, |\phi_i\rangle \tag{3.132}$$

Note that the coefficients c_i are the same in both (3.131) and (3.132). It is required that T be a linear transformation, the deduction that can now be made is that the coefficients c_i must be linear functionals of the PS wavefunctions.

$$c_i = \langle \tilde{p}_i | \tilde{\Psi} \rangle \tag{3.133}$$

Where $\langle \tilde{p}_i|$ are classified as projector functions and that one exists for every single $\tilde{\phi}_i$. Projector functions are radial functions times spherical harmonics which only exist in the Ω_R and exhibit the property that

$$\delta_{ij} = \langle \tilde{p}_i | \tilde{\phi}_j \rangle \tag{3.134}$$

The conclusion of the above mathematical analysis is an expression of the PAW basis set.

$$|\Psi\rangle = |\tilde{\Psi}\rangle + \sum_i (|\phi_i\rangle - |\tilde{\phi}_i\rangle) \langle \tilde{p}_i | \tilde{\Psi}\rangle \tag{3.135}$$

Similarly to the plane-wave and APW based methods truncation by the use of $E_{cut-off}$, in addition to this the truncation must maintain the one to one relationship between KS and PS waves by truncating the two in the same way (this is called additive augmentation which does not impact the completeness of the basis set). The errors introduced for total energy via truncation are typically small due to the fact that the operator used is quasilocal and that the one centre expansions for the KS and PS wavefunctions are typically largest in opposite spacial regions (note that difference between KS and PS waves decline at high energies due to the fact that electrons become less effected by the potential at high energies).

The PAW method is known to be able to treat first row and transition elements effectively as the LAPW method can. It is to be noted that the frozen core approximation is employed in the PAW approach (negating the necessity of projector functions for the core states) opting to use the core states from an isolated atom. Note however that in this implementation some mixing of core states due to changing potential is allowed.

There is a plethora of ways to deduce the projector functions and KS and PS waves-functions, but the way Blöchl calculates them is as follows. KS wavefunctions are calculated by first radially integrating the Schrödinger equation for the self consistent atomic

potential at a set of energies ϵ_i^1 the first of which is determined as the lowest bound valence state. The rest of the energies are determined using scattering properties, with the number of waves determined to be sufficient when scattering properties are adequately determined (note that systems of generation are insensitive to chosen energies due to whatever the choice a similar region of the Hilbert space will be spanned by the KS waves).

The PS waves can be deduced by first defining PS potential corresponding to each of the KS waves.

$$\omega_i(r) = \tilde{v}_{at}(r) + c_i k(r) \tag{3.136}$$

where $k(r)$ is called the cut-off function which has coefficients selected to match as well as possible the PS and KS waves outside of Ω_R and $\tilde{v}_{at}$ is a self consistent atomic potential. The PS waves are then calculated as a solution to the non-relativistic Schrödinger equation

$$(-1/2\nabla^2 + \omega_i(r) - \epsilon_i^1)\,|\tilde{\phi_i}\rangle = 0 \tag{3.137}$$

The projector functions can be produced from the following equation.

$$|\tilde{p_i}\rangle = (-1/2\nabla^2 + \tilde{v}_{at} - \epsilon_i^1)\,|\tilde{\phi_i}\rangle \tag{3.138}$$

Where the condition of (3.134) is imposed iteratively on each wave. It is important to

note that some of the modifications to these techniques facilitate the usage of a larger augmentation region, the inclusion of unbound states and relaxation of the norm conservation condition. Note extensions to this method exist such as a scheme where the partial waves are used to adjust the potential and the relaxation of the frozen core approximation (the latter can be done by mixing the types of states and imposing orthogonality).

Chapter 4

Theoretical Basis: High Temperature Calculations

4.1 Introduction

The ab initio approach has many advantages such as high accuracy and the ability to simulate and assess structures which are metastable or unstable and scenarios which would be hard or impossible to replicate experimentally[99, 101]. A substantial issue with ab initio calculations is that they are only operable at absolute zero[101]. This problem is enhanced in importance for superalloys due to their employment at high temperatures. In order to determine how thermal expansion impacts the planar fault energies the quasiharmonic Debye model (QHDM hereafter) can be employed[101]. M. S. Titus[34] outlined this in his doctoral thesis in 2015 mentioning there were no studies into changes in fault energies at high temperatures and that such research was necessary.

The first study of this in γ' binary systems would later be conducted by Breidi, Allen and Mottura in 2017[101] and was later expanded on[145, 146]. An explanation of the QHDM as well as limitations and some details of more advanced techniques for the purpose of comparison will be outlined in the following sections.

4.2 The Quasiharmonic Debye Model

The free energy of a system which is subject to a constant temperature T and a constant hydrostatic pressure P can be expressed as a non-equilbrium Gibbs function G^* (where the asterisk denotes non-equilibrium)[147, 148].

$$G^*(\mathbf{x}; P, T) = E(\mathbf{x}) + PV(\mathbf{x}) + A_{vib}(\mathbf{x}; T) \tag{4.1}$$

Where V is the volume, $\mathbf{x}$ is the configuration vector; which is composed of all the quantities needed to describe uniquely the crystal structure i.e. lattice parameters and atomic positions, E is the cohesive energy (the energy of the atoms at 0 K in the given structure vs the energy with their components spaced infinitely far apart) and A_{vib} is the vibrational Helmholtz free energy (the additional energy induced through lattice vibrations)[101, 147, 148]. As mentioned previously the goal of any system is to minimise its free energy; hence reaching equilibrium, thus the structure which achieves this is called the equilibrium state[147]. It is the goal of this section to derive the equation of state (EOS hereafter) $V = f(P, T)$ of the system[4, 147]. It is to be noted that in real substances there will be additional terms to (4.1) for the energy of defects and

the electronic contribution to the energy but they are assumed in this approach to be small[148, 149]. The quasiharmonic approximation is defined as follows; the harmonic approximation assumes that the vibration of each atom is impacted only by neighbouring atoms (effects of higher order neighbours being called anharmonic effects) meaning the system behaves essentially as a series of harmonic oscillators[150, 151]. However the harmonic approximation has no mechanism for vibrational frequencies ω to vary with V; hence fails to account for any form of thermal expansion, in addition to other unphysical behaviours[147, 148]. To simply reintroduce anharmonicity the quasiharmonic approach assumes harmonic behaviour even in non-equilibrium geometries[147, 148].

The third term in (4.1) can be partitioned into two terms by application of the quasiharmonic approximation[147, 149].

$$A_{vib}(\mathbf{x};T) = \int_0^\infty \left[\frac{\hbar \cdot \omega}{2} + kT \cdot ln(1 - e^{\frac{-\hbar \cdot \omega}{kT}})\right] g(\mathbf{x};\omega) d\omega \tag{4.2}$$

Where g is the vibrational (phonon) density of states[147, 149]. The first term in (4.2) is called the zero point energy and it arises from quantum mechanical uncertainty in the positions of atoms resulting in the presence of phonons even at 0 K, the second term arises from the production of phonons as temperature increases. g is a very complex quantity that in order to deduce in full detail requires vast computational expense with calculations in a whole host of supercell configurations[149]. g for any substance has its own nuances and features due to its dependence on interatomic force constants (see figure 4.1). In the Debye model g is deduced by accounting for only long wavelength

modes, where all of the atoms can be seen to move in phase; resulting in the dispersion relation[125, 150].

$$\omega = v_s \hat{k} \tag{4.3}$$

where v_s is the velocity of sound in the material. It is the combination of the aforementioned quasiharmonicity with this aspect of the Debye model which combine to form the QHDM. This results in the following density of states in 3 dimensions[125, 150].

$$g(\omega) = \frac{3V\omega^2}{2\pi^2 v_s^3} \tag{4.4}$$

Note the multiplication by 3 is due to the fact that each mode can be seen to account for one longitudinal and two transverse waves (assuming the same sound velocity for both types)[125, 150].v_s can be expressed as the average velocity of transverse and longitudinal sound in an isotropic solid[152].

$$v_s = \sqrt{\frac{B_s V}{M}} f(\sigma) \tag{4.5}$$

Where B_s is the adiabatic bulk modulus, $f(\sigma)$ is a function of Poisson ratio and M is the molecular mass per formula unit[147, 152]. $f(\sigma)$ will be defined later in this section, the reader should assume for now that it is known.

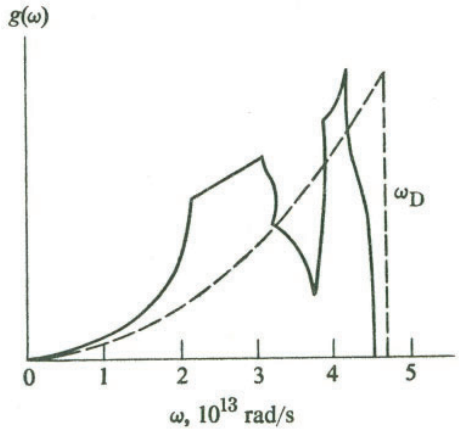

Figure 4.1: g vs ω, where the dotted line is the Debye approximation and the solid line is g in Cu derived from neutron scattering data. Note the area under both curves is identical and ω_D is the Debye frequency. (taken from [125]).

It is now necessary to introduce the Debye frequency ω_D, it exists primarily as a limit to the following integral

$$\int_0^{\omega_D} g(\omega)d\omega = 3N_A \tag{4.6}$$

where N_A is the number of atoms in the system, making $3N_A$ the number of vibrational modes in the system[125]. This defines ω_D as the upper frequency limit where all of the modes are active[125]. Now that ω_D has been introduced substituting (4.4) into (4.6) and integrating yields the following result

$$\omega_D = v_s\left(6\pi^2\frac{N_A}{V}\right)^{\frac{1}{3}} \tag{4.7}$$

hence ω_D has now been deduced[125]. Equation (4.2) can further be simplified by intro-

ducing the Debye temperature θ_D (the temperature which corresponds to ω_D)[125, 150]

$$\theta_D = \frac{\hbar\omega_D}{k} \tag{4.8}$$

in addition to the dimensionless variable $x = \frac{\hbar\omega}{kT}$

$$A_{vib}(\theta_D, T) = nk_BT\left[\frac{9\theta_D}{8T} + 3kTln(1 - e^{\frac{-\theta_D}{T}}) - D\left(\frac{\theta_D}{T}\right)\right]. \tag{4.9}$$

The Debye integral $D(\frac{\theta_D}{T})$ is as follows

$$D\left(\frac{\theta_D}{T}\right) = 3\left(\frac{T}{\theta_D}\right)^3 \int_0^{\frac{\theta_D}{T}} \frac{x^3}{e^x - 1} dx \tag{4.10}$$

θ_D can be computed as follows in the instance of an isotropic solid (note more advanced modelling would require calculation of average sound velocities of longitudinal and transverse waves at each volume)[148].

$$\theta_D = \frac{\hbar}{k_B}[6\pi^2 V^{\frac{1}{2}} n]^{\frac{1}{3}} f(\sigma)\sqrt{\frac{B_S}{M}} \tag{4.11}$$

Where n is the number of atoms per formula unit. B_S can be simplified as the static compressibility; due to the fact that it measures the compressibility for fixed quantum state populations[147].

$$B_S \simeq B_{Static}(\mathbf{x}) \simeq V\left(\frac{d^2E(V)}{d^2V}\right) \tag{4.12}$$

This introduces an important approximation and that is that vibrational effects are isotropic; meaning that changes over $\mathbf{x}$ are equivalent to changes over V (this correspondence usually holds well under pressure conditions)[147]. $f(\sigma)$ is given as follows, this term accounting for the appearance of transverse waves[152].

$$f(\sigma) = \left[3\left[\left(\frac{2}{3}\frac{1+\sigma}{1-2\sigma}\right)^{3/2} + \left(\frac{1}{3}\frac{1+\sigma}{1-\sigma}\right)^{3/2}\right]^{-1}\right]^{1/3} \tag{4.13}$$

The selection of the value of σ is of some importance, either a specifically calculated or experimental value can be used, but typically $\sigma = 0.25$ (the value of a Cauchy solid is used)[148]. This allows G^* to be expressed as follows

$$G^*(V;P,T) = E(V) + PV + A_{vib}(\theta(V);T) \tag{4.14}$$

In this equation E depends on V directly whilst, θ does so indirectly by alterations in vibrational frequencies[101]. The EOS is now able to be deduced simply by minimising (4.14) under different pressure and temperature conditions[147].

$$\left(\frac{\delta G^*(V;P,T)}{\delta V}\right)_{P,T} = 0 \tag{4.15}$$

Note there is a large array of thermodynamic quantities that can be deduced using this model for example heat capacity and entropy[147, 148].

4.3 More Advanced Models

One of the more advanced models is the Quasiharmonic approach (QHA), as the name implies the Debye aspect is removed opting for the full g or a mesh of phonon frequencies at each relevant volume. As mentioned previously the full g requires a large degree of computational expense to calculate. The approximation of g however is not the key driver of errors rather the treatment of quasiharmonicity is[148]. An improvement to the QHDM is the Debye-Grünisen model which remedies errors in the treatment of quasiharmonicity as follows. The QHDM assumes that σ has no variation with volume (and by extension temperature)[148]. In the Debye-Grünisen model θ_D varies as follows[148].

$$\theta_D(V) = \theta_D(V_0)\frac{(B_S/B_0)^a}{(V/V_0)^b} \tag{4.16}$$

Where B_0 is the static equilibrium bulk modulus and V_0 is the static equilibrium volume, a and b are parameters selected from the approximation of the Grünisen ratio J_{GR}. Example values are $a = -1/6$ and $b = 1/2$ but there are other values present in literature[148].

$$J_{GR} = a - b\frac{d\ln(B_S)}{d\ln(V)} \tag{4.17}$$

At this point it is important to introduce the concept of optical and acoustical modes. Optical modes occur in the scenario when there are two or more atoms per primitive basis, figure 4.2 is a diagram depicting a transverse optical and transverse acoustical

mode (branch)[150].

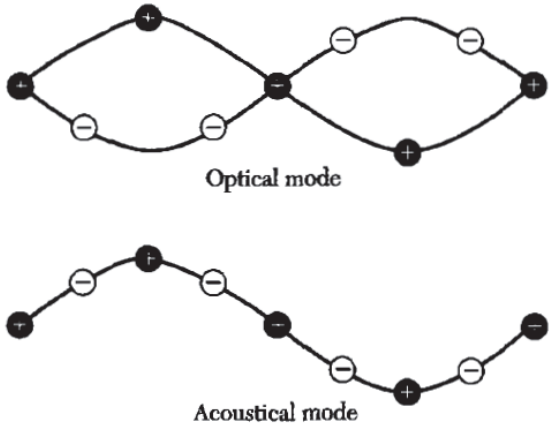

Figure 4.2: Diagram depicting a transverse optical and transverse acoustical mode (taken from [150]).

This results in the dispersion curves displayed in figure 4.3. Note that unlike (4.3), high wavelength modes are included resulting in the curves levelling off. This is due to the wavelength becoming comparable to the iteratomic distances causing atoms to scatter the wave reducing velocity, and at the edge of the BZ ($\hat{k}_{max} \pm \pi/r$ where r is the distance between identical planes) result in the formation of a standing wave) see figure 4.3[125, 150].

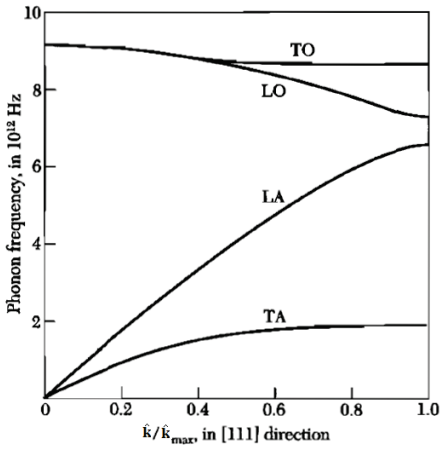

Figure 4.3: Dispersion curve in Germanium (two atoms per primitive basis) at 80 K (T represents transverse, L represents longitudinal, O represents optical and A represents acoustical) (taken from [150]).

In the Debye model optical modes are modelled as acoustical, this approximation breaks down in certain scenarios such as closely packed materials[148]. In the Debye-Einstein model the approximation for g takes into account both optical and acoustical branches, by using single frequencies for the optical branches and renormalising the Debye temperature to the acoustic branches[148].

$$g = \frac{9n\omega^2}{\omega_{DE}^3} \text{ if } \omega \ < \ \omega_{DE} \tag{4.18}$$

$$g = \sum_{j=1}^{3n-3} \delta(\omega - \omega_j) \text{ if } \omega \ \geq \ \omega_{DE} \tag{4.19}$$

Where n is the number of atoms per primitive basis ($3n-3$ corresponding to the number of optical modes per primitive basis) and ω_{DE} corresponds to the Debye-Einstein

frequency which is related to ω_D as follows.

$$\theta_{DE} = \frac{\theta_D}{n^{1/3}} \tag{4.20}$$

The order of increasing complexity (and accuracy) of the models is as follows: QHDM, Debye-Grünisen, Debye-Einstein and finally the QHA[148].

Chapter 5

Methodology

5.1 First-Principles Calculations

As alluded to in chapter 3 there are a large degree of facets that go in to the process of producing accurate first-principles calculations. These include the selection of various algorithms and convergence testing. These factors are to be explained in the proceeding subsections. The software used for all first-principles calculations in this research is the Vienna ab initio simulation package (VASP hereafter). This package is used to determine the energies and volumes in the equations (3.9-12). A point of note is that in this research whenever a calculation is conducted involving either the $D0_{19}$, $D0_{24}$ or HCP phases the c/a ratio is assumed to not deviate from its ideal value ensuring that the relevent dimensions in these structures correspond respectively to the $L1_2$ and FCC lattices[101, 145, 146]. The physical reasoning behind this assumption is that the phase change which occurs locally after the generation of either a ISF (local change to HCP)

or SISF (local change to $D0_{19}$[81]) does not exist in isolation and would be constrained in this way, to the geometry of the underlying FCC or $L1_2$ lattice. It is possible that at higher compositions this assumption may break down somewhat. However, instituting ways around the use of this assumption to give way to a more advanced model would be fraught with difficulty. As in the VASP program there is no way to relax a cell specifically in one direction hence a large number of calculations for different c/a ratios at constant volume would have to be undertaken (computationally intensive). Or alternatively a single estimate proposed based off of the atomic radii could be used, which is potentially unreliable due to magnetic effects.

5.1.1 Starting Estimates

VASP calculations require initial estimates of both the structure, volume and atomic positions of the element, compound or alloy on which the calculation is to be performed. In these calculations the structure is obviously already defined, the atomic positions are always assumed to be undistorted, and the volume was either calculated by using the relative atomic radii of the various elements in a results set, or a single reasonably sized estimate selected for every calculation in each results set. Which of these competing methodologies was employed seemed to have no detectable effect on the end result in the vast majority of cases.

5.1.2 Convergence Testing

In order to ensure that the use of a certain k-point density (k_{den}) (The factor in VASP which after selection determines the number of k-points in the BZ) and $E_{cut-off}$ is resulting in accurate converged results, a convergence test is necessary. This is a process by which a calculation of the fault energy is repeated at a series of $E_{cut-off}$s whilst keeping k_{den} constant and vice-versa for a small sample of the dataset. The final fault energies are in both cases compared with the value from the most accurate calculation of that set. The behaviour of the curves are as follows; a period of large deviations for the more inaccurate calculations followed by a flat section. The significance of this flat section is that it is where the results can be said to be properly converged, and the final values of k_{den} and $E_{cut-off}$ for the whole of the data set should be taken. There is no rigid accepted standard in the literature for how little difference is acceptable. However it seems logical to keep the difference to no greater than a few mJ/m^2. An example convergence test graph can be seen in figure 5.1.

The relationship between k_{den} and the number of k-points is defined according to equations (5.1-3).

$$N_1 = max(1, k_{den} \cdot |\hat{b}_1| + 0.5) \tag{5.1}$$

$$N_2 = max(1, k_{den} \cdot |\hat{b}_2| + 0.5) \tag{5.2}$$

$$N_3 = max(1, k_{den} \cdot |\hat{b}_3| + 0.5) \tag{5.3}$$

where N_1, N_2 and N_3 are the numbers of subdivisions along each reciprocal lattice vector

and $|\hat{b}_1|$ $|\hat{b}_2|$ and $|\hat{b}_3|$ are the norms of the reciprocal lattice vectors. Note the units of k_{den} are Angstroms.

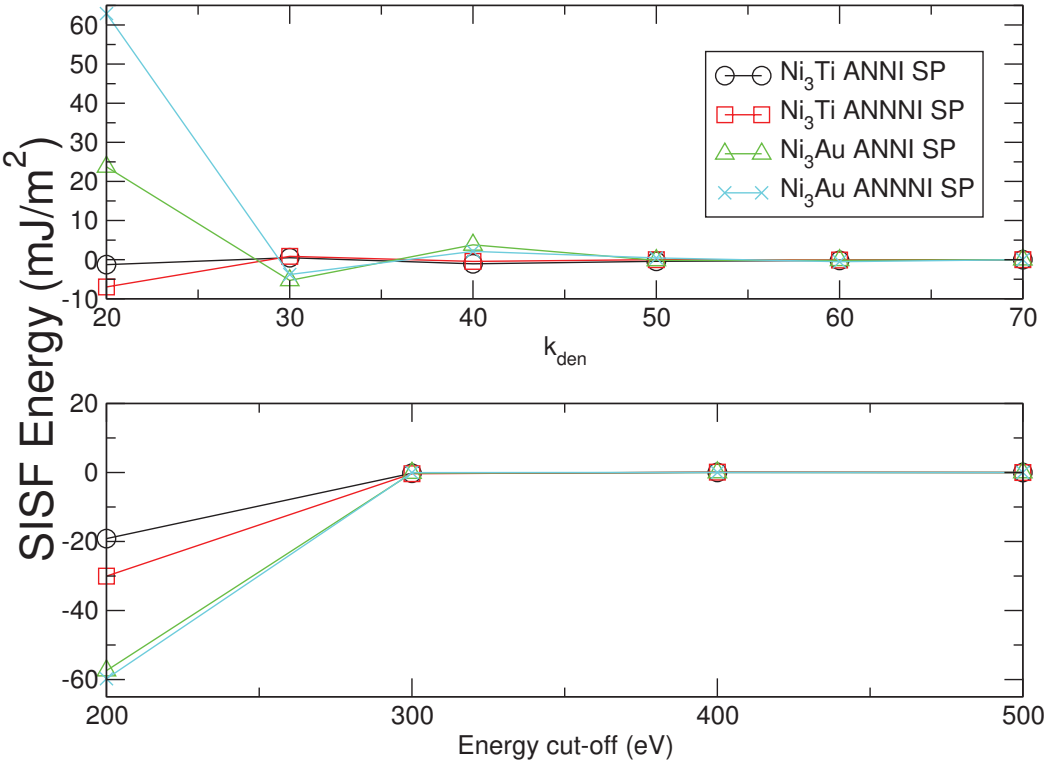

Figure 5.1: Convergence testing for both k_{den} and energy cut-off for 2 of the binary compounds. In this case k_{den}=60 corresponds to 4096 k-points for Ni_3Au and 4913 k-points for Ni_3Ti. The number of irreducible k-points in both cases is 165.

5.1.3 Algorithm Selection

Energy Minimisation:Electronic

Both of the algorithms the RMM-DIIS algorithm and the blocked Davidson algorithm are employed in different capacities based on the nuance of the situation. It is noted in the VASP manual that if convergence is attained the values should be identical between

algorithms but the RMM-DIIS algorithm is more likely to fail to find convergence[129]. However the RMM-DIIS algorithm does exhibit faster performance[129] providing increased utility especially where large supercells are concerned.

Energy Minimisation:Atomic Positions

The algorithm used in all calculations for the atomic positions is the conjugate-gradient scheme (section 3.6.1). The quasi-Newton algorithm is highly efficient and converges rapidly but has one significant drawback, the starting point of the calculation has to be very close to the minima in question, otherwise it will fail to find convergence[129]. The conjugate-gradient algorithm is not bound by this constraint and this is what makes it the superior method for high throughput calculations, as it will require less micromanagement and alleviate the need for high quality starting estimates for large datasets[129].

Another issue with these calculations is that it is possible to find local minima instead of the desired global minima[129]. The technique for ensuring that the global minimum is found to a high degree of confidence would be to run the calculations at a large number of starting positions. However, for the research of this thesis which is very high throughput this is unachievable due to computational expense.

5.1.4 SQS vs SPCM

Whilst both of these techniques are perfectly viable for the calculations conducted in this research, the SPCM technique is selected. The reasoning behind this is that the key difference between the two techniques is that SQS takes into account figures which

include more than 2 atoms whilst SPCM only takes into account figures with 2 atoms. This means that SQS's are more complex and hence will require larger cells and hence more computational expense, but also it will mean slightly more accuracy. As in this project a large amount of calculations are conducted SPCMs were used for all calculations that required random substitution to be a factor.

5.1.5 K-point Generation

K-points were in all calculations generated in accordance with the Monkhorst-Pack scheme[122], the reasoning behind this is not particularly profound, other than it is the standard scheme for first-principles calculations with a proven track record.

5.1.6 Partial Occupancies

The technique for determining partial occupancies was varied depending on the calculation. In static calculations the optimum technique is to use the Blöchl interpolation, whereas in the case of a calculation with relaxation of volume or atomic positions the Methfessel-Paxton technique is the most accurate. The technique for obtaining the most accurate energy value for a calculation with relaxation in it however is as follows. Relax using the Methfessel-Paxton technique, then afterwards run a continuation job which is static using the Blöchl interpolation, this was done where possible[129].

5.1.7 Relaxation Scheme

There are 2 main schemes for performing relaxation of energy, the 3DOF (3 Degrees of Freedom) scheme and the volume-atomic positions-volume scheme. As the name implies the 3DOF scheme involves relaxation which occurs during one calculation and it allows relaxation of volume, atomic positions and cell shape[129]. The volume-atomic positions-volume scheme is more computationally intensive due to having 3 steps. In step 1 just the volume is allowed to relax, in the second step the atomic positions are able to relax at the volume determined by step 1 and finally in step 3 the volume is again relaxed starting from the volume and atomic positions determined in step 2[145]. However, it has a key protection against the cell changing shape and possibly relaxing to a different structure which would invalidate the calculations being conducted[145, 146]. In this research the volume-atomic positions-volume relaxation scheme is employed in all calculations for the purpose of ensuring correct convergence at the expense of speed[145, 146].

5.1.8 Basis Set Selection

The basis set used was in all calculations the PAW basis set. As mentioned previously this basis set is non-biased and efficient[119, 144]. In addition this basis set has been found to give equivalent cohesive energy results to the LAPW and pseudopotential methods in various crystals[153]. The PAW basis set has the advantages that it grants access to the full wave function and is able to perform well for the transition metal elements[144]. Typical errors involved in the usage of the PAW method are errors in bond length of 1-2% and errors in E of a few 10ths of an electron volt[154]. This technique was found

to have similar efficiency to the pseudopotential approach[154]. The PAW method has been shown to have superior convergence properties to the Vanderbilt USPPs with plane-wave basis set, as the basis set can be smaller and yet yield superior convergence (note PAW convergence properties are similar to LAPW)[144]. One of the reasons for this is that it uses radial grids for the one centre expansions vs plane-waves of the Vanderbilt USPPs[144]. Also the PAW basis set has increased flexibility relative to the LAPW basis set allowing more adjustment to potentials[144].

5.1.9 Semi-Core States

For a selection of the available elements (X=(Ti, Zr)sv potentials, (Ag, Cu, Ni, Os, Pd, Pt, Re, Rh, Ta, W)pv potentials, (Co, Cr, Fe, Hf, Mn, Mo, Nb, Ru, Tc, V) both) within the PAW basis set it was possible to introduce semi-core states (where pv and sv potentials treat the p and s semi-core states as valence states respectively)[129]. As expected this will increase the accuracy but require increased computational expense. These were employed where reasonably possible.

5.1.10 Exchange-Correlation Function Selection

In all calculations the exchange correlation function used was the GGA-PBE. A large amount of the reasoning for this selection is explained in section 3.5. Whilst more advanced functionals are implemented in VASP[129], their reliability in the literature for fault energy calculations in an array of circumstances has yet to be substantiated in the same way as GGA functionals (for example many of the first-principles literature

values given in this and the proceeding chapters employ the GGA).

5.2 High Temperature Calculations

For a lot of the high temperature calculations conducted in this study the GIBBS package was used[147]. The GIBBS package uses the quasiharmonic Debye model[147], as established previously the QHDM operates on a series of assumptions such as that the system behaves as a series of harmonic oscillators, that harmonic behaviour is assumed even at non-equilibrium geometries and only long wavelength modes are in existence (see section 4.2). The steps of determining stacking fault energies and volumes at high temperatures are as follows.

1. Standard relaxation (of FCC/$L1_2$) at 0 K using VASP

2. VASP calculations at expanded and contracted volumes from the equilibrium volume determined in step 1) to produce an energy vs volume curve (note it is very important that this curve is smooth otherwise it risks rejection by the GIBBS package)

3. Inputting the points of the curve into the GIBBS package. The GIBBS package takes in the points of this curve and fits it to an analytical function. The energy vs volume curve will typically be of a parabolic shape. However fitting to a simple polynomial has the issue that there are large errors especially at large volumes. In order to reduce these errors a reduced unit of length $R = (\frac{V}{V_r})^{\frac{1}{3}}$ is defined, where V_r is the volume where the energy is minimised. However this change in isola-

tion only partially alleviates the issues with polynomial fitting, the derivatives still remaining highly dependent on the endpoints of the dataset and the polynomial order. The full fitting procedure involves fitting a large number of polynomials with different orders to eliminate the influence of the end points of the data. Each one of these polynomials is assigned a weighting dependent on the order. This procedure preserves the simplicity of polynomial fitting, whist ensuring numerical stability. After this fit has taken place in the GIBBS program and E(R) is in an analytical form, $\theta_D(R)$ can be deduced by an analytical derivation of said polynomial. As $\theta_D(R)$ is known the $(A^*(R;T),R)$ data can easily be obtained. All of the components are now in place to produce a polynomial of the non-equilibrium Gibbs function $G^*(R;p,T)$. Equation (4.12) can now be solved by utilising bisection and the Newton-Raphson method. After the equilibrium state at a certain pressure and temperature has been determined, the vibrational internal energy (U_{vib})(5.4), the heat capacity (C_v)(5.5), A_{vib} and the Helmholtz's entropy (S_{vib})(5.6) can be calculated.

4. VASP calculations at the same volumes per atom corresponding to the elevated temperatures of FCC/$L1_2$ given by the GIBBS package in the HCP/$D0_{19}$ (also DHCP/$D0_{24}$ if the ANNNI model is used)

5. Computation of the fault energies at all of the elevated temperatures used by employing equations (3.9-12)-(5.7)

$$U_{vib} = nkT\left[\frac{9\theta}{8T} + 3D\left(\frac{\theta_D}{T}\right)\right] \tag{5.4}$$

$$C_v = 3nk\left[4D\left(\frac{\theta_D}{T}\right) - \frac{3\theta/T}{e^{\theta/T} - 1}\right] \tag{5.5}$$

$$S_{vib} = nk\left[4D\left(\frac{\theta_D}{T}\right) - 3ln(1 - e^{-\theta/T})\right] \tag{5.6}$$

$$E_{L1_2} = G^*(V, P; T) - U_{vib} + (TS_{vib}) \tag{5.7}$$

What is described above is a quasistatic approach which is where the volume expansion is the only effect of temperature which is accounted for[145, 146]. This may at first glance appear to be crude but it has been validated by multiple experiments[155–157]. The evidences in favor of the approach of particular importance to this study are firstly the accurate calculation of Ni_3Al elastic constants[158, 159]. A theoretical investigation concerning the change of the elastic constants of Ta with temperature where the largest factor in the changes was found to be thermal expansion with other effects, such as phonon excitation and electronic excitation being of relatively minor impact at constant volume[158]. Validation of this approach has also been successfully carried out in the following cases for the SISF energies of systems which exhibit complex magnetic behaviors; pure compounds[101], unaries[160] and alloys[161].

There are two variants of such calculations IR (internal relaxation) and IS (internally static). Variant IS calculations rely on the assumption that in the case of FCC/$L1_2$ the ground state atomic positions at equilibrium are the same as the atomic positions at expanded and contracted volumes. Also in the case of HCP/$D0_{19}$ there is no relaxation of the default atomic positions. IR calculations do not rely on these assumptions as atomic positions are relaxed across the board. It is noted that the GIBBS package

requires the entry of the Poisson ratio[147]. There exists no apparent clear answer as to what this should be, due the the heavy elastic anisotropy of nickel and derived alloys and compounds[162–164]. GIBBS only allows the input of one value so this particular nuance cannot be accounted for[147]. The value chosen was 0.40 (this is for both data sets in chapters 7 and 8) as this is in the range of the experimentally determined values for the [100] family of directions (v_{100} hereafter) (Note v_{100} was found to be between 0.37-0.41 for a host of $L1_2$ compounds at room temperature[163]).

The [001] direction is highly significant as it is noted by Matan et.al to be the predominant crystal growth direction in single-crystal superalloys[64]. Crystals oriented in this direction were found to exhibit many superior properties to those which do not exhibit alignment along the [001] direction[64]. In addition this is the most common crystal orientation used for single-crystal components[165]. In terms of the primary creep regime of Mar-M247 single-crystals aligned at or near the [001] direction at the conditions 1047±2 K and 724 MPa, they were found to have long stress rupture lives but were outclassed by crystals oriented near $[\bar{1}11]$[165]. Note that crystals oriented near the [001] direction, had superior stress rupture lives when oriented near the [001]-[011] boundary rather than when near the [001]-$[\bar{1}11]$ boundary[165]. In creep of Mar-M200 at 1130 K and 410 Mpa (it is noted that with these conditions the behavior corresponds most closely to the tertiary creep regime, however precipitate shearing occurs instantaneously upon loading) the best creep behavior was found to be from perfect alignment in the [001] direction or along the [001]-$[1\bar{1}1]$ boundary[166]. The v_{100} value is also in the middle of the range of values for different directions making it more general. A single value for

Table 5.1: Table of Poisson ratio from simulation and experimental data for γ'-Ni_3Al

Direction	Value	Details
100	0.391[162]	Coaxial model, single-crystal
100	0.433[164]	FLMTO theoretical equilibrium volumes
100	0.41257[170]	PWPP-GGA-PW91
100	0.3443[169]	Rod resonance Technique, single-crystal 283 K
100	0.39784[171][1]	Ultrasonic Measurements Single-Crystal
100	0.4000[172]	Pulse superposition pulse/pulse-echo overlap
110	0.32520[170]	PWPP-GGA-PW91
110	0.2830[169]	Rod resonance Technique, single-crystal 283 K
110	0.3295[172]	Pulse superposition pulse/pulse-echo overlap
111	0.49578[170]	PWPP-GGA-PW91
111	0.3532[169]	Rod resonance Technique, single-crystal 283 K
111	0.4635[172]	Pulse superposition pulse/pulse-echo overlap

[1] Was calculated by averaging 4 values at 273 K and 296.5 K calculated from the adiabatic and isothermal elastic constants.

all alloys appears justified as v_{100} was found not to differ significantly with addition of several alloying elements[167, 168]. Also temperature was found to not change the ratio substantively either[162, 169].

5.3 Validation

5.3.1 Pure FCC Metals

Before this methodology can be confidently employed, validation against existing models and experimental results is necessary. The simplest system to analyse within this methodology is a pure metal, in order for validation the metal must in actuality be stable (or metastable) in the FCC structure and have experimental results for lattice parameter

and ISF energy. Table 5.2 is a table of lattice parameter results for pure metals extracted from the set of results later detailed in chapter 6. There exists in many of the results a subtle increase in the lattice parameter as the supercell size is increased. Four of the elements however are in contravention of this and decline with an increase in supercell size. It is to be noted that the results taken in table 5.2 are not completely systematic and use slightly different VASP input settings (see table 5.4) and that these differences can also possibly be attributed to these changes. The most important variable to change is k_{den} which is smaller in the 128 supercell calculations.

It is important at this juncture to re-establish what an ISF actually is, a change in the stacking sequence locally to a HCP structure for 2 planes. Hence when an element exhibits a negative ISF energy it is implied that said element is more stable in the HCP structure as opposed to the FCC structure. There are two elements from the sample that exhibit a negative ISF energy, Co and Fe. The most stable stacking sequences at room temperature for Co and Fe are HCP and BCC respectively (whilst for all other elements detailed in table 5.3 it is FCC). This is congruent with Co having an energetic preference for the HCP stacking sequence and Fe having a stronger energetic preference for the HCP stacking sequence as opposed to the FCC stacking sequence. The latter point was proven by conducting an additional calculation of Fe in the BCC structure where the free energy per atom in said structure was the lowest followed by the HCP, and FCC structures respectively.

There is one key nuance which needs to be introduced when the results of this thesis are compared to experimental results of the lattice parameter for this and all datasets

that are documented in subsequent chapters. It is that most experimental results are taken at room temperature whilst first-principles results are calculated at 0 K. Using the GGA expands and softens bonds relative to the LDA, it is for this reason that it simulates the room temperature experimental values well. This is a benefit of using the GGA but it is important to note that it is fortuitous.

5.3.2 Differing VASP Settings

The set of results SISF energy at 0 K of the γ' binary systems was repeated using a large number of different settings for the purpose of assessing the reliability of the VASP program. Figures 5.2 and 5.3 are diagrams depicting the difference between the set deemed most reliable (see section 7.5) and the other settings.

Table 5.2: Lattice parameter data for pure elements in the FCC crystal structure at a series of different supercell sizes, as a comparison to literature (all values are in Å).

Element	Present Work			Other Calculations		Experiments	
	4 Supercell	32 Supercell	128 Supercell	Value	Details	Value	Details
Ni	3.520	3.520	3.521	3.526[173]	EMTO-CPA	3.5240[174]	Elasticity Inclusion Model, Apparent Size
						3.499±0.003[175]	X-ray Diffraction
						3.516[176]	X-ray Diffraction
Al	4.038	4.038	4.044	4.045[173]	EMTO-CPA	4.0496[174]	Elasticity Inclusion Model, Apparent Size
						4.046±0.004[175]	X-ray Diffraction
Co	3.519	3.519	3.522	3.53[177]	Theoretical	3.544[178]	unknown
Cu	3.630	3.631	3.633	3.638[173]	EMTO-CPA	3.6146[174]	Elasticity Inclusion Model, Apparent Size
						3.597±0.004[175]	X-ray Diffraction
Rh	3.843	3.845	3.838	3.77[179]	TB	3.80[150]	ICSD Database
Pd	3.952	3.950	3.944	3.957[180]	Theoretical Calculation	3.859±0.004[175]	X-ray Diffraction
Ag	4.153	4.155	4.148	4.164[173]	EMTO-CPA	4.0857[174]	Elasticity Inclusion Model, Apparent Size
						4.079±0.004[175]	X-ray Diffraction
Pt	3.976	3.976	3.974	3.987[173]	EMTO-CPA	3.912±0.004[175]	X-ray Diffraction
Au	4.171	4.173	4.165	4.197[181]	GGA-PW91	4.0784[174]	Elasticity Inclusion Model, Apparent Size
						4.065±0.004[175]	X-ray Diffraction
						4.07042±0.0005[182]	XRD Symmetrical Focusing Cameras

Table 5.3: ISF energy data for pure elements in the FCC crystal structure at a series of different supercell sizes, as a comparison to literature (all values are in mJ/m^2).

Element	Present Work			Other Calculations		Experiments	
	4 Supercell	32 Supercell	128 Supercell	Value	Details	Value	Details
Ni	144.344	145.821	138.491	127.2[92]	Supercell-PAW-GGA	120-130[183]	Electron microscopy, anisotropic elasticity theory
				131-137[184]	PW91-Alias Shear		
				182[185]	LDA-Slab		
Al	149.769	153.142	147.551	158[186]	PAW-GGA-PBE	135±20[187]	Electron microscopy measure annealing
						167±33[188]	Summary of Data
Ag	17.728	13.456	27.530			25[189]	TEM Node (corrected)
						18±3[188]	Summary of Data
Au	32.059	32.457	58.870			52±15[189, 190]	
						37±8[188]	Summary of Data
Co	-102.355	-100.729	-110.392				
Cu	43.390	42.326	75.129	43[186]	PAW-GGA-SLAB	61±17[187]	Summary of Data
				58[97]	Supercell-GGA-PW91		
Pd	141.382	141.307	161.276	122[186]	PAW-GGA-Slab	180±40[190]	Texture method new calibration
						177±3[187]	Summary of Data
Pt	349.869	346.828	379.186	282[186]	PAW-GGA-Slab		
Rh	188.490	187.939	180.345				
Fe	-180.619[1]	-311.201	-345.197				
Ir	359.905	370.214	373.986	359[186]	PAW-GGA-Slab	390±90[187]	Summary of Data

[1] Large difference caused by significant differences in magnetism for 4 atom supercell.

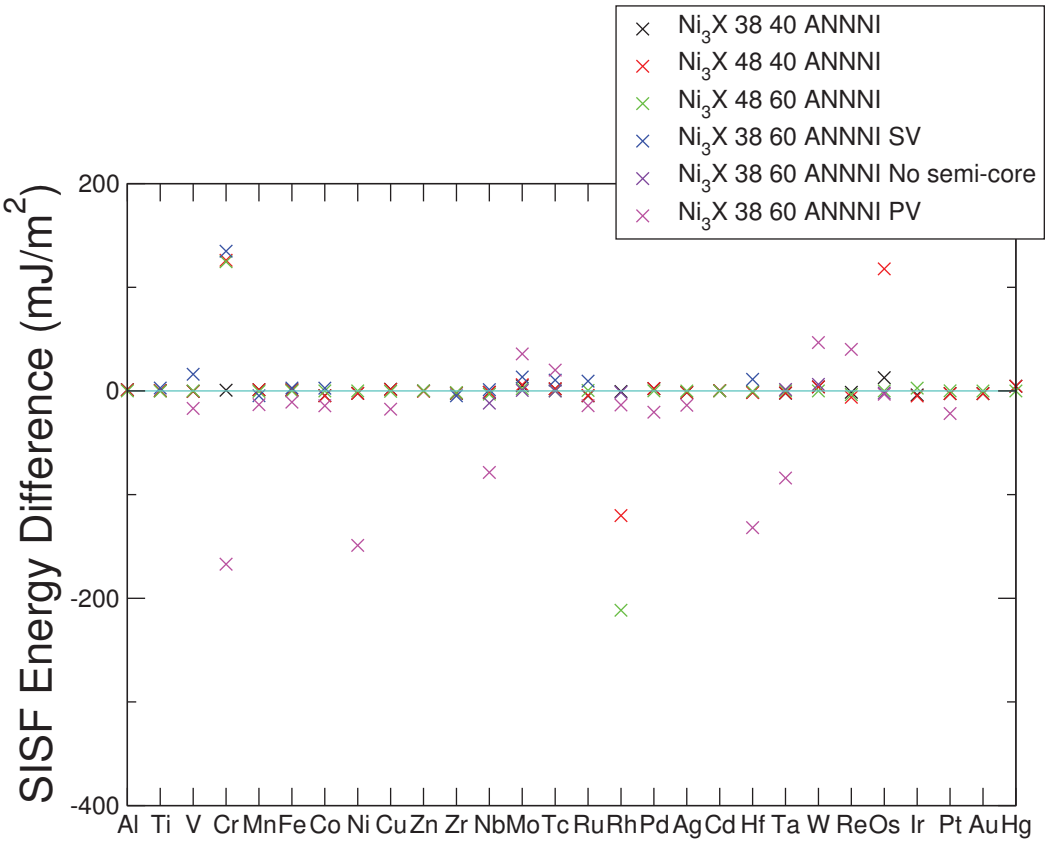

Figure 5.2: Graph demonstrating the differences in the SISF energy in the Ni_3X binary systems generated by a range of different settings in VASP in the spin-polarised implementation. The legend of this graph can be explained as follows: the first numerical value refers to the electronic minimisation algorithm (38 means blocked Davidson and 48 means RMM-DIIS), the second numeric value refers to k_{den} and ANNNI refers to the axial next nearest neighbour ising model. SV and PV refer to which types of semi-core states were treated as valence states, no semi-core of course meaning no semi-core states treated as valence states (if semi-core states are not mentioned semi-core states are utilised as valence states as follows pv for Mo Tc Rh Ta W and Os, sv for Nb).

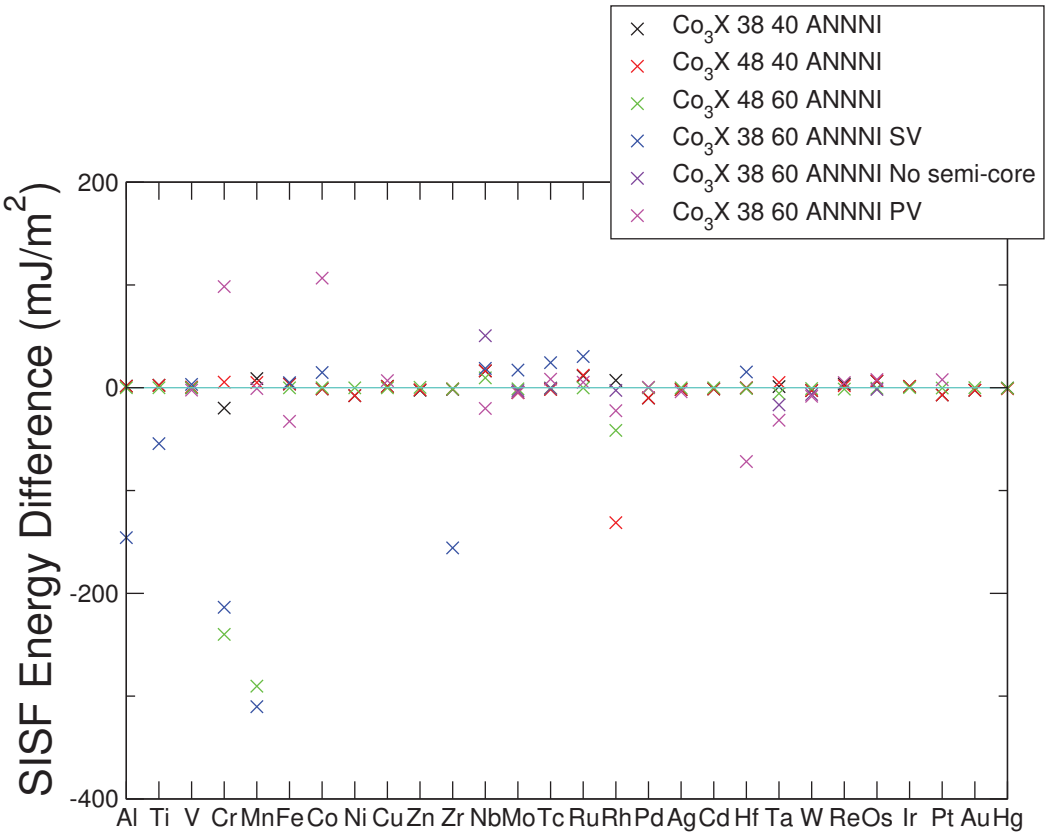

Figure 5.3: Graph demonstrating the differences in the SISF energy in the Co_3X binary systems generated by a range of different settings in VASP in the spin-polarised implementation. The legend of this graph can be explained as follows: the first numerical value refers to the electronic minimisation algorithm (38 means blocked Davidson and 48 means RMM-DIIS), the second numeric value refers to k_{den} and ANNNI refers to the axial next nearest neighbour ising model. SV and PV refer to which types of semi-core states were treated as valence states, no semi-core of course meaning no semi-core states treated as valence states (if semi-core states are not mentioned semi-core states are utilised as valence states as follows pv for Mo Tc Rh Ta W and Os, sv for Nb).

For the most part the results between all of the settings show clear agreement in both of the sets of compounds, however there is a set of cases where the difference is very large. Most cases where the fault energy is significantly different involve the change in the approach to the use of semi-core states (especially in the case of PV). It is also

noted that the element Cr has a very strong sensitivity to the used setting with most of the points experiencing large deviations. This data reveals that where for fault energy calculations undertaken in the future, caution should be used as results could differ by a large margin. It is also a point of note that it is important to ensure consistent VASP settings between the crystal structures used in fault energy calculations. This is because each k-point density, energy cut-off, exchange-correlation functional etc is subject to certain systematic errors. Due to the fact that it is not the raw energies that are important to fault energy calculations, rather the differences between said raw energies, it is imperative to keep these systematic errors as consistent between the calculated structures as possible. This is because cancellation of systematic errors is necessary to ensure the highest accuracy in the calculations. The effects of changing the settings for each of the structures in the calculations were not quantified for the data of this thesis.

In addition to the factors outlined in figures 5.2 and 5.3 there is strong sensitivity in some cases to the initialisation of the spin degrees of freedom. A small trial was conducted involving 3 compounds and 3 other starting conditions nonmagnetic, antiferromagnetic and nested magnetism (where all first sublattice atoms are up and all second sublattice atoms are down). The 3 compounds Ni_3Fe, Ni_3Cd and Ni_3W were investigated in the trail. These magnetisation conditions prevented the Fe atom from developing a strong magnetic moment which had drastic effects on the SISF energy on the order of 10^3 mJ/m^2. In all scenarios for Ni_3Cd the fault energy remained approximately the same despite magnetism varying somewhat. For Ni_3W in the nested and antiferromagnetic scenarios the SISF and the magnetism did not vary significantly, but for the nonmag-

netic condition all of the phases were prevented from developing magnetism and resulted in a change to the SISF of the order of $50\,mJ/m^2$. This emphasises the importance of the initialisation of the spin degrees of freedom. In all of the calculations of this thesis the initial estimate is always that of ferromagnetism. This approach is justified by the favourable comparison to other computational and experimental work. For example the experimental value for the magnetic moment Fe is $2.97\pm0.15\,\mu_B$ and another computational value is $2.94\,\mu_B$ and the value for our ferromagnetic result of this thesis is 2.900 μ_B, in all of the other conditions the value was $0.007\,\mu_B$.

5.3.3 Differing GIBBS Settings

For the following sample of elements in the dataset presented in section 7.6 Fe, Au, Ru and Cu (note for Co_3Cu in the case of spin-polarised results 0.45 and 0.5 had to be excluded due to rejection by GIBBS) calculations were undertaken for a series of different Poisson ratios 0.1, 0.2, 0.3, 0.35, 0.4, 0.45 and 0.5 to investigate further the validity of using one single Poisson ratio in all cases. The induced alteration to the fault energy change across the temperature range is minimal, frequently less than $1\,mJ/m^2$ with the highest being $\approx 9.2mJ/m^2$. This investigation concludes that scarcely is the set Poisson ratio significant to the calculated fault energy.

This still does present somewhat of a missed opportunity as the Poisson ratio could have been directly calculated by the author. This was later done using the internal algorithm in VASP which operates by carrying out 6 distortions of the lattice and uses the stress-strain relationship to calculate the elastic constants from which the Poisson

ratio can then be derived [129, 191]. The results are as follows 0.387, 0.362 and 0.428 for the 100, 110 and 111 directions respectively which is in line with the data as presented from other literature in table 5.1. However, as stated in the previous paragraph this missed opportunity is of very little consequence.

5.4 Results Sets

In this section is a group of tables detailing the selections used for the aforementioned categories in the proceeding results chapters. I will reiterate here that in all calculations the Monkhorst-Pack scheme, PAW basis set, volume-atomic positions-volume relaxation scheme, conjugate-gradient scheme, ferromagnetic initial starting estimate (where spin-polarised) and GGA-PBE were employed. Tables only state factors which differ. The limits for the iterative solving for both types of iteration (electronic and atomic positions) are also listed.

5.4.1 Formation Enthalpy Calculation

The formation enthalpies for binary systems/compounds were calculated using the following equation

$$\Delta H_{strut} = E_{strut} - xE^{A}_{nat} - (1-x)E^{B}_{nat} \tag{5.8}$$

where A and B are the two elements of the binary, x is the atomic fraction of the element A, E_{strut} is the energy per atom of the structure also E^{A}_{nat} and E^{B}_{nat} are the energies per

Table 5.4: VASP settings selected for each of the results sets in this thesis. Note that these are the settings for the majority of calculations in a set; the electronic minimisation would have been changed in individual calculations if convergence could not be attained. The unit for E_{cut}, Energy Difference Limit:Electronic and Energy Difference Limit:Atomic Positions is eV. The unit for k_{den} is Å

Category	Chap. 6	Chap. 7	Chap. 8: Coarse Compositions	Chap. 8: Finite Temperature	Chap. 8: Fine Compositions
k_{den}	40	60	60	60	60
irreducible k-points[2]	28 FCC, 26 HCP	165 $L1_2$, 192 $D0_{19}$	260 $L1_2$, 200 $D0_{19}$ $1^{st} sub$,	63 $L1_2$, 63 $D0_{19}$	68 $L1_2$, 74 $D0_{19}$ 1^{st} sub,
		96 $D0_{24}$	132 $L1_2$, 172 $D0_{19}$ 2^{nd} sub		36 $L1_2$ 32 $D0_{19}$ 2^{nd} and both
E_{cut}	350	400	400	400	350
Electronic mimimalisation	Blocked Davidson	RMM-DIIS	RMM-DIIS	RMM-DIIS	RMM-DIIS
Semi-Core States	Not Utilized	Utilized[1]	Utilized[1]	Not-Utilized	Utilized[1]
Partial occupancies	Blöchl interpolation	full scheme	full scheme	full scheme	Blöchl interpolation
Energy Difference Limit:Electronic	1×10^{-4}	1×10^{-5}	1×10^{-5} [3]	1×10^{-5}	1×10^{-4}
Energy Difference Limit:Atomic Positions	1×10^{-3}	1×10^{-3}	1×10^{-3}	1×10^{-3}	1×10^{-3}
Supercell Size	128 $L1_2$, 128 $D0_{19}$	4 $L1_2$,8 $D0_{19}$, 16-$D0_{24}$	32 $L1_2$, 32 $D0_{19}$ 1^{st} Sub	108 $L1_2$, 216 $D0_{19}$	128 $L1_2$, 32 $D0_{19}$ 1^{st} sub
			64 $L1_2$ and $D0_{19}$ 2^{nd} sub		256 $L1_2$, 256 $D0_{19}$ 2^{nd} and both subs

[1] Utilised as valence states as follows pv for Mo Tc Rh Ta W and Os, sv for Nb
[2] It is to be noted that where the initial estimates were tuned based on the atomic radii of the elements involved the numbers of irreducuble k-points was found to vary with the estimate for lattice parameter. The values used in this table represent the most common values of each of the results sets.
[3] Note that this only applies completely to the second sublattice results in the 1st sublattice results the limit of 1×10^{-4} was used for all results other than the final step with Blöchl interpolation in both $L1_2$ and $D0_{19}$ structures.

atom of A and B respectively in their most stable stacking sequences. In pseudo-binary systems the formation enthalpy is calculated as follows.

$$\Delta H_{strut} = E_{strut} - aE^{A}_{nat} - bE^{B}_{nat} - cE^{C}_{nat} \tag{5.9}$$

Where C is the third element and E^{C}_{nat} is the energy of C in it most stable structure. a, b and c are the atomic fractions of the 3 elements.

5.4.2 Solid Solubility

Solid solubility of certain alloy systems were calculated as a part of this research. Where calculations were performed they were done using the Thermo-Calc software. The database used was the TCNi8 database version 8.1 This database is purpose built for superalloys and is based on a critical evaluation of binary, ternary and in some cases higher order systems. Thermo-Calc employs the CALPHAD (CALculation of PHAse Diagrams or alternatively computer coupling of phase diagrams and thermochemistry) methodology[192]. The CALPHAD methodology simulates multicomponent behaviour in a system by modelling thermodynamic properties in each of the phases[193]. This modelling of the Gibbs energy is done by utilising both phase equilibrium and thermodynamic data[194]. CALPHAD modelling operates on the premise that the properties in each phase are homogeneous, hence molar quantities can be deduced by taking the sum of each of the phases[194].

5.5 Summary

In the thesis thus far a large amount of techniques and algorithms for different aspects of a DFT calculation which utilises AIM models have been detailed and compared. In a wider context the reasoning behind using these techniques will now be discussed. There are two main competing techniques to the employed in this thesis, the first principles supercell calculations and experimental measurements. The former is subject to the following two constraints that make it inappropriate for the current study. One of these is that in order to introduce a fault in the cell that is not a primitive lattice vector, multiple faults are needed such that the sum of the shift vectors is a primitive lattice vector (the shift vectors of ISF and SISF are not primitive lattice vectors), such faults have to be sufficiently far apart in order to avoid significant interaction[92]. This creates a key difficulty with supercell calculations. The other constraint is over computational resources which will mean that the number of atoms needs to be kept within reason, practically speaking these 2 concerns result in a thin elongated cell. In this cell it is difficult to manipulate the composition at the fault plane as for in the example of the APB calculations by Chandran[100] the fault plane consists of 9 atoms the minimum composition available in this scenario is 11.1% (see figure 5.4).

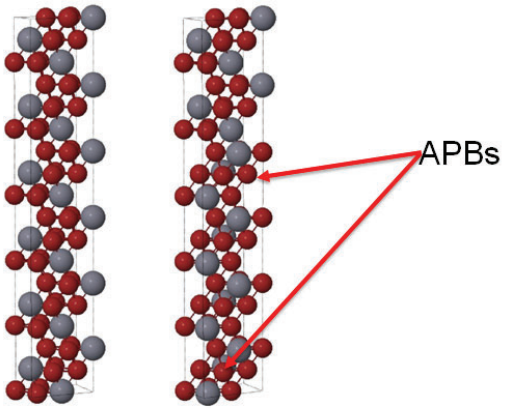

Figure 5.4: The supercells used in the research of Chandran[100]. On the left is the unfaulted cell and on the right is the faulted cell with 2 anti-phase boundaries. The large atoms are nickel and the small atoms are aluminium (taken from [100]).

This issue is exacerbated further once sublattices are considered and the minimum composition which can be introduced the first sublattice in the fault plane is 33%. This contributes to a secondary concern solute-solute interactions. In order to take into account solute-solute interactions in the first sublattice 66% of the composition of the sublattice at the fault plane must be solute which is a very high number. Meaning that the low sublattice composition calculations with solute-solute interaction, a very important part of this study which facilitated the production of the model, are exceedingly difficult using the supercell approach.

Experimental measurements of fault energies are typically taken by measuring the separation distance of the two partial dislocations which bound the fault, as this has a relationship of inverse proportionality to fault energy. Such measurements are difficult to perform accurately[103] due to the errors brought in from the following 4 factors. i) thin film issues, ii) the ratio of experimental error to the measured distance can

be substantial[195], iii) uncertainty about how to apply the right corrections to the measured distances[49], iv) difficulty in finding an isolated enough fault such that it is in equilibrium and not impacted by other faults in the material. In addition to this experiments would be exceptionally difficult to perform in such a high throughput study of fault energies due to the factors outlined above and the expense of having to fabricate the large number of alloys such research demands. This is why to the author knowledge, there exists no high throughput data for the alloy systems studied in this research.

It is noted that the experimental results for stacking fault in pure Ni range from 79-450 mJ/m^2, however the most accurate experimental value the author is aware of is reported as 120-130 mJ/m^2[183, 196, 197]. The reason for this result being determined as the most reliable is as follows, many of the older results were conducted using unreliable indirect methods, for example deriving the SFE from equations that describe creep or the assessment of deformation texture as this is known to be related to SFE[183, 197]. The value of 120-130 mJ/m^2 was determined using the more reliable method of employing weak-beam electron microscopy to assess the separation of partial dislocations[183, 197]. There is a more reliable technique for assessing fault energies called high resolution electron microscopy (HREM) however no result for the ISF energy of nickel exists using this technique[197].

Chapter 6

Results: γ Binary System ($Ni_{1-x}X_x$)

6.1 Introduction

In order to build up a full picture of how the various transition metal elements impact superalloys it is necessary to first examine the γ phase. This analysis is required to understand deformation behavior in superalloys, as deformation always commences in the γ phase before the γ' phase. Fault energies in the γ phase were found by a series of authors to be informative of or significantly impact the following. Cross-slip occurs more readily as the fault energy is increased due to the fact that partials are closer together in high fault energy materials[197–200]. The normalized minimum grain size due to milling was also found to increase with fault energy[201]. A decrease in the fault energy was found to correspond with a reduction in the steady state creep rate[40, 202, 203]. The higher the stacking fault the lesser the ability for recrystallization twins to form and reduction of the solid solution strengthening and strain hardening coefficients[197, 200].

It is also highly important to conduct an enthalpy analysis in both phases (both sublattices investigated in the γ' phase) to determine where the elements should segregate to in the γ' phase and assess relative stabilities of the studied systems. Fault energies in FCC-$Ni_{1-x}X_x$ phase have previously been investigated using first-principles calculations that utilize alias shear (but never AIM models as far as the author is aware)[40], a follow up study employing this data as well data from CALPHAD was used to assess synergistic effects by studying FCC-$Ni_{1-x-y}X_xY_y$ which were found to be very small[196].

6.2 Lattice Parameters

The way that lattice parameters vary with composition and alloying element was assessed, figure 6.1 is a diagram of how for all of the studied compositions the lattice parameter varies with d-band filling. Note the in this figure the following colour scheme is first defined, black for the 3d series, green for the 4d series and red for the 5d series, this is the standard colour scheme for this thesis throughout all of the remaining chapters. As can be seen from this diagram there exists a parabolic relationship of lattice parameter with d-band filling. Note the similarity between the values of the two curves for the 4d and 5d elements and that the minima of the curves lies in the centre of the series where the cohesive energy for half the d-band elements is the highest[101, 204]. Another observation is that as the composition is increased the parabolas get steeper due to the increased influence of the alloying addition. Another key factor is that in the case of alloys containing the 3d elements near the centre of the transition metal series, notably Mn and Fe, the lattice parameters are larger then what would be expected purely

from the parabolic relationship. The cause for this is established later in this chapter by an analysis of magnetic moments. Note that with regard to pure elements x=1, Mn and Fe now agree with the parabolic relationship whereas Zn significantly lower then the parabolic expectation. This too was investigated in the analysis of magnetic moments.

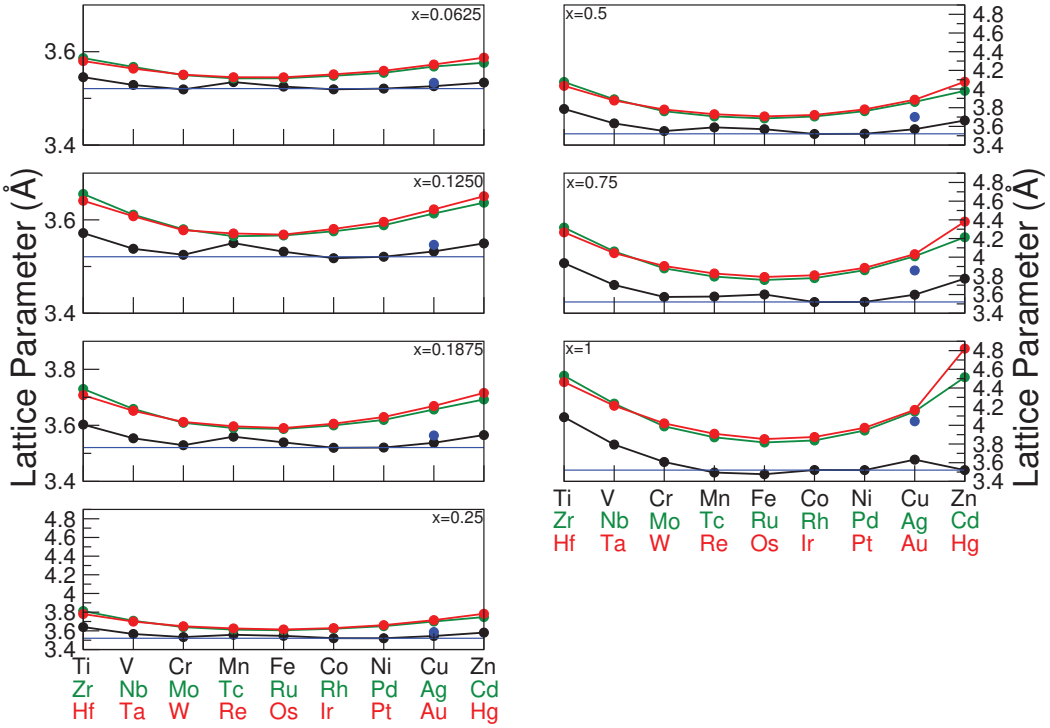

Figure 6.1: Lattice parameter vs d-band filling for Ni-X-FCC Binary systems in the spin-polarised implementation. Blue dots represent $Ni_{1-x}Al_x$. Blue lines represent the lattice parameter of pure nickel.

Figure 6.2 is the same data however displayed as a dependence of composition. As can be seen the lattice parameter increases (in either a linear or curved fashion) in all cases as the alloying element is added except in the cases of X=Co where no appreciable change is observed, X=Cr where a slight decrease occurs followed by the typical increase,

finally X=Fe and X=Mn where a strong decline is observed after x=0.75. The reason that increases are observed in the overwhelming majority of cases can be understood simply by the employment of the atomic size argument. Nickel is a small atom relative to the majority of the transition metal elements. Hence alloying with larger atoms will result in an increase in the lattice parameter relative to pure nickel. This also explains why alloying with Co scarcely changes the lattice parameter due to the very similar atomic radii of these two elements. This data is compared with Vegard's law (coefficients taken from [205]) which is derived from experimental data in general showing very good agreement at low x but diverging at higher compositions especially in the cases of V, Fe, Tc, Rh, Ag, Os, Ir, Pt. This is unsurprising as the data used to derive Vegard's law was for dilute alloying compositions[205]. This is important as at these dilute compositions interactions between the solute and nickel are very important at informing the lattice parameter however, these cease to be as important at high compositions hence the disagreement.

The data was also compared with other simulation and experimental data although unfortunately such data is scarce. There only exists experimental data across a large range of compositions for 6 X elements Cr, Fe, Co, Cu and Pt. Strong agreement is found with this data for X = Ti, Fe, Co, Cu. In the case of X=Pt our results are significantly higher then the available experiment and simulation data. In the case of X = Cr our results are acutely lower then the literature data. In the research of Gan[206] there are a series of single data points using XRD for an array of alloys, our data agrees strongly with these points.

Another facet to be investigated is the solid solubility of the transition metal elements in nickel, which was evaluated at 2 temperatures, room temperature and a typical superalloy operational temperature 1173 K. The solid solubility is important as it serves as a maximum of each alloying element that can be placed into the γ phase and hence the maximum that the lattice parameter and ISF energy can be changed. Alloys which exist above the solid solubility limit cannot physically exist in reality but still are important for the to research from a theoretical perspective as the topic of can fault energies be extrapolated back from higher compositions (as they can be computed with smaller supercells and hence at lower computational expense) to lower compositions is a very important topic of discussion in this thesis.

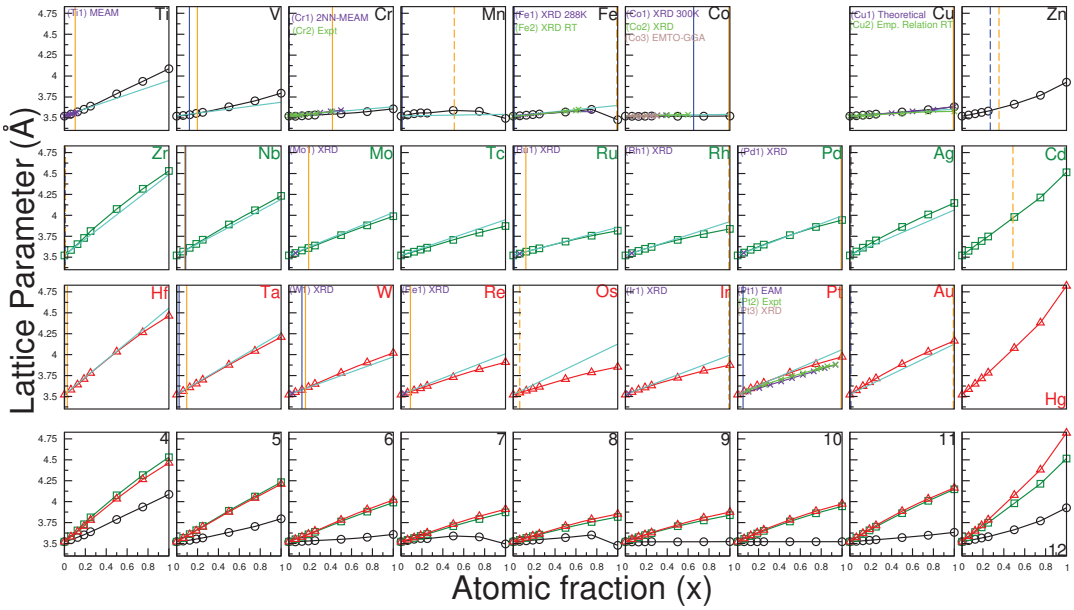

Figure 6.2: The variation of equilibrium lattice parameter as a function of atomic fraction of the soulte element x. The available experimental and simulation data is also shown. The turquoise lines denote the equilibrium lattice parameters calculated using Vegard's law. Orange and blue lines represent solid solubility at 900°C and 20°C respectively determined via Thermocalc. Dashed orange and blue lines represent the same except determined using phase diagrams from one of the following sources[207, 208] or by the use of the FactSage or MTDATA (note no data was no available data for Cu, Rh, Cd, Os, Ir at room temperature; Tc and Hg at both temperatures). The lines between points exist simply for visual purposes. Citations: Ti1[209], Cr1[210], Cr2[211], Fe1[212] (points from 0-0.5 determined via fitting point at 0.75 determined via interpolation), Fe2[176], Co1[213], Co2[214], Co3[215], Cu1[180], Cu2[216], Mo1[206],Ru1[206], Rh1[206], Pd1[206], W1[206], Re1[206], Ir1[206], Pt1[217], Pt2[218], Pt3[206].

6.3 Magnetic Moments

The data for the magnetic moments of all of the alloys is displayed as a dependence with composition in figure 6.3. The first observation to be made is that appreciable magnetism is found for almost all of the X elements. The magnetic moments are in

general a lot more pronounced at lower composition. The reason for the declines of the lattice parameters in the systems featuring Mn and Fe can be explained as a magnetic phenomenon as magnetism is significantly reduced in the case of Fe and borderline no existent in the case of Mn. The sudden increase of the lattice parameter of the alloy system with X=Zn can also be explained by magnetism as there is a sudden increase at x=1 in the magnetic moment of the alloying element Zn. It appears also that it is not only the similar atomic radii of Ni and Co that informs the scarce change in lattice parameter as significant magnetism is observed in the NiCo alloy system. The same data except expressed as a dependence with d-band filling is displayed in figures 6.4-10.

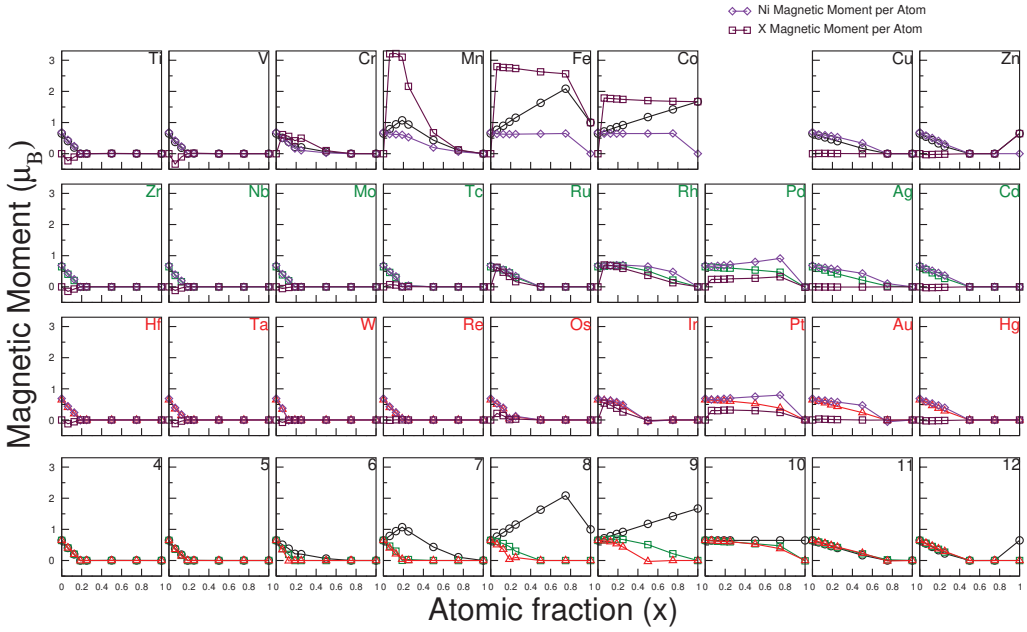

Figure 6.3: The total magnetic moment per atom in addition to the average magnetic moment per atom of the nickel and X atoms in the the γ phase. Standard colour scheme in use for total magnetic moment of each system.

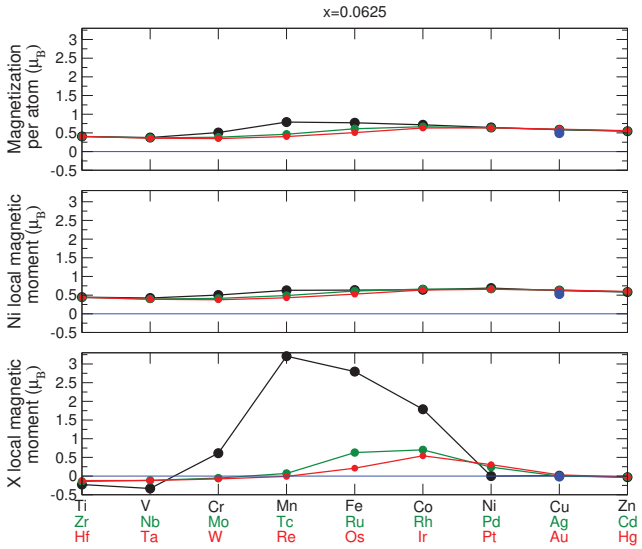

Figure 6.4: The total magnetic moment per atom in addition to the average magnetic moment per atom of the nickel and X atoms in the γ phase. Expressed as a dependence with d-band filling for the composition x=0.0625. Blue lines represent zero magnetic moment.

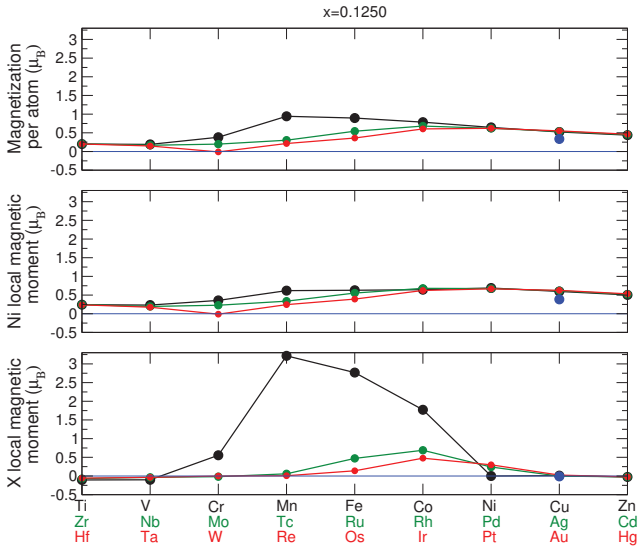

Figure 6.5: The total magnetic moment per atom in addition to the average magnetic moment per atom of the nickel and X atoms in the γ phase. Expressed as a dependence with d-band filling for the composition x=0.1250. Blue lines represent zero magnetic moment.

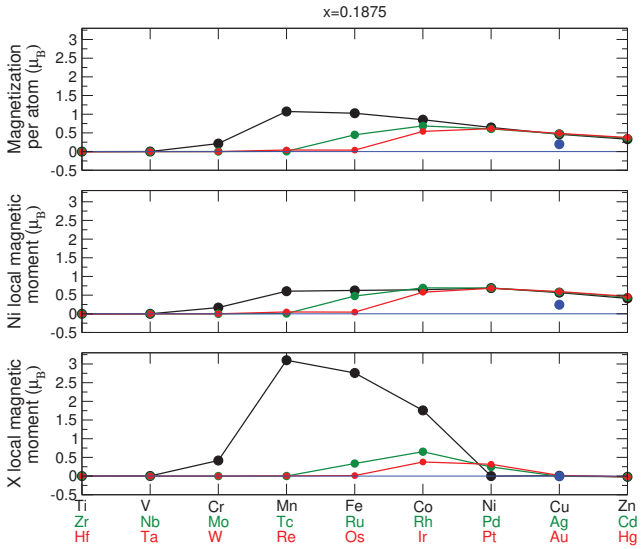

Figure 6.6: The total magnetic moment per atom in addition to the average magnetic moment per atom of the nickel and X atoms in the γ phase. Expressed as a dependence with d-band filling for the composition x=0.1875. Blue lines represent zero magnetic moment.

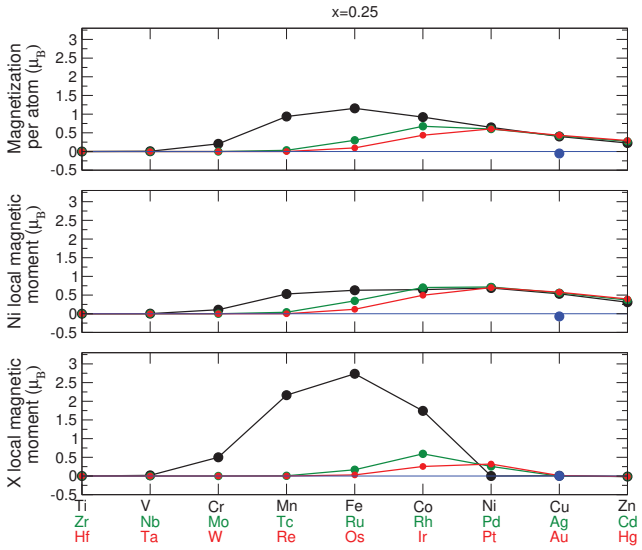

Figure 6.7: The total magnetic moment per atom in addition to the average magnetic moment per atom of the nickel and X atoms in the γ phase. Expressed as a dependence with d-band filling for the composition x=0.25. Blue lines represent zero magnetic moment.

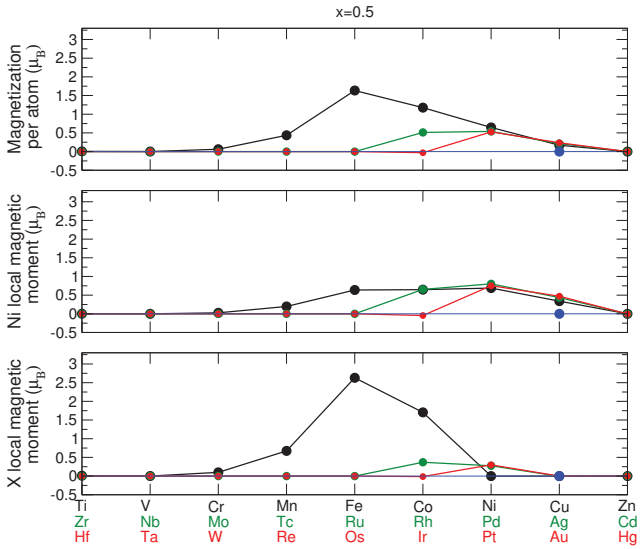

Figure 6.8: The total magnetic moment per atom in addition to the average magnetic moment per atom of the nickel and X atoms in the γ phase. Expressed as a dependence with d-band filling for the composition x=0.5. Blue lines represent zero magnetic moment.

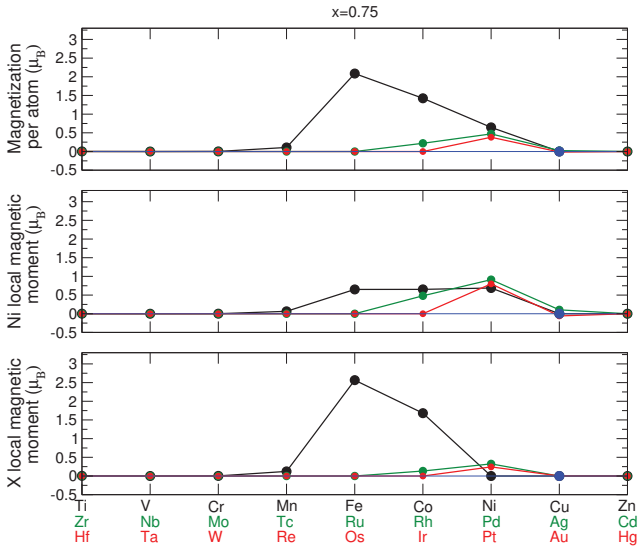

Figure 6.9: The total magnetic moment per atom in addition to the average magnetic moment per atom of the nickel and X atoms in the γ phase. Expressed as a dependence with d-band filling for the composition x=0.75. Blue lines represent zero magnetic moment.

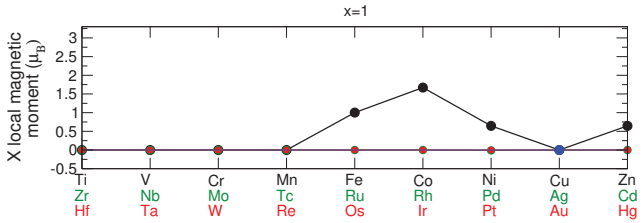

Figure 6.10: The total magnetic moment per atom in addition to the average magnetic moment per atom of the nickel and X atoms in the γ phase. Expressed as a dependence with d-band filling for the composition x=1. Blue line represents zero magnetic moment.

6.4 Formation Enthalpies

The formation enthalpies of all of the studied alloys expressed as a function of composition is displayed in figure 6.11. As can be seen from this figure the majority of the relationships exist as curves. Two of the alloying elements Co and Cu result in only small changes to the formation enthalpy. It is noted that alloying with elements from groups 4 and 5 results in significant decreases at lower compositions. The importance of formation enthalpy is that should it be negative it indicates an alloy which is at the very least metastable. Formation enthalpy alone cannot be used to determine if an alloy is stable as without data on every other stacking sequence it is possible to know if FCC is the lowest energy stable structure. A positive formation enthalpy guarantees that the alloy is fundamentally unstable. One observation of importance is that there appears to be no correspondence between negative formation enthalpy and solid solubility for example for the studied elements of groups 4 and 5 large declines in formation enthaply are observed with alloying, however these elements have very low solid solubility limits.

Another point of note is that the large decrease in the lattice parameter of the

system containing Zn also corresponds with an incredibly large decrease in the formation enthalpy. The result for the NiZn system at x=1 is anomalously lower than all of the other results. The reason for this can be attributed to the individual nuances of the calculation of Zn in its most stable structure, that being HCP. The result in question was found to be non-magnetic, whilst the result for FCC was found to be ferromagnetic with a moment of $0.646\,\mu_B$. When a result for the HCP structure was used which had relaxed to a magnetic state with a magnetic moment of $0.635\,\mu_B$, the formation enthalpy was reduced in magnitude to a non-anomalous value of -2.244 $kJ/mol.atom$[†]. The same data presented in figure 6.11 is presented as a dependence with d-band filling in figure 6.12.

[†]Note the parameters of the two calculations of Zn in the HCP structure would have had different computational parameters contributing to their different magnetic convergence and the result in other ways. Since Zn is known to be a diamagnetic material[219] (approximated better by no magnetism then ferromagnetism) the nonmagnetic result was used for all other enthalpy calculations in this thesis involving Zn.

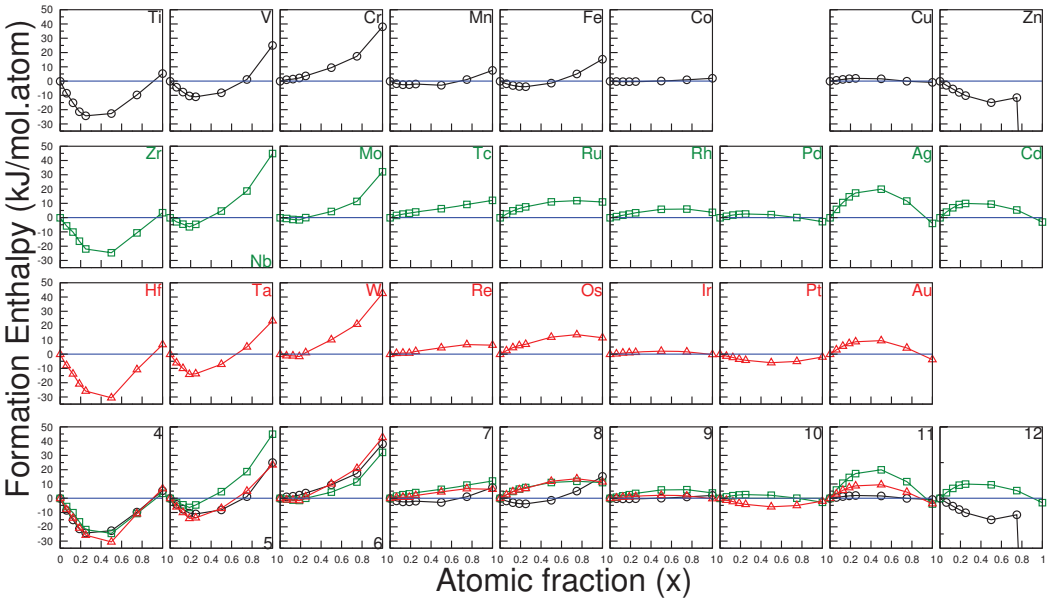

Figure 6.11: The formation enthalpy in the spin-polarised implementation in the γ phase. Blue lines represent zero formation enthalpy. Note one point Ni_0Zn_1 is -417.026 $kJ/mol.atom$ but is not displayed due to convenience with regard to the y-axis.

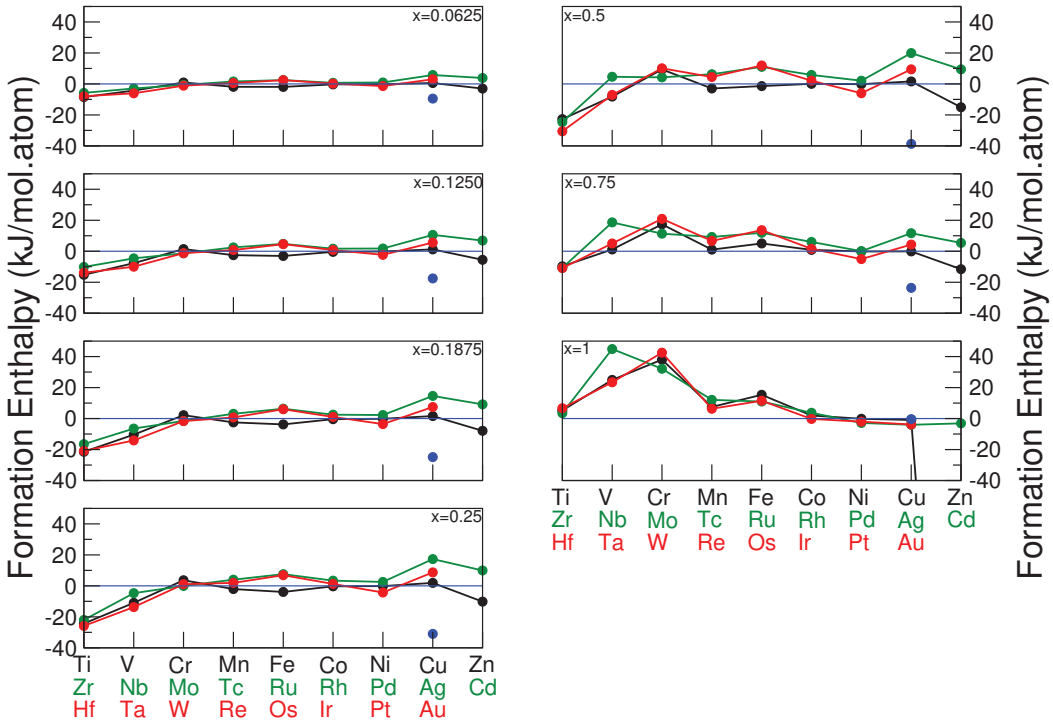

Figure 6.12: The formation enthalpy in the spin-polarised implementation in the γ phase. This time expressed as a dependence on d-band filling. Blue lines represent zero formation enthalpy. Note one point Ni_0Zn_1 is -417.026 $kJ/mol.atom$ but is not displayed due to convenience with regard to the y-axis.

6.5 ISF Energies

Figure 6.13 displays how for each individual alloying element the ISF energy varies with composition. One important point to note is that in many cases elements with the same d-band filling have similar behaviour (this observation was also found to be true in the case of the lattice parameters as well). There is unfortunately a large lack of literature data to corroborate these results, but where experimental or simulation data exists it is

compared with the results from this study. In the alloy $Ni_{1-x}Fe_x$ good agreement is found with the experimental results of Charnock[220] up to x=0.25 divergence however was found a the higher compositions, nevertheless our results agree very strongly with the simulation data point of Limmer[96]. For $Ni_{1-x}Co_x$ the results of the present study and the experimental data of Beeston and Humble[92, 221, 222] observe a linear decline of similar gradient, the values however are significantly different. Chowdury et.al[223] also conducted simulation data for this alloy system, with which the results of the present study disagree. Strong agreement is found between our results and the first-principles simulations of Li et.al.[180] and Zhao et.al[224] for elements Cu and Mo respectively, both of these researchers used the supercell approach. This is of importance as it provides more evidence that the AIM models provide accurate approximations to the supercell approach.

Previous research by Shang.et.al[40] used the alias shear technique to analyse the ISF formation energy for a similar selection of alloying elements as those in this thesis. Significant disagreement is found between these results and those of this thesis. For example in the results of Shang et.al all solute elements were found to reduce the ISF formation energy. This is potentially due to the fact that only 1 solute atom was included (on the fault plane) in [40]. This means the key factor of solute-solute interaction was not present in the calculations of Shang et.al[40].

Note that the ISF formation energy is a representation of how stable the compound is in the FCC structure relative to the HCP structure, if the ISF formation energy of a compound is negative it implies that the alloying element stabilizes the HCP structure

relative to the FCC structure. In the case of a positive ISF energy the opposite is true and it is the FCC structure which is stabilised by the alloying element.

An investigation was carried out as to whether the room temperature native stacking sequence of the alloying element affects significantly the ISF energy. The room temperature native stacking sequence of all of the elements is depicted in figure 6.14. The reason why this is of importance is that the creation of an ISF results in the creation of 2 planes which exist in the HCP stacking sequence. Hence logically speaking an element which exists in the HCP stacking sequence should reduce the ISF formation energy (hence destabilising the FCC stacking sequence) more then an element which exists in the FCC stacking sequence (with a BCC element somewhere in between). The averages of all of the changes at the lowest studied composition (x=0.0625) are as follows, as expected FCC elements cause the least average variation in the ISF formation energy of -1.18 mJ/m^2, BCC elements cause the largest variation -26.62 mJ/m^2 with HCP elements in between the two -17.11 mJ/m^2. The implication of this is that there appears to be some impact of the native stacking sequence on the ISF energy but it is far from the most prominent effect of alloying.

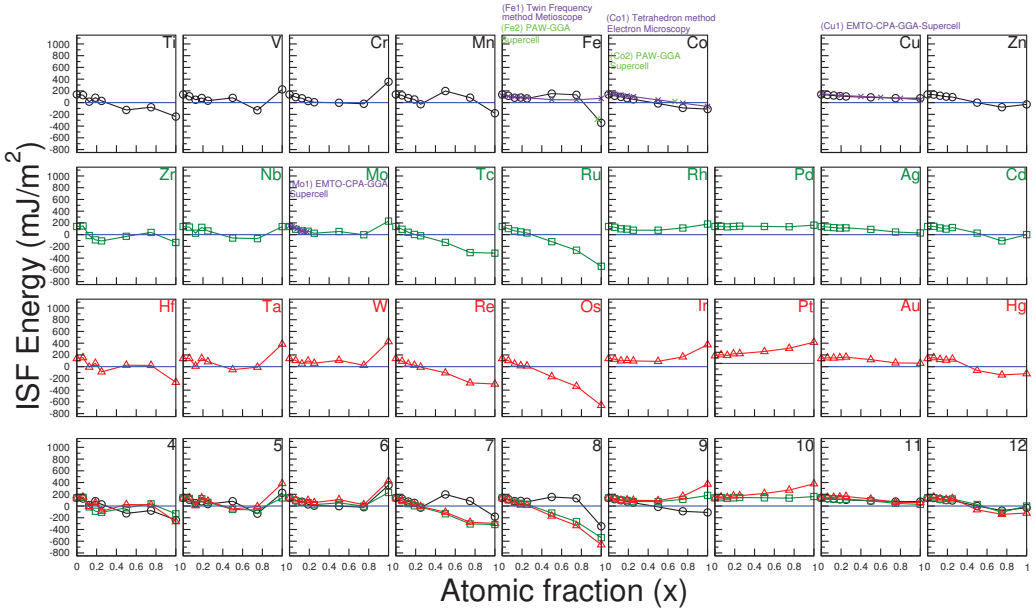

Figure 6.13: The variation of ISF formation energy as a function of atomic fraction of the solute element x in the spin-polarised implementation of the data for the γ phase. The available experimental and simulation data is also shown. The lines between points exist simply for visual purposes. Blue lines represent zero ISF energy. Citations: Fe1[220] fitting, 0 value extrapolation, Fe2[96], Co1[92, 221, 222](note linear fit with extrapolation above 0.68 and below 0.20), Co2[223], Cu1[180](linear fitting), Mo1[224].

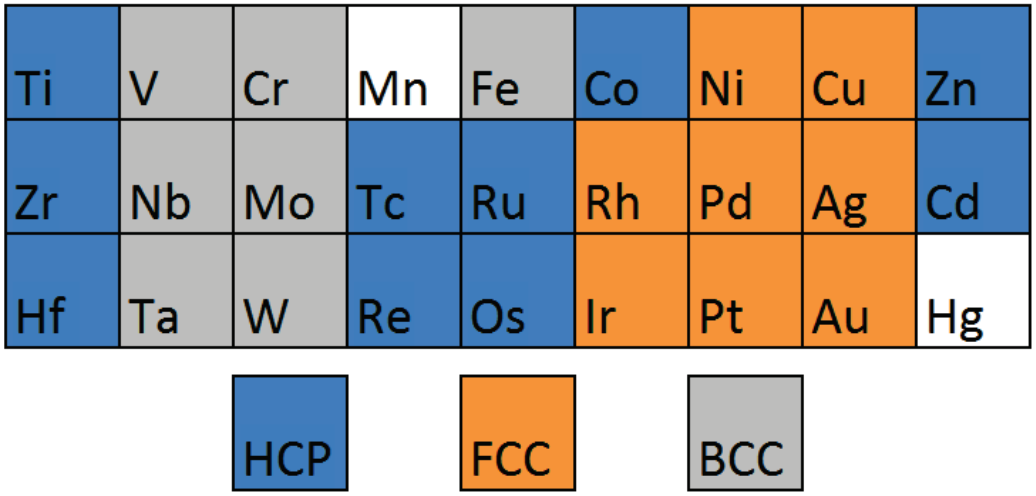

Figure 6.14: Native stacking sequences of the transition metal elements at room temperature. Note that Al is also FCC, Mn is a complex cubic structure and Hg is rhombohedral. Data taken from [150].

Figure 6.15 demonstrates how the ISF energy varies with the d-band filling as the composition is increased. Similar to the case of the lattice parameter the 4d and 5d curves for the most part are similar in nature. One particular point of note is that at low compositions all of the ISF energies are positive but as composition is increased some of the ISF energies of the binary compounds become negative, destabilizing the compound in the FCC configuration relative to the HCP structure. Also to be noted is that the respective peaks and troughs of the curves in question become more extreme as the composition is increased.

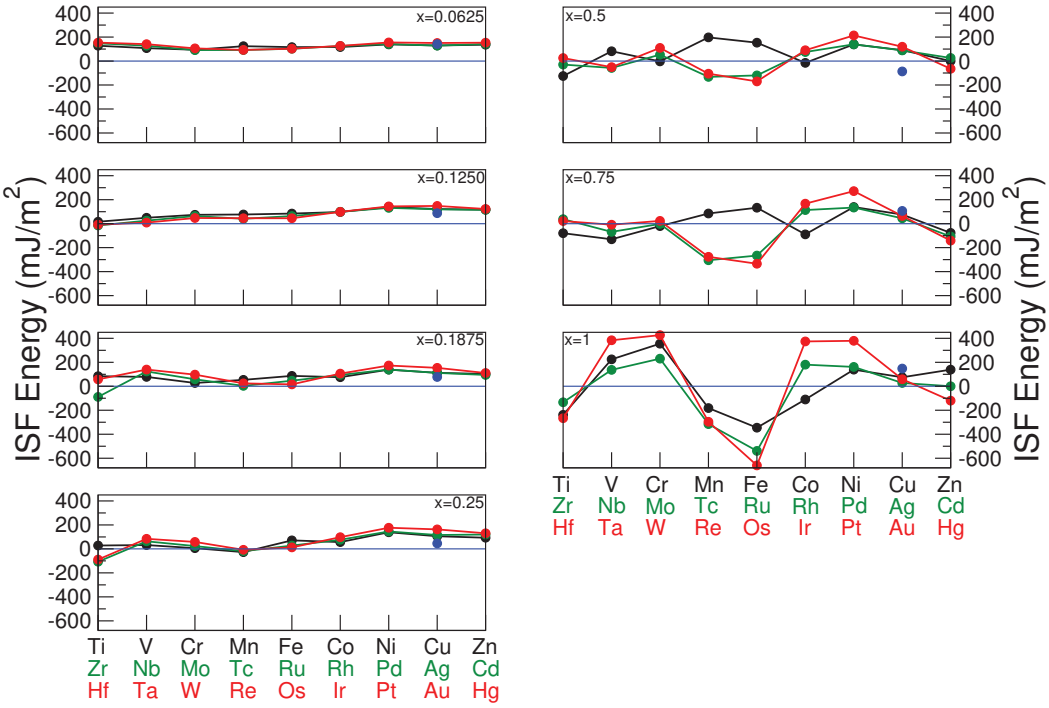

Figure 6.15: The ISF formation energy in the spin-polarised implementation in the γ phase, this time expressed as a function of d-band filling. Blue lines represent zero ISF energy.

Figure 6.16 is a series of scatter plots of lattice parameter vs ISF energy at all of the compositions. The justification for the plotting of said graphs is that the larger the difference in lattice parameter from that of the host lattice, the greater the change of said unalloyed host lattice during alloying, hence there is the potential for a correlation between the two variables. As can be seen however, this potential correlation does not manifest in reality, as there exists no significant correlation between the lattice parameter and the ISF formation energy in these alloys.

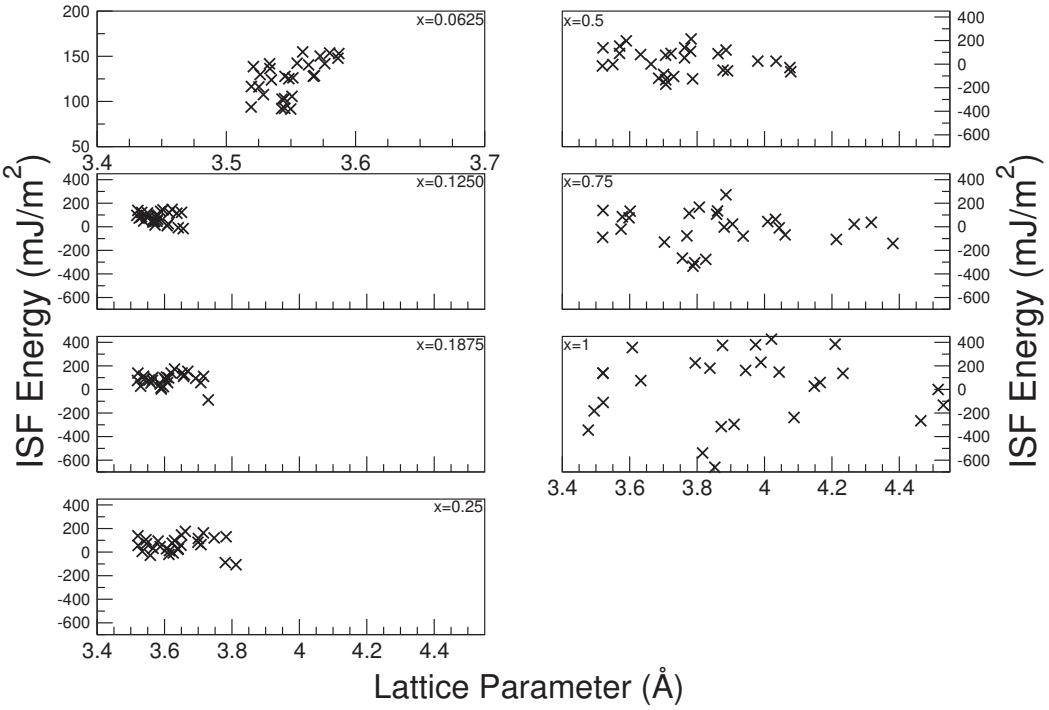

Figure 6.16: Scatter graphs at each composition for ISF energy vs lattice parameter for the spin-polarised implementation of the data for the γ phase (note that no clear correlation is observed at any composition).

6.6 High-Temperature Calculations

Data at higher temperature was taken by inserting experimentally determined volumes of these alloys where data is found to exist into VASP and performing an ANNI model calculation at said volumes. Figure 6.17 displays how for all of the experimental data how lattice parameter and ISF (calculated) vary with temperature. As expected the lattice parameter increases with temperature in a slightly curved fashion. Unfortunately such data is relatively scarce and where it does exist the temperature range is only a few 100

K in many cases. This is not ideal as it would be better to form an understanding of the variation over large temperature ranges (idealistically from 0 K to superalloy operational temperature). However if changes are insignificant over small temperature ranges there is some degree of extrapolation to larger temperature ranges that can be performed. Also data on finite temperature effects in other chapters confirms small changes over large temperature ranges.

The ISF energies in the cases of pure Ni, Ni-Al, Ni-Cr, Ni-Fe, Ni-Mo, Ni-Re display a decrease across the temperature range (note for Ni-Fe at x=0.5, Ni-Cr at x=0.1250 and Ni-Al at x=0.1875 the decrease is not smooth). For the case of Ni-Co the ISF formation energy behaves erratically showing no dominant increase or decrease. The observation of mostly subtle declines in the ISF formation energy with temperature is further corroborated by the work of Zhao[224, 225] who used first-principles and the quasiharmonic approximation to determine the ISF formation energy in $Ni_{0.95}Mo_{0.05}$ which predicted a decline of $\approx 12.68\, mJ/m^2$ from 0 to 1400 K. However when electronic excitation was factored in the decline became more pronounced ($\approx 32.78\, mJ/m^2$ over the same temperature range). This result implies that other thermal effects then thermal expansion do in some cases play a role but the data in this field is not adequate to determine how significant that role is.

Another study by Zhao on $Ni_{0.5}Co_{0.5}$ used the AIMD1 model to determine that ISF formation energy increases in a pronounced way in this alloy with temperature (≈ 30.41 mJ/m^2 from 0 to 1000 K)[226]. This increase is shown to steepen at higher temperature, the same pattern may be present at the lower compositions analysed in this study, but

the temperatures analysed are not high enough to be certain of this. Shang employed the quasistatic and supercell approaches to determine the ISF energy in the alloy $Ni_{71}Os_1$ (note that the solute atom is placed on the fault plane)[40]. A subtle decline with temperature was observed from $112\,mJ/m^2$ at 0 K to $97\,mJ/m^2$ at 1600 K[40]. With regard to the available experimental data Pettinari[227] used TEM and observed subtle declines in two model alloys one containing Re and the other containing Ru. The extent of the declines being $6\,mJ/m^2$ for the Ru containing alloy and $5\,mJ/m^2$ for the Re containing alloy over a temperature range from room temperature to $1323\,K$[227].

This investigation when viewed in the context of the high temperature investigations in the other chapters of this thesis is rather limited. As was established earlier, the GIBBS code can be used in conjunction with first principles calculations to determine the dependence of fault energy with temperature. This is however more complicated as a large number of data points (hence large computational expense) have to be taken (both above and below the equilibrium volume) to form the initial free energy vs volume curve (also this curve has to be smooth for use with the GIBBS code i.e. no magnetic transitions that distort the shape of the parabola). Alternatively, first principles calculations can be used to calculate the thermal expansion coefficient and how it varies with temperature. This can be done by using the methodology outlined in Jin[228], however this methodology appears equally subject to the fitting constraints previously mentioned. As implied computational expense was the driver of this chapter featuring a smaller scale investigation of high temperatures relative to the others.

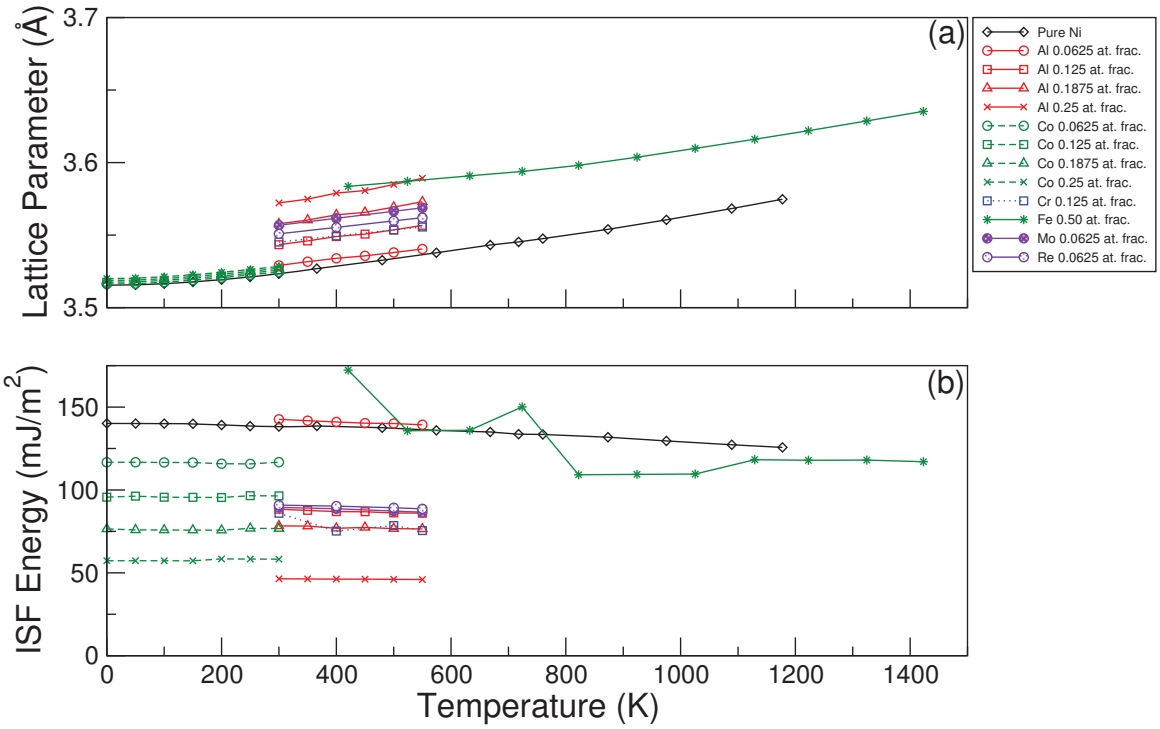

Figure 6.17: ISF energy and Lattice parameter vs temperature at volumes from the literature for the spin-polarised implementation of the data for the γ phase. Sources for data; Pure Ni [229, 230], Al[231, 232](fitting), Co[213](fitting), Cr[233](interpolation), Mo[233](interpolation), Re (1)[233](interpolation), Fe (1)[176, 234](taken from fitted line).

Chapter 7

Results: γ' Binary Systems (Ni_3X and Co_3X)

7.1 Introduction

First the simplest implementation of the γ' phase was assessed, binary compounds where the whole of the second sublattice is inhabited by a single element. It is to be noted that only a handful of these compounds have been observed experimentally. This is because as will be discussed later in this chapter most are fundamentally unstable or if metastable many would require arcane heat treatment techniques to produce[101, 235]. As it stands Co_3(X=Ti, Ta and V)(Ta and V metastable) and Ni_3(X=Mn, Pt, Fe and Al) have been experimentally observed[†]. Assessing compounds which can only theoretically exist still does have its merits as many assessments about the behavior of the element at

[†]For the sources for each of these observations refer to the proceeding paragraphs

lower compositions could possibly be made and extrapolations performed. For example it stands to reason that if one binary compound Ni_3X is less stable than Ni_3Y then $Ni_3(Al_{1-x}X_x))$ should be less stable than $Ni_3(Al_{1-x}Y_x))$ or possibly statements about more complex systems could be made, as is one of the main goals of this thesis.

Of the experimentally observed systems the following information exists in the literature. Firstly for Ni_3Al this compound exists as a weak itinerant ferromagnet exhibiting a Curie temperature of 41.5 K[236]. It retains its γ' ordered nature until the solidus temperature of 1660 K[237]. Ni_3Fe is subject to a second order ferromagnetic-to-paramagnetic transition at its Curie temperature of 870 K, It also loses the order at a temperature of 780 K becoming FCC[238]. Hence where Ni_3Fe exists in the $L1_2$ phase it is ferromagnetic. Ni_3Pt exists as a ferromagnet below 373 K[239] and has the equilibrium phase of $L1_2$ until approximately 850 K[239, 240].

Co_3Ti is paramagnetic up until it is destabilized at ≈1400 K. Ni_3Mn transitions to $L1_2$ order at around 753 K and becomes subject to ferromagnetic behavior at ≈700 K[241, 242]. Co_3V was experimentally determined to exist in equilibrium in a narrow temperature range in the $L1_2$ structure from 1283 K (below which it is ordered hexagonal(hP24)) to 1308K (where it transforms to FCC)[243]. However this compound was later found to be metastable existing when quenched from temperatures in the FCC region in the phase diagram with the hP24 to FCC, the transformation occurring at approximately 1318K[243–246]. Co_3Ta is also a metastable compound in the $L1_2$ structure, which can be formed by aging various Co-Ta binary alloys with $L1_2$ forming from FCC Co solid solution[244, 247]. This was found to transform to a four layered hexagonal

structure with similar characteristics to $MgCu_2$ upon further aging which is the equilibrium phase[247]. Note this is only true below 1273 K above which only the equilibrium phase is observed[247].

7.2 Lattice Parameters

Figure 7.1 displays the lattice parameters of all of the assessed binary compounds in both the spin-polarised and non spin-polarised implementation[†].

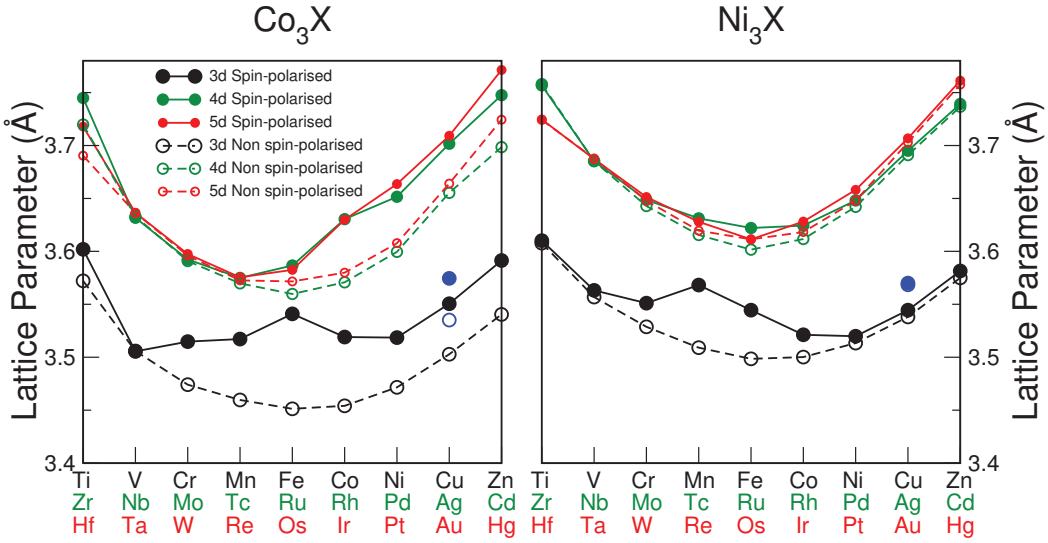

Figure 7.1: Diagram displaying the lattice parameters of the γ' binary compounds in both the spin-polarised and non spin-polarised implementations. Note the blue dots represent Ni_3Al and Co_3Al in their respective panels with the dots with the solid fill representing spin-polarised data.

As can clearly be seen all of the non spin-polarised curves exhibit a general parabolic shape as the d-band is filled with the minima occurring in the Fe/Ru/Os column. It is

[†]This data was published in ref [101], it is to be noted however that the data in this thesis will differ acutely from exact values published due to the fact that the data in this chapter is updated.

Table 7.1: Theoretical 0 K and experimental (at Room Temperature (RT)) lattice parameters of γ' binary compounds (All values are in units of Angstrom Å).

compound	present calculation (0 K)		other calculations (0 K)		experiments (RT)
	SP	NSP	method	value	
Co_3Ta	3.637	3.636	PAW-GGA-PW91	3.637[244]	3.647±0.004[247]
			PAW-GGA	3.64[248]	3.65[248]
					3.67[249]
Co_3Ti	3.602	3.572	PAW-GGA-PW91	3.601[244]	3.612[250]
			LMTO-ASA-LDA	3.58[251]	3.597[252][2]
Co_3V[1]	3.506	3.506	PAW-GGA-PW91	3.514[244]	-
			LMTO-ASA-LSDA	3.54[253]	
			LMTO-ASA-LDA	3.51[254]	
Ni_3Fe	3.544	3.499	LMTO-ASA-LSDA	3.54[253]	3.545[255]
					3.5550[256]
Ni_3Mn	3.568	3.509	LMTO-ASA-LSDA	3.55[253]	3.59[257]
Ni_3Pt	3.658	3.648	PP-PW-GGA-PBE	3.667[258]	3.646[259, 260]
Ni_3Al	3.570	3.568			3.5635[261]
					3.5718±0.00002[262]

[1] Note is Metastable
[2] Was found to vary very slightly with the sintering temperature

clear however that in the case of spin-polarisation the magnetic behavior causes significant deviation from said parabola. The former effect is caused by the fact that cohesive energies are maximum for half d-band filled elements. The magnetic disruption is especially true in the case of the 3d elements and the 4d and 5d elements in the Co-based compounds. It is noted that very similar observations were made for the lattice parameters of the binary Ni-alloys presented in the previous chapter. This data was compared with other experimental and simulation data (where compounds exist) demonstrating for the most part very good agreement with said data (see table 7.1).

7.3 Magnetic Moments

Figure 7.2 displays the magnetic moments of all of the investigated γ' binary compounds. It can be seen that the magnetic moment of the base element is suppressed by elements with lesser d-band filling but is effected to a much lesser degree as the d-bands are filled. Elements in the of the transition metal series (especially 3d elements) can develop large magnetic moments of their own. With regard to total magnetization the Co_3X compounds exhibit a rapid increase in the middle of the range followed by a subtle linear decline. Ni_3X compounds exhibit more of a parabolic shape across the range (with Ni_3Os providing a notable exception due to the much lower local magnetic moment of Os). It is to be noted that the overwhelming majority of the featured elements are not ferromagnetic in their pure forms. The only ones which exhibit ferromagnetism are Fe, Ni and Co (Pd remains paramagnetic despite coming close to fulfilling the Stoner criterion for ferromagnetism)[101, 263]. As can be seen from table 7.2 the results agree well with other simulations and experiments. Except for the case of the Ni local magnetic moment in the following compounds Ni_3(Al, Pt and Mn) when comparing to experiments. This disparity is caused by the tendency of the GGA algorithms to overestimate the magnetism in certain compounds (note that the LDA is also subject to the same effect)[264, 265].

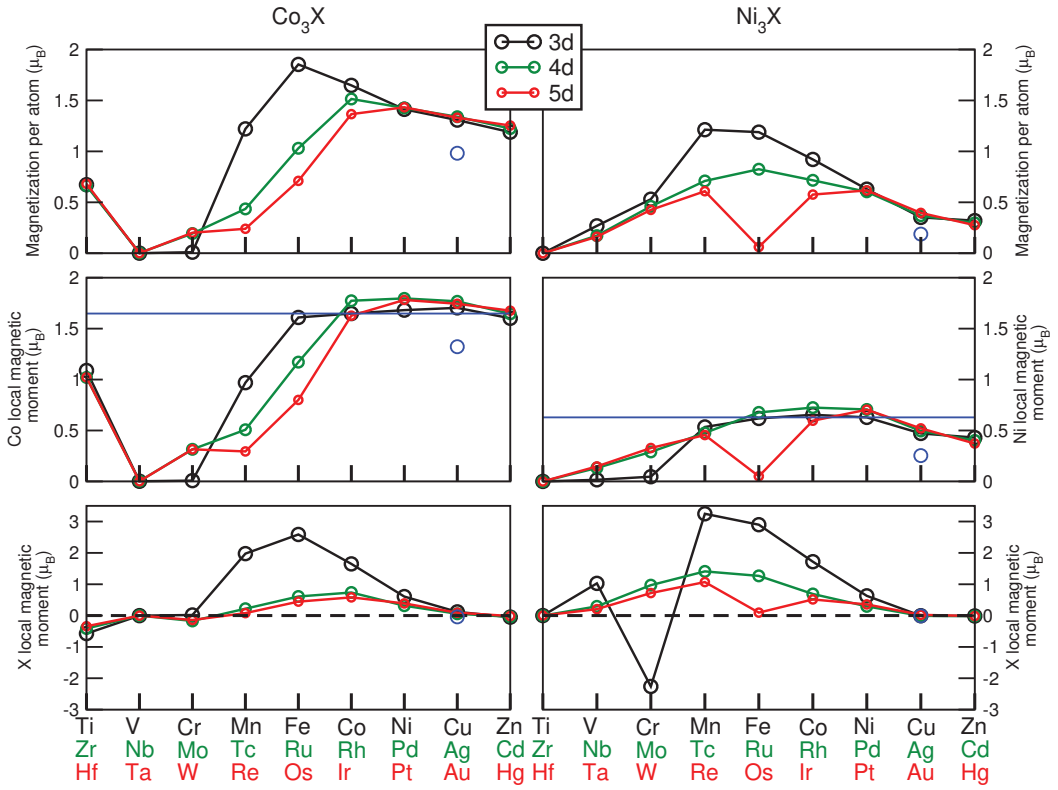

Figure 7.2: Magnetic moments of all of the studied γ' binary compounds where blue lines represent the magnetic moment of the pure FCC Co and Ni respectively and dashed black lines represent 0 magnetic moment. Blue dots represent Ni_3Al and Co_3Al respectively.

7.4 Formation Enthalpies

The main purpose of the investigation of the formation enthalpies is to assess as with other properties whether there is a dependence with d-band filling. As can be seen in figure 7.3 there does exist such a dependence. Compounds to the left of the Cr/Mo/W column exhibit negative formation enthalpies and can be classified as compound forming (note this is true whether or not spin-polarisation is featured). As mentioned in the

Table 7.2: Total magnetic moment per atom (Tot) and local magnetic moments of both elements in the binary compound Co/Ni and X respectively (all values are in units of Bohr magneton μ_B).

compound	present calculations			other calculations			experiments		
	Tot	Co/Ni	X	Tot	Co/Ni	X	Tot	Co/Ni	X
Co_3Ti	0.673	1.089	-0.574						
Ni_3Fe	1.189	0.619	2.900	1.23[266][1]	0.66[266][1]	2.94[266][1]	1.2075[238][3]	0.62±0.05[238][3]	2.97±0.15[238][3]
Ni_3Mn	1.213	0.534	3.249	1.25[266][1]	0.57[266][1]	3.31[266][1]	1.02[238]	0.30±0.05[238][4]	3.18±0.25[238][4]
Ni_3Pt	0.617	0.704	0.356	0.60[267][2]	-	-	0.424[268]	0.48[268]	0.254[268]
Ni_3Al	0.188	0.254	-0.009	0.236[264][5]	-	-	0.0575[269]	0.077[269]	-

[1] FLAPW-GGA-PBE
[2] PAW-GGA-PBE
[3] Note another less likely solution is given in [238] (corresponds also to 74.3 at % Ni)
[4] Note another less likely solution is given in [238] (corresponds also to 74.0 at % Ni)
[5] FLAPW-LDA

previous chapter, this is a different classification to stable, as the enthalpies of all other random and ordered structures are not known (it would need to be lower than all of these in order to be stable and appear on the equilibrium phase diagram). Speaking generally compounds in and to the right of this column have positive formation enthalpies and are unstable. Note the following exceptions to this statement Co_3(Pt(SP), W(SP and NSP)) and Ni_3(Pt(SP and NSP), Zn(SP and NSP), Cr(SP), Mn(SP), Fe(SP)). These results when spin-polarised align with the experimental appearance of compounds, where Co_3(X=Ti, Ta and V) and Ni_3(X=Mn, Pt, Fe and Al) feature negative formation enthalpies.

The results of Co-based compounds have ramifications for the quaternary system, $Co_3(Al_{1/2-x}W_{1/2-x}X_{2x})$. As the 6 elements from the first two rows, with the exception of V (which has a minor preference for the Co sublattice) were found by first-principles calculations to have a preference for segregation to the W sublattice of the compound Co_3W[270]. This implies that fine tuning of their compositions can lead to increases in the stability in the aforementioned quaternary system[101]. These enthalpy values also correspond to the literature discussed in section 2.5.4 where these elements (with the exception of Zr where no data exists) all are recorded as stabilizing the γ' phase in the Co-Al-W system[25, 63, 75, 81, 86].

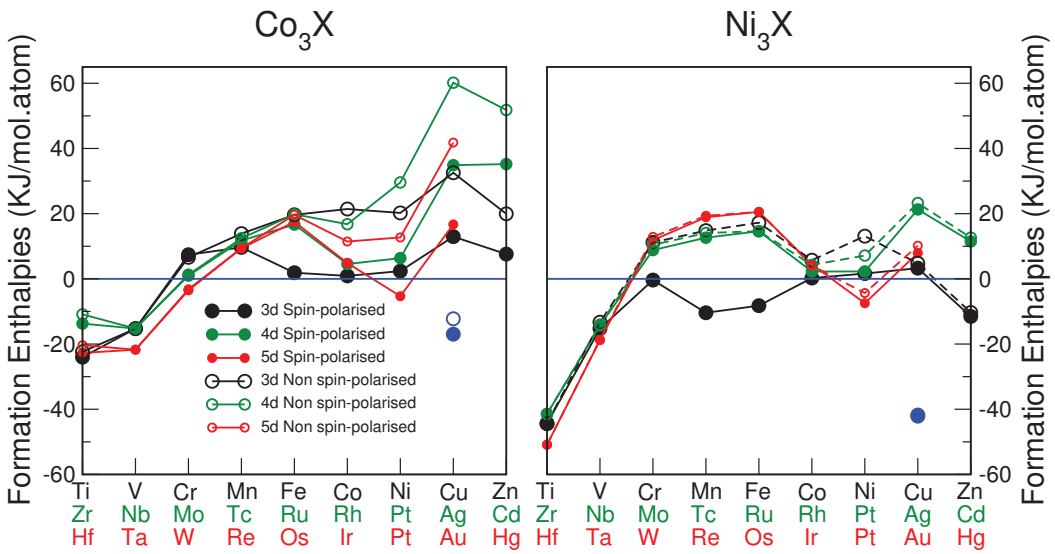

Figure 7.3: Formation enthalpies of investigated γ' binary compounds, blue lines represent 0. Blue dots represent Ni_3Al and Co_3Al respectively, where the dots with the solid fill represent the spin-polarised data.

7.5 SISF Energies

Figure 7.4 displays the SISF energies of all of the compounds in both the spin-polarised and non spin-polarised implementations of both the ANNI and ANNNI models. As can be seen from this figure for the overwhelming majority of elements the ANNI and ANNNI models show good agreement bolstering the assertion that for metals interactions are typically only short range in nature. In the non spin-polarised implementation for both of the compound systems a curve resembling a cosine wave with an exaggerated trough is exhibited (although this effect is more prounced in the Ni_3X compounds). Again similarly to the lattice parameters magnetism disrupts this curve having the most profound effect on the 3d elements and 4d and 5d elements in Co-based compounds.

Table 7.3: Formation enthalpies of investigated γ' binary compounds as compared with data from literature (all values are in $kJ/mol.atom$).

compound	present work (0 K)		other calculations (0 K)		experiments
	SP	NSP	method	value	
Co_3Ta	-21.717	-21.717	PAW-GGA	-30.875[248]	-
			PAW-GGA-PBE	-22[271]	
			PAW-GGA-PW91	-24.844[244]	
Co_3Ti	-24.015	-22.371	PAW-GGA-PW91	-25.843[244]	-26.18±1.5[272] (298K)
			LMTO-ASA-LDA	-26.5[251]	
			PAW-GGA-PBE	-25[271]	
Co_3V	-15.270	-15.272	PAW-GGA-PW91	-18.380[244]	-
Ni_3Fe	-8.217	17.235	LAPW-GGA-PW91	-8.6[273]	-
Ni_3Mn	-10.406	14.806	-	-	-7.93[274][1]
Ni_3Pt	-7.475	-4.359	USPP-LDA	-6.31[275]	-
Ni_3Al	-42.139	-41.774	USPP-GGA	-41.1[276](300 K)	-47[277]
					-37.6±4.2[278]
					-38.2±5[279]
					40.6±1[280]

[1] The prepared alloy is non-stoichiometric: 76.2 at % Mn.

Note the sign is even reversed in the following compounds, Co_3(X = Mn, Fe(ANNI Only), Co, Ni, Cu, Zr (ANNI only), Rh, Pd, Ir, Pt) Ni_3(X = Cr, Mn, Rh, Ir (only ANNNI)) this is very important as if magnetism were to be disregarded the phase the element stabilizes would be different from the spin-polarised reality as is discussed in the proceeding paragraph.

Note that the SISF energy is a representation of how stable the compound is in the $L1_2$ structure relative to the $D0_{19}$ (ANNI model) and $D0_{24}$ (both $D0_{19}$ and $D0_{24}$ in ANNNI model) structures, if the SISF energy of a compound is negative it implies that the second sublattice element stabilizes the $D0_{19}$ and $D0_{24}$ structures relative to the $L1_2$ structure. It is now investigated whether the native room temperature stacking sequence of the second sublattice element correlates with the SISF energy (see table 7.5). As can be seen the most positive on average is the non spin-polarised Ni FCC compounds, this makes sense as in this case Ni_3X is a compound of 2 FCC metals. Magnetism in all cases except for BCC second sublattice elements (Co ANNNI model excuded where a acute stabilisation is observed) degrades the stability of $L1_2$ relative to the ordered hexagonal structures. The most important demonstration of the power of magnetism is in Co FCC as the value flips from slightly positive to strongly negative. All of the HCP values are negative as would be logically expected however they are not the most negative values which are the Ni BCC set. This would not be logically expected, proving that the effects of native stacking sequence is present but does not exist as the be all and end all with magnetism and d-band filling playing substantial roles.

Next it was tested as to whether there is any correlation between the lattice parameter

and the SISF energy by the plotting scatter graphs (see figure 7.5). The rationale behind the plotting of said graphs is that the bigger the difference in lattice parameter from that of the Ni_3Al or Co_3Al host lattice, the greater the change in said host lattice, hence there exists the potential of a correlation between the two variables. However, there is no clear correlation shown in any of the data sets, meaning that lattice parameter has very little impact on the SISF energy. It is to be noted that the quality of correlation does not improve with the removal of spin-polarisation unlike with the native stacking sequence analysis.

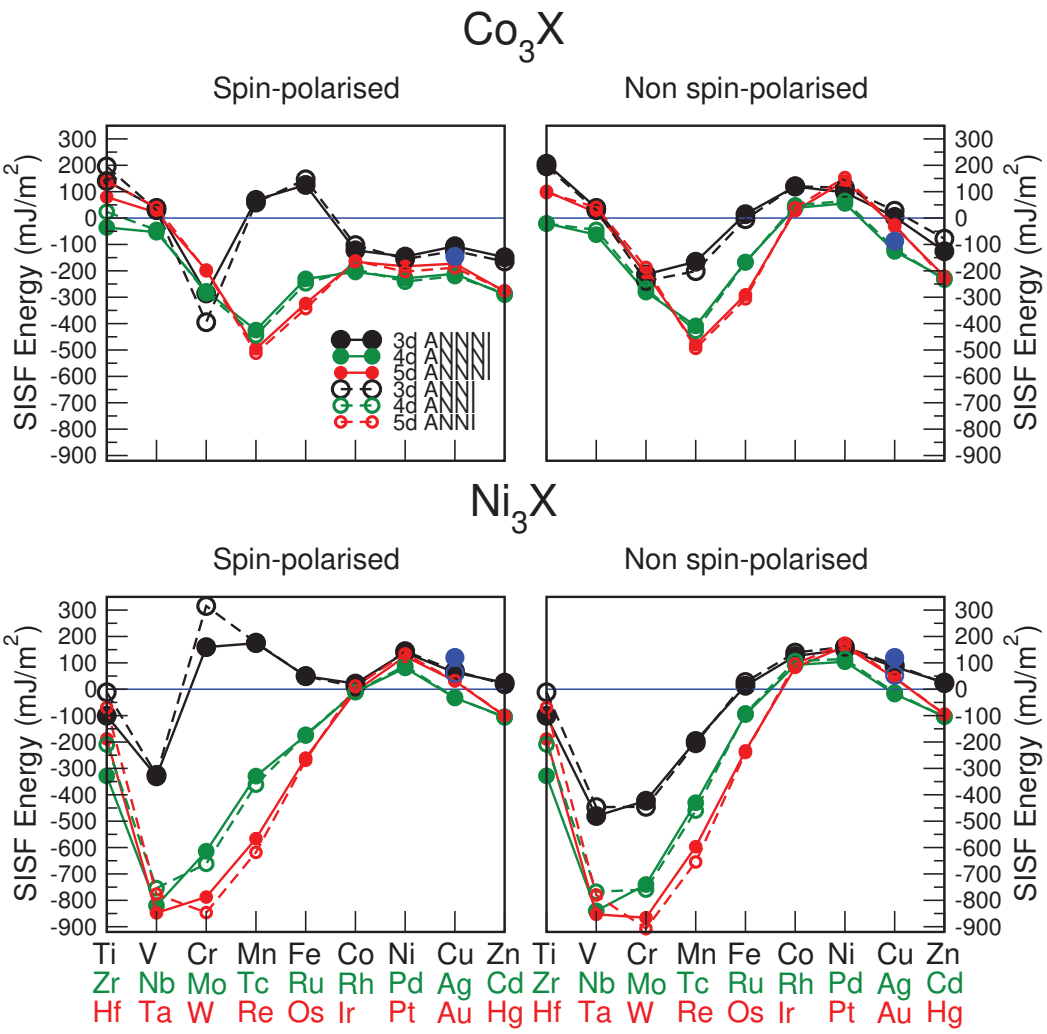

Figure 7.4: SISF energies of all investigated γ' binary compounds, blue lines represent 0, blue dots represent Co_3Al and Ni_3Al respectively, where the solid filled dot represents ANNNI data.

Table 7.5: Average SISF energy relative to the native stacking sequence (note that Mn and Hg are not featured).

NSS	SP?	Co SISF		Ni SISF	
		ANNNI	ANNI	ANNNI	ANNI
FCC	Yes	-173.769	-181.718	56.280	55.758
	No	13.039	23.859	91.239	92.146
BCC	Yes	-90.041	-101.235	-455.836	-428.325
	No	-98.701	-96.074	-598.654	-582.850
HCP	Yes	-185.177	-174.108	-200.766	-179.127
	No	-129.440	-131.601	-192.696	-167.889

Table 7.4: SISF energies of γ' binary compounds as compared with literature data (All values are in units of mJ/m^2).

compound	present calculation (0 K)				other calculations (0 K)		experiments
	ANNNI		ANNI		method	value	
	SP	NSP	SP	NSP			
Co_3Ti	140.515	205.898	195.651	196.047	TB-LMTO	175[281]	-
					PP-PAW	210[282]	-
Ni_3Fe	49.687	13.093	49.487	27.379	-	-	-
Ni_3Mn	174.687	-196.131	176.679	-204.744	-	-	-
Ni_3Pt	124.415	162.414	134.142	174.739	-	-	-
Ni_3Al	120.065	120.247	60.527	52.846	TB-LMTO	147[281]	5-15[283](623 K)
					FLAPW	40[284]	6±0.5[49](673 K)[1]
					FP-LMTO	60[285]	
					Empirical Potential	11[286]	
					PP-PAW	43[282]	
					FP-LMTO	80[287]	
					PP-PAW	66.81[288]	

[1] The prepared alloy is non-stoichiometric: $Ni_{0.78}Al_{0.22}$

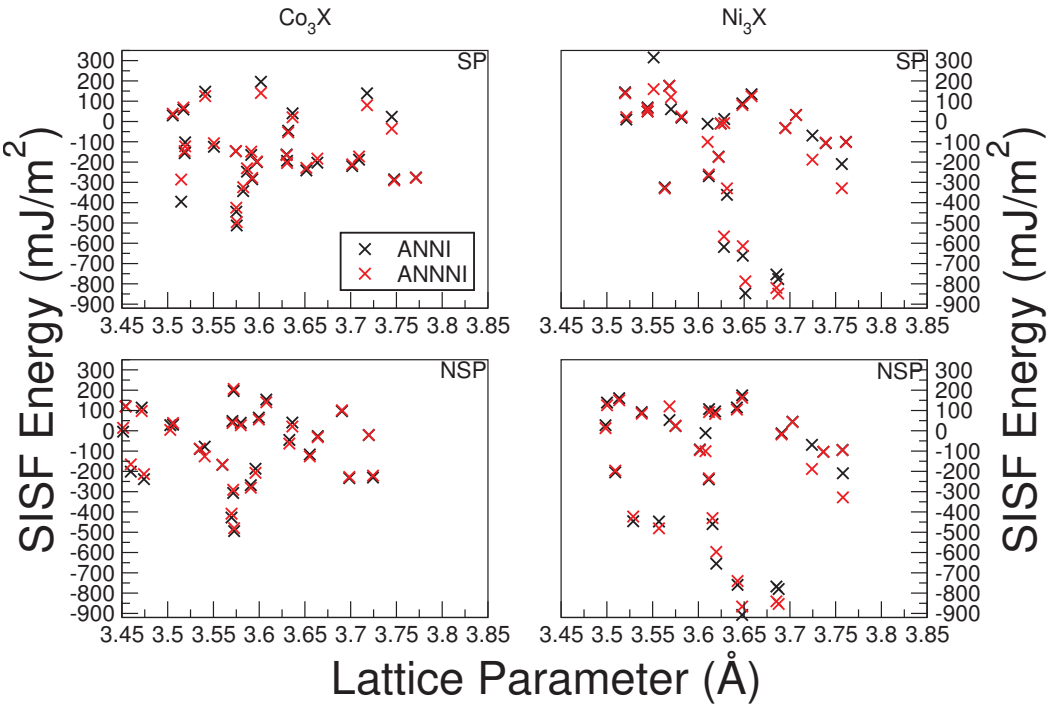

Figure 7.5: Scatter graphs of lattice parameter vs SISF energy for the ANNI and ANNNI datasets of both the spin and non spin-polarised implementations, as can clearly be seen there is no significant correlation in any of the datasets.

7.6 High-Temperature Calculations

The calculations conducted using the GIBBS code in conjunction with first-principles for both the Co_3X and Ni_3X systems for a sample of the transition metals are displayed in figures 7.6 and 7.7 respectively.

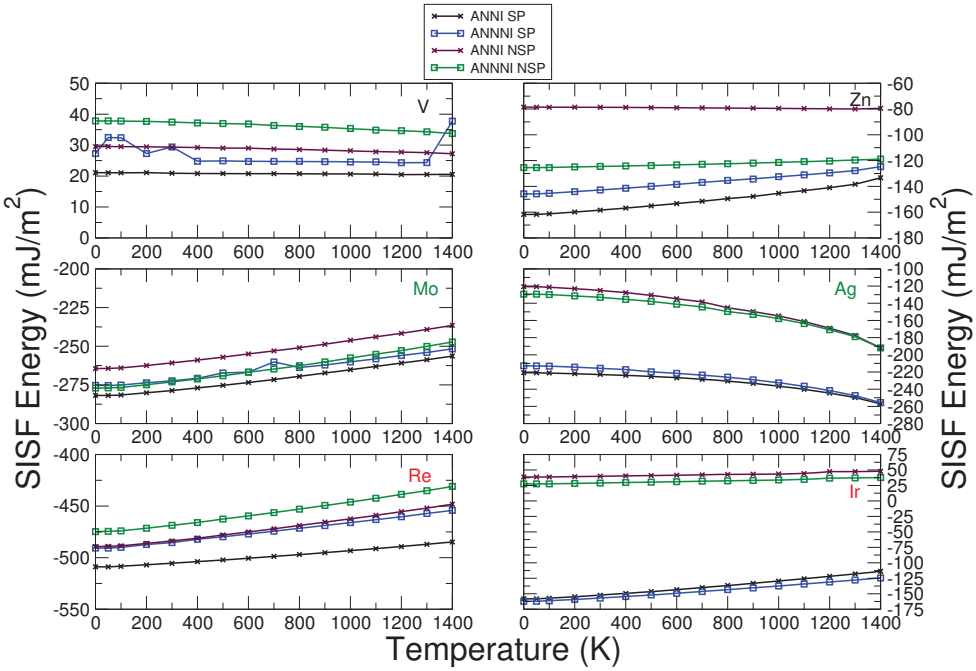

Figure 7.6: The relationship between SISF energy and temperature for a sample of the Co_3X compounds in the spin-polarised and non spin-polarised implementations of the ANNI and ANNNI models. Finite temperature results conducted using first-principles in conjunction with the quasiharmonic Debye model and the quasistatic approach.

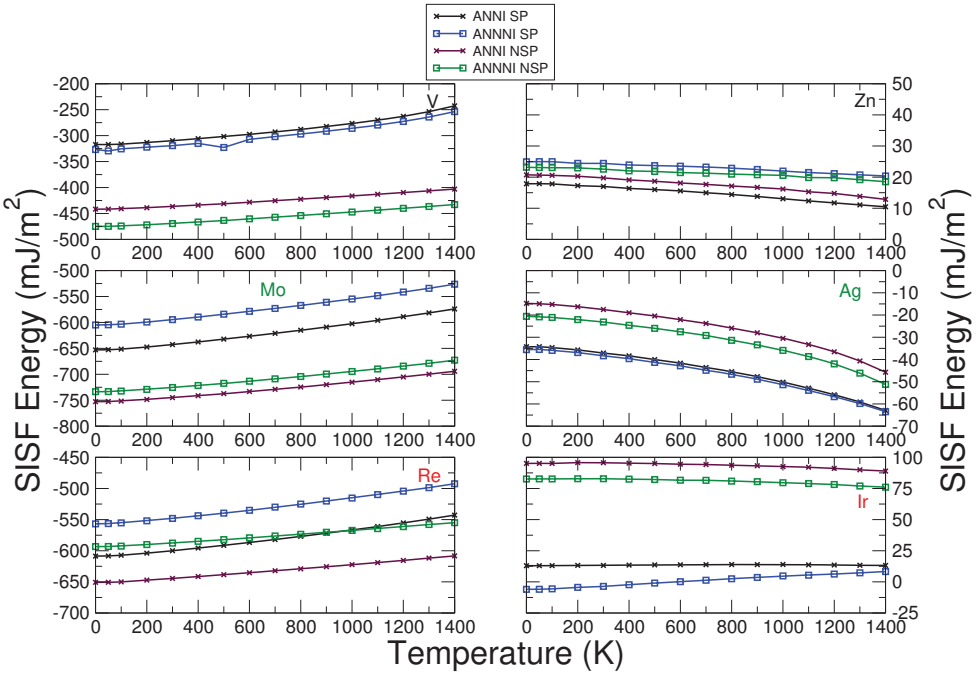

Figure 7.7: The relationship between SISF energy and temperature for a sample of the Ni_3X compounds in the spin-polarised and non spin-polarised implementations of the ANNI and ANNNI models. Finite temperature results conducted using first-principles in conjunction with the quasiharmonic Debye model and the quasistatic approach.

As can be seen in the majority of cases regardless of the approximation a smooth quasilinear change is observed as temperature is increased. The seemingly anomalous point for the ANNNI SP data set in the Co_3V compound at 1400 K is caused by strong magnetism being present at the volume associated with 1400 K. In some cases this change manifests itself as a decline and in others as an increase. In order to determine whether the sign of the SISF energy determines whether the change manifests as an increase or decrease the change was plotted vs the SISF formation energy at 0 K. This data is plotted for the Co_3X compounds in figures 7.8 and 7.9 and for the Ni_3X compounds in figures 7.10 and 7.11 (note the change over 0-1400 K is computed as the value at 1400 K

minus the value at 0 K and not the other way around).

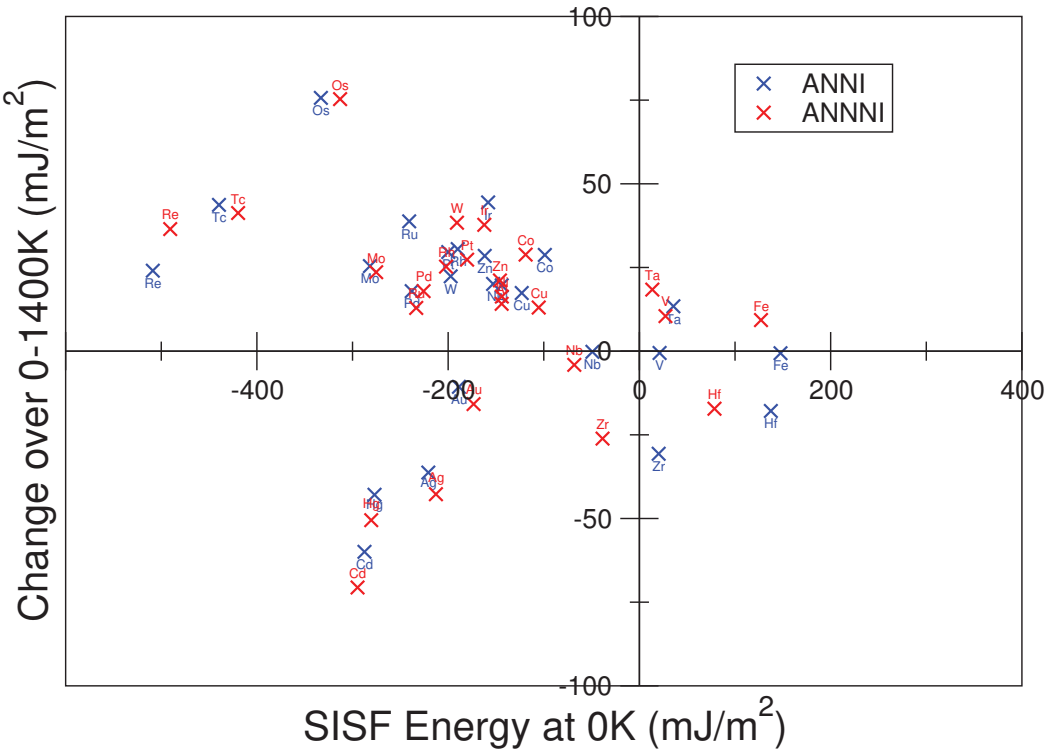

Figure 7.8: The change in SISF energy with temperature vs the 0 K SISF energy for the spin-polarised implementation of the ANNI and ANNNI models for the Co_3X compounds. Finite temperature results conducted using first-principles in conjunction with the quasiharmonic Debye model and the quasistatic approach.

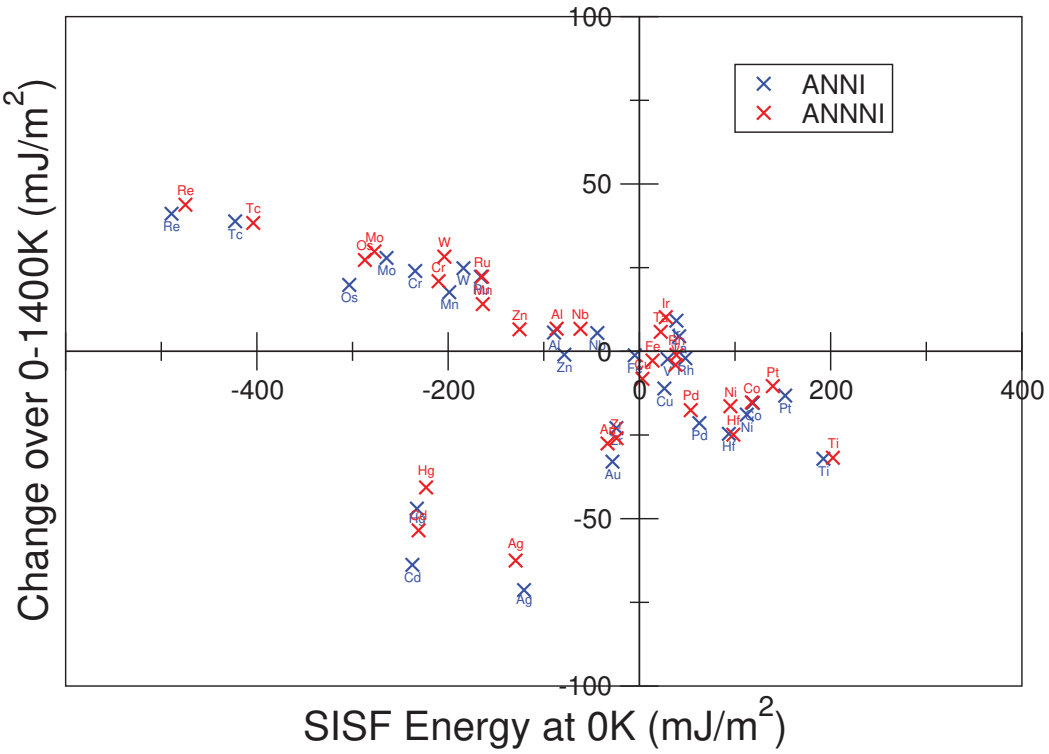

Figure 7.9: The change in SISF energy with temperature vs the 0 K SISF energy for the non spin-polarised implementation of the ANNI and ANNNI models for the Co_3X compounds. Finite temperature results conducted using first-principles in conjunction with the quasiharmonic Debye model and the quasistatic approach.

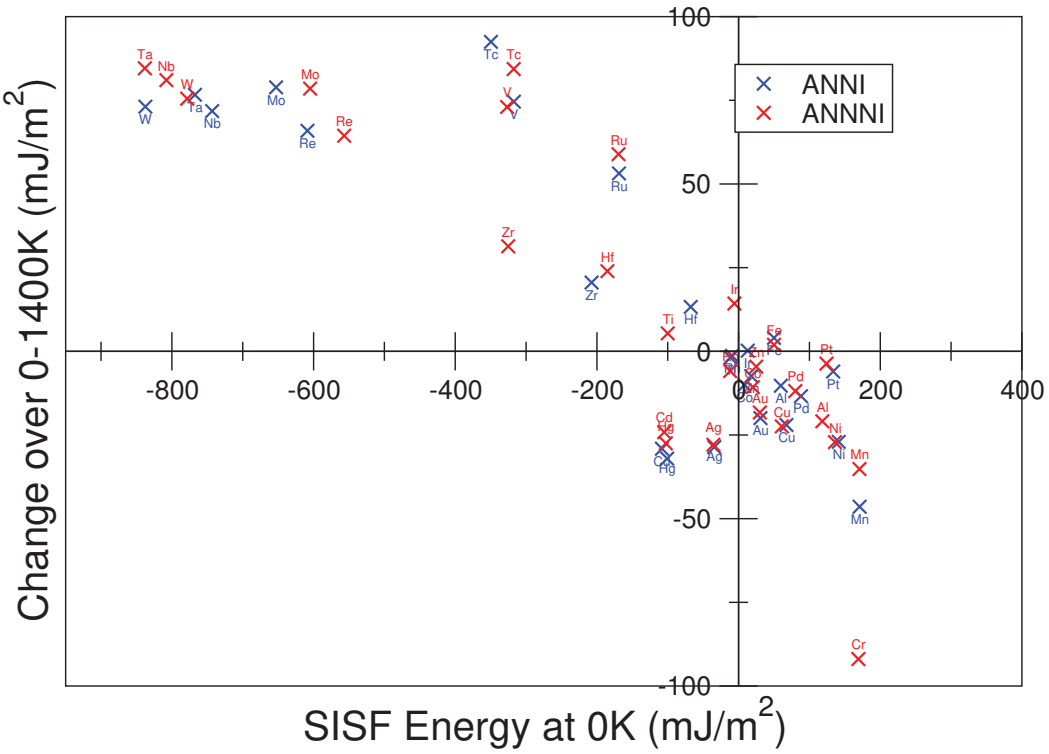

Figure 7.10: The change in SISF energy with temperature vs the 0 K SISF energy for the spin-polarised implementation of the ANNI and ANNNI models for the Ni_3X compounds. Finite temperature results conducted using first-principles in conjunction with the quasiharmonic Debye model and the quasistatic approach.

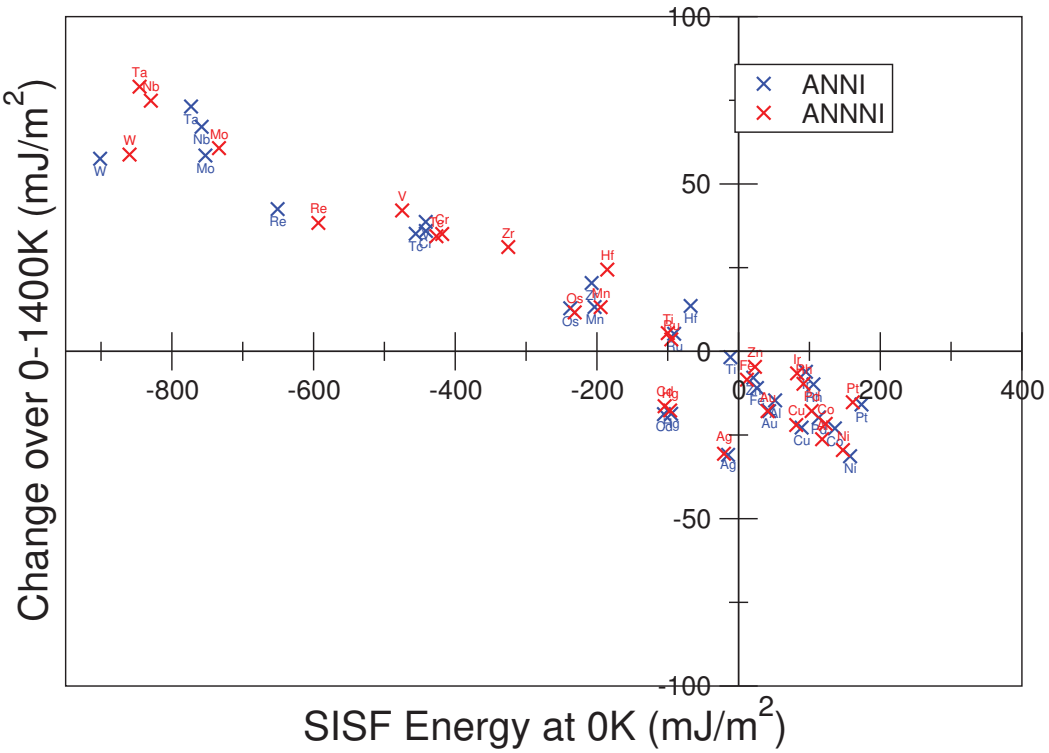

Figure 7.11: The change in SISF energy with temperature vs the 0 K SISF energy for the non spin-polarised implementation of the ANNI and ANNNI models for the Ni_3X compounds. Finite temperature results conducted using first-principles in conjunction with the quasiharmonic Debye model and the quasistatic approach.

Two pieces of key information can be ascertained from these graphs, there does in a large part appear to be a dependence on the sign of the SISF energy with the sign of the change with temperature. Negative SISF Energy compounds experience on the whole positive decays meaning they become closer to zero (and hence appear in the top left quadrant of their respective graphs). Likewise positive SISF energy compounds experience negative changes again causing the SISF to become closer to zero (hence appearing in the bottom right quadrant of their respective graphs). The role of the inclusion of magnetism is now investigated by counting the numbers of elements that

defy this trend in each of the SP and NSP datasets. In both the Co_3X and Ni_3X compounds there are more elements (although note the difference is only 1 on the case of the Co_3X compounds and by a SISF energy less then $1\,mJ/m^2$) in defiance of the trend for the SP dataset then for the respective NSP dataset proving that at least in some capacity magnetism has the ability to disrupt this trend. It is also important to note that the raw numbers of elements that are in defiance of this trend is higher for the case of the Co-based compounds then for the Ni-based compounds. Finally for the elements that do follow the trend there appears to be a correlation (which is stronger in the case of the Ni_3X compounds) implying that the larger the absolute value of the SISF energy the larger the extent of the decay towards zero.

Chapter 8

Results: γ' Pseudo-binary Systems

$((Ni_{1-x}X_x)_3Al$ and $Ni_3(Al_{1-x}X_x))$

8.1 Introduction

Pseudo-binary systems in this research were analysed using two approaches, the first being a high throughput approach in which the full set of transition metals were analysed using smaller supercells and coarser compositions x=0, 0.25, 0.5, 0.75 and 1 (32-atom supercells for first sublattice 64-atom supercells for second sublattice). The second was where a selection of systems which have direct verification in the literature to exist were analysed using larger supercells and finer compositions which are within the solid solubility. These two sets of results were later compared to see whether interpolation between the two results x=0 and x=0.25 in the coarser set of data agreed with the data at finer compositions.

The data for the finer compositions was not conducted for all of the transition metal elements in both sublattices due to the computational expense. Rather it was only conducted where said elements had either a basis in literature, be that experimental[55, 289, 290] or simulation[291–293] to segregate to a certain sublattice or partition evenly between the two. Of the elements which have evidence to support them most of the elements were found to segregate to the second sublattice of γ' Ti, V, Zr, Nb, Mo, Hf, Ta and W, where the only ones to segregate to the first sublattice are Co, Cu, Pd and Pt, where Cr, Mn and Fe were found in [55] to distribute evenly between the two sublattices. Some of the elements Mn, Fe, Co, Cu, Ag and Au were found to experience different site preferences based on the composition of the γ' phase[292]. Hence the results presented in this thesis do not provide an exact understanding of site preference, rather a working approximation.

8.2 Lattice Parameters

8.2.1 First Sublattice

Coarse Compositions

The lattice parameter vs composition for the high throughput set of data was displayed in figure 8.1. As the composition is increased there is in general a linear or slightly curved increase in the lattice parameter in both SP and NSP sets of data. It is to be noted that magnetism in this set of data seems to only have a significant effect in the case of a few elements Mn, Fe and Co. In the case of the following elements Ti, V,

Cr, Fe, Zr, Nb, Mo, Tc, Ru, Hf, Ta, W and Re there exists a large disagreement with Vegard's law, the only elements which agree well with the law being Rh, Pd, Os, Ir, Pt and Co. The reason for this disagreement could be due to the nuance in how unlike in the γ binary systems reviewed in chapter 6 where agreement is much better, there exist 2 distinct sublattices in γ'. All of the elements where data exists, which were experimentally observed to segregate to mainly the Ni sublattice offer good agreement, wheras all of the elements found to segregate to the Al sublattice were found to result in poor agreement with Vegard's law as would be expected. The elements which were found to partition evenly have large disagreement with Vegard's law also (note Mn agrees at the end points but has significant disagreement in the middle of the composition range). Again the same logic as detailed in section 6.2 of chapter 6 applies to comparisons where high compositions are concerned in this chapter. Vegard's law is derived from data at dilute compositions where interactions between nickel and the solute are very important in informing the lattice parameter unlike at high compositions.

One point of note is that for alloying elements V, Cr and Fe declines are predicted by Vegard's law in the lattice parameter with increased alloying composition whereas the simulations of this research increases are found. This can potentially be attrubuted to the strong magnetic nature of these 3 alloying elements. Both the 4d and 5d elements behave similarly to eachother as demostrated in the final row of graphs of figure 8.1.

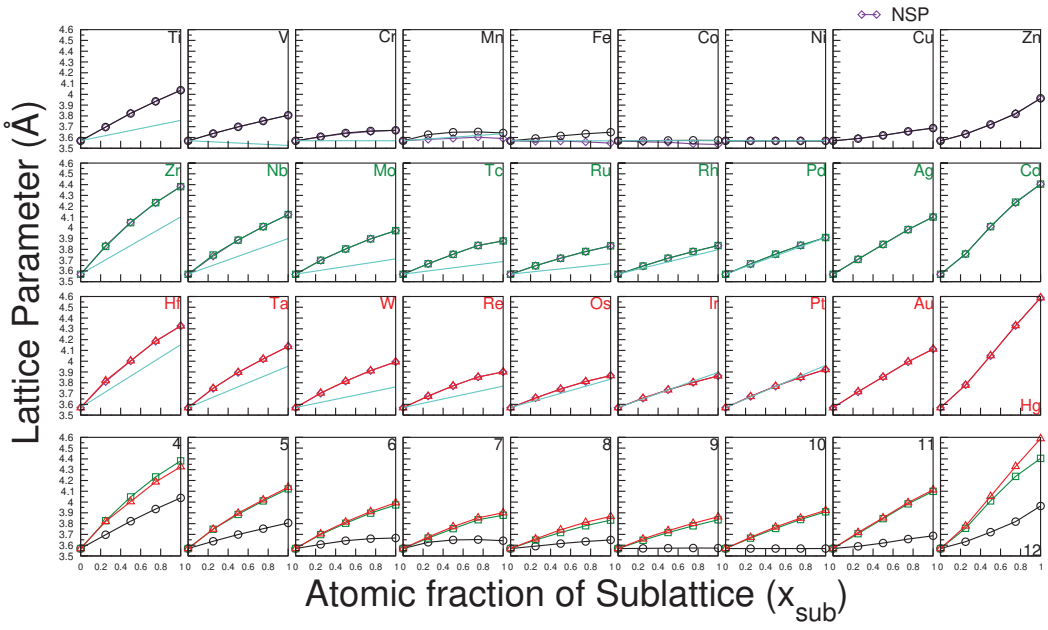

Figure 8.1: Equilibrium lattice parameters in both spin-polarised and non spin-polarised implementations for the coarse compositional data in the first sublattice of the γ' phase. Standard colour scheme in use for spin-polarised lattice parameter of each system. Turquoise lines correspond to Vegard's law.

Figure 8.2 contains the same data but expressed as a relationship with d-band filling. As can be seen there is a broad parabolic shape in all of the curves caused by the strong binding energies associated with half d-band filled elements. Noted is the disruption to the parabolic behavior that is caused by magnetism in the compounds near the centre of the 3d series. Another observation is that as x is increased the parabolas become steeper due the the increased influence of the alloying elements which are mostly larger in atomic size then nickel.

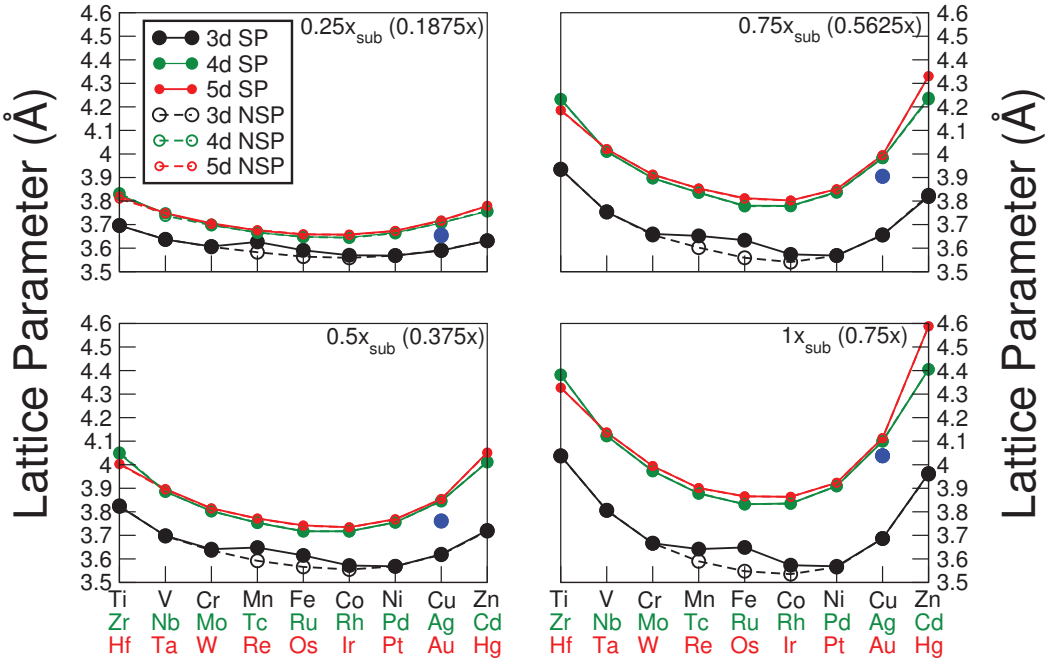

Figure 8.2: Equilibrium lattice parameters in both spin-polarised and non spin-polarised implementations for the coarse computational data in the first sublattice of the γ' phase. This time expressed as expressed as a dependence on d-band filling. Blue dots represent where Al is used as an alloying element.

Fine Compositions

Figure 8.3 is data compared with experimental results for the 4 elements found to segregate to the first sublattice of the γ' phase.

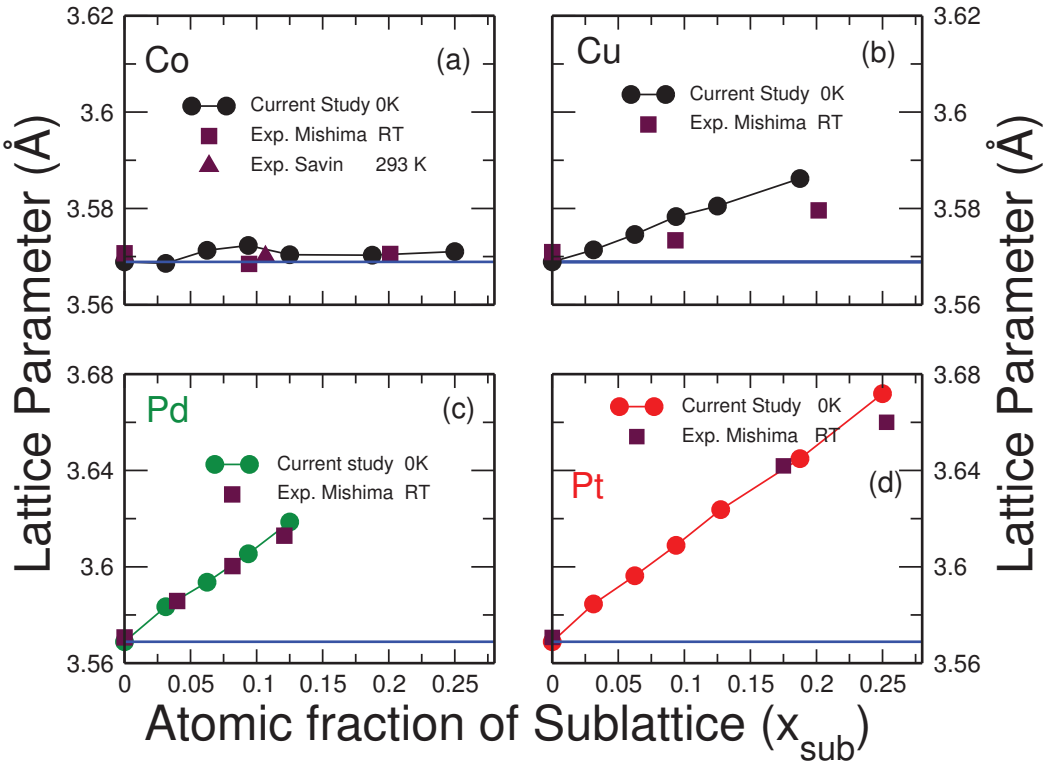

Figure 8.3: The lattice parameter data for the fine compositions of the elements found to segregate to the first sublattice of the γ' phase in the spin-polarised implementation. Comparison is also made with the experimental observations of Mishima[55] and Savin[294]. The blue lines represent the lattice parameter of Ni_3Al.

As can be seen in all cases except for X=Co where the lattice parameter remains approximately the same, a linear increase in lattice parameter with composition is observed. The results in this research display very strong agreement with the experimental results in the literature. Unfortunately however such data is scarce with only Mishima[55] featuring results at multiple compositions hence displaying the dependence on lattice parameter with composition. The dependence of d-band filling is assessed at the lowest calculated composition as can be seen in figure 8.4. As can be seen the observations of

the previous subsection concerning the data for coarse compositions are corroborated.

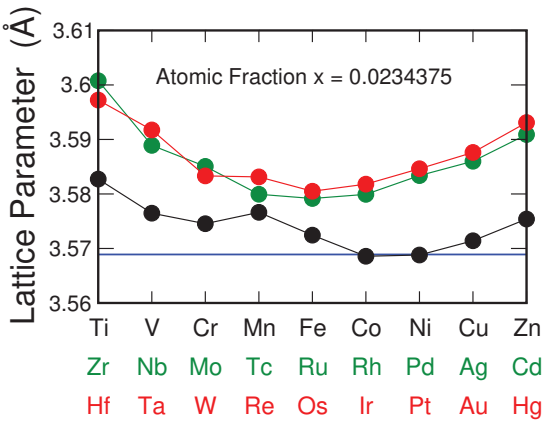

Figure 8.4: Equilibrium lattice parameters for all of the transition metals added to the first sublattice of γ'(whether they segregate to it or not) at the bulk composition of 0.0234375 atomic fraction (0.017578125 atomic fraction of sublattice x_{sub}) in the spin-polarised implementation. The blue line represents the lattice parameter of Ni_3Al.

8.2.2 Second Sublattice

Coarse Compositions

The data for all transition metals substituting to the second sublattice is displayed in figure 8.5. As expected all of the elements that substitute to the first sublattice disagree with Vegard's law and all of the elements which naturally substitute to the second sublattice with the exceptions of (Ti, Mo and Hf) agree well as would be expected. Also again all of the elements which partition evenly were found to disagree. 4d and 5d elements were found to offer similar behaviour as can be seen from the bottom row of figure 8.5 and the changes in lattice parameter with composition are linear or slightly curved. The relationship between lattice parameter and d-band filling is expressed in figure 8.6. A parabolic relationship is observed with d-band filling with the minimums

lying in the centre of the transition metal series caused by the high binding energies of these elements. Elements near the centre of the 3d series experience magnetic disruption to the typical parabolic shape when spin-polarisation is factored in due to the complex magnetic nature of these elements.

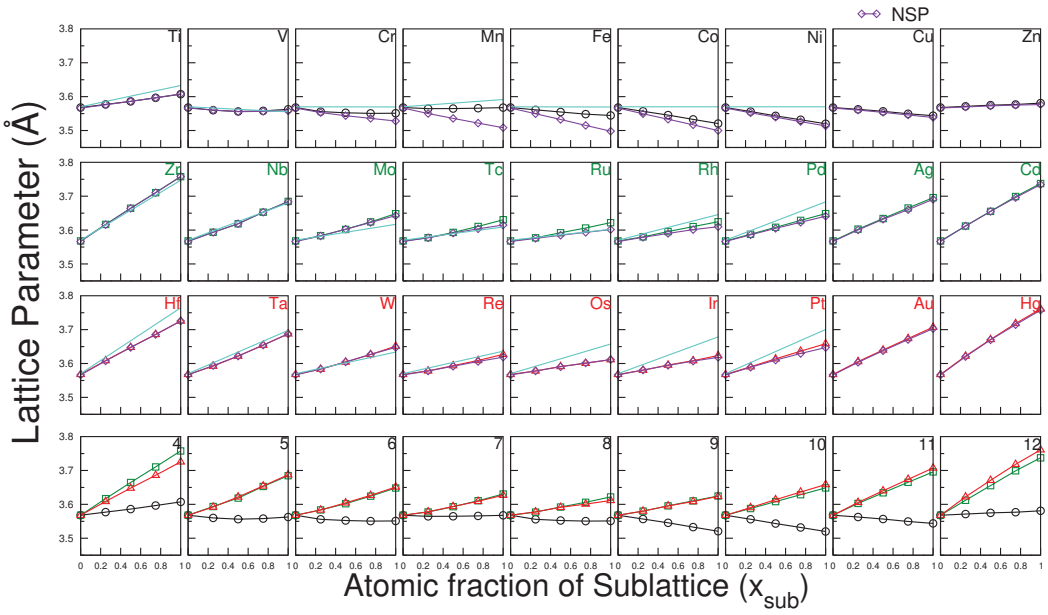

Figure 8.5: Equilibrium lattice parameters in both spin-polarised and non spin-polarised implementations for the coarse compositional data in the second sublattice of the γ' phase. Standard colour scheme in use for total spin-polarised lattice parameter of each system. Turquoise lines correspond to Vegard's law.

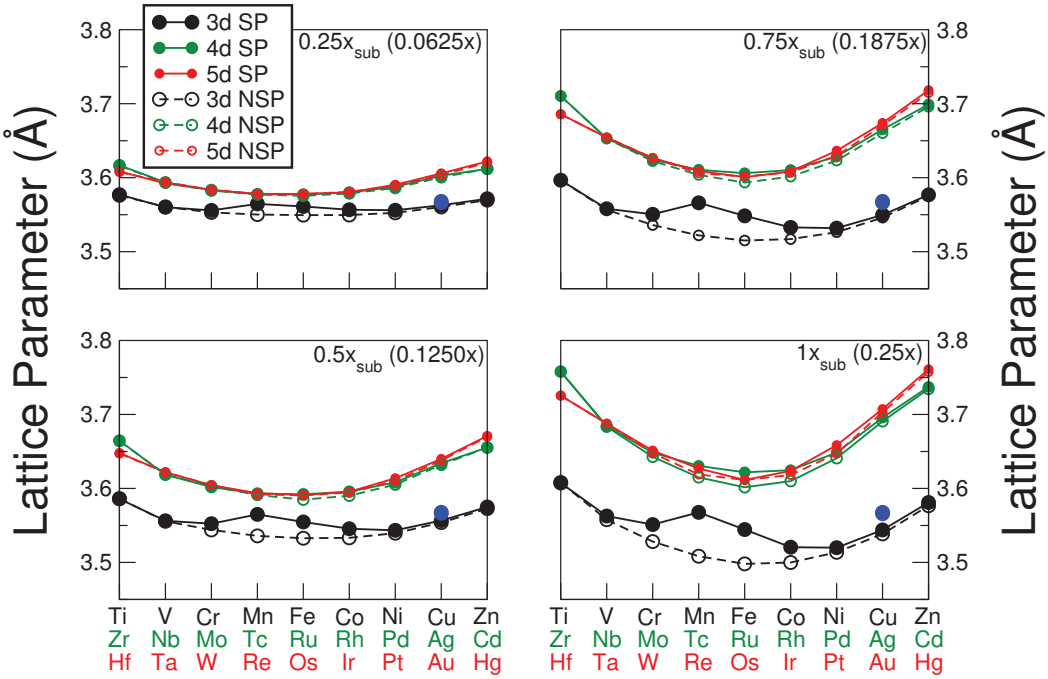

Figure 8.6: Equilibrium lattice parameters in both spin-polarised and non spin-polarised approximations for the coarse compositional data in the second sublattice of the γ' phase for the spin-polarised implementation. This time expressed as expressed as a dependence on d-band filling.

Fine Compositions

The data and its comparison to experimental data is presented in figure 8.7. Like for the first sublattice only Mishima[55] has results for multiple compositions of each alloy for the purpose of assessing the dependence of lattice parameter on composition. Agreement with experimental data is good with the largest disagreement being 0.36% for where X=Ti at the composition $x_{sub} \approx 0.48$. V is the only alloying element found to decrease the lattice parameter, this is attributed to the complex magnetic nature of this element. The dependence on d-band filling is assessed in figure 8.8 for the lowest

calculated composition. Where the observations made about d-band filling for the coarse set of data hold true for this dataset. Comparing figures 8.4 and 8.8 reveals that on average when substitution for nickel is made the lattice parameter is much higher. This is attributed to atomic size effects as nickel has a smaller atomic radius then majority of the transition metals and on the contrary aluminum has a larger atomic radius then the majority of transition metals.

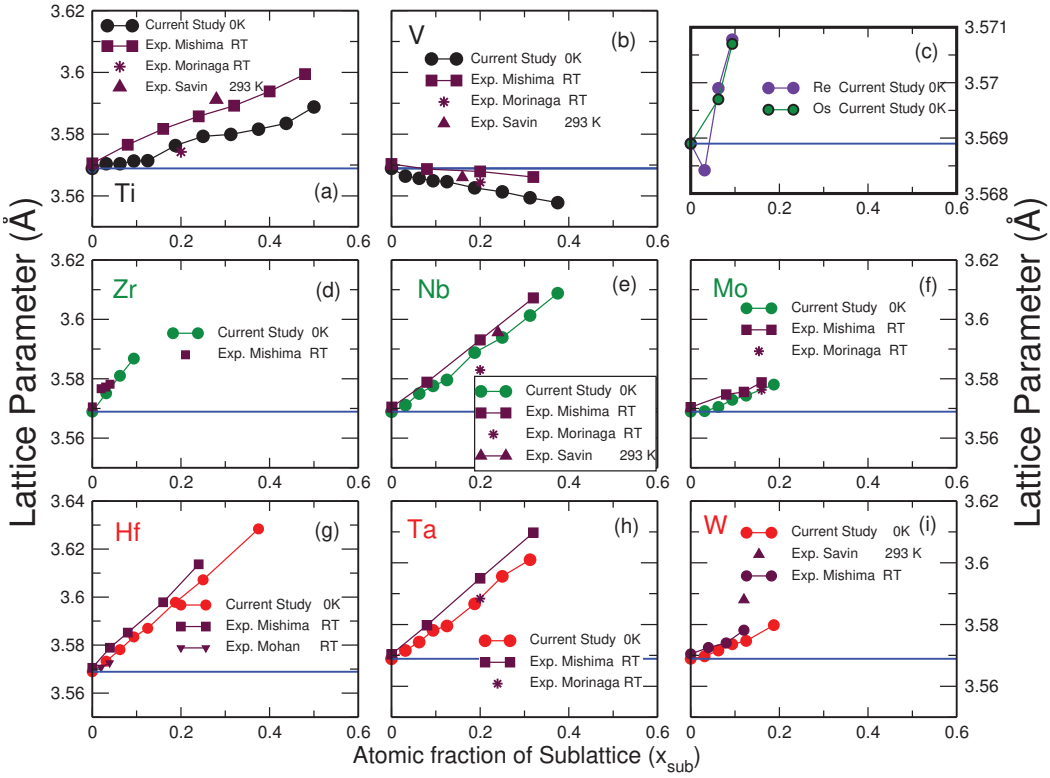

Figure 8.7: The lattice parameter data for the fine compositions of the elements found to segregate to the second sublattice of the γ' phase for the spin-polarised implementation. Comparison is also made with the experimental observations of Mishima[55], Savin[294], Morinaga[295] and Mohan[296]. The blue lines represent the lattice parameter of Ni_3Al.

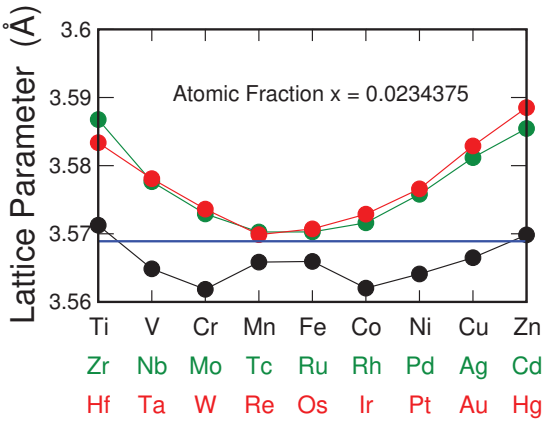

Figure 8.8: Equilibrium lattice parameters for all of the transition metals added to the second sublattice of γ'(whether they segregate to it or not) at the bulk composition of 0.0234375 atomic fraction (0.005859375 atomic fraction of sublattice x_{sub}) for the spin-polarised implementation. The blue line represents the lattice parameter of Ni_3Al.

8.2.3 Both Sublattices

Fine Compositions

The dependence of the lattice parameter on composition for the elements found to partition evenly between the two sublattices is displayed in figure 8.9. As can be seen strong agreement is found between the results of this thesis and the available experimental data.

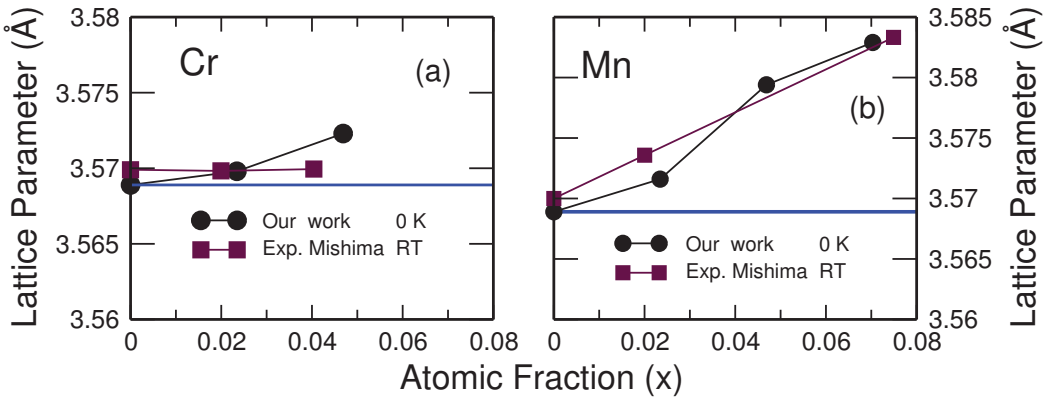

Figure 8.9: The lattice parameter data for the fine compositions of the elements found to partiotion to both sublattices of the γ' phase equally for the spin-polarised implementation. Comparison is also made with the experimental observations of Mishima[55]. The blue lines represent the lattice parameter of Ni_3Al.

There exists an additional nuance with regard to the alloying element Fe which was found to significantly change its site preference based on the composition of the γ' phase, hence calculations in all 3 scenarios; segregation to the first sublattice, segregation to the second sublattice, and partitioning evenly between the two were conducted (see figure 8.10).

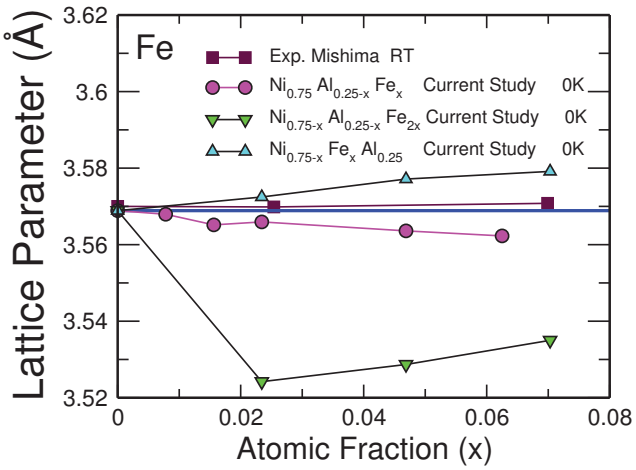

Figure 8.10: The lattice parameter data for the equilibrium lattice parameter of iron modelled as segregating to the first and second sublattices as well as partitioning between the two sublattices of the γ' phase equally for the spin-polarised implementation. Comparison is also made with the experimental observations of Mishima[55]. Blue line represnts the lattice parameter of Ni_3Al.

As can be seen from the graph the experimental data predicts very little change with increasing composition. Segregation to the first sublattice results in a slight increase whereas partitioning to the second sublattice results in a slight decrease with a much larger decrease predicted for the even distribution between both sublattices. Whilst even distribution between both sublattices renders results that have the largest disagreement with the available experimental data, this was in the end chosen to extend to the results for the SISF. This is as this type of splitting is the only type of with experimental data concerning the lattice parameter[55] to the authors knowledge.

8.3 Magnetic Moments

8.3.1 First Sublattice

Coarse Compositions

The analysis for the magnetic moments of the individual species as well as the average magnetic moment per atom are displayed in figure 8.11.

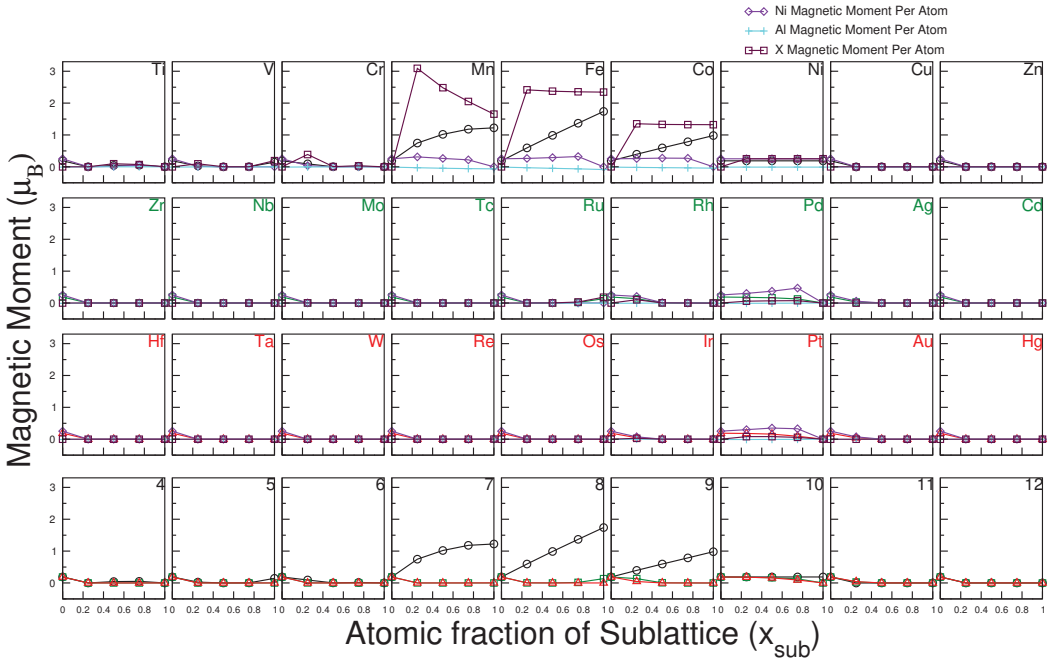

Figure 8.11: The total magnetic moment per atom in addition to the average magnetic moment per atom of the nickel, aluminium and X atoms of the coarse compositional data for the first sublattice of the γ' phase. Standard colour scheme in use for total magnetic moment of each system.

One clear conclusion from this data is that overall magnetism is weak in these alloys. with only a few alloys where x= Mn, Fe, Co, Pd, Cr and Pt exhibiting any significant magnetism. It is noted that aluminium does not gain significant magnetism in any

of the circumstances and frequently develops small magnetic moments in the opposite orientation to that of the Ni and X magnetic moments.

An interesting nuance concerning the cases where x= Mn, Fe and Co is that the average magnetic moment of X peaks at x=0.25 and decays beyond (most notably where X=Mn the decay is only slight in the cases of the other 2 alloying elements) however due to the increasing amount of the element the total magnetisation increases with x. In the case of X=Pd and X=Pt the solute element does not exhibit significant magnetism however nickel does. It appears significant to this observation that Pd and Pt are both in the same group as nickel. In the case of X=Cr, chromium develops a significant magnetic moment at x=0.25 but no significant magnetic moment beyond.

The same data except expressed as a function of d-band filling is expressed in figures 8.12-15.

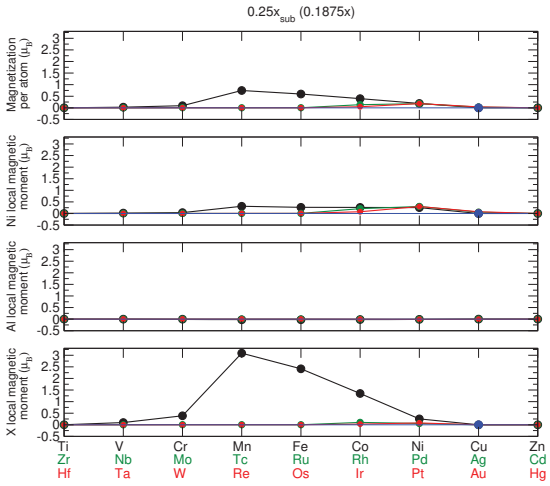

Figure 8.12: The total magnetic moment per atom in addition to the average magnetic moment per atom of the nickel, aluminium and X atoms of the coarse compositional data for the first sublattice of the γ' phase. Expressed as a dependence with d-band filling for the composition $0.25x_{sub}$. Blue lines represent zero magnetic moment.

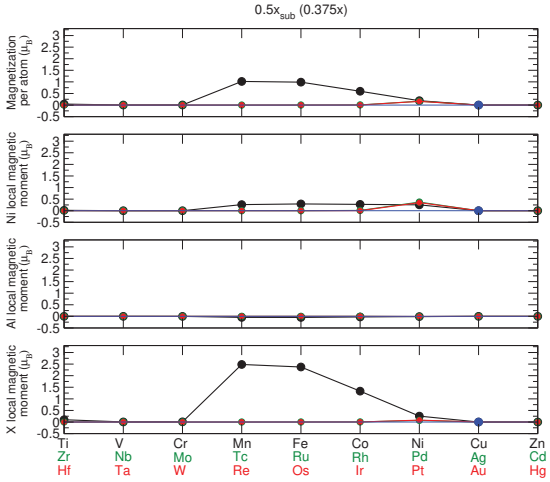

Figure 8.13: The total magnetic moment per atom in addition to the average magnetic moment per atom of the nickel, aluminium and X atoms of the coarse compositional data for the first sublattice of the γ' phase. Expressed as a dependence with d-band filling for the composition $0.5x_{sub}$. Blue lines represent zero magnetic moment.

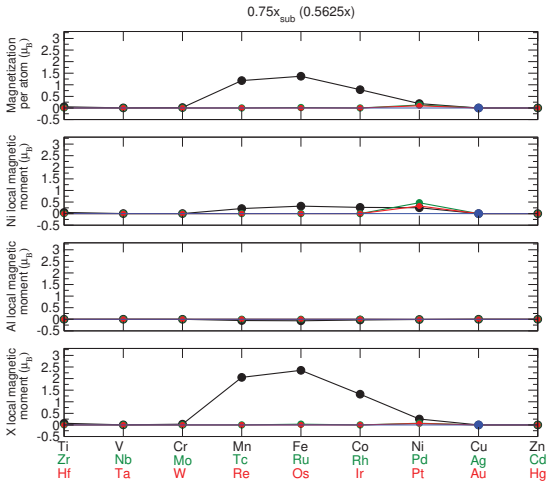

Figure 8.14: The total magnetic moment per atom in addition to the average magnetic moment per atom of the nickel, aluminium and X atoms of the coarse compositional data for the first sublattice of the γ' phase. Expressed as a dependence with d-band filling for the composition $0.75x_{sub}$. Blue lines represent zero magnetic moment.

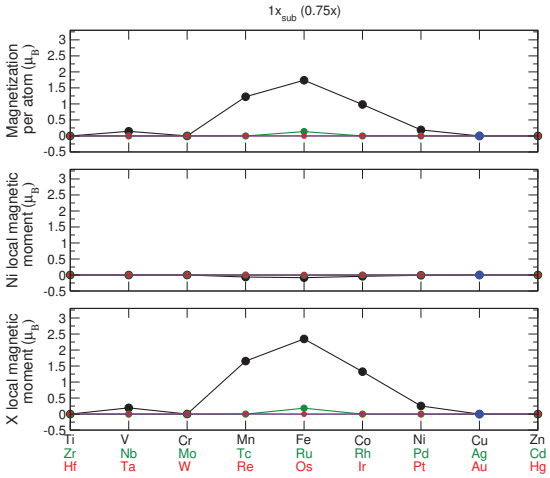

Figure 8.15: The total magnetic moment per atom in addition to the average magnetic moment per atom of the nickel, aluminium and X atoms of the coarse compositional data for the first sublattice of the γ' phase. Expressed as a dependence with d-band filling for the composition $1x_{sub}$. Blue lines represent zero magnetic moment.

8.3.2 Second Sublattice

Coarse Compositions

The data for all of the calculated alloy systems is presented in figure 8.16.

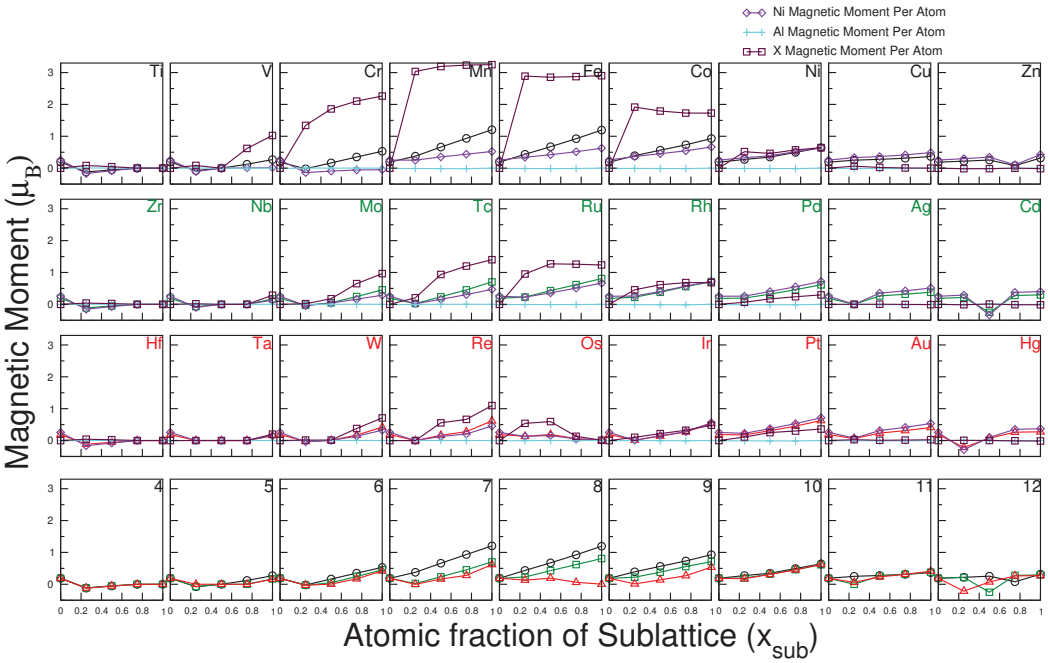

Figure 8.16: The total magnetic moment per atom in addition to the average magnetic moment per atom of the nickel, aluminium and X atoms of the coarse compositional data for the second sublattice of the γ' phase. Standard colour scheme in use for total magnetic moment of each system.

It is noted that magnetism is far more significant in the second sublattice as opposed to the first with a lot more alloys displaying significant magnetism. These alloys are typically concentrated toward the centre of the transition metal series with groups 7, 8 and 9 displaying the most magnetism. Again Al exhibits no significant magnetism in any alloy and frequently develops small magnetic moments in the opposite direction to Ni and X. Ni is found to develop magnetism of higher moments in many cases then that of the first sublattice alloys. One key difference between the datasets of the first and second sublattices is that in the case of X=Cr significant magnetism is observed across the whole of the compositional range. Another notable difference is that despite the

enhanced magnetism in the 4d and 5d series there appear no disruption the the lattice parameters unlike in the 3d series as can be seen in figure 8.6. This data is also presented as a dependence with d-band filling in figures 8.17-8.20.

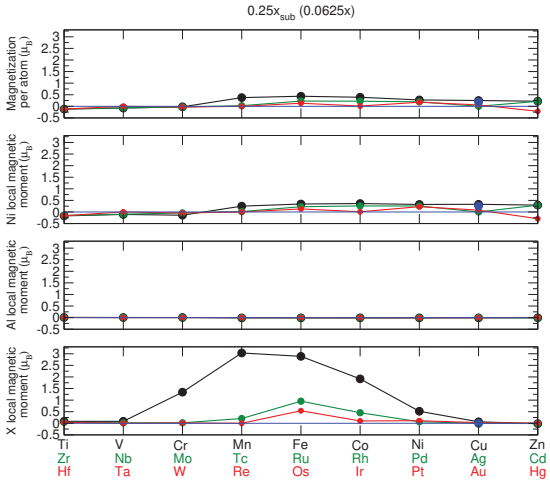

Figure 8.17: The total magnetic moment per atom in addition to the average magnetic moment per atom of the nickel, aluminium and X atoms of the coarse compositional data for the second sublattice of the γ' phase. Expressed as a dependence with d-band filling for the composition $0.25x_{sub}$. Blue lines represent zero magnetic moment.

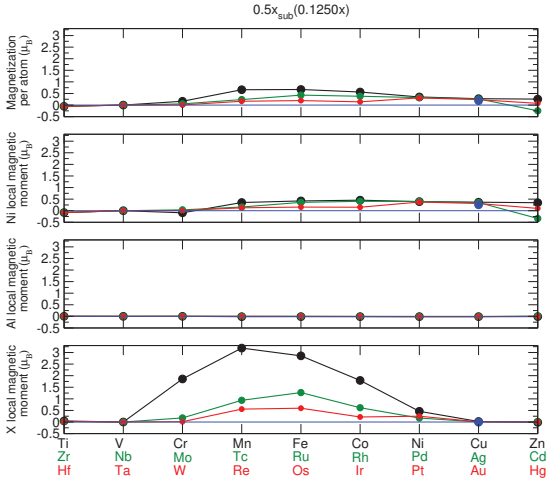

Figure 8.18: The total magnetic moment per atom in addition to the average magnetic moment per atom of the nickel, aluminium and X atoms of the coarse compositional data for the second sublattice of the γ' phase. Expressed as a dependence with d-band filling for the composition $0.5x_{sub}$. Blue lines represent zero magnetic moment.

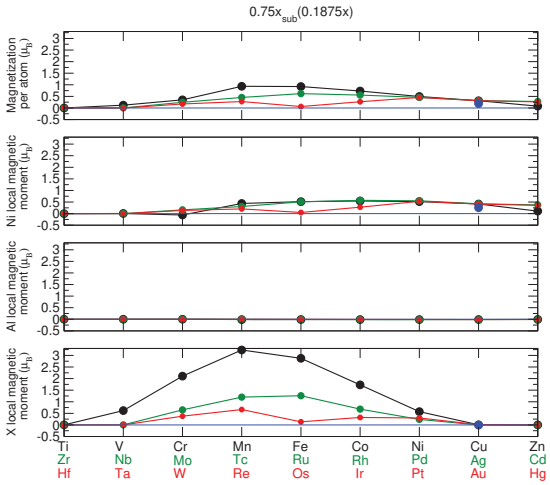

Figure 8.19: The total magnetic moment per atom in addition to the average magnetic moment per atom of the nickel, aluminium and X atoms of the coarse compositional data for the second sublattice of the γ' phase. Expressed as a dependence with d-band filling for the composition $0.75x_{sub}$. Blue lines represent zero magnetic moment.

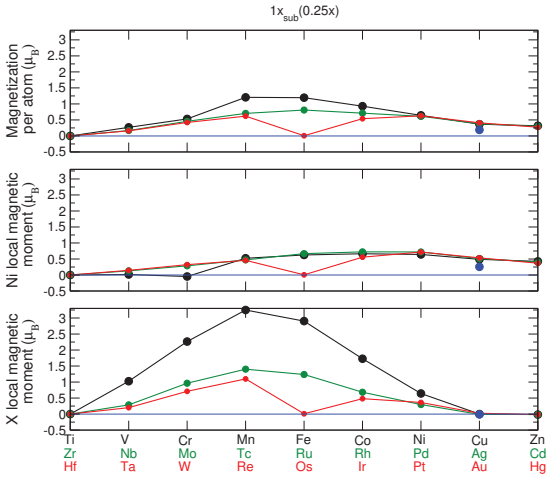

Figure 8.20: The total magnetic moment per atom in addition to the average magnetic moment per atom of the nickel and X atoms of the coarse compositional data for the second sublattice of the γ' phase. Expressed as a dependence with d-band filling for the composition $1x_{sub}$. Blue lines represent zero magnetic moment.

8.4 Formation Enthalpies

8.4.1 First Sublattice

Coarse Compositions

The formation enthalpies are displayed in figure 8.21. In general the formation energy increases in a linear or slightly curved fashion as the composition is increased (the exceptions being compounds involving Rh, Pd, Pt). It is to be noted in the cases of Mn, Fe and Co magnetism has a significant stabilizing effect on the pseudo-binary alloys. An important observation comes from that it is very rare for the formation enthalpies to ever exceed $0\,kJ/mol.atom$ hence completely destabilizing the pseudo-binary alloy. Another key observation is that replacing Ni with an element from the same period (Pd and Pt)

results in a significant reduction on the formation enthalpy providing some degree of validation as to why these elements segregate to the Ni sublattice. The largest increases occur close to the centre of the transition metal series with the majority (6 out of 8 the remainder being Zn and Cd from the group 12) of elements that cross the 0 line being from groups 7, 8 and 9 of the periodic table.

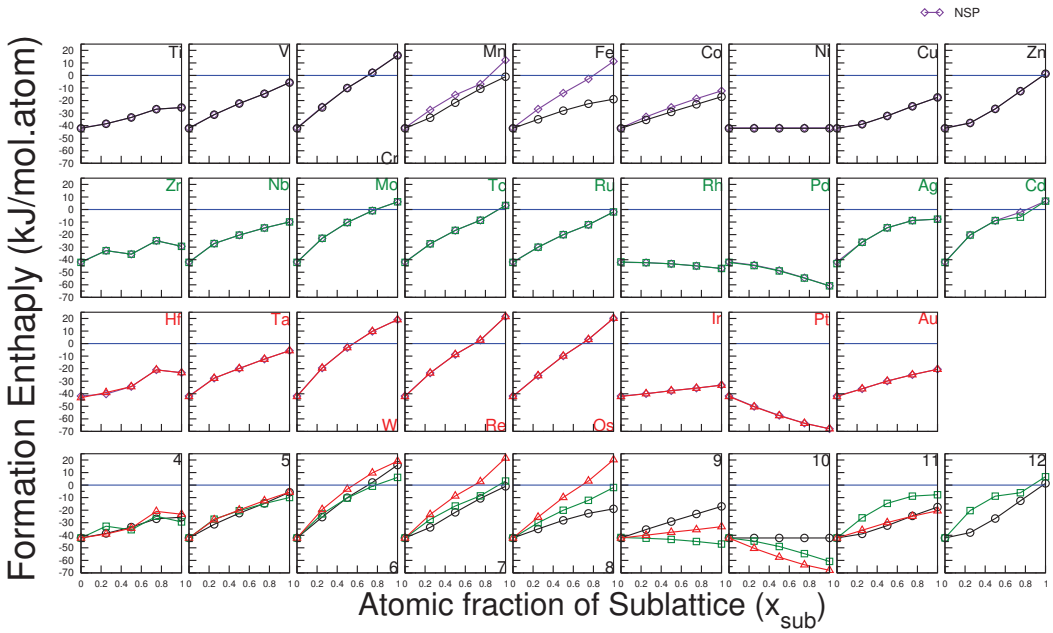

Figure 8.21: The formation enthalpy in both the spin-polarised and non spin-polarised implementation of the coarse compositional data for the first sublattice of the γ' phase. Standard colour scheme in use for the spin-polarised formation enthalpy of each system. Blue lines represent zero formation enthalpy.

Figure 8.22 is the same data except displayed as a dependence with d-band filling, there does not appear to be a large number of profound statements that can be made based on this other than that groups 6, 7, 8 11 and 12 are generally high and periods 4, 5, 9 and 10 are generally low. Another observation is that similarly to the lattice

parameter the range of the formation enthalpies increases with composition.

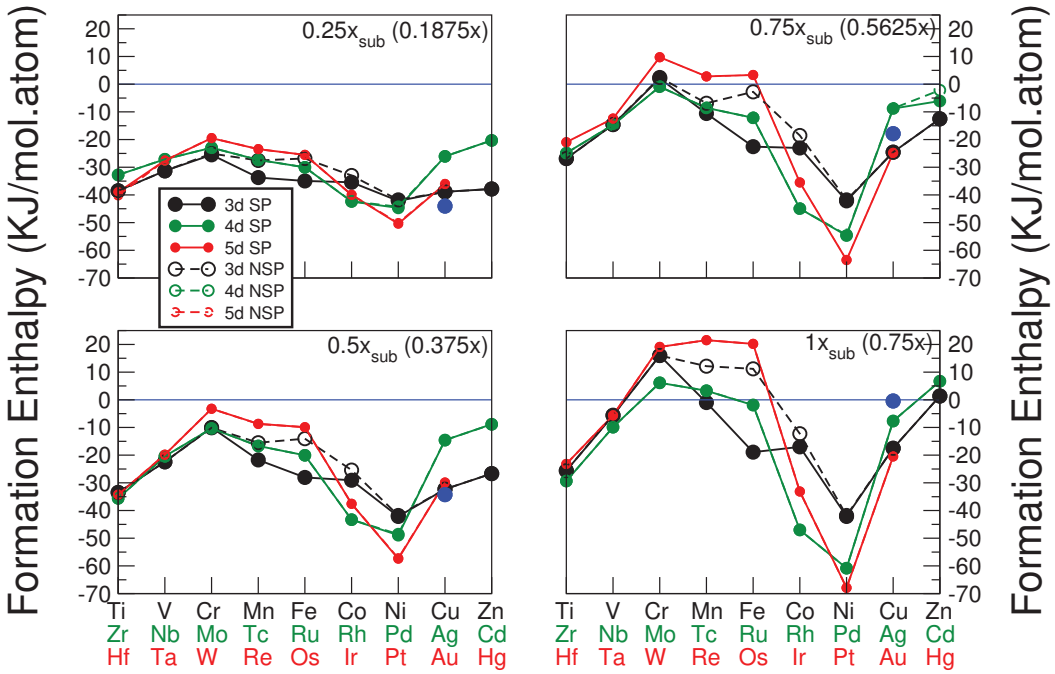

Figure 8.22: The formation enthalpy in both the spin-polarised and non spin-polarised implementation of the coarse compositional data for the first sublattice of the γ' phase. This time expressed as a dependence with d-band filling. Blue lines represent zero formation enthalpy.

8.4.2 Second Sublattice

Coarse Compositions

Many of the observations remain similar between the two data sets. For the elements in the centre of the 3d series magnetism provides significant stabilisation of the alloy, but has very small impact elsewhere. Again the relationship of formation enthalpy with composition is linear or slightly curved in all cases. In this data set however crossing the zero line is a lot more common with 15 elements crossing as opposed to 8 in the dataset

for the first sublattice.

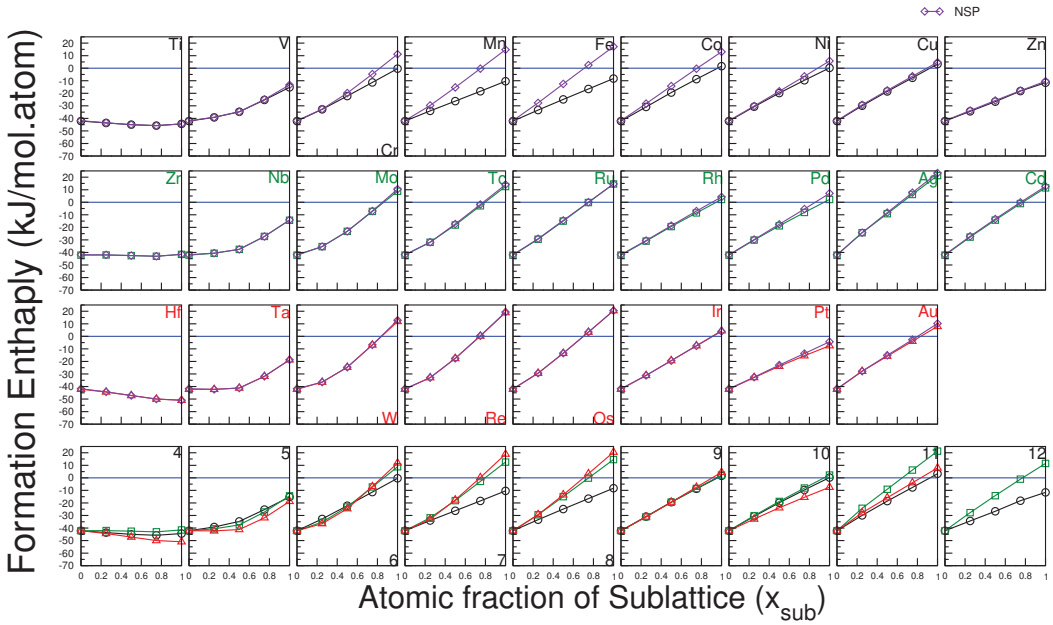

Figure 8.23: The formation enthalpy in both the spin-polarised and non spin-polarised implementation, of the coarse compositional data for the second sublattice of the γ' phase. Standard colour scheme in use for the spin-polarised formation enthalpy of each system. Blue lines represent zero formation enthalpy.

The same data expressed as a dependence on d-band filling is expressed in figure 8.24 and like in the first sublattice data from groups 6, 7, 8, 11 and 12 are generally high and 4, 5, 9 and 10 are generally low, meaning the pattern remains similar. Also the range of the formation enthalpies increases with composition.

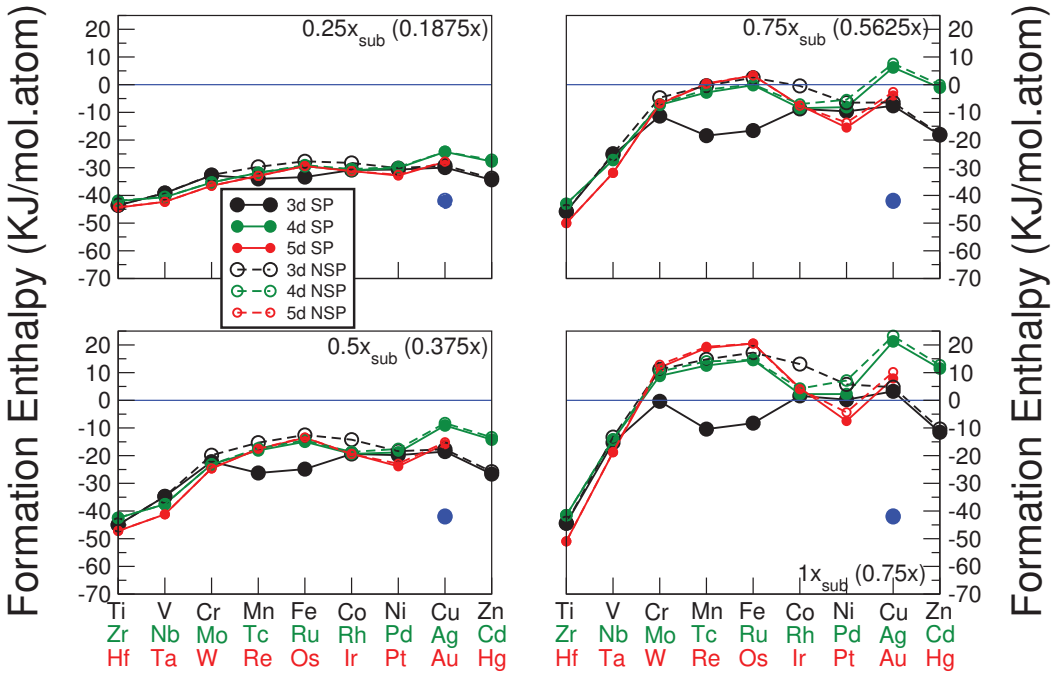

Figure 8.24: The formation enthalpy in both the spin-polarised and non spin-polarised implementation of the coarse compositional data for the second sublattice of the γ' phase. This time expressed as a dependence on d-band filling. Blue lines represent zero formation enthalpy.

The observations from both the datasets for the first and second sublattice reveal that formation enthaplies are overall "well behaved" in that they do not fluctuate wildly with composition, this validates the observations of chapter 7 where it was assumed that if an element strongly stabilises γ' at 100% composition of the sublattice it will stabilise it at significantly smaller compositions. For the γ phase however this is not true as the relationship of formation enthalpy with composition is heavily curved and changes gradient sign in a large amout of cases. Unfortunately data for finer compositions in Co-based alloys for the $Co_3(Al_{1-2x}W_{1-2x}X_x)$ alloy system were not able to be taken

as a part of this research (due to the exceptionally large computational expense), for the purpose of explicitly verifying the claims made in chapter 7 about which elements stabilise the γ' phase in Co-based alloys.

8.5 SISF Energies

8.5.1 First Sublattice

Coarse Compositions

The SISF energies of the various alloys are displayed in figure 8.25. four sets of data are represented in this figure as can be seen, there is a significant difference the internally static and internally relaxed data. The internally static calculations yield significantly higher SISF energies then the internally relaxed calculations, this reveals that the assumption that the default atomic positions in the $D0_{19}$ supercell sufficiently approximate those of the relaxed calculations is largely false. Hence attempting to reduce the computational expense of such DFT calculations through such means is inappropriate and compromises accuracy significantly. Further discussion of this dataset will concern only the data with internal relaxation as this data is the most accurate, and most relevent to comparisons between other simulation data and experiments. It can be seen that except for the following elements Ti, Mn, Fe, Cd and Hf magnetism has no significant impact on the SISF formation energy. Similarly to the lattice parameters of the alloys for this dataset the 4d and 5d series are found to behave very similarly. The same data except expressed as a dependence with d-band filling is displayed in figure 8.26.

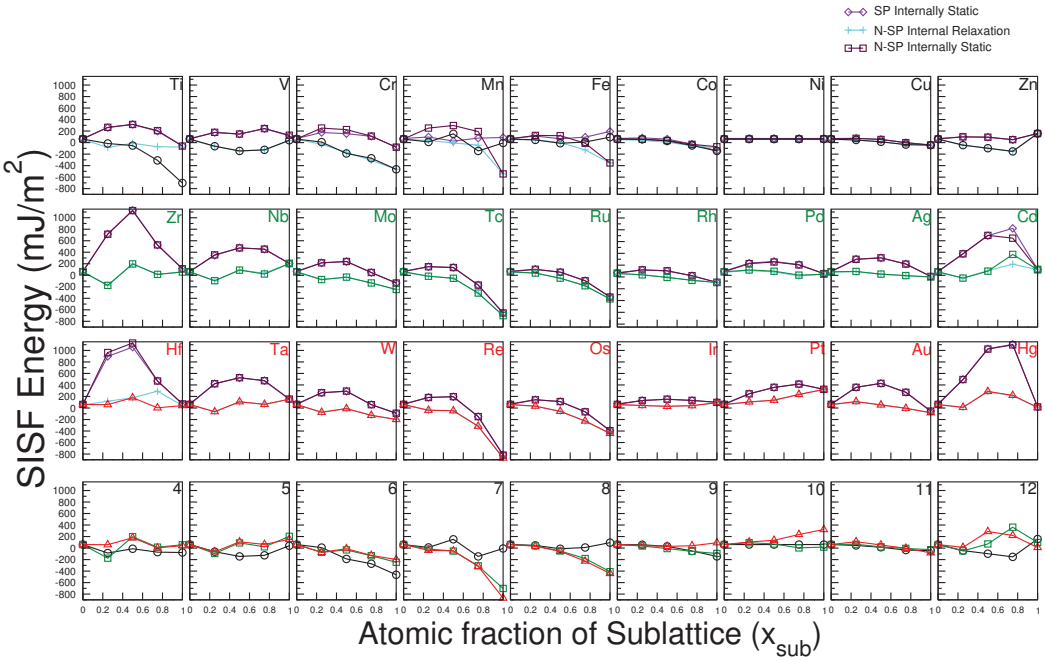

Figure 8.25: The SISF formation energy in both the spin-polarised and non spin-polarised implementation of the coarse compositional data for the first sublattice of the γ' phase. Standard colour scheme in use for the spin-polarised internal relaxation data of each system. Included also is the IS and IR implementation for the $D0_{19}$ sublattice.

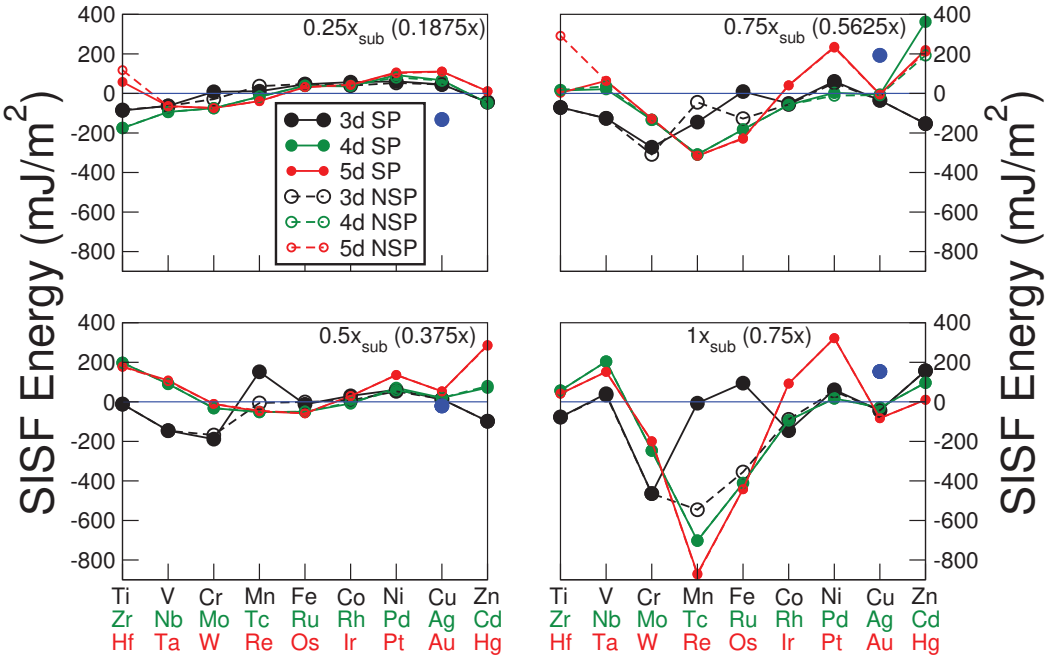

Figure 8.26: The SISF formation energy in both the spin-polarised and non spin-polarised implementation of the coarse compositional data for the first sublattice of the γ' phase, this time expressed as a function of d-band filling. In this graph only the IR data is featured. Blue lines represent a SISF formation energy of $0\,mJ/m^2$.

It is important to also investigate if there exists a dependence on SISF energy with lattice parameter, for this purpose a scatter graph of the spin-polarised data is plotted in figure 8.27. The rationale behind the plotting of the graphs is as follows, it is predicted that there will be a correlation between the change in lattice parameter from that of the host lattice and the scale of changes in said host lattice, hence the potential for a correlation between lattice parameter and SISF energy. As can be seen from this graph there is no correlation between the two variables and the data becomes closer to a random spread the greater the composition. Also the same graph was plotted

for the non spin-polarised data in figure 8.28 and again no significant correlation is observed (note in the SP and NSP IS datasets there appears a weak correlation at lower compositions). Another important assessment to make is as to whether the room temperature native stacking sequence of the solute impacts the SISF energy. The change in SISF energy from adding in x_{sub}=0.25 of the solute elements of the FCC, HCP and BCC stacking sequences is as follows -14.927(-8.979 NSP), -83.491(-70.982 NSP) and -106.022(-103.505 NSP) respectively. The observations from the SP data and NSP are mostly as expected with the averages for BCC and HCP being strongly negative (though HCP would be expected to be the most negative) this suggests that the native room temperature stacking sequence of the solute has some degree of impact on the SISF energy but is far from being the most significant factor in the discussion.

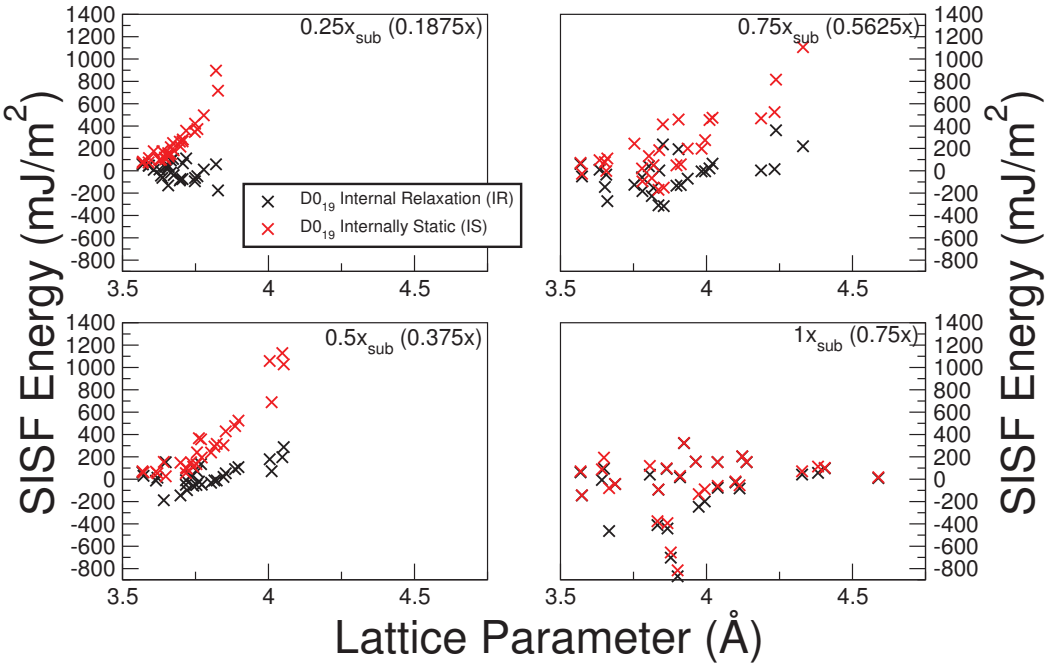

Figure 8.27: Scatter graphs of the SISF formation energy vs the lattice parameter for both the IR and IS implementations of the spin-polarised coarse compositional data in the first sublattice of the γ' phase.

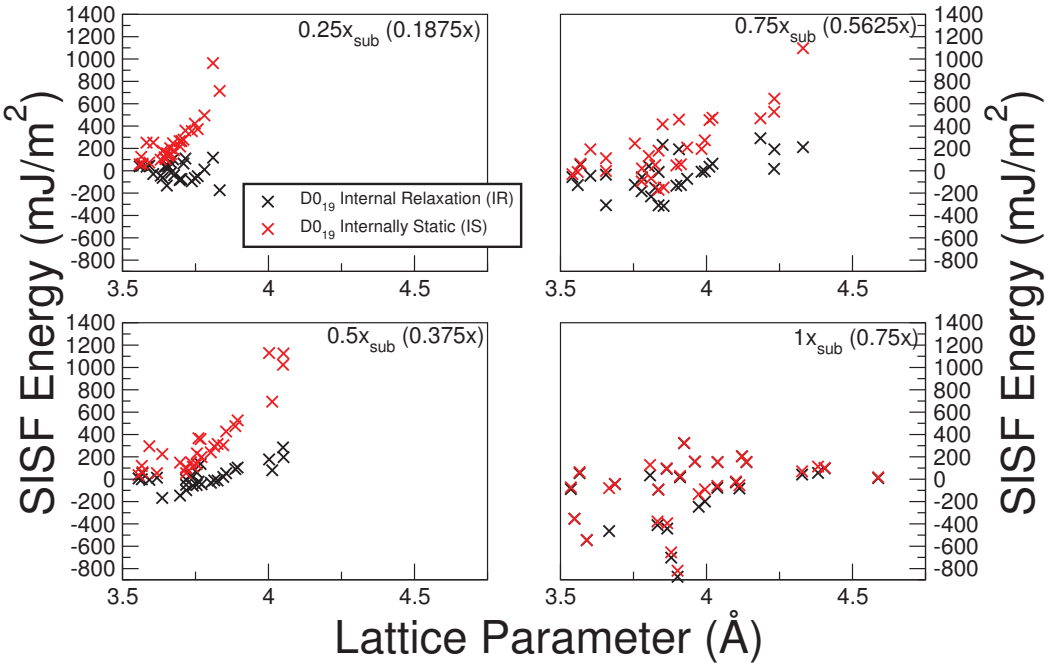

Figure 8.28: Scatter graphs of the SISF formation energy vs the lattice parameter for both the IR and IS implementations of the non spin-polarised coarse compositional data in the first sublattice of the γ' phase.

Fine Compositions

The data for the SISF energies for the fine compositions are expressed in figure 8.29.

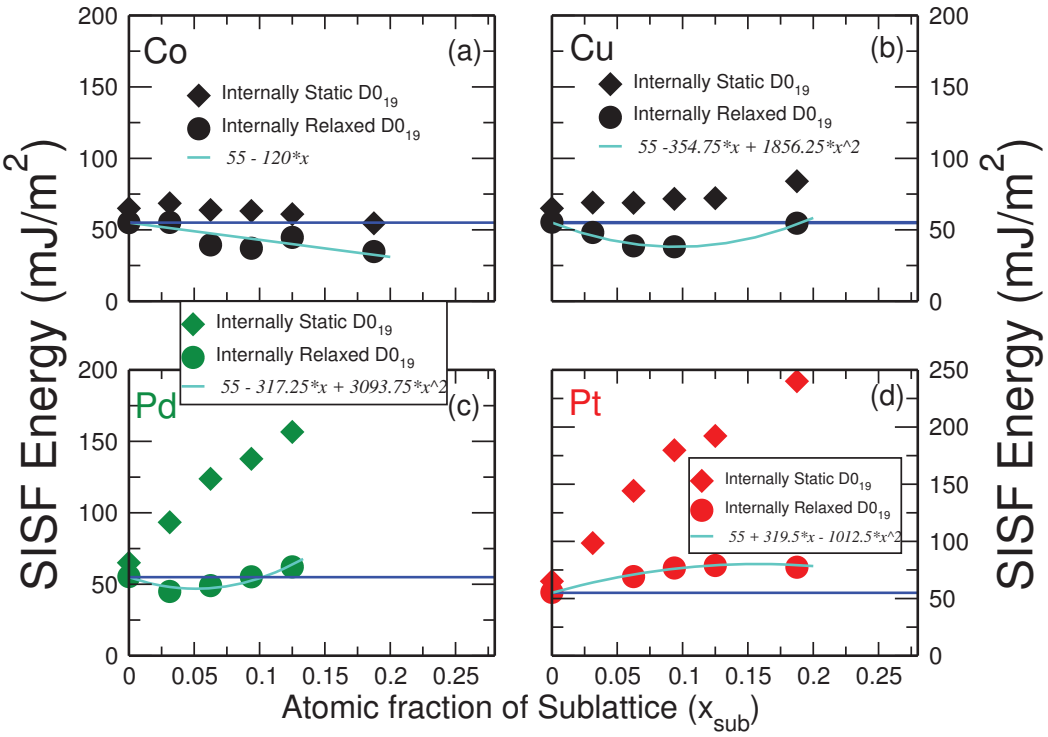

Figure 8.29: The SISF energy data for the fine compositions of the elements found to partition to the first sublattice of the γ' phase for the spin-polarised implementation. The blue lines represent the SISF formation energy of Ni_3Al. Turquoise lines represent fits to the IR data.

Again the same observation regarding the magnitudes of the results from the two datasets (relaxed and static) made for the coarse compositions set holds true here also. Fits are also made to the set of data which features relaxation for the atomic positions in the $D0_{19}$ phase.

8.5.2 Second Sublattice

Coarse Compositions

The data for all of the systems in the second sublattice is displayed in figure 8.30.

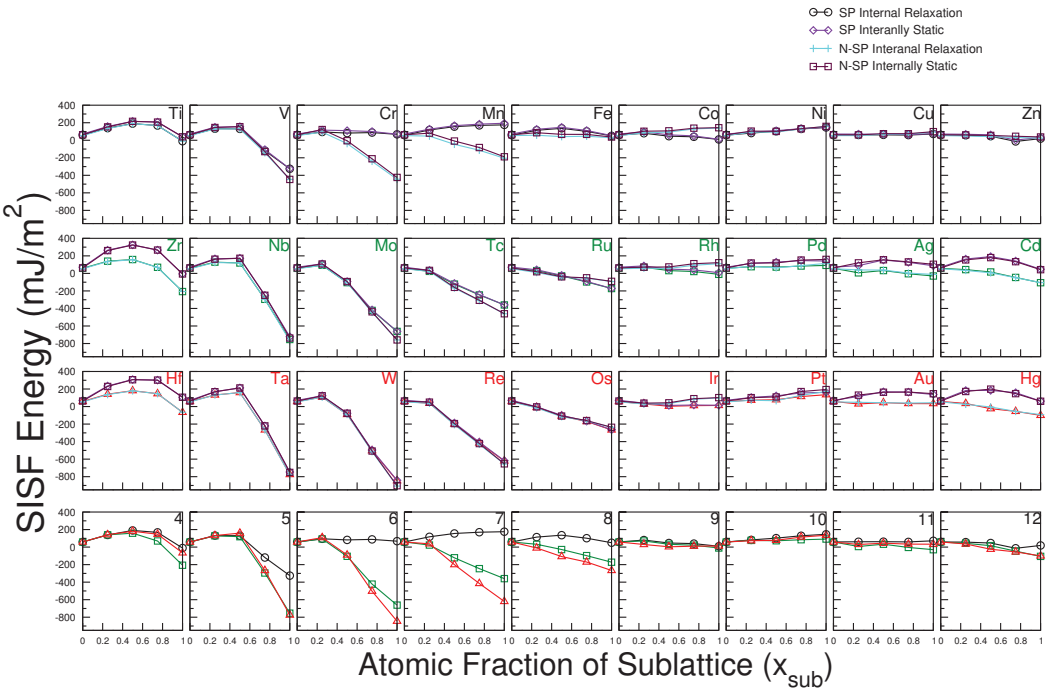

Figure 8.30: The SISF formation energy in both the spin-polarised and non spin-polarised implementation of the coarse compositional data for the second sublattice of the γ' phase. Standard colour scheme in use for the spin-polarised internal relaxation data of each system. Included also is the IS and IR implementations for the $D0_{19}$ sublattice.

Again the IR data set is significantly lower in a large number of cases then the IS data set meaning that the previous observations made about these data sets in the preceding sections remain relevant for this data set. It is important to observe however that the difference between the IR and IS datasets is not nearly as large in this sublattice relative to the first sublattice. This is simply due to the observation that the larger the increase

in lattice parameter from the base alloy (Ni_3Al-γ') the more significant the role of atomic relaxations. As in this case we are substituting on a minority sublattice hence the scope for the change in lattice parameter is reduced. Again the 4d and 5d series elements produce alloys which behave in a similar manner. The same data except expressed as a function of d-band filling is represented in figure 8.31.

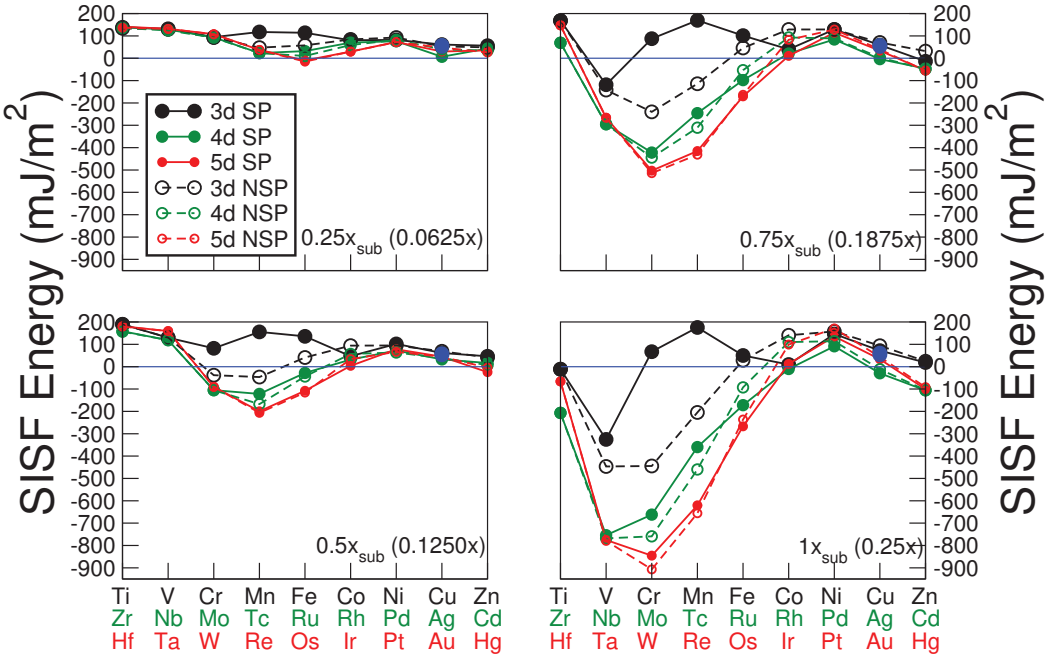

Figure 8.31: The SISF formation energy in both the spin-polarised and non spin-polarised implementation of the coarse compositional data for the second sublattice of the γ' phase, this time expressed as a function of d-band filling. In this graph only the IR data is featured. Blue lines represent a SISF formation energy of $0\,mJ/m^2$.

In this data inclusion of spin-polarisation produces large changes in the fault energies for x=Cr, Mn, Fe and Co, this corresponds to the large magnetic moments documented in section 8.3.2. Again a check was made to see if there is significant correlation between the

SISF energy and the lattice parameter by the plotting of scatter graphs. The reasoning behind the plotting of said graphs, was that the bigger the lattice parameter the greater the change of the host lattice, hence there exists the potential of a correlation between the two variables of lattice parameter and SISF energy. As can be seen from figures 8.32 and 8.33 there exists no significant correlation between these two factors. This data also progresses more to a random spread the greater the composition of the alloying element.

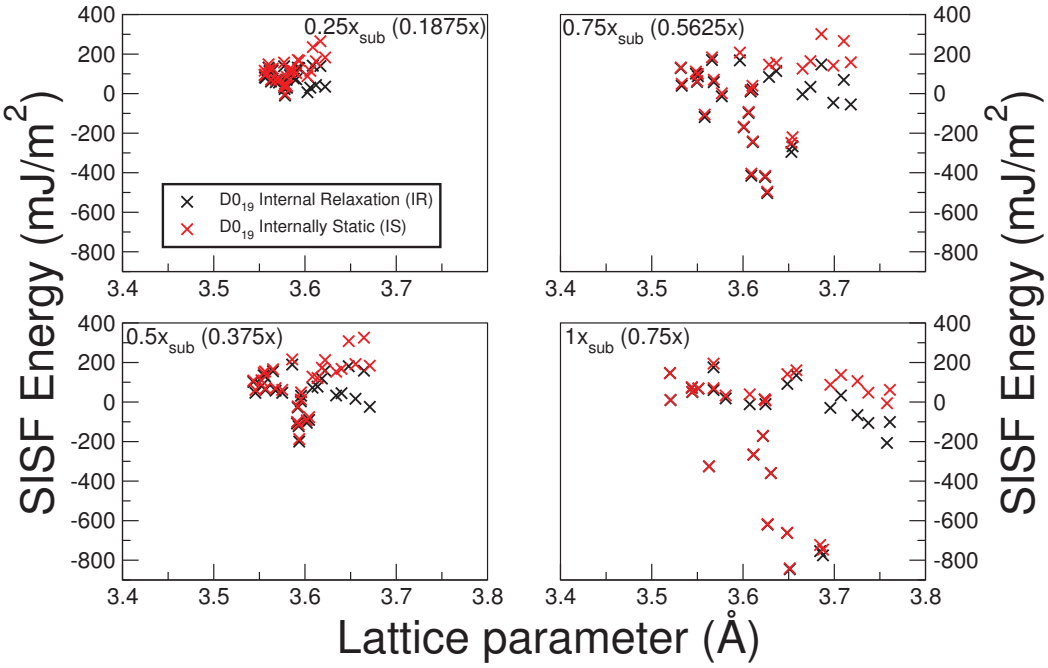

Figure 8.32: Scatter graphs of the SISF formation energy vs the lattice parameter for both the IR and IS implementations of the spin-polarised coarse compositional data in the second sublattice of the γ' phase. Compositions are given in the from of x_{sub}, x given in brackets.

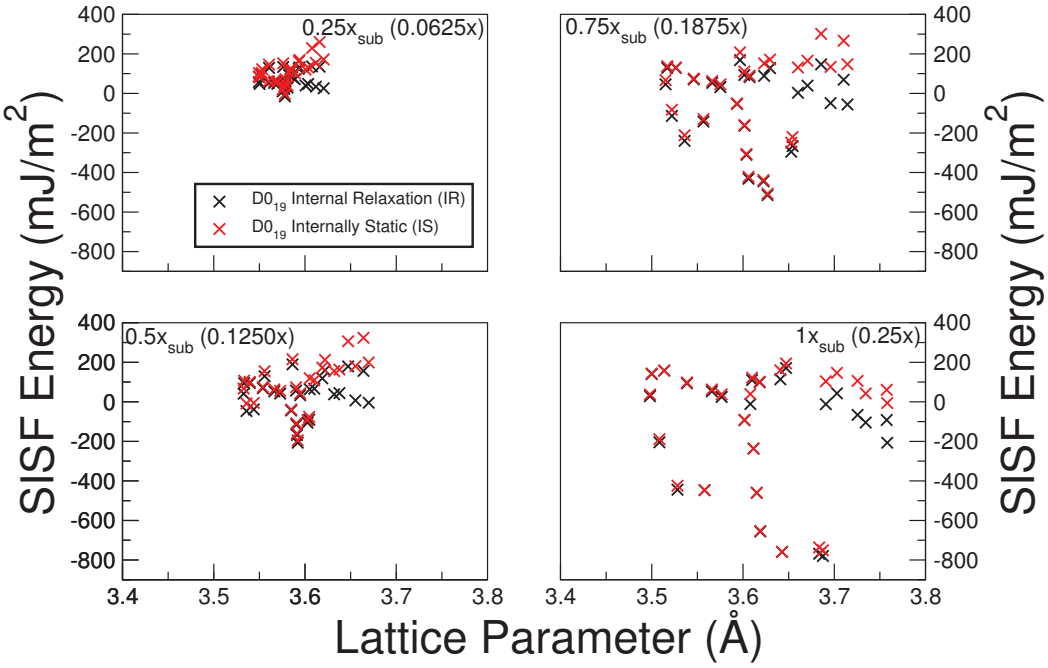

Figure 8.33: Scatter graphs of the SISF formation energy vs the lattice parameter for both the IR and IS implementations of the non spin-polarised coarse compositional data in the second sublattice of the γ' phase. Compositions are given in the from of x_{sub}, x given in brackets.

It was also important to test the dependence of the native room temperature stacking sequence on the SISF energy, the average change in the SISF energy from introducing FCC, BCC and HCP elements at x_{sub}=0.25 is -4.383(6.455 NSP), 56.508(51.879 NSP) and 10.198(9.760 NSP) respectively. In the case of the spin-polarised data the normal expectation is not met with FCC elements having on average a decrease whilst BCC elements result in a large increse in the SISF energy, with the HCP elements in between. In the case of non spin-polarised data all on average result in increases however again the natural expectation is not met. This provides evidence that in the case of this system

the native room temperature stacking sequence of the alloying element has little impact relative to the other factors.

Fine Compositions

The data for the full set of elements for the fine compositions is presented in figure 8.34.

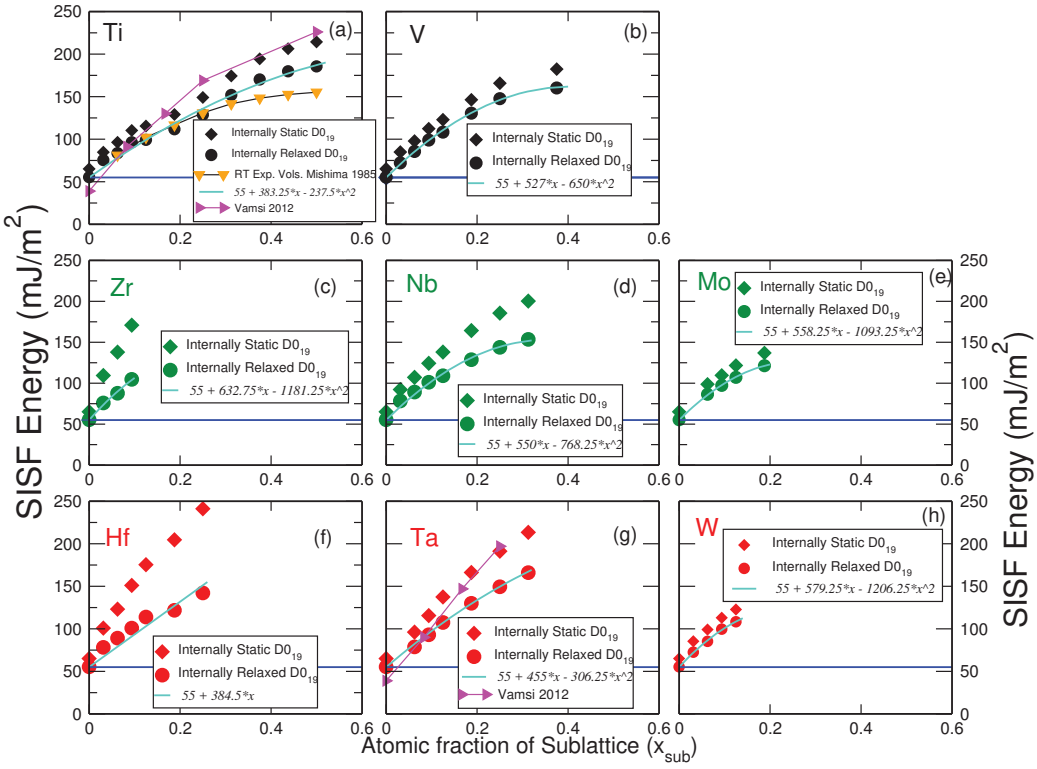

Figure 8.34: The SISF energy data for the fine compositions of the elements found to partition to the second sublattice of the γ' phase for the spin-polarised implementation. The blue lines represent the SISF formation energy of Ni_3Al. Turquoise lines represent fits to the IR data. Comparison to the the simulation data of Vamsi[95] and where results are calculated by plugging experimental data of Mishima[55] into simulation are also made.

Again the same observations previously made about the difference between the IR

and IS results applies for this data set also. Unfortunately the same with the fine compositions first sublattice data there is no direct experimental evidence to compare with for the property of the SISF energy. The data of Vamsi[95] empolyed the supercell approach, and also ensured that the composition in the bulk and fault region were identical. In the case of both X = Ti and Ta the composition dependence trend is consistent with the results of Vamsi[95]. This observation validates the assertion that the AIM models form an suitable approximation to the supercell approach. For X=Ti experimental values of the lattice parameter were used to calculate the SISF energy using first-principles (in the same vein to the data in chapter 6), these results unsurprisingly agree largely with the dependence of the calculations purely from first-principles.

8.5.3 Both Sublattices

Fine Compositions

The SISF energy data for the elements modelled as partitioning evenly between the two sublattices are displayed in figure 8.35.

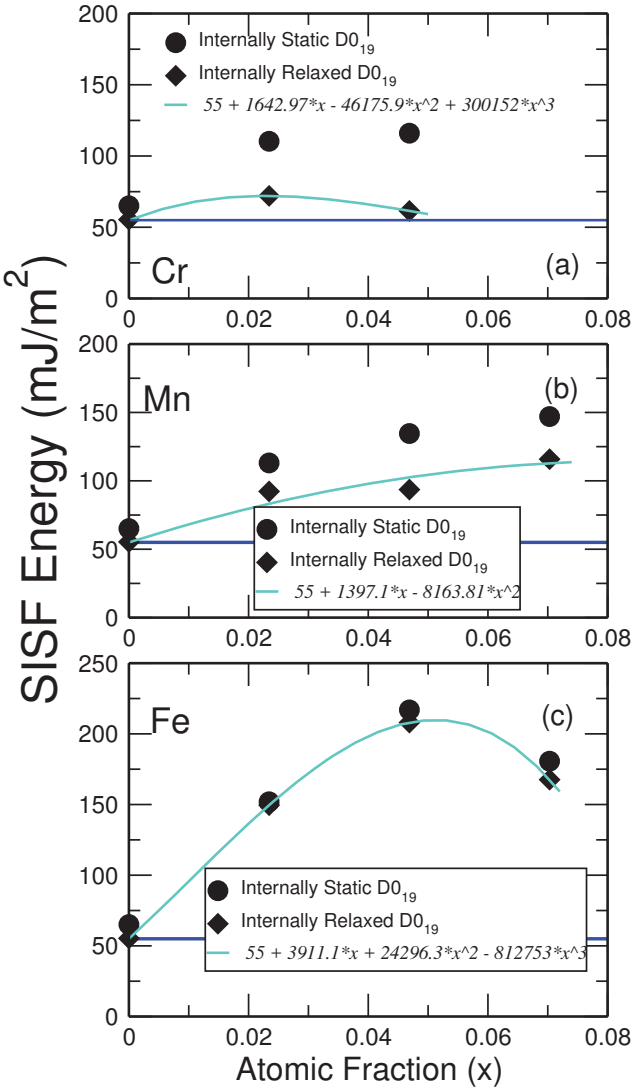

Figure 8.35: The SISF energy data for the fine compositions of the elements found to partition to the second sublattice of the γ' phase for the spin-polarised implementation. The blue lines represent the SISF formation energy of Ni_3Al. Turquoise lines represent fits to the IR data.

As can be seen form the data for where Cr and Fe are used as alloying additions the relationship is strongly curved whereas in the case of Mn it is a lot straighter. In the case of Cr the decline takes the SISF energy almost back to what it was at x=0. Iron is

significant as it produces the largest increase of any of the elements investigated for the fine compositional systems. This means that it has the largest scope for the frustration of shearing in the primary creep regime for single-crystal alloys[145]. Another point of note is that the two datasets IR and IS generate very similar results in this instance.

8.6 High-Temperature Calculations

8.6.1 First Sublattice

Fine Compositions

The dependence of the SISF formation energy on temperature for the 4 calculated alloys is displayed in figures 8.36-39. Unfortunately such data is limited to these 4 alloys and there exists no data for dilute compositions within the second sublattice. This is due to the large computational expense of such calculations (especially in the second sublattice where supercells for dilute compositions are even larger), however for the calculations in this subsection there is a large array of different approximations presented. Assessing first the results for the fixed atomic positions. In all cases irrespective of whether the calculations are spin-polarised or not a decline with temperature was observed between 0-1400 K(0-700 K in the case of the spin-polarised result for 0.06173 x_{sub}). Note this decline can be incredibly subtle for example where X=Co at x_{sub}=0.12346 the decline is only 6.194 mJ/m^2 over a temperature range of 1400 K. However in the cases of X= Pd or Pt the declines can be more substantial especially as the composition is increased for example in the case of where X=Pt the decline reaches 70.587 mJ/m^2 over 1400

K at x_{sub} = 0.24690. While this decline and the others in the alloy systems X=Pt and Pd are large it is important to remember that they are not large enough to make the SISF energies negative or even close to zero. These large declines may initially seem discouraging for the prospect of calculations of fault energies by first-principles techniques as it appears that the 0 K SISF energies do not successfully approximate the SISF energies at operational temperatures.

However in the case of the results with the atomic positions of the $D0_{19}$ phase relaxed these large declines cease to exist (for example the decline in the case of X=Pt at x_{sub}=0.24690 is 20.662 mJ/m^2 in this dataset). Another point of note was partially established previously in this chapter but can now be further elaborated on. That is the observation that the energies in general are significantly reduced when local atomic relaxations are factored in. However a nuance not previously established is that the relative increase in the lattice parameter plays heavily into the scale of this decline with temperature. Such that the larger the expansion of the lattice parameter relative to unalloyed γ' the more significant the role of local atomic relaxations becomes. Hence the large declines when Pt and Pd are used as alloying additions relative to when relative to Co and Cu are utilised. This again emphasised the importance of ensuring good practice by relaxing the atomic positions in the $D0_{19}$ phase. These results are very encouraging to the prospect of using first-principles calculations which are traditionally active at 0 K to determine the SISF energies of high temperature superalloys due to the fact that the 0 K SISF energy accurately approximates the operational temperature SISF energy. For example the average decline (which includes both SP and NSP data) is 9.272 mJ/m^2.

Another relevant nuance to the situation is that magnetism seems to make the scale of the decay slightly smaller in all of the cases where data is available for the IR data. Preliminary evidence also suggests that the higher the composition of the solute the greater the deviation between the 0 K SISF energy and the experimental reality. This can be seen in figure 8.34(a) where as the Ti composition is increased so does the difference between the first-principles results and results which use the experimental values of lattice parameter as an input. The difference a the maximum studied composition x_{sub}=0.5 is approximately $30\,mJ/m^2$ whereas at lower compositions for example the difference is very minimal.

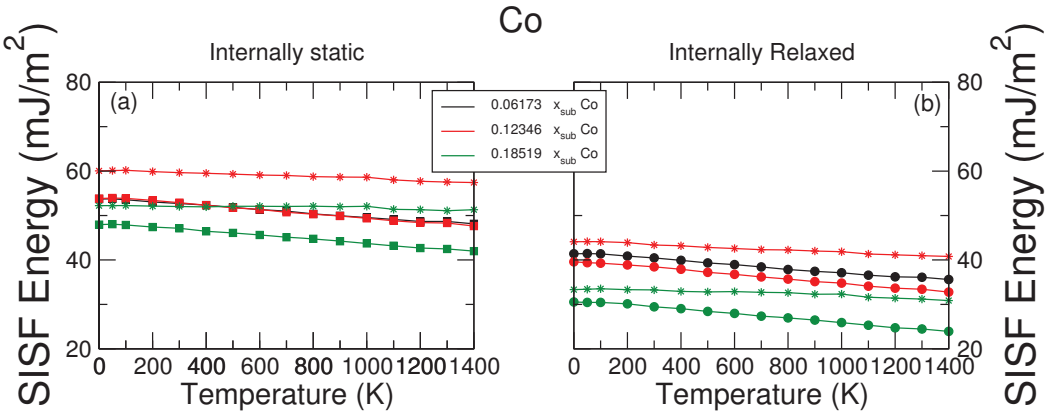

Figure 8.36: The relationship between the SISF energy and the temperature for both the IR (a) and IS (b) data in the spin-polarised and non spin-polarised implementations for where Co is used as an alloying element in the first sublattice of γ' for fine compositions. Stars represent spin-polarised data. Finite temperature results conducted using first-principles in conjunction with the quasiharmonic Debye model and the quasistatic approach.

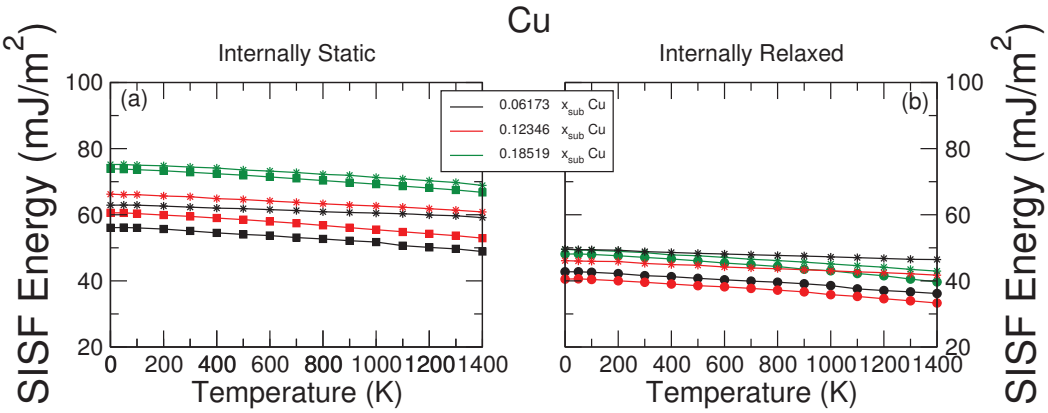

Figure 8.37: The relationship between the SISF energy and the temperature for both the IR (a) and IS (b) data in the spin-polarised and non spin-polarised implementations for where Cu is used as an alloying element in the first sublattice of γ' for fine compositions. Stars represent spin-polarised data. Finite temperature results conducted using first-principles in conjunction with the quasiharmonic Debye model and the quasistatic approach.

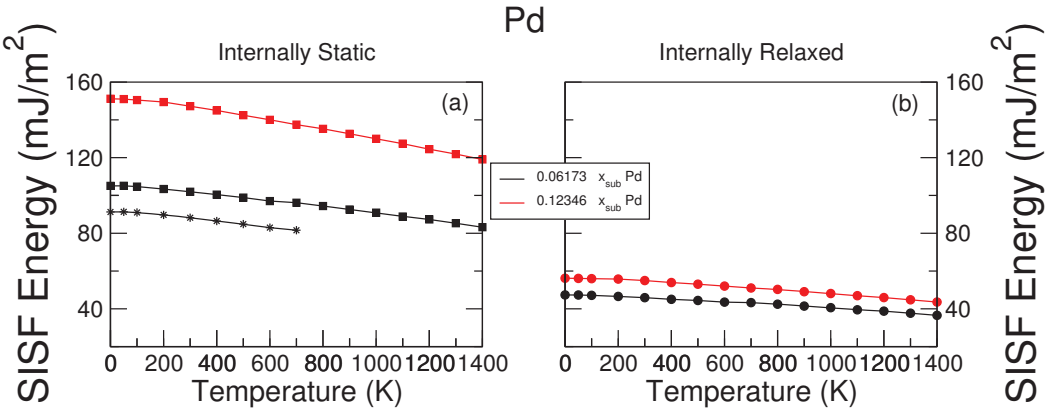

Figure 8.38: The relationship between the SISF energy and the temperature for both the IR (a) and IS (b) data in the spin-polarised and non spin-polarised implementations for where Pd is used as an alloying element in the first sublattice of γ' for fine compositions. Stars represent spin-polarised data. Finite temperature results conducted using first-principles in conjunction with the quasiharmonic Debye model and the quasistatic approach.

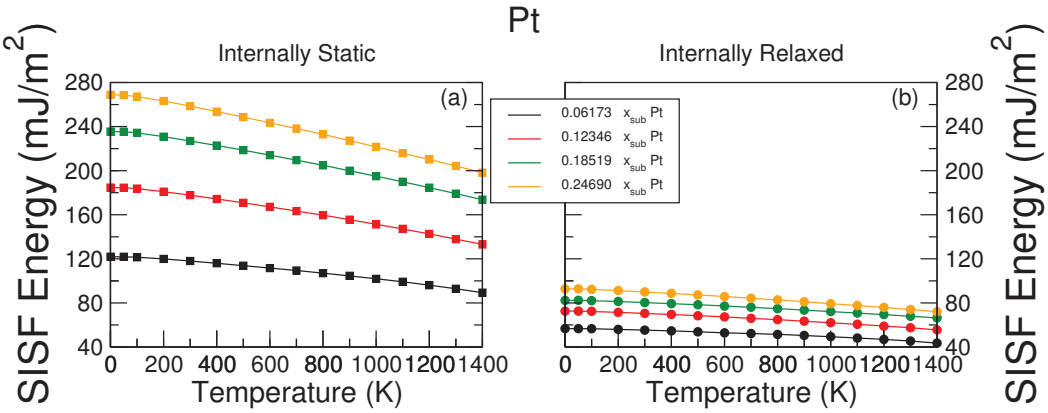

Figure 8.39: The relationship between the SISF energy and the temperature for both the IR (a) and IS (b) data in the non spin-polarised implementations for where Pt is used as an alloying element in the first sublattice of γ' for fine compositions. Stars represent spin-polarised data. Finite temperature results conducted using first-principles in conjunction with the quasiharmonic Debye model and the quasistatic approach.

Chapter 9

Discussion

9.1 Proposed Relationships for ISF and SISF formation energies, Formation Enthalpy and Misfit

Thus the main goal of this thesis can now be realised, the proposition of a predictive model for ISF and SISF energies, formation enthalpy, misfit and lattice parameter for proposed arbitrary alloy compositions. The first phase of this model is the use of the formation enthalpies to determine where in the alloy an element would be expected to segregate.

9.1.1 Formation Enthalpies and Segregation

A model of where the alloying elements in the γ' phase would be expected to segregate can be produced by analysing formation enthaplies at the lowest analysed composition for all alloy systems (atomic fraction of sublattice is x_{sub}=0.25). Linear interpolation

is performed between x_{sub}=0 and x_{sub}=0.25 and this is used to determine how much a change of x_{sub} will change the formation enthalpy of $L1_2$-Ni_3Al. This change is the V factor which are given for each alloy in table 9.1. Using these V factors the formation enthalpy of an arbitrary alloying composition can be approximated using the following equations.

$$H\gamma = 0 + \sum_i x_i V_i \tag{9.1}$$

$$H\gamma' = -42.13855 + \sum_i x_{subi} V_i \tag{9.2}$$

where x_i and x_{subi} are the atomic fraction of solute element i in the γ phase and the atomic fraction of i in the relevant sublattice in the γ' phase respectively. 0 and -42.13855 are the formation enthalpy of γ-Ni and $L1_2$-Ni_3Al respectively. This model in terms of where elements in the γ' will segregate agrees well with experimental observations layed out in chapter 8. The only instance where this model disagrees is where X= Mo. Also note that this model cannot take into account the elements which partition equally between the two sublattices and implies that those that do would in fact segregate to the Ni sublattice.

Table 9.1: Model parameters (V) for the formation enthalpy in addition to the expected segregation. The expected segregation is derived by assessing which one of the 1^{st} sub. factor and 2^{nd} sub. factor is lowest. A value of 1 means the 1^{st} sub. factor is lower hence the element would be expected to segregate to the first sublattice. A value of 2 means the 2^{nd} sub. factor is lower hence the element would be expected to segregate to the second sublattice.

Element	1^{st} sub. factor	2^{nd} sub. factor	Expected Segregation	γ phase factor
Al	-7.542	0.000	1	-148.680
Ti	14.474	-5.900	2	-133.530
V	43.300	11.855	2	-66.277
Cr	66.525	37.560	1	17.696
Mn	33.650	32.484	1	-27.502
Fe	28.782	35.070	1	-28.062
Co	26.775	45.172	1	-2.331
Ni	0.000	45.892	1	0.000
Cu	13.038	48.769	1	11.358
Zn	17.136	31.084	1	-45.269
Zr	37.462	0.441	2	-90.213
Nb	60.001	6.025	2	-44.976
Mo	76.736	27.245	1	-7.328
Tc	59.170	41.230	1	26.971
Ru	48.464	50.759	1	41.981
Rh	-0.980	44.794	1	13.779
Pd	-10.187	48.120	1	17.338
Ag	64.218	71.546	1	94.837
Cd	87.327	57.651	1	64.160
Hf	12.620	-8.987	2	-124.773
Ta	58.191	-0.598	2	-94.104
W	90.621	22.486	2	-15.362
Re	74.699	36.693	2	11.258
Os	66.420	51.008	2	41.387
Ir	8.698	43.810	1	5.718
Pt	-33.166	37.232	1	-19.645
Au	24.297	57.071	1	50.773

9.1.2 Unconstrained Lattice Misfit

The lattice parameters of both of the phases γ' and γ of an arbitrary alloy can be expressed using the following equations

$$a_{\gamma'} = 3.5682 + \sum_i x_{subi} Y_i \tag{9.3}$$

$$a_{\gamma} = 3.5209 + \sum_i x_i Y_i \tag{9.4}$$

where 3.5682 and 3.5209 are the lattice parameters of unalloyed γ' and γ respectively, Y factors are found in table 9.2. The Y factors are derived for the γ' phase by taking the lowest studied composition in each scenario (x_{sub}=0.25) and linearly interpolating back to x_{sub}=0 to get the gradient of a line between the two points. In the case of the γ phase the factors are the gradients of linear fits from between the points x=0 and x=0.25. This allows one who has the composition of each phase and where the elements segregate to, to compute the unconstrained lattice misfit by equation (9.5).

$$\sigma_{misfit} = 2 \cdot \left(\frac{a_{\gamma'} - a_{\gamma}}{a_{\gamma'} + a_{\gamma}} \right) \tag{9.5}$$

For five sample alloys with experimental composition measurements in each phase CMSX-10[297] (in the instance of dendrite region standard heat treatment), Waspaloy[298] (primary γ' detector 2), Inconel-939[299] (average atom probe data in the as heat treated material) (note very small amount of carbon and boron unaccounted for in the model), N18[300] (secondary γ') and René88 DT[301] (secondary γ') the lattice parameters of

both phases and misfit was calculated. In addition, the model of this thesis was compared to Vegard's law. The lattice parameters in the case of CMSX-10 are 3.592 Å (3.596 Å Vegard's law) for the γ' phase and 3.588 Å (3.554 Å Vegard's law) for the γ phase. For the alloy Waspaloy the lattice parameters are 3.603 Å (3.585 Å Vegard's law) and 3.573 Å (3.589 Å Vegard's law) for the γ' and γ phases respectively. For Inconel-939 the lattice parameter is 3.652 Å (3.611 Å Vegard's law) for the γ' phase and 3.558 Å (3.573 Å Vegard's law) for the γ phase. For N18 the lattice parameter is 3.760 Å (3.597 Å Vegard's law) for the γ' phase and 3.567 Å (3.598 Å Vegard's law) for the γ phase. Finally for René88 DT the lattice parameter is 3.740 Å (3.624 Å Vegard's law) for the γ' phase and 3.618 Å (3.642 Å Vegard's law) for the γ phase.

This results in the following misfits for CMSX-10 0.00129% (0.0119% Vegard's law), Waspaloy 0.00832% (-0.00117% Vegard's law), Inconel-939 0.0263% (0.0105% Vegard's law), N18 0.0526% (-0.000506% Vegard's law) and finally René88 DT 0.0332% (-0.00491% Vegard's law). The model of this thesis always produces a positive misfit whilst using Vegard's law results in a negative misfit in 3 out of the 5 alloys. Experimental results for the misfit for each of the alloys are as follows, -0.11% for CMSX-10[20], 0.209% for Waspaloy[302] (average of many results), 0.04% for Inconel-939[303], -0.00298% for N18[300] and 0.000752% for René88 DT[301]. For the experimetal results the order from highest to lowest is Waspaloy, Inconel-939, René88 DT, N18 and CMSX-10. Unfortunately for the available sample of alloys both of the models fail to produce anything close to this order, meaning that neither model seems to reproduce experimental data qualitatively or quantitatively. One important nuance to note that in actuality misfit

is dependent on a large array of factors, for example in another experimental condition the lattice misfit of Inconel-939 is -0.58% making it the lowest by far[303].

Finally it is necessary to ensure that extrapolation using the coarse compositional values accurately approximates the fine compositional values. Both sets are displayed for both the first and second sublattice in figure 9.1 and figure 9.2. As can be seen from these graphs there is negligible difference between the two datasets.

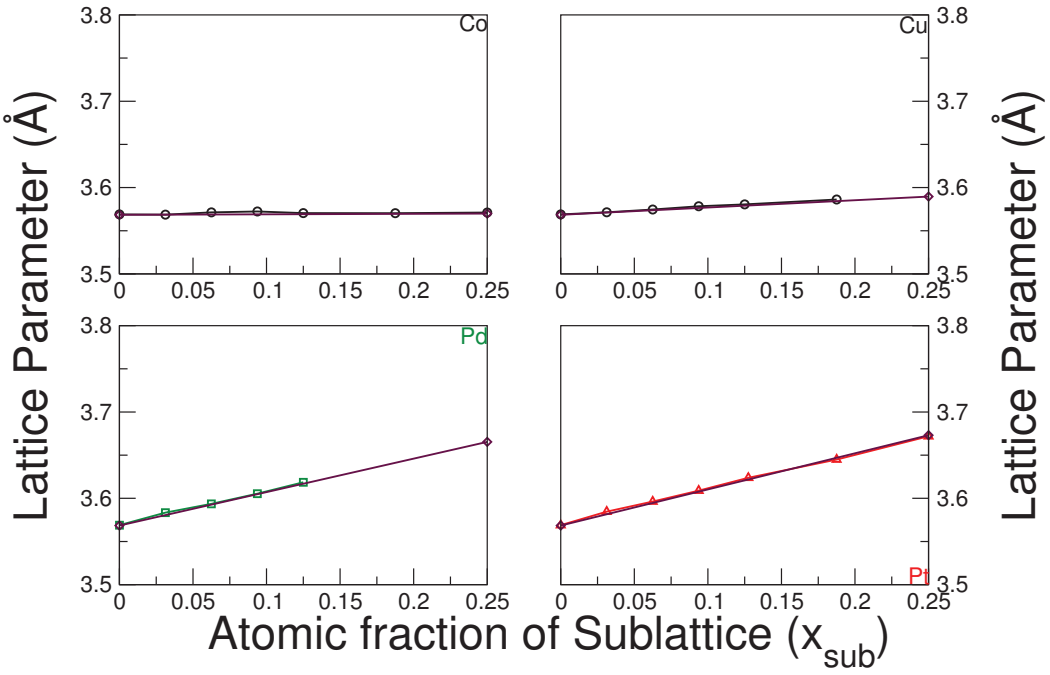

Figure 9.1: Comparison between the lattice parameters of the coarse and fine compositional data for the first sublattice of the γ' phase in the spin-polarised implementation. Standard colour scheme in use for the fine compositional data. Maroon lines in use for the course compostional data.

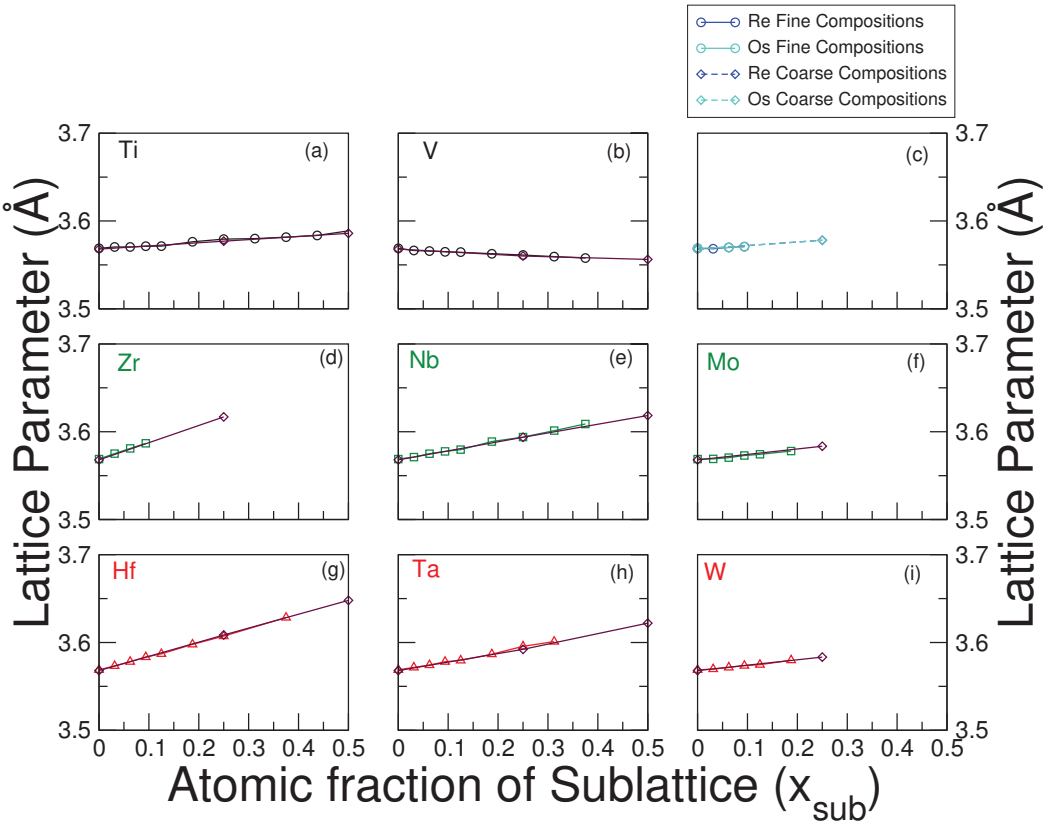

Figure 9.2: Comparison between the lattice parameters of the coarse and fine compositional data for the second sublattice of the γ' phase in the spin-polarised implementation. Standard colour scheme in use for the fine compositional data. Maroon lines in use for the course compostional data.

9.1.3 Fault Formation Energies

The SISF and ISF formation energies in the γ' and γ phases respectively can be expressed using the following equations.

$$\gamma_{SISF} = 59.4758 + \sum_i x_{subi} Z_i \tag{9.6}$$

Table 9.2: Model parameters for the lattice parameter (Y), note that for Vegard's law x as opposed to x_{sub} is used.

Element	1^{st} sub. factor	2^{nd} sub. factor	γ phase factor	Vegard γ'	Vegard γ
Al	0.352	0.000	0.260	-	-
Ti	0.512	0.036	0.475	0.252	0.422
V	0.272	-0.031	0.185	-0.059	0.163
Cr	0.154	-0.048	0.057	-0.001	0.109
Mn	0.233	-0.014	0.158	0.086	0.292
Fe	0.089	-0.028	0.104	-0.002	0.125
Co	0.005	-0.045	0.004	0.000	0.018
Ni	0.000	-0.048	0.000	0.000	-0.001
Cu	0.084	-0.021	0.095	-	0.080
Zn	0.253	0.014	0.243	-	-
Zr	1.035	0.196	1.161	0.707	0.965
Nb	0.718	0.103	0.745	0.440	0.666
Mo	0.520	0.062	0.474	0.188	0.449
Tc	0.390	0.039	0.370	0.156	0.423
Ru	0.317	0.037	0.342	0.129	0.333
Rh	0.308	0.048	0.408	0.303	0.400
Pd	0.388	0.079	0.518	0.453	0.470
Ag	0.553	0.139	0.716	-	0.540
Cd	0.752	0.176	0.910	-	-
Hf	1.007	0.162	1.034	0.778	1.033
Ta	0.720	0.097	0.711	0.512	0.732
W	0.548	0.062	0.508	0.255	0.510
Re	0.427	0.041	0.418	0.265	0.486
Os	0.358	0.040	0.372	0.350	0.602
Ir	0.358	0.049	0.436	0.434	0.470
Pt	0.418	0.090	0.563	0.522	0.536
Au	0.598	0.151	0.776	-	0.601
Hg	0.840	0.216	1.044	-	-

$$\gamma_{ISF} = 138.4905 + \sum_i x_i Z_i \tag{9.7}$$

Where Z_i is the relevant factor for element i taken from table 9.3. 59.4758 and 138.4905 are the SISF energy of unalloyed γ' and ISF energy of unalloyed γ respectively. The Z factors are determined by linear interpolation between the values of fault energy between x_{sub}=0 and x_{sub}=0.25 in the case of γ' and the gradient of a linear fit between x=0 and x=0.25 in the case of γ. These fits are not all good quality, however, even the ones which are not, serve as a first degree approximation of the behaviour of the alloying element. With regard to the quality of the fitting, R^2 values were generally closer to 1 (note one is the value for an ideal fit) for the 3d series then the 4d and 5d series. Also the values get smaller the further away from the 3 centre periods 7, 8 and 9 (note this analysis does not include the R^2 values of the alloys containing Ta and Pd due to their significantly worse fitting then the other alloys).

For the same sample of alloys analysed in section 9.1.2. The results for the fault energies are as follows. For CMSX-10 the SISF is calculated as 114.108 mJ/m^2 and the ISF as -5.505 mJ/m^2. For Waspaloy the SISF energy and ISF energy are 81.374 mJ/m^2 and -47.693 mJ/m^2 respectively. For Inconel-939 the SISF energy is 247.335 mJ/m^2 and the ISF energy is -121.106 mJ/m^2. For the alloy N18 the SISF and ISF energies are 153.229 mJ/m^2 and -119.723 mJ/m^2 respectively. Finally for René88 DT the SISF energy is 225.937 mJ/m^2 and the ISF energy is -77.292 mJ/m^2. Inconel-939 has the highest SISF energy which is derived due to the large amount of titanium in the γ' phase of the alloy.

Unfortunately since there is a small amount of experimental data for fault energies there is limited means to assess the veracity of this model. However this model should serve adequately as a first degree approximation of the (S)ISF energies of multicomponent alloy systems. For the SISF energy in the γ' phase to the author knowledge there exists no experimental data. With regard to the ISF energy in the γ phase, for the alloy MC2, Benyoucef[304] determined the ISF energy using TEM to be $\approx 31\, mJ/m^2$. The calculated value in the model of this thesis is -63.120 mJ/m^2. For the two model alloys analysed by Pettinari[227] using TEM, the Re containing alloy was observed to have an ISF energy of $32\pm3\, mJ/m^2$ (-38.296$\pm$3 mJ/m^2 in our model) and the Ru containing alloy was found to have a ISF energy of $31\pm3\, mJ/m^2$ (-31.416$\pm$3 mJ/m^2 in our model). Cui[305] did an analysis of a series of multicomponent alloys using TEM reveling that ISF energy declines with increases in cobalt composition, decaying from $40.1\pm1.2\, mJ/m^2$ at 4.40 atomic percent to $24.9\pm0.5\, mJ/m^2$ at 20.3 atomic percent.

There is a consistent theme between the available experimental data for real superalloys and that is that all of the results are significantly reduced from the value of pure Ni but non have crossed over to become negative. This strongly contrasts with the results of our model in which all of the values are negative. This could be for many potential reasons, one is that there is a number of phenomena which the model cannot account for, including clustering and segregation which may become significant at higher alloying compositions. Also it may be possible that real alloy systems have mechanisms which are able to partially self-correct beyond a certain limit, setting a de facto limit for how much the ISF energy can be reduced. It is clear that the model of the thesis does not yield

quantitatively correct results. Assessing whether the results are qualitatively correct is also difficult, due to the small amount of experimental data and the close proximity of said data. For the ISF there does exist a model produced based on the work of Shang[40], this model results in far less accurate quantitative results, for example the alloy MC2 is predicted to have an ISF energy of -549.27 mJ/m^2. This model is designed for only use in dilute alloys (alloying fraction less then 0.1), however the same concerns surrounding qualitative assessment apply. This model can be accessed at the following web address: http://www.phases.psu.edu/Tools/VBSFEscripts/VBSFE.html.

One facet that is important to assess is whether extrapolating for the coarse compositions accurately approximates the nuances found in the data for the fine compositions. To determine this data from both of the datasets is plotted on a single graph for the first and second sublattices respectively in figures 9.3 and 9.4.

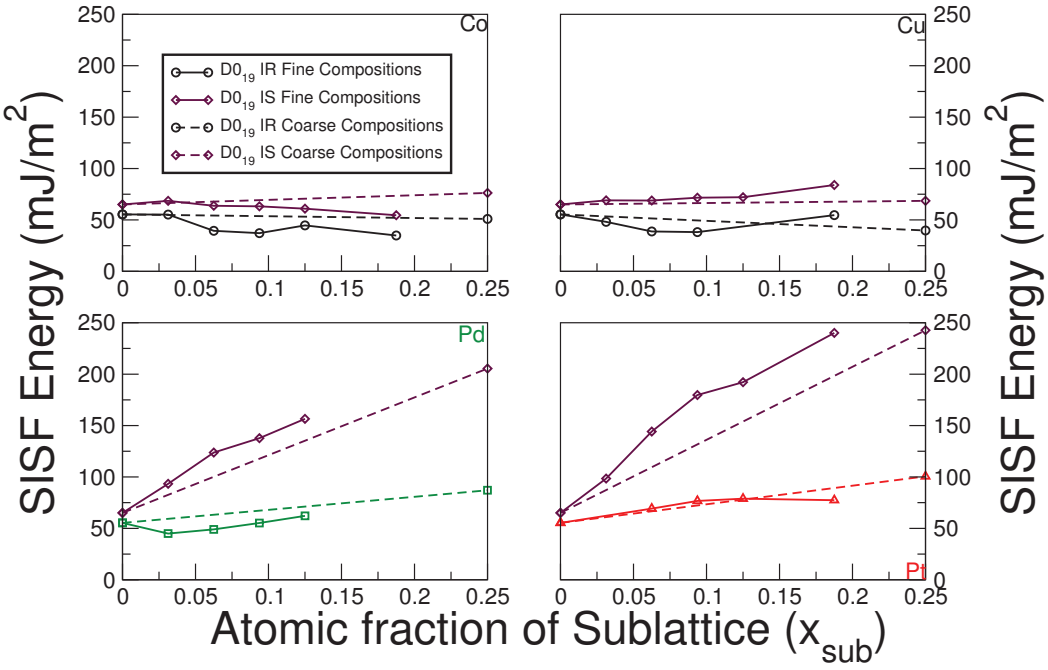

Figure 9.3: Comparison between the SISF formation energies of the coarse and fine compositional data for the first sublattice of the γ' phase in the spin-polarised implementation. Black lines in the legend should be taken as representing the standard colour scheme. Note that this data was adjusted such that both data sets have the exact same starting point.

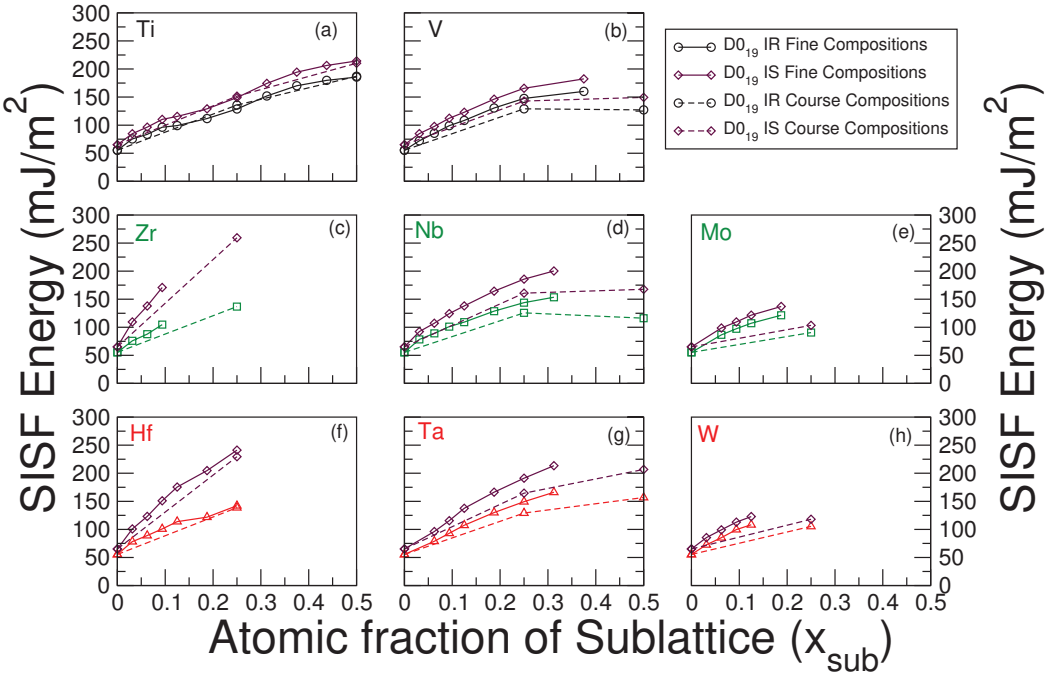

Figure 9.4: Comparison between the SISF formation energies of the coarse and fine compositional data for the second sublattice of the γ' phase in the spin-polarised implementation. Black lines in the legend should be taken as representing the standard colour scheme. Note that this data was adjusted such that both data sets have the exact same starting point.

As can be seen from these two figures agreement is relatively good when it comes to the overall shape of the dependence of SISF energy on composition, however some of the values especially in the case of X=W and Mo have large deviations. This model can still serve as a reasonably good approximation to the SISF energy changes with the addition of these alloying elements. However it is possible to propose as second and more accurate version of the model which employs the fitting equations from the figures 8.29 and 8.34. Under this version of the model the SISF energies are 154.508, 135.562, 212.166, 181.133 and 276.452 mJ/m^2 for CMSX-10, Waspaloy, Inconel-939, N18 and

René88 DT respectively. The differences in the SISF energies are caused chiefly by the following factors. The effects of W and Ta are much greater in the more advanced model for the case of CMSX-10 resulting in a higher SISF Energy. In the case of Waspaloy, the effect of Mo is significantly different, positive instead of negative in the more advanced model, due to the differing segregation of this element in the two models. If in the simpler model Mo is assumed to segregate to the second sublattice the SISF energy becomes $111.024\,mJ/m^2$, making the results of the two models a lot closer. In the case of Inconel-939 the difference in SISF energy is chiefly caused by the difference in the behaviour of Ti. It is important to realise that for both the models this result is extrapolated, but the influence of Ti in the simpler interpretation of the model is calculated as much greater for high compositions. For the case of N18 the difference in the behaviour of Mo accounts mostly for the difference between the two models, where changing the segregation makes the result for the more primitive model $172.422\,mJ/m^2$. Finally for the alloy René88 DT there is significant differences in the behaviour for Mo (opposite effect in the more primitive model due to different partitioning) and Nb (smaller effect in the more primitive model).

A linear model is assumed in this research, one of the reasons for this was that it is the simplest model to implement as it only requires 2 points to interpolate between them. One of the issues with more advanced models (this also extends to the more advanced model of SISF energy in this thesis) is that there can be problems with overfitting, additionally there are issues regarding physical justification for such curves be they quadratics or exponentials etc. Use of the linear relationship is in line with the goals

of this thesis, which is to provide a model to serve as a first-degree approximation. The development of more advanced models would require all of the elements in the first and second sublattices of the γ' phase to have a large number of calculations at computationally intensive low compositions carried out, the resources of which were not available for this project.

A quantitative test of the data was performed for the fault energies. It was commonly observed in all of the results chapters that the 4d and 5d alloying elements behave similarly. It was tested if for the sample of real alloys that they can be interchanged. Hence 2 scenarios were analysed. In the first the Z factors for the 4d elements were swapped with those of the 5d elements of the same group. In the second scenario the factors of the 5d elements were swapped with those of the 4d elements of the same group. Differences in the fault energies in both scenarios are typically low around or significantly lower than $10\,mJ/m^2$ with the highest being just under $20\,mJ/m^2$ for the SISF energy of the alloy René88 DT, which was caused by the swapping of W and Mo. This small-scale investigation backs up the assertion that 4d and 5d elements are somewhat interchangeable for the all-important real alloy compositions.

The models in this thesis are expected to be valid for the compositions between x=0-0.25 for the γ phase and x_{sub}=0-0.25 for the γ' phase (note the more advanced model which is based on the fine compositional data is expected to be valid for the range which data was taken) and due to extrapolation may be highly unreliable at higher compositions. This range was selected since it covers the solid solubility of most of the elements and was convenient to implement as 8 (where the higher compositions are

covered much thinner) and 5 points respectively is not enough for a good fit over the whole range of x and x_{sub} which is 0-1. The model can be trivially extended to a larger range by simply interpolating between points at higher compositions for example 0.25 and 0.5.

In some cases there were values exceeding x_{sub}=0.25, this is true in the γ' phase for Ti in the alloys Inconel-939 and N18 and for both Ti and W in the alloy René88 DT. Similarly, the value of x=0.25 is exceeded in the γ phase for the alloys Inconel-939, N18, MC2 and the two model alloys analysed by Pettinari[227]. However, in all of the cases apart from Inconel-939 the increases are very marginal (less than or just over 1 percent) and shall not be considered further. In excess of x_{sub}=0.25 the new factors become -0.219 for Ti and 0.119 for W in the second sublattice γ' phase for the formation enthalpy. The new factors for the SISF energy in excess of x_{sub}=0.25 are 8.207 for Ti and -31.731 for W in the second sublattice of the γ' phase. Similarly the factors for the lattice parameter become 0.001 for Ti and 0.003 for W. In the γ phase in excess of x=0.25 the factors for the formation enthalpy, ISF energy and lattice parameter of Cr are 0.337, -0.189 and -0.001 respectively.

These new factors make the values for the SISF energy of Inconel-939 and N18 and René88 DT 270.171, 199.818 and 250.114 respectively. This makes the values for the lattice parameter of γ' for Inconel-939, N18 and René88 DT 3.652, 3.760 and 3.742 respectively. The lattice parameter of γ and ISF energy for Inconel-939 are 3.542 and -85.052 respectively. Another point of note with regard to the ISF energy is that it can be used to approximate both the extrinsic stacking fault energy γ_{ESF} and the twin

boundary energy γ_{TB} by the usage of the following relationship $\gamma_{ISF} \approx \gamma_{ESF} \approx 2\gamma_{TB}$, this equation is justified by the usage of a bond counting procedure[92].

9.2 Temperature Effect

With regard to the temperature effect data of the ISF for the binary nickel FCC compounds, the lack of data makes it difficult to draw any significant conclusions. But the data that is there points to the conclusion that there would be small decays over the temperature range from 0 K to 1400 K. The data presented in both chapters 7 and 8 validate the following observations. The larger the 0 K SISF energy in general the larger the scale of the change with temperature. The change in the SISF energy with temperature generally takes the SISF energy closer to $0\,mJ/m^2$. However the change is scarcely significant enough to change the energy to the extent where it is close to zero, or further yet result in change of the sign of the SISF energy. The latter is important as it would change the phases which were stabilised by the alloying addition. Overall the effect of alloying appears to be much greater the the effect of temperature for both of the fault energy types investigated in this study.

Table 9.3: Model parameters (Z) for the SISF and ISF energies in the γ' and γ phases respectively.

Element	1^{st} sub. factor	2^{nd} sub. factor	γ phase factor
Al	-769.997	0.000	-398.610
Ti	-588.891	321.624	-422.370
V	-496.502	294.923	-387.250
Cr	-211.612	145.285	-529.620
Mn	-199.719	238.471	-641.300
Fe	-58.584	224.492	-262.200
Co	-17.412	89.588	-326.850
Ni	0.000	96.826	0.000
Cu	-62.369	12.459	-133.680
Zn	-420.205	-6.703	-197.230
Zr	-947.309	325.972	-1164.100
Nb	-618.719	281.495	-246.480
Mo	-542.795	141.030	-421.940
Tc	-309.811	-139.027	-646.500
Ru	-91.022	-103.765	-443.510
Rh	-101.754	47.874	-248.220
Pd	126.962	74.182	16.180
Ag	22.280	-205.265	-100.590
Cd	-438.398	-58.467	-134.370
Hf	-12.264	333.378	-880.130
Ta	-500.306	295.007	-176.770
W	-540.097	199.993	-270.290
Re	-398.716	-82.421	-575.130
Os	-115.612	-272.277	-542.450
Ir	-72.463	-112.895	-162.900
Pt	180.801	58.766	149.370
Au	198.884	-112.201	84.340
Hg	-198.857	-91.413	-93.370

Chapter 10

Conclusions

Many alloy systems as well as compounds which are relevent to development of superalloys have been analysed in this thesis. The main purpose being planar fault engineering, in order to increase creep resistance, hence enabling increases in operational temperatures and jet engine efficiency. The most significant conclusions from this work are as follows

– Where finer compositions are considered, alloying in the γ phase in general decreases the ISF energy (and presumably the ESF and twin boundary energies as well) whilst alloying in the γ' phase increases the SISF energy.

–Despite the fact that many different alloy systems and compounds are analysed in this research. With regard to the dependence of lattice parameter on the d-band filling, the relationship always has the same general shape, a parabola with minima at the centre of the transition metal series. The magnetism of the 3d elements near the centre of the d-band disrupts the shape, increasing the lattice parameters where these elements are

concerned (note there is also significant magnetic disruption in the 4 and 5d series in the Co_3X compounds).

–The following elements Ti, Zr, Hf, Nb and Ta were confirmed to have the potential to enhance the stability of $Co_3(Al_{1/2-x}W_{1/2-x}X_{2x})$ and hence increase the γ' solute temperature capacity as well as operational temperature of Co-based and CoNi-based alloys.

–With regard to the temperature effect, in general the fault energy decays towards $0\,mJ/m^2$ irrespective of whether it is positive or negative and the scale of the decay is informed by the magnitude of the 0 K fault energy. Where larger decays are experienced in alloys and compounds with fault energies which are larger in magnitude at 0 K. Overall the alloying composition appears to have a much more dramatic effect on the fault energy than the temperature. This is encouraging for the prospect of using first-principles 0 K fault energies as a working approximation to operational temperature fault energies.

–With regard to how coarse highly stoichometric compositions through interpolation simulate the fault energy results of finer compositions. The sign of the change in addition to the general shape is always correct. However a large degree of nuance is lost and accuracy changes depending on the composition. The dependence is approximated much more accurately in some cases then others, for example much better approximations are found for X=Ta and Hf as opposed to X=Mo and X=W. However the interpolations serve in most cases as a suitable first approximation to the fault energy.

– A model is proposed for the ISF and SISF energies as well as the formation enthalpies and lattice parameters (hence misfit can be proposed) for multicomponent alloys

unfortunately no experimental data exists for the purpose of validation for the SISF and ISF. For the case of misfits both qualitative and quantitative disagreement is found for the sample of alloys analysed with experimental data.

– The proposed model has the potential to be used in advanced physics based deformation models of superalloys improving significantly scientific understanding of deformation.

Chapter 11

Future Work

It is clear that the research within this thesis presents a significant leap forward in human understanding of ISF and SISF formation energies in nickel and to a certain extent cobalt based alloys, which will hopefully pave the way for future alloy design innovation and improved TETs. However due to the large amount of different fault types APB, CSF, SISF and SESF there is still a lot of research to be conducted in this field. The author of this thesis has identified that the most useful research to be conducted is as follows.

–A similar approach using first-principles calculations for the other fault types at a large array of alloy chemistries. It is important to note that for faults which do not modify the stacking sequence, the fault formation energy cannot be analysed by the use of AIM models and the more intensive supercell approach is necessary.

–Tests at a series of alloy compositions using a set of more advanced models then the QHDM for the temperature effect, to further validate this data.

–Validation of the data in this research (especially for the γ' pseudo-binary systems)

experimentally would be a good avenue to pursue, however due to the issues conerning fault energy measurements direct validation could prove difficult. However modifications in creep properties could be used as an indirect observation of fault energy changes.

– An extensive investigation in the same vein as ref[92] where the data from the supercell and AIM models are compared. Also a deeper delve into the phenomenon of where results between the two models differ by using even higher approximations of AIM.

–An investigation of the γ' phase in Co-Based alloys by the same technique for the pseudo-ternary system $Co_3(Al_{1-2x}W_{1-2x}X_x)$. This is for the purpose of improving the understanding of Co-based and CoNi-based alloys.

– Extending the investigation in Ni-based systems to pseudo-ternary and beyond (note that due to the large number of possible systems and larger supercells required, in excess of 300 atoms) that all these systems could not be analysed. However data for a few key systems could provide further analysis into whether synergistic effects play a role in the modification of the fault energies.

11.1 Data Access Statement

There currently exist plans to make all of the calculations and scripts of this thesis available for public consumption. For the time being for any queries regarding data email the author at the address jdtallenresearch@gmail.com.

Bibliography

[1] F. Yin and A. G. Rao. Performance analysis of an aero engine with inter-stage turbine burner. *Aeronautical Journal*, 121:1605–1626, 2017. doi: 10.1017/aer.2017.93.

[2] C. T. Sims. A History of Superalloy Metallurgy for Superalloy Metallurgists. *Superalloys 1984*, pages 399–419, 1984. doi: 10.7449/1984/Superalloys_1984_399_419.

[3] A. Suzuki and T. M. Pollock. High-temperature strength and deformation of γ/γ' two-phase Co–Al–W-base alloys. *Acta Materialia*, 56(6):1288–1297, 2008. doi: 10.1016/j.actamat.2007.11.014.

[4] A. J. Bradley, A. Taylor, and W. L. Bragg. An x-ray analysis of the nickel-aluminium system. *Proceedings of the Royal Society of London. Series A - Mathematical and Physical Sciences*, 159(896):56–72, 1937. doi: 10.1098/rspa.1937.0056.

[5] R. C. Reed. *The Superalloys: Fundamentals and Applications*. Cambridge University Press, 2006.

[6] M. E. Kassner. *Fundamentals of Creep in Metals and Alloys*.

Butterworth-Heinemann, 3^{rd} edition, 2015. ISBN 978-0-08-099427-7. doi: https://doi.org/10.1016/B978-0-08-099427-7.00011-6.

[7] M. Igarashi and S. Muneki. Heat resisting steel containing a ferrite or tempered martensite structure. *US Patent 6,299,704*, 2001.

[8] M. J. Donachie and S. J. Donachie. *Superalloys: A Technical Guide*. ASM International, 2^{nd} edition, 2002.

[9] J. Belan. GCP and TCP Phases Presented in Nickel-base Superalloys. *Materials Today: Proceedings*, 3(4):936 – 941, 2016. doi: https://doi.org/10.1016/j.matpr.2016.03.024. 32^{nd} Danubia Adria Symposium on Advanced in Experimental Mechanics.

[10] M. Durrand-Charre. *The Microstructure of Superalloys*. CRC Press, 1^{st} edition, 1997.

[11] A. K. Jena and M. C. Chaturvedi. The role of alloying elements in the design of nickel-base superalloys. *Journal of Materials Science*, 19(10):3121–3139, 1984. doi: 10.1007/BF00549796.

[12] T. M. Smith, B. D. Esser, N. Antolin, A. Carlsson, R. E. A. Williams, A. Wessman, T. Hanlon, H. L. Fraser, W. Windl, D. W. Mccomb, and M. J. Mills. Phase transformation strengthening of high-temperature superalloys. *Nature Communications*, 7:1–7, 2016. doi: 10.1038/ncomms13434.

[13] Nickel-based super alloys. *International Nickel Study Group Insight*, 20:1–9, 2013.

[14] A. Mottura, M. W. Finnis, and R. C. Reed. On the possibility of rhenium clustering in nickel-based superalloys. *Acta Materialia*, 60(6-7):2866–2872, 2012. doi: 10.1016/j.actamat.2012.01.051.

[15] V. Koteski, H.-E. Mahnke, J. Belošević-Čavor, B. Cekić, and G. Schumacher. Experimental and theoretical study of lattice relaxation around refractory atoms in nickel. *Acta Materialia*, 56(17):4601 – 4607, 2008. doi: https://doi.org/10.1016/j.actamat.2008.05.015.

[16] T. Wang, L.-Q. Chen, and Z.-K. Liu. Lattice Parameters and Local Lattice Distortions in FCC-Ni Solutions. *Metallurgical and Materials Transactions A*, 38(3): 562–569, 2007. doi: 10.1007/s11661-007-9091-z.

[17] E. W. Ross T. M. Pollock W. S. Walston, K. S. O'Hara and W. H. Murphy. RENÉ N6: Third Generation Single Crystal Superalloy. *Superalloys 1996*, pages 27–34, 1996.

[18] S. Walston, A. Cetel, R. MacKay, K. O'Hara, D. Duhl, and R. Dreshfield. Joint Development of a Fourth Generation Single Crystal Superalloy. *Superalloys 2004*, pages 15–24, 2004.

[19] K. Kawagishi, A. Yeh, T. Yokokawa, T. Kobayashi, Y. Koizumi, and H. Harada. Development of an Oxidation-Resistant High-Strength Sixth-Generation Single-Crystal Superalloy TMS-238. *Superalloys 2012*, pages 189–95, 2012.

[20] T. Yokokawa J. Zhang M. Osawa H. Harada Y. Aoki Y. Koizumi, T. Kobayashi

and M. Arai. Development of next-generation ni-base single crystal superalloys. *Superalloys 2004*, pages 35–43, 2004.

[21] A. Sato, H. Harada, A. Yeh, K. Kawagishi, T. Kobayashi, Y. Koizumi, T. Yokokawa, and J-X. Zhang. A 5th Generation SC Superalloy With Balanced High Temperature Properties and Processability. *Superalloys 2008*, pages 131–138, 2008.

[22] R. W. Fawley (edited by C.T. Sims and W. C. Hagel). *The Superalloys: Superalloy Progress*. Wiley, 1972.

[23] I. Povstugar, C. H. Zenk, R. Li, P.-P. Choi, S. Neumeier, O. Dolotko, M. Hoelzel, M. Göken, and D. Raabe. Elemental partitioning, lattice misfit and creep behaviour of Cr containing γ' strengthened Co base superalloys. *Materials Science and Technology*, 32(3):220–225, 2016. doi: 10.1179/1743284715Y.0000000112.

[24] J. Wahl and K. Harris. New Single Crystal Superalloys, CMSX®-7 and CMSX®-8. *Superalloys 2012*, pages 179–188, 2012. doi: 10.7449/2012/Superalloys˙2012˙179˙188.

[25] A. Suzuki, H. Inui, and T. M. Pollock. $L1_2$-Strengthened Cobalt-Base Superalloys. *Annual Review of Materials Research*, 45(1):345–368, 2015. doi: 10.1146/annurev-matsci-070214-021043.

[26] K. Shinagawa, T. Omori, and K. Oikawa. Ductility enhancement by boron addition

in Co – Al – W high-temperature alloys. *Scripta Materialia*, 61(6):612–615, 2009. doi: 10.1016/j.scriptamat.2009.05.037.

[27] M. Gell, D. N. Duhl, and A. F. Giamei. The Development of Single Crystal Superalloy Turbine Blades. *Superalloys 1980*, pages 205–214, 1980. doi: 10.7449/1980/Superalloys˙1980˙205˙214.

[28] M. Kamaraj. Rafting in single crystal nickel-base superalloys — An overview. *Sadhana*, 28(1):115–128, 2003. doi: 10.1007/BF02717129.

[29] China Daily.com.cn. Top 10 most commonly sold commercial planes. 2014. URL `http://www.chinadaily.com.cn/bizchina/2014-03/11/content_17336773_9.htm`.

[30] Rolls-Royce. *The Jet Engine*. Rolls-Royce Plc, 2005.

[31] Type Certificate Data Sheet for RB211 Trent 800 series engines. *European Aviation Safety Agency*, 2018.

[32] J. M. Owen. Developments in Aeroengines. *Pertanika Journal of Science and Technology*, 9:127–138, 2001.

[33] C. M. Rae and L. Zhang. Primary creep in single crystal superalloys: Some comments on effects of composition and microstructure. *Materials Science and Technology*, 25:228–235, 2009. doi: 10.1179/174328408X369311.

[34] M. S. Titus. High temperature deformation mechanisms of $L1_2$-containing Co-based superalloys: PhD Thesis. *University of California, Santa Barbara*, 2015.

[35] A. M. Elsayed, F. M. Owis, and M. M. A. Rahman. Film Cooling Optimization Using Numerical Computation of the Compressible Viscous Flow Equations and Simplex Algorithm. *International Journal of Aerospace Engineering*, 2013:1–24, 2013. doi: http://dx.doi.org/10.1155/2013/859465.

[36] L. M. Al-hadhrami, S. M. Shaahid, and A. Al-Mubarak. Jet Impingement Cooling in Gas Turbines for Improving Thermal Efficiency and Power Density Jet Impingement Cooling in Gas Turbines for Improving Thermal Efficiency and Power Density. *Advances in Gas Turbine Technology*, 2011. doi: 10.5772/22020.

[37] D. L. Klarstrom. The development of HAYNES 230 alloy. *Materials Design Approaches and Experiences as held during the TMS Fall Meeting*, 79:849–857, 2001. doi: 10.1080/095008399176544.

[38] M. Valenti. Reaching for 60 percent. *Mechanical Engineering*, 124:35–39, 2002. doi: doi:10.1115/1.2002-APR-1.

[39] P. J. H. Denteneer and W. van Haeringen. Stacking-fault energies in semiconductors from first-principles calculations. *Journal of Physics C: Solid State Physics*, 20(32):L883–L887, 1987. doi: 10.1088/0022-3719/20/32/001.

[40] S.-L. Shang, C. L. Zacherl, H. Z. Fang, Y. Wang, Y. Du, and Z. K. Liu. Effects of alloying element and temperature on the stacking fault energies of dilute ni-base superalloys. *Journal of Physics: Condensed Matter*, 24(50):505403–14, 2012. doi: https://doi.org/10.1088/0953-8984/24/50/505403.

[41] F. R. N. Nabarro and J. P. Hirth. *Dislocations in Solids*, volume 12. Wiley, 2004.

[42] R. E. Voskoboinikov and C. M. F. Rae. A new γ-surface in {111} plane in $L1_2$ Ni_3Al. *IOP Conference Series: Materials Science and Engineering*, 3:012009–6, 2009. doi: 10.1088/1757-899x/3/1/012009.

[43] D. Hull and D. J. Bacon. *Introduction to Dislocations*. Elsevier, 5^{th} edition, 2011.

[44] Y. Kaneno and T. Takasugi. Grain-boundary character distribution in recrystallized $L1_2$ ordered intermetallic alloys. *Metallurgical and Materials Transactions A*, 34(11):2429–2439, 2003. doi: 10.1007/s11661-003-0003-6.

[45] Fu-Gao Wei and Yoshinao Mishima. Annealing Twinning in Boron-Doped Ni_3Al. *Materials Transactions*, 43(6):1283–1290, 2002. doi: 10.2320/matertrans.43.1283.

[46] Y. Kaneno and T. Takasugi. Effects of stacking fault energy and ordering energy on grain boundary character distribution of recrystallized $L1_2$-type ordered alloys. *Materials Science and Engineering A*, 393(1-2):71–79, 2005. doi: https://doi.org/10.1016/j.msea.2004.11.001.

[47] J. Wang and H. Sehitoglu. Intermetallics Dislocation slip and twinning in Ni-based $L1_2$ type alloys. *Intermetallics*, 52:20–31, 2014. doi: 10.1016/j.intermet.2014.03.009.

[48] G. Schoeck, S. Kohlhammer, and M. Fahnle. Planar dissociations and recombination energy of [110] superdislocations in Ni_3Al: Generalised Peierls model in

combination with ab initio electron theory. *Philosophical Magazine Letters*, 79 (11):849–857, 1999. doi: 10.1080/095008399176544.

[49] H.P. Karnthaler, E.Th Mühlbacher, and C. Rentenberger. The influence of the fault energies on the anomalous mechanical behaviour of Ni_3Al alloys. *Acta Materialia*, 44:547–560, 1996. doi: 10.1016/1359-6454(95)00191-3.

[50] M. H. Yoo. On the theory of anomalous yield behavior of Ni_3Al — Effect of elastic anisotropy. *Scripta Metallurgica*, 20(6):915 – 920, 1986. doi: https://doi.org/10.1016/0036-9748(86)90466-7.

[51] L. Shi, J. J. Yu, C. Y. Cui, and X. F. Sun. Temperature dependence of deformation behavior in a Co – Al – W-base single crystal superalloy. *Materials Science and Engineering A*, 620:36–43, 2015. doi: 10.1016/j.msea.2014.09.074.

[52] A. Suzuki, G. C. DeNolf, and T. M. Pollock. Flow stress anomalies in γ/γ' two-phase Co-Al-W-base alloys. *Scripta Materialia*, 56(5):385–388, 2007. doi: 10.1016/j.scriptamat.2006.10.039.

[53] W. W. Milligan and S. D. Antolovich. Yielding and deformation behavior of the single crystal superalloy PWA 1480. *Metallurgical Transactions A*, 18(1):85–95, 1987. doi: 10.1007/BF02646225.

[54] W. W. Milligan and S. D. Antolovich. The mechanisms and temperature dependence of superlattice stacking fault formation in the single-crystal superal-

loy PWA 1480. *Metallurgical Transactions A*, 22(10):2309–2318, 1991. doi: 10.1007/BF02664997.

[55] Y. Mishima, S. Ochiai, and T. Suzuki. Lattice parameters of Ni(γ), Ni_3Al(γ') and Ni_3Ga(γ') solid solutions with additions of transition and B-subgroup elements. *Acta Metallurgica*, 33(6):1161 – 1169, 1985. doi: https://doi.org/10.1016/0001-6160(85)90211-1.

[56] J. K. Tien, J. P. Collier, and G. Vignoul. The role of niobium and other refractory elements in superalloys. *Superalloy 718– Metallurgy and Applications*, pages 553–566, 1989.

[57] R. T. Holt and W. Wallace. Impurities and trace elements in nickel-base superalloys. *International Metals Reviews*, 21(1):1–24, 1976. doi: 10.1179/imtr.1976.21.1.1.

[58] T. M. Smith Jr. Orientation and Alloying Effects on Creep Strength in Ni-Based Superalloys: PhD Thesis. *Ohio State University*, 2016.

[59] A. Ahmadieh and A. K. Mukherjee. Stress-temperature-time correlation for high temperature creep curves. *Materials Science and Engineering*, 21:115 – 124, 1975. doi: https://doi.org/10.1016/0025-5416(75)90205-0.

[60] O. D. Sherby and P. M. Burke. Mechanical behavior of crystalline solids at elevated temperature. *Progress in Materials Science*, 13:323 – 390, 1968. doi: https://doi.org/10.1016/0079-6425(68)90024-8.

[61] R.C. Reed, N. Matan, D. C. Cox, M. A. Rist, and C. M. F. Rae. Creep of CMSX-4 superalloy single crystals: effects of rafting at high temperature. *Acta Materialia*, 47(12):3367 – 3381, 1999. doi: https://doi.org/10.1016/S1359-6454(99)00217-7.

[62] T. M. Pollock and A. S. Argon. Creep resistance of CMSX-3 nickel base superalloy single crystals. *Acta Metallurgica et Materialia*, 40(1):1 – 30, 1992. doi: https://doi.org/10.1016/0956-7151(92)90195-K.

[63] M. S. Titus, Y. M. Eggeler, A. Suzuki, and T. M. Pollock. Creep-induced planar defects in $L1_2$-containing Co- and CoNi-base single-crystal superalloys. *Acta Materialia*, 82:530–539, 01 2015. doi: 10.1016/j.actamat.2014.08.033.

[64] N. Matan, D. C. Cox, P. Carter, M. A. Rist, C. M. F. Rae, and R. C. Reed. Creep of CMSX-4 superalloy single crystals: effects of misorientation and temperature. *Acta Materialia*, 47(5):1549 – 1563, 1999. doi: https://doi.org/10.1016/S1359-6454(99)00029-4.

[65] B. T. Dubiel and A. Czyrska-Filemonowicz. Microstructural changes during creep of CMSX-4 single crystal Ni base superalloy at 750°C. *Journal of Microscopy*, 237 (3):364–369, 2010. doi: 10.1111/j.1365-2818.2009.03261.x.

[66] T. P. Gabb, S. L. Draper, D. R. Hull, R. A. Mackay, and M. V. Nathal. The role of interfacial dislocation networks in high temperature creep of superalloys. *Materials Science and Engineering: A*, 118:59 – 69, 1989. doi: https://doi.org/10.1016/0921-5093(89)90058-0.

[67] J. X. Zhang, T. Murakumo, H. Harada, Y. Koizumi, and T. Kobayashi. Creep Deformation Mechanisms in Some Modern Single-Crystal Superalloys. *Superalloys 2004*, pages 189–195, 2004. doi: 10.7449/2004/Superalloys˙2004˙189˙195.

[68] J. S. Van Sluytman and T. M. Pollock. Optimal precipitate shapes in nickel-base γ – γ' alloys. *Acta Materialia*, 60(4):1771–1783, 2012. doi: 10.1016/j.actamat.2011.12.008.

[69] R. Ricks, A.J. Porter, and R.C. Ecob. The growth of γ' precipitates in nickel-base superalloys. *Acta Metallurgica*, 31:43–53, 1983. doi: 10.1016/0001-6160(83)90062-7.

[70] R.J. Mitchell, M. Hardy, M. Preuss, and S. Tin. Development of γ' morphology in p/m rotor disc alloys during heat treatment. *Superalloys 2004*, pages 361–370, 2004. doi: 10.7449/2004/Superalloys˙2004˙361˙370.

[71] D. Locq, P. Caron, S. Raujol, F. Pettinari-Sturmel, A. Coujou, and N. Clément. On the Role of Tertiary γ' Precipitates in the Creep Behaviour at 700°C of a PM Disk Superalloy. *Superalloys 2004*, pages 179–187, 2004. doi: 10.7449/2004/Superalloys˙2004˙179˙187.

[72] D.Y. Li and L.Q. Chen. Computer simulation of morphological evolution and rafting of γ' particles in Ni-based superalloys under applied stresses. *Scripta Materialia*, 37(9):1271 – 1277, 1997. doi: https://doi.org/10.1016/S1359-6462(97)00276-5.

[73] R. A. MacKay and L. J. Ebert. The development of directional coarsening of the γ' precipitate in superalloy single crystals. *Scripta Metallurgica*, 17(10):1217 – 1222, 1983. doi: https://doi.org/10.1016/0036-9748(83)90287-9.

[74] J Svoboda. Modelling of kinetics of directional coarsening in Ni-superalloys. *Acta Materialia*, 44:2557–2565, 06 1996. doi: 10.1016/1359-6454(95)00349-5.

[75] A. Bauer, S. Neumeier, F. Pyczak, and M. Göken. Microstructure and creep strength of different γ/γ'-strengthened Co-base superalloy variants. *Scripta Materialia*, 63(12):1197 – 1200, 2010. doi: https://doi.org/10.1016/j.scriptamat.2010.08.036.

[76] H. Yan, V. A. Vorontsov, and D. Dye. Effect of alloying on the oxidation behaviour of Co – Al – W superalloys. *Corrosion Science*, 83:382–395, 2014. doi: 10.1016/j.corsci.2014.03.002.

[77] J. Sato, T. Omori, K. Oikawa, I. Ohnuma, R. Kainuma, and K. Ishida. Cobalt-Base High-Temperature Alloys. *Science*, 312(5770):90–91, 2006. doi: 10.1126/science.1121738.

[78] X. Ding, T. Mi, F. Xue, H. J. Zhou, and M. L. Wang. Microstructure formation in γ–γ' Co–Al–W–Ti alloys during directional solidification. *Journal of Alloys and Compounds*, 599:159–163, 2014. doi: 10.1016/j.jallcom.2014.02.068.

[79] J. E. Saal and C. Wolverton. Thermodynamic stability of

Co–Al–W $L1_2$. *Acta Materialia*, 61(7):2330 – 2338, 2013. doi: https://doi.org/10.1016/j.actamat.2013.01.004.

[80] R. K. Rhein, P. C. Dodge, M.-H. Chen, M. S. Titus, T. M. Pollock, and A. Van der Ven. Role of vibrational and configurational excitations in stabilizing the $L1_2$ structure in Co-rich Co-Al-W alloys. *Physical Review B*, 92:174117–7, 2015. doi: DOI: 10.1103/PhysRevB.92.174117.

[81] M. S. Titus, A. Mottura, G. B. Viswanathan, A. Suzuki, M. J. Mills, and T. M. Pollock. High resolution energy dispersive spectroscopy mapping of planar defects in $L1_2$-containing Co-base superalloys. *Acta Materialia*, 89:423–437, 2015. doi: 10.1016/j.actamat.2015.01.050.

[82] M. Knop, P. Mulvey, F. Ismail, A. Radecka, K. M. Rahman, T. C. Lindley, B. A. Shollock, and M. C. Hardy. A New Polycrystalline Co-Ni Superalloy. *The Journal of The Minerals, Metals and Materials Society*, 66:2495–2501, 2014. doi: 10.1007/s11837-014-1175-9.

[83] K. Shinagawa, T. Omori, J. Sato, K. Oikawa, I. Ohnuma, R. Kainuma, and K. Ishida. Phase Equilibria and Microstructure on γ' Phase in Co-Ni-Al-W System. *Materials Transactions*, 49(6):1474–1479, 2008. doi: 10.2320/matertrans.MER2008073.

[84] L. Kovarik, R. R. Unocic, J. Li, and M. J. Mills. The intermediate temperature deformation of Ni-based superalloys: Importance of reordering. *JOM*, 61(2):42–48, 2009. doi: 10.1007/s11837-009-0026-6.

[85] L. Shi, J. J. Yu, C. Y. Cui, and X. F. Sun. Effect of Ta additions on microstructure and mechanical properties of a single-crystal Co – Al – W-base alloy. *Materials Letters*, 149:58–61, 2015. doi: 10.1016/j.matlet.2015.01.133.

[86] L. Klein, Y. Shen, M. S. Killian, and S. Virtanen. Effect of B and Cr on the high temperature oxidation behaviour of novel γ/γ' -strengthened Co-base superalloys. *Corrosion Science*, 53(9):2713–2720, 2011. doi: 10.1016/j.corsci.2011.04.020.

[87] F. Zhong, F. Fan, S. Li, and J. Sha. High-temperature oxidation behaviour of novel Co-Al-W-Ta-B-(Mo,Hf,Nb) alloys with a coherent $\gamma/\ \gamma'$ – dominant microstructure. *Progress in Natural Science: Materials International*, 26(6):600–612, 2017. doi: 10.1016/j.pnsc.2016.11.005.

[88] T. M. Pollock, J. Dibbern, M. Tsunekane, J. Zhu, and A. Suzuki. New Co-based γ-γ high-temperature alloys. *JOM*, 62(1):58–63, Jan 2010. doi: 10.1007/s11837-010-0013-y.

[89] L. Klein, M. S. Killian, and S. Virtanen. The effect of nickel and silicon addition on some oxidation properties of novel Co-based high temperature alloys. *Corrosion Science*, 69:43–49, 2013. doi: 10.1016/j.corsci.2012.09.046.

[90] J. Zhu, M. S. Titus, and T. M. Pollock. Experimental Investigation and Thermodynamic Modeling of the Co-Rich Region in the Co-Al-Ni-W Quaternary System. *Journal of Phase Equilibria and Diffusion*, 35(5):595–611, 2014. doi: 10.1007/s11669-014-0327-5.

[91] M. Knop, V. A. Vorontsov, M. C. Hardy, and D. Dye. High-temperature γ (FCC)/γ' ($L1_2$) Co-Al-W based superalloys. *MATEC Web of Conferences*, 14: 18003, 2014. doi: 10.1051/matecconf/20141418003.

[92] M. Chandran and S. K. Sondhi. First-principle calculation of stacking fault energies in Ni and Ni-Co alloy. *Journal of Applied Physics*, 109(10):1–6, 2011. doi: 10.1063/1.3585786.

[93] A. Zunger, S.-H. Wei, L. G. Ferreira, and J. E. Bernard. Special quasirandom structures. *Physical Review Letters*, 65:353–356, 1990. doi: 10.1103/PhysRevLett.65.353.

[94] A. Mottura, A. Janotti, and T. M. Pollock. A first-principles study of the effect of Ta on the superlattice intrinsic stacking fault energy of L1 2 -Co 3 (Al,W). *Intermetallics*, 28:138–143, 2012. doi: 10.1016/j.intermet.2012.04.020.

[95] K. V. Vamsi and S. Karthikeyan. Effect of Off-Stoichiometry and Ternary Additions on Planar Fault Energies in Ni_3Al. *Superalloys 2012*, pages 521–530, 2012. doi: 10.1002/9781118516430.ch57.

[96] K. R. Limmer, J. E. Medvedeva, D. C. Van Aken, and N. I. Medvedeva. Ab initio simulation of alloying effect on stacking fault energy in FCC Fe. *Computational Materials Science*, 99:253 – 255, 2015. doi: https://doi.org/10.1016/j.commatsci.2014.12.015.

[97] Q. Q. Shao, L. H. Liu, T. W. Fan, D. W. Yuan, and J. H. Chen. Effects

of solute concentration on the stacking fault energy in copper alloys at finite temperatures. *Journal of Alloys and Compounds*, 726:601 – 607, 2017. doi: https://doi.org/10.1016/j.jallcom.2017.07.332.

[98] M. Y. Chou, Marvin L. Cohen, and Steven G. Louie. Theoretical study of stacking faults in silicon. *Physical Review B*, 32:7979–7987, 1985. doi: 10.1103/PhysRevB.32.7979.

[99] D. S. Sholl and J. A. Steckel. *Density Functional Theory: A Practical Introduction*. Wiley, 2009. doi: 10.1002/9780470447710.

[100] M. Chandran and S. K. Sondhi. First-principle calculation of APB energy in Ni-based binary and ternary alloys. *Modelling and Simulation in Materials Science and Engineering*, 19(2):025008–7, 2011. doi: 10.1088/0965-0393/19/2/025008.

[101] A. Breidi, J. Allen, and A. Mottura. First-principles calculations of thermodynamic properties and planar fault energies in Co_3X and Ni_3X $L1_2$ compounds. *Physica Status Solidi B*, 254:1–12, 2017. doi: 10.1002/pssb.201600839.

[102] A. Dick, T. Hickel, and J. Neugebauer. The Effect of Disorder on the Concentration-Dependence of Stacking Fault Energies in $Fe_{1-x}Mn_x$ – a First Principles Study. *Steel Research International*, 80(9):603–608, 2009. doi: 10.2374/SRI09SP015.

[103] L. Vitos, J. O. Nilsson, and B. Johansson. Alloying effects on the stacking fault

energy in austenitic stainless steels from first-principles theory. *Acta Materialia*, 54(14):3821–3826, 2006. doi: 10.1016/j.actamat.2006.04.013.

[104] K. Tomihisa, Y. Kaneno, and T. Takasugi. Phase relation and microstructure in multi-phase intermetallic alloys based on Ni_3Si–Ni_3Ti–Ni_3Nb pseudo-ternary alloy system. *Intermetallics*, 12(3):317 – 325, 2004. doi: https://doi.org/10.1016/j.intermet.2003.11.004.

[105] H. Suzuki. Segregation of solute atoms to stacking faults. *Journal of the Physical Society of Japan*, 17(2):322–325, 1962. doi: 10.1143/JPSJ.17.322. URL `https://doi.org/10.1143/JPSJ.17.322`.

[106] T. Hickel, S. Sandlöbes, R. K. W. Marceau, A. Dick, I. Bleskov, J. Neugebauer, and D. Raabe. Impact of nanodiffusion on the stacking fault energy in high-strength steels. *Acta Materialia*, 75:147 – 155, 2014. doi: https://doi.org/10.1016/j.actamat.2014.04.062.

[107] G. B. Viswanathan, R. Shi, A. Genc, V. A. Vorontsov, L. Kovarik, C. M. F. Rae, and M. J. Mills. Segregation at stacking faults within the phase of two Ni-base superalloys following intermediate temperature creep. *Scripta Materialia*, 94:5 – 8, 2015. doi: https://doi.org/10.1016/j.scriptamat.2014.06.032.

[108] D. Shin, R. Arróyave, Z.-K. Liu, and A. Van de Walle. Thermodynamic properties of binary HCP solution phases from special quasirandom structures. *Physical Review B*, 74:024204–13, 2006. doi: 10.1103/PhysRevB.74.024204.

[109] C. Jiang, L.-Q. Chen, and Z.-K. Liu. First-principles study of constitutional point defects in B2 NiAl using special quasirandom structures. *Acta Materialia*, 53(9): 2643 – 2652, 2005. doi: https://doi.org/10.1016/j.actamat.2005.02.026.

[110] S.-H. Wei and A. Zunger. Band offsets and optical bowings of chalcopyrites and Zn-based II-VI alloys. *Journal of Applied Physics*, 78(6):3846–3856, 1995. doi: 10.1063/1.359901.

[111] D. J. Crudden, A. Mottura, N. Warnken, B. Raeisinia, and R. C. Reed. Modelling of the influence of alloy composition on flow stress in high-strength nickel-based superalloys. *Acta Materialia*, 75:356 – 370, 2014. doi: https://doi.org/10.1016/j.actamat.2014.04.075.

[112] J. M. Cowley. X-Ray Measurement of Order in Single Crystals of Cu_3Au. *Journal of Applied Physics*, 21(1):24–30, 1950. doi: 10.1063/1.1699415.

[113] J. M. Cowley. An Approximate Theory of Order in Alloys. *Physical Review*, 77: 669–675, 1950. doi: 10.1103/PhysRev.77.669.

[114] B. E. Warren. *X-ray diffraction*. Dover publications, 1990.

[115] A. Ceguerra, M. P. Moody, R. Powles, T. Petersen, R. Marceau, and S. Ringer. Short-range order in multicomponent materials. *Acta Crystallographica Section A*, 68:547–560, 2012. doi: 10.1107/S0108767312025706.

[116] T. Abbas, M. Ullah, A. M. Rana, and R. M. Arif Khalil. Calculation of short

range order in Ni–Rh, Ni–Pd and Cu–Rh alloys. *Materials Science-Poland*, 25: 1161–1172, 2007.

[117] L. R. Owen, H. Y. Playford, H. J. Stone, and M. G. Tucker. A new approach to the analysis of short-range order in alloys using total scattering. *Acta Materialia*, 115:155 – 166, 2016. doi: https://doi.org/10.1016/j.actamat.2016.05.031.

[118] H. S. Oh, D. Ma, G. P. Leyson, B. Grabowski, E. S. Park, F. Körmann, and D. Raabe. Lattice Distortions in the FeCoNiCrMn High Entropy Alloy Studied by Theory and Experiment. *Entropy*, 18:321, 2016. doi: https://doi.org/10.3390/e18090321.

[119] S. Cottinier. *Density Functional Theory and the Family of (L)APW-methods: a step-by-step introduction.* Addison-Wesley Publishing Company, 2^{nd} edition, 2013.

[120] H. Gholizadeh. The Influence of Alloying and Temperature on the Stacking-fault Energy of Iron-based Alloys: PhD Thesis. *Montanuniversität Leoben (University of Leoben)*, 2013.

[121] P. E. Blöchl, O. Jepsen, and O. K. Andersen. Improved tetrahedron method for Brillouin-zone integrations. *Physical Review B*, 49(23):16223–16233, 1994. doi: 10.1103/PhysRevB.49.16223.

[122] H. J. Monkhorst and J. D. Pack. Special points for Brillouin-zone integrations. *Physical Review B*, 13:5188–5192, 1976. doi: 10.1103/PhysRevB.13.5188.

[123] D. J. Chadi and M. L. Cohen. Special points in the brillouin zone. *Physical Review B*, 8:5747–5753, 1973. doi: 10.1103/PhysRevB.8.5747.

[124] M. Methfessel and A. T. Paxton. High-precision sampling for Brillouin-zone integration in metals. *Physical Review B*, 40:3616–3621, 1989. doi: 10.1103/PhysRevB.40.3616.

[125] M. A. Omar. *Elementary Solid State Physics*. Addison-Wesley Publishing Company, 1975.

[126] R. M. Martin. *Electronic Structure Basic Theory and Practical Methods*. Cambridge University Press, 2004.

[127] C. Pisani. *Quantum-Mechanical Ab-initio Calculation of the Properties of Crystalline Materials*. Springer, 1996.

[128] A. Baldereschi. Mean-Value Point in the Brillouin Zone. *Physical Review B*, 7: 5212–5215, 1973. doi: 10.1103/PhysRevB.7.5212.

[129] G. Kresse and J. Furthmüller. VASP the Guide. 2014.

[130] J. Hafner. Materials simulations using VASP-a quantum perspective to materials science. *Computer Physics Communications*, 177:6–13, 2007. doi: 10.1016/j.cpc.2007.02.045.

[131] J. Tao, J. P. Perdew, Viktor N. Staroverov, and G. E. Scuseria. Climbing the Density Functional Ladder: Nonempirical Meta–Generalized Gradient Approximation

Designed for Molecules and Solids. *Physical Review Letters*, 91:146401–4, 2003. doi: 10.1103/PhysRevLett.91.146401.

[132] J. P. Perdew, K. Burke, and M. Ernzerhof. Generalized Gradient Approximation Made Simple. *Physical Review Letters*, 78(7):3865–3868, 1997. doi: 10.1103/PhysRevLett.78.1396.

[133] Y. Wang and John P. Perdew. Correlation hole of the spin-polarized electron gas, with exact small-wave-vector and high-density scaling. *Physical Review B*, 44: 13298–13307, 1991. doi: 10.1103/PhysRevB.44.13298.

[134] E. H. Lieb. A lower bound for Coulomb energies. *Physics Letters A*, 70(5):444 – 446, 1979. doi: https://doi.org/10.1016/0375-9601(79)90358-X.

[135] E. H. Lieb and S. Oxford. Improved lower bound on the indirect Coulomb energy. *International Journal of Quantum Chemistry*, 19(3):427–439. doi: 10.1002/qua.560190306.

[136] G. K.-L. Chan and N. C. Handy. Optimized Lieb-Oxford bound for the exchange-correlation energy. *Physical Review A*, 59:3075–3077, 1999. doi: 10.1103/PhysRevA.59.3075.

[137] M. Levy and J. P. Perdew. Tight bound and convexity constraint on the exchange-correlation-energy functional in the low-density limit, and other formal tests of generalized-gradient approximations. *Physical Review B*, 48:11638–11645, 11 1993. doi: 10.1103/PhysRevB.48.11638.

[138] W. H. Press, S. A. Teukolsky, W. T. Vetterling, and B. P. Flannery. *Numerical Recipes The Art of Scientific Computing*. Cambridge University Press, 3rd edition, 2007.

[139] D. M. Wood and A. Zunger. A new method for diagonalising large matrices. *Journal of Physics A: Mathematical and General*, 18(9):1343–1359, 1985. doi: 10.1088/0305-4470/18/9/018.

[140] T. Archer, C. D. Pemmaraju, and S. Sanvito. Magnetic interaction of Co ions near the $\{10\bar{1}0\}$ ZnO surface. *New Journal of Physics*, 12(8):083061, 2010. doi: 10.1088/1367-2630/12/8/083061.

[141] K. Sun, Z. Q. Fan, and X. Y. Liu. Density Functional Theory Study of Influence of Hydrogen Absorption on the Field Emission Properties of Carbon Nanotubes. *Emerging Focus on Advanced Materials*, 306:1166–1169, 2011. doi: 10.4028/www.scientific.net/AMR.306-307.1166.

[142] E. N. Almutib. Quantum and Classical Dynamics of Molecular Scale Structures. *Lancaster University*, 2016.

[143] M. Noori, H. Sadeghi, Q. Al-Galiby, S. W. D. Bailey, and C. J. Lambert. High cross-plane thermoelectric performance of metallo-porphyrin molecular junctions. *Physical Chemistry Chemistry Physics*, 19:17356–17359, 2017. doi: 10.1039/C7CP02229H.

[144] P. E. Blöchl. Projector augmented-wave method. *Physical Review B*, 50:17953–17979, 1994. doi: 10.1103/PhysRevB.50.17953.

[145] A. Breidi, J. Allen, and A. Mottura. First-principles modeling of superlattice intrinsic stacking fault energies in Ni_3Al based alloys. *Acta Materialia*, 145:97 – 108, 2018. doi: https://doi.org/10.1016/j.actamat.2017.11.042.

[146] J. D. T. Allen, A. Mottura, and A. Breidi. First-Principles Modeling of the Temperature Dependence for the Superlattice Intrinsic Stacking Fault Energies in $L1_2$ $Ni_{75-x}X_xAl_{25}$. *Metallurgical and Materials Transactions A*, 49(9):4167–4172, 2018. doi: 10.1007/s11661-018-4763-4.

[147] M. A. Blanco, E. Francisco, and V. Luaña. GIBBS: Isothermal-isobaric thermodynamics of solids from energy curves using a quasi-harmonic Debye model. *Computer Physics Communications*, 158(1):57–72, 2004. doi: 10.1016/j.comphy.2003.12.001.

[148] A Otero-de-la Roza, David Abbasi-Pérez, and Víctor Luaña. Gibbs2: A new version of the quasiharmonic model code. II. Models for solid-state thermodynamics, features and implementation. *Computer Physics Communications*, 182(10):2232–2248, 2011. doi: 10.1016/j.cpc.2011.05.009.

[149] C. Toher, J. J. Plata, O. Levy, M. de Jong, M. Asta, M. B. Nardelli, and S. Curtarolo. High-throughput computational screening of thermal conductivity, Debye temperature, and Grüneisen parameter using a quasiharmonic Debye model. *Physical Review B*, 90:174107–14, 2014. doi: 10.1103/PhysRevB.90.174107.

[150] C. Kittel. *Introduction to Solid State Physics*. John Wiley & Sons, Inc., 8th edition, 2005.

[151] M. T. Dove. *Introduction to Lattice Dynamics*. Cambridge University Press, 1993.

[152] A. Breidi. Quasiharmonic debye model. pages 1–13, 2016.

[153] N. A. W. Holzwarth, G. E. Matthews, R. B. Dunning, A. R. Tackett, and Y. Zeng. Comparison of the projector augmented-wave, pseudopotential, and linearized augmented-plane-wave formalisms for density-functional calculations of solids. *Physical Review B*, 55:2005–2017, 1997. doi: 10.1103/PhysRevB.55.2005.

[154] P. E. Blöchl, J. Kästner, and C. J. Först (edited by S. Yip). *Handbook of Materials Modeling*. Springer, 2005.

[155] C. A. Swenson. Equation of state of cubic solids; some generalizations. *Journal of Physics and Chemistry of Solids*, 29(8):1337 – 1348, 1968. doi: https://doi.org/10.1016/0022-3697(68)90185-6.

[156] O. L. Anderson and D. G. Isaak. Elastic Constants of Mantle Minerals at High Temperature. *Mineral Physics & Crystallography: A Handbook of Physical Constants*, pages 64–97, 2013. doi: 10.1029/RF002p0064.

[157] E. F. Wasserman. *Handbook of Ferromagnetic Materials Chapter 3 Invar: Moment-volume instabilities in transition metals and alloys*, volume 5. Elsevier, 1990. doi: https://doi.org/10.1016/S1574-9304(05)80063-X.

[158] Y. Wang, J. J. Wang, H. Zhang, V. R. Manga, S. L. Shang, L.-Q. Chen, and Z.-K. Liu. A first-principles approach to finite temperature elastic constants. *Journal of Physics: Condensed Matter*, 22(22):225404–8, 2010. doi: https://doi.org/10.1088/0953-8984/22/22/225404.

[159] S.-L. Shang, H. Zhang, Y. Wang, and Z.-K. Liu. Temperature-dependent elastic stiffness constants of α and θAl_2O_3. *Journal of Physics: Condensed Matter*, 22 (37):375403–8, 2010. doi: https://doi.org/10.1088/0953-8984/22/37/375403.

[160] I. Bleskov, T. Hickel, J. Neugebauer, and A. Ruban. Impact of local magnetism on stacking fault energies: A first-principles investigation for fcc iron. *Physical Review B*, 93:214115–10, 2016. doi: 10.1103/PhysRevB.93.214115.

[161] V. I. Razumovskiy, A. Reyes-Huamantinco, P. Puschnig, and A. V. Ruban. Effect of thermal lattice expansion on the stacking fault energies of FCC $Fe_{75}Mn_{25}$. *Physical Review B*, 93:054111–8, 2016. doi: 10.1103/PhysRevB.93.054111.

[162] C.-M. Kuo. Temperature Dependent Elastic Constants of Directionally Solidified Superalloys. *Journal of Engineering Materials and Technology*, 134:024501–4, 2012. doi: doi:10.1115/1.4006228.

[163] H. Yasuda, T. Takasugi, and M. Koiwa. Elasticity of Ni-based $L1_2$-type intermetallic compounds. *Acta Metallurgica et Materialia*, 40(2):381 – 387, 1992. doi: https://doi.org/10.1016/0956-7151(92)90312-3.

[164] D. Iotova, N. Kioussis, and S. P. Lim. Electronic structure and elastic properties

of the Ni_3X (X=Mn, Al, Ga, Si, Ge) intermetallics. *Physical Review B*, 54:14413–14422, 1996. doi: 10.1103/PhysRevB.54.14413.

[165] R. A. MacKay and R. D. Maier. The influence of orientation on the stress rupture properties of nickel-base superalloy single crystals. *Metallurgical Transactions A*, 13(10):1747–1754, 1982. doi: 10.1007/BF02647830.

[166] G. R. Leverant, B. H. Kear, and J. M. Oblak. Creep of precipitation-hardened nickel-base alloy single crystals at high temperatures. *Metallurgical Transactions*, 4(1):355–362, 1973. doi: 10.1007/BF02649637.

[167] D. E. Kim, S. L. Shang, and Z. K. Liu. Effects of alloying elements on elastic properties of Ni_3Al by first-principles calculations. *Intermetallics*, 18(6):1163 – 1171, 2010. doi: https://doi.org/10.1016/j.intermet.2010.02.024.

[168] M. Chaudhari, J. Tiley, R. Banerjee, and J. Du. Site preference and interaction energies of Co and Cr in gamma prime Ni_3Al: A first-principles study. *Modelling and Simulation in Materials Science and Engineering*, 21:055006–20, 2013. doi: 10.1088/0965-0393/21/5/055006.

[169] R. W. Dickson, J. B. Wachtman Jr., and S. M. Copley. Elastic Constants of Single-Crystal Ni_3Al from 10°C to 850°C . *Journal of Applied Physics*, 40(5):2276–2279, 1969. doi: 10.1063/1.1657972.

[170] B. Ghebouli M. Fatmi S. Boucetta, T. Chihi. First-principles study of the elastic

and mechanical properties of Ni_3Al under high pressure. *Materials Science-Poland*, 28:347–55, 2010.

[171] F. X. Kayser and C. Stassis. The elastic constants of Ni_3Al at 0 and 23.5°C. *Physica Status Solidi A*, 64(1):335–342. doi: 10.1002/pssa.2210640136.

[172] J. Frankel, J. Vassiliou, J. C. Jamieson, D. P. Dandekar, and W. Scholz. The elastic constants of Ni_3Al to 1.4 GPa. *Physica B+C*, 139-140:198 – 201, 1986. doi: https://doi.org/10.1016/0378-4363(86)90557-7.

[173] R. Li, S. Lu, D. Kim, S. Schönecker, J. Zhao, S. K. Kwon, and L. Vitos. Stacking fault energy of face-centered cubic metals: thermodynamic and ab initio approaches. *Journal of Physics: Condensed Matter*, 28(39):395001–10, 2016. doi: https://doi.org/10.1088/0953-8984/28/39/395001.

[174] V. A. Lubarda. On the effective lattice parameter of binary alloys. *Mechanics of Materials*, 35(1):53 – 68, 2003. doi: https://doi.org/10.1016/S0167-6636(02)00196-5.

[175] W. P. Davey. Precision Measurements of the Lattice Constants of Twelve Common Metals. *Physical Review*, 25:753–761, 1925. doi: 10.1103/PhysRev.25.753.

[176] M. Kadziołka-Gaweł, W. Zarek, E. Popiel, and A. Chrobak. The Crystal Structure and Magnetic Properties of Selected FCC FeNi and $Fe_{40}Ni_{40}B_{20}$ Alloys. *Acta Physica Polonica A*, 117:412–414, 2010. doi: 10.12693/APhysPolA.117.412.

[177] L.-Y. Tian, R. Lizárraga, H. Larsson, E. Holmström, and L. Vitos. A first principles

study of the stacking fault energies for FCC Co-based binary alloys. *Acta Materialia*, 136:215 – 223, 2017. doi: https://doi.org/10.1016/j.actamat.2017.07.010.

[178] K. Ishida and T. Nishizawa. *Bulletin of Alloy Phase Diagrams*, 11(4):387, 1990. doi: 10.1007/BF02843315.

[179] M. J. Mehl and D. A. Papaconstantopoulos. Applications of a tight-binding total-energy method for transition and noble metals: Elastic constants, vacancies, and surfaces of monatomic metals. *Physical Review B*, 54:4519–4530, 1996. doi: 10.1103/PhysRevB.54.4519.

[180] W. Li, S. Lu, Q.-M. Hu, S. K. Kwon, B. Johansson, and L. Vitos. Generalized stacking fault energies of alloys. *Journal of Physics: Condensed Matter*, 26(26): 265005–12, 2014. doi: https://doi.org/10.1088/0953-8984/26/26/265005.

[181] T. Huang X. Xue F. Qiu Q. Jiang C. Wang, H. Wang. Generalized-stacking-fault energy and twin-boundary energy of hexagonal close-packed au: A first-principles calculation. *Scientific Reports*, 5(10213):1–11, 2015.

[182] E. R. Jette and F. Foote. Precision determination of lattice constants. *The Journal of Chemical Physics*, 3(10):605–616, 1935. doi: 10.1063/1.1749562.

[183] C. B. Carter and S. M. Holmes. The stacking-fault energy of nickel. *The Philosophical Magazine: A Journal of Theoretical Experimental and Applied Physics*, 35(5):1161–1172, 1977. doi: 10.1080/14786437708232942.

[184] S.-L. Shang, W. Y. Wang, Y. Wang, Y. Du, J. X. Zhang, A. D. Patel, and Z. K.

Liu. Temperature-dependent ideal strength and stacking fault energy of fcc ni: a first-principles study of shear deformation. *Journal of Physics: Condensed Matter*, 24(15):155402–10, 2012. doi: 10.1088/0953-8984/24/15/155402.

[185] J. Hartford, B. von Sydow, G. Wahnström, and B. I. Lundqvist. Peierls barriers and stresses for edge dislocations in Pd and Al calculated from first principles. *Physical Review B*, 58:2487–2496, Aug 1998. doi: 10.1103/PhysRevB.58.2487.

[186] R. Wang, S. Wang, and X. Wu. Edge dislocation core structures in FCC metals determined from ab initio calculations combined with the improved Peierls–Nabarro equation. *Physica Scripta*, 83(4):045604–7, 2011. doi: https://doi.org/10.1088/0031-8949/83/04/045604.

[187] P. S. Dobson, P. J. Goodhew, and R. E. Smallman. Climb kinetics of dislocation loops in aluminium. *The Philosophical Magazine: A Journal of Theoretical Experimental and Applied Physics*, 16(139):9–22, 1967. doi: 10.1080/14786436708229253.

[188] N. Bernstein and E. B. Tadmor. Tight-binding calculations of stacking energies and twinnability in FCC metals. *Physical Review B*, 69:094116–10, 2004. doi: 10.1103/PhysRevB.69.094116.

[189] A. Howie and P. R. Swann. Direct measurements of stacking-fault energies from observations of dislocation nodes. *The Philosophical Magazine: A Journal of Theoretical Experimental and Applied Physics*, 6(70):1215–1226, 1961. doi: 10.1080/14786436108243372.

[190] I. L. Dillamore and R. E. Smallman. The stacking-fault energy of FCC. metals. *The Philosophical Magazine: A Journal of Theoretical Experimental and Applied Physics*, 12(115):191–193, 1965. doi: 10.1080/14786436508224959.

[191] Y. Le Page and P. Saxe. Symmetry-general least-squares extraction of elastic data for strained materials from ab initio calculations of stress. *Physical Review B*, 65: 104104, Feb 2002. doi: 10.1103/PhysRevB.65.104104.

[192] Thermo-Calc Version 2019b. *Thermo-Calc Documentation Set*. Thermo-Calc Software, 2019.

[193] B. Sundman H. L. Lukas, S. G. Fries. *Computational thermodynamics: the CALPHAD method*. Cambridge University Press, 2007.

[194] Z.-K. Liu and Y. Wang. *Computational Thermodynamics of Materials*. Cambridge University Press, 2016.

[195] Y. Qi and R. K. Mishra. Ab initio study of the effect of solute atoms on the stacking fault energy in aluminum. *Physical Review B*, 75:224105 – 5, 2007. doi: 10.1103/PhysRevB.75.224105.

[196] S.-L. Shang, Y. Wang, Y. Du, M. A. Tschopp, and Z.-K. Liu. Integrating computational modeling and first-principles calculations to predict stacking fault energy of dilute multicomponent Ni-base alloys. *Computational Materials Science*, 91:50 – 55, 2014. doi: https://doi.org/10.1016/j.commatsci.2014.04.040.

[197] M. F. de Campos. Selected values for the stacking fault energy of face centered

cubic metals. *Materials Science Forum: Advanced Powder Technology VI*, 591-593: 708–711, 2008. doi: 10.4028/www.scientific.net/MSF.591-593.708.

[198] Y. Chino, M. Kado, and M. Mabuchi. Enhancement of tensile ductility and stretch formability of magnesium by addition of 0.2wt%(0.035at%)Ce. *Materials Science and Engineering: A*, 494(1):343 – 349, 2008. doi: https://doi.org/10.1016/j.msea.2008.04.059. Advances in microstructure-based modeling and characterization of deformation microstructures held at the TMS Annual Meeting 2007, Orlando, Florida.

[199] D.T. Pierce, J Jiménez, J Bentley, D. Raabe, and J.E. Wittig. The Influence of Stacking Fault Energy on the Microstructural and Strain-hardening Evolution of Fe-Mn-Al-Si Steels During Tensile Deformation. *Acta Materialia*, 100:178–190, 2015. doi: https://doi.org/10.1016/j.actamat.2015.08.030.

[200] X. S. Xie, G. L. Chen, P. J. McHugh, and J. K. Tien. Including stacking fault energy into the resisting stress model for creep of particle strengthened alloys. *Scripta Metallurgica*, 16(5):483 – 488, 1982. doi: https://doi.org/10.1016/0036-9748(82)90254-X.

[201] F. A. Mohamed. A dislocation model for the minimum grain size obtainable by milling. *Acta Materialia*, 51(14):4107 – 4119, 2003. doi: https://doi.org/10.1016/S1359-6454(03)00230-1.

[202] A. S. Argon and W. C. Moffatt. Climb of extended edge dislocations. *Acta Metallurgica*, 29(2):293 – 299, 1981. doi: https://doi.org/10.1016/0001-6160(81)90156-5.

[203] S. Ma, L. Carroll, and T. M. Pollock. Development of phase stacking faults during high temperature creep of Ru-containing single crystal superalloys. *Acta Materialia*, 55(17):5802 – 5812, 2007. doi: https://doi.org/10.1016/j.actamat.2007.06.042.

[204] A. Breidi, S. G. Fries, and A. V. Ruban. Ideal compressive strength of FCC Co, Ni, and Ni-rich alloys along the ⟨001⟩ direction: A first-principles study. *Physical Review B*, 93:144106–7, 2016. doi: 10.1103/PhysRevB.93.144106.

[205] P. Nash and ASM International. *Phase diagrams of binary nickel alloys*. Materials Park, OH : ASM International, 1991.

[206] B. Gan and S. Tin. Assessment of the effectiveness of transition metal solutes in hardening of Ni solid solutions. *Materials Science and Engineering: A*, 527(26): 6809 – 6815, 2010. doi: https://doi.org/10.1016/j.msea.2010.06.071.

[207] T. B. Massalski. *Bnary Alloy Phase Diagrams*, volume 1 and 2. American Society for Metals, 1986.

[208] T. Y. Velikanova, T. G. Mazhuga, O. L. Semenova, and P. S. Martsenyuk. Phase Diagram of the Ni — Os System. *Powder Metallurgy and Metal Ceramics*, 41(5): 288–295, 2002. doi: 10.1023/A:1020587516715.

[209] Y.-K. Kim, H.-K. Kim, W.-S. Jung, and B.-J. Lee. Development and application of Ni-Ti and Ni-Al-Ti 2NN-MEAM interatomic potentials for Ni-

base superalloys. *Computational Materials Science*, 139:225 – 233, 2017. doi: https://doi.org/10.1016/j.commatsci.2017.08.002.

[210] C. Wu, B.-J. Lee, and X. Su. Modified embedded-atom interatomic potential for Fe-Ni, Cr-Ni and Fe-Cr-Ni systems. *Calphad*, 57:98 – 106, 2017. doi: https://doi.org/10.1016/j.calphad.2017.03.007.

[211] W. B. Pearson and L. T. Thompson. The Lattice Spacings of Nickel Solid Solutions. *Canadian Journal of Physics*, 35(4):349–357, 1957. doi: 10.1139/p57-040.

[212] E. A. Owen, E. L. Yates, and A. H. Sully. An X-ray investigation of pure iron-nickel alloys. Part 4: the variation of lattice-parameter with composition. *Proceedings of the Physical Society*, 49(3):315, 1937. doi: https://doi.org/10.1088/0959-5309/49/3/313.

[213] J. Bandyopadhyay and K. P. Gupta. Low temperature lattice parameter of nickel and some nickel-cobalt alloys and Grüneisen parameter of nickel. *Cryogenics*, 17 (6):345 – 347, 1977. doi: https://doi.org/10.1016/0011-2275(77)90130-8.

[214] M. Y. Rafique, L. Pan, and A. Farid. From nano-dendrite to nano-sphere of Co100xNix alloy: Composition dependent morphology, structure and magnetic properties. *Journal of Alloys and Compounds*, 656:443 – 451, 2016. doi: https://doi.org/10.1016/j.jallcom.2015.09.263.

[215] Z.-B. Yang, J. Sun, S. Lu, and L. Vitos. Assessing elastic property and solid-solution strengthening of binary Ni–Co, Ni–Cr, and ternary Ni–Co–Cr alloys from

first-principles theory. *Journal of Materials Research*, 33(18):2763–2774, 2018. doi: 10.1557/jmr.2018.174.

[216] M. Shiga. Correlation between Lattice Constant and Magnetic Moment in 3d Transition Metal Alloys. *AIP Conference Proceedings*, 18(1):463–477, 1974. doi: 10.1063/1.3141758.

[217] S. Divi, G. Agrahari, S. R. Kadulkar, S. Kumar, and A. Chatterjee. Improved prediction of heat of mixing and segregation in metallic alloys using tunable mixing rule for embedded atom method. *Modelling and Simulation in Materials Science and Engineering*, 25(8):085011–24, 2017. doi: https://doi.org/10.1088/1361-651X/aa92d3.

[218] W. B. Pearson. *A Handbook of Lattice Spacings and Structures of Metals and Alloys* . Pergamon, 1967.

[219] D. R. Lide. *Handbook of Chemistry and Physics*. CRC press, 87$^{\text{th}}$ edition, 2006.

[220] W. Charnock and J. Nutting. The Effect of Carbon and Nickel upon the Stacking-Fault Energy of Iron. *Metal Science Journal*, 1(1):123–127, 1967. doi: 10.1179/msc.1967.1.1.123.

[221] B. E. P. Beeston, I. L. Dillamore, and R. E. Smallman. The Stacking-Fault Energy of Some Nickel-Cobalt Alloys. *Metal Science Journal*, 2(1):12–14, 1968. doi: 10.1179/030634568790443468.

[222] P. Humble, M. H. Loretto, and L. M. Clarebrough. The nature of de-

fects in quenched nickel. *The Philosophical Magazine: A Journal of Theoretical Experimental and Applied Physics*, 15(134):297–303, 1967. doi: 10.1080/14786436708227702.

[223] P. Chowdhury, H. Sehitoglu, W. Abuzaid, and H. J. Maier. Mechanical response of low stacking fault energy Co–Ni alloys – Continuum, mesoscopic and atomic level treatments. *International Journal of Plasticity*, 71:32 – 61, 2015. doi: https://doi.org/10.1016/j.ijplas.2015.04.003.

[224] W. Zhao, W. Li, Z. Sun, S. Gong, and L. Vitos. Tuning the plasticity of Ni-Mo solid solution in Ni-based superalloys by ab initio calculations. *Materials Design*, 124:100 – 107, 2017. doi: https://doi.org/10.1016/j.matdes.2017.03.057.

[225] W. Zhao, W. Li, X. Li, S. Gong, L. Vitos, and Z. Sun. Thermo-mechanical properties of Ni-Mo solid solutions: A first-principles study. *Computational Materials Science*, 158:140 – 148, 2019. doi: https://doi.org/10.1016/j.commatsci.2018.11.027.

[226] S. Zhao, G. M. Stocks, and Y. Zhang. Stacking fault energies of face-centered cubic concentrated solid solution alloys. *Acta Materialia*, 134:334 – 345, 2017. doi: https://doi.org/10.1016/j.actamat.2017.05.001.

[227] F. Pettinari, J. Douin, G. Saada, P. Caron, A. Coujou, and N. Clément. Stacking Fault Energy in Short-Range Ordered -Phases of Ni-Based Superalloys. *Materials Science and Engineering A*, 325(1):511 – 519, 2002. doi: https://doi.org/10.1016/S0921-5093(01)01765-8.

[228] H. M. Jin and P. Wu. First principles calculation of thermal expansion coefficient: Part 1. Cubic metals. *Journal of Alloys and Compounds*, 343(1):71 – 76, 2002. doi: https://doi.org/10.1016/S0925-8388(02)00309-2.

[229] J.-W. Hwang. Thermal expansion of nickel and iron, and the influence of nitrogen on the lattice parameter of iron at the Curie temperature: Masters Thesis. *University of Missouri-Rolla*, 1972.

[230] R. Kohlhaas, P. H. Dünner, N. Schmitz-Pranghe, and Z. Agnew. *Phys.*, 23:245, 1967.

[231] T. Wang, J. Zhu, L. Chen, Z.-K. Liu, and R. A. Mackay. Modeling of lattice parameter in the Ni-Al system. *Metallurgical and Materials Transactions A*, 35: 2313–2321, 08 2004. doi: 10.1007/s11661-006-0211-y.

[232] J. Bøttiger, N. Karpe, J. P. Krog, and A. V. Ruban. Measured and calculated thermoelastic properties of supersaturated FCC Ni(Al) and Ni(Zr) solid solutions. *Journal of Materials Research*, 13(6):1717–1723, 1998. doi: 10.1557/JMR.1998.0238.

[233] A. S. Pavlovic, V. Suresh Babu, and M. Seehra. High-temperature thermal expansion of binary alloys of Ni with Cr, Mo and Re: A comparison with molecular dynamics simulations. *Journal of Physics: Condensed Matter*, 8:3139, 01 1999. doi: https://doi.org/10.1088/0953-8984/8/18/007.

[234] B. Church, T. Sanders, R. F. Speyer, and J. K. Cochran. Thermal

expansion matching and oxidation resistance of Fe–Ni–Cr interconnect alloys. *Materials Science and Engineering A*, 452:334–340, 2007. doi: https://doi.org/10.1016/j.msea.2006.10.149.

[235] X. He, W.-C. Wang, and B.-X. Liu. Ferromagnetic states in Fe-Ru systems studied by ab initio calculation and ion-beam mixing. *Physical Review B*, 77:012401–4, 2008. doi: 10.1103/PhysRevB.77.012401.

[236] D. J. Singh. Electronic structure and weak itinerant magnetism in metallic Y_2Ni_7. *Physical Review B*, 92:174403–5, 2015. doi: 10.1103/PhysRevB.92.174403.

[237] H.-P. Wang, P. Lü, K. Zhou, and B.-B. Wei. Thermal Expansion of Ni_3Al Intermetallic Compound: Experiment and Simulation. *Chinese Physics Letters*, 33(4): 046502–4, 2016. doi: https://doi.org/10.1088/0256-307X/33/4/046502.

[238] C. G. Shull and M. K. Wilkinson. Neutron Diffraction Studies of the Magnetic Structure of Alloys of Transition Elements. *Physical Review*, 97:304–310, 1955. doi: 10.1103/PhysRev.97.304.

[239] P. Nash and M. F. Singleton. The Ni-Pt (Nickel-Platinum) System. *Bulletin of Alloy Phase Diagrams*, 10:258–262, 1989. doi: 10.1007/BF02877507.

[240] X.-G. Lu, B. Sundman, and J. Agren. Thermodynamic assessments of the Ni–Pt and Al–Ni–Pt systems. *Calphad*, 33(3):450 – 456, 2009. doi: https://doi.org/10.1016/j.calphad.2009.06.002.

[241] G. D. Mukherjee, C. Bansal, and A. Chatterjee. Vibrational and Magnetic

Contribution to Entropy of an $L1_2$ Ordered and a Partially Ordered Ni_3Mn Alloy: Results from Thermal Expansion Measurements and Model Calculations. *International Journal of Modern Physics B*, 12(22):2233–2246, 1998. doi: 10.1142/S0217979298001307.

[242] N. Thompson. The order-disorder transformation in the alloy Ni_3Mn. *Proceedings of the Physical Society*, 52(2):217–228, 1940. doi: 10.1088/0959-5309/52/2/308.

[243] Y. Aoki and J. Echigoya. Phase separation in an 18.2 at% V-Co alloy annealed at 1073 K. *Scripta Metallurgica*, 19(5):639 – 642, 1985. doi: https://doi.org/10.1016/0036-9748(85)90352-7.

[244] W. W. Xu, J. J. Han, Z. W. Wang, C. P. Wang, Y. H. Wen, X. J. Liua, and Z. Z. Zhu. Thermodynamic, structural and elastic properties of Co_3X (X=Ti, Ta, W, V, Al) compounds from first-principles calculations. *Intermetallics*, 32:303 – 311, 2013. doi: https://doi.org/10.1016/j.intermet.2012.08.022.

[245] L. J. Nagel, B. Fultz, and J. L. Robertson. Phase equilibria of Co_3V. *Journal of Phase Equilibria*, 18(1):21–23, 1997. doi: 10.1007/BF02646756.

[246] Y. Aoki, K. Asami, and M. Yamamoto. Transformation temperatures and magnetic properties of the ordered hexagonal VCo_3 compound. *physica Status Solidi A*, 23 (2):K167–K169, 1974. doi: 10.1002/pssa.2210230260.

[247] R. D. Dragsdorf and W. D. Foreing. The Intermetallic Phases in the

Cobalt–Tantalum System. *Acta Crystallographica*, 15(6):531–536, 1962. doi: 10.1107/S0365110X62001371.

[248] X. He, L. Kong, and B. Liu. Stability of the Metastable Phases in the Co–Ta System Studied by ab initio and Thermodynamic Calculations Together with Ion-Beam-Mixing Experiment. *Journal of the Physical Society of Japan*, 74(9):2501–2505, 2005. doi: 10.1143/jpsj.74.2501.

[249] V. Pétkov, Y. Kocherzhinskii, and V Markiv. *Proceedings of the USSR Academy of Sciences*, pages 852–854, 1971.

[250] A. K. Sinha. *Transactions of the Metallurgical Society of AIME*, 245:911, 1969.

[251] J. Xu, W. Lin, and A. J. Freeman. Electronic structure and phase stability of A_3Ti (A=Fe, Co, Ni, and Cu). *Physical Review B*, 48:4276–4286, 1993. doi: 10.1103/PhysRevB.48.4276.

[252] F. Cruz-Gandarilla, R. Gayosso-Armenta, M. Hesiquio, J. Cabanas-Moreno, and R. Martínez-Sánchez. XRD Studies of Co-Fe-Ti Nanocrystalline Intermetallics. *Materials Science Forum*, 442:109–114, 2003. doi: https://doi.org/10.4028/www.scientific.net/MSF.442.109.

[253] Y. Tanaka, S. Ishida, and S. Asano. Deep Potential Effect on Magnetism of Binary Including Spintronic Material. *Materials Transactions*, 46(2):355–360, 2005. doi: 10.2320/matertrans.46.355.

[254] W. Lin, J.-H. Xu, and A. J. Freeman. Electronic structure, cohesive properties,

and phase stability of Ni_3V, Co_3V, and Fe_3V. *Physical Review B*, 45:10863–10871, 1992. doi: 10.1103/PhysRevB.45.10863.

[255] M. King, W. F. McClune, L. C. Andrews, M. A. Holomany, T. M. Kahmerand, B. Lawyer, L. Zwell, B. Post, S. Weissmann, H. F. McMrdie, P. Bayliss, and M. E. Mrose. *Mineral Powder Diffraction File Databook Sets 1-42*. CPDS-International Centre for Diffraction, 1993.

[256] A. Lutts and P. M. Gielen. The Order-Disorder Transformation in $FeNi_3$. *Physica Status Solidi B*, 41(1):K81–K84, 1970. doi: 10.1002/pssb.19700410169.

[257] E. A. Brandes and G. B. Brook. *Smithells Metals Reference Book*. Butterworth-Heinemann, 7^{th} edition, 1992.

[258] Q. Chen, Z. Huang, Z. Zhao, and C. Hu. First-principles study on the structural, elastic, and thermodynamics properties of Ni_3X (X: Al, Mo, Ti, Pt, Si, Nb, V, and Zr) intermetallic compounds. *Applied Physics A*, 116(3):1161–1172, 2014. doi: 10.1007/s00339-013-8201-6.

[259] A. Pisanty, C. Amador, Y. Ruiz, and M. de la Vega. Band structures of Ni_3Pt and $NiPt_3$. *Zeitschrift für Physik B*, 80(2):237–239, 1990. doi: 10.1007/BF01357508.

[260] C. E. Dahmani. PhD Thesis. *Universite Louis Pasteur, Strasbourg*, 1985.

[261] K. Aoki and O. Izumi. Defect Structures and Long-Range-Order Parameters in Off-Stoichiometric Ni_3Al. *Physica Status Solidi A*, 32(2):657–664, 1975. doi: 10.1002/pssa.2210320240.

[262] P. V. M. Rao, S. V. Suryanarayana, K. S. Murthy, and S. V. N. Naidu. The high-temperature thermal expansion of Ni_3Al measured by X-ray diffraction and dilation methods. *Journal of Physics: Condensed Matter*, 1(32):5357–5361, 1989.

[263] H. Chen, N. E. Brener, and J. Callaway. Electronic structure, optical and magnetic properties of FCC palladium. *Physical Review B*, 40:1443–1449, 1989. doi: 10.1103/PhysRevB.40.1443.

[264] A. Aguayo, I. I. Mazin, and D. J. Singh. Why Ni_3Al is an Itinerant Ferromagnet but Ni_3Ga is Not. *Physical Review Letters*, 92:147201–4, 2004. doi: 10.1103/PhysRevLett.92.147201.

[265] L. Ortenzi, I. I. Mazin, P. Blaha, and L. Boeri. Accounting for spin fluctuations beyond local spin density approximation in the density functional theory. *Physical Review B*, 86:064437–6, 2012. doi: 10.1103/PhysRevB.86.064437.

[266] S. E. Kulkova, D. V. Valujsky, J. S. Kim, G. Lee, and Y. M. Koo. The electronic properties of FeCo, Ni_3Mn and Ni_3Fe at the order–disorder transition. *Physica B: Condensed Matter*, 322(3):236 – 247, 2002. doi: https://doi.org/10.1016/S0921-4526(02)01188-2.

[267] S. Shang, Y. Wang, Y. Du, and Z. Liu. Entropy favored ordering: Phase stability of Ni_3Pt revisited by first-principles. *Intermetallics*, 18(5):961 – 964, 2010. doi: https://doi.org/10.1016/j.intermet.2010.01.011.

[268] R. E. Parra and J. W. Cable. Neutron study of magnetic-moment distribution

in Ni-Pt alloys. *Physical Review B*, 21:5494–5504, 1980. doi: 10.1103/PhysRevB.21.5494.

[269] F. R. de Boer, C. J. Schinkel, J. Biesterbos, and S. Proost. Exchange-Enhanced Paramagnetism and Weak Ferromagnetism in the Ni_3Al and Ni_3Ga Phases; Giant Moment Inducement in Fe-Doped Ni_3Ga. *Journal of Applied Physics*, 40(3):1049–1055, 1969. doi: 10.1063/1.1657528.

[270] S. R. Joshi, K. V. Vamsi, and K. Subramanian. First principles study of structural stability and site preference in Co_3(W,X). *MATEC Web of Conferences*, 14:18001–6, 2014. doi: https://doi.org/10.1051/matecconf/20141418001.

[271] J. Koßmann, T. Hammerschmidt, S. Maisel, S. Müller, and R. Drautz. Solubility and ordering of Ti, Ta, Mo and W on the Al sublattice in $L1_2$-Co_3Al. *Intermetallics*, 64:44 – 50, 2015. doi: https://doi.org/10.1016/j.intermet.2015.04.009.

[272] M. Balarin and K. Bartsch. Thermochemische Untersuchungen zu den Systemen Ti/Ni und Ti/Co. *Zeitschrift für anorganische und allgemeine Chemie*, 622(5):919–921. doi: 10.1002/zaac.19966220529.

[273] Y. Mishin, M. J. Mehl, and D. A. Papaconstantopoulos. Phase stability in the Fe–Ni system: Investigation by first-principles calculations and atomistic simulations. *Acta Materialia*, 53(15):4029 – 4041, 2005. doi: https://doi.org/10.1016/j.actamat.2005.05.001.

[274] A. Stephen, F. Rossi, L. Nasi, C. Ferrari, N. Ponpandian, M. V. Ananth, and

V. Ravichandran. Induced ordering in electrodeposited nanocrystalline ni–mn alloys. *Journal of Applied Physics*, 103(5):053511–8, 2008. doi: 10.1063/1.2844211.

[275] M. Sanati, L. G. Wang, and A. Zunger. Adaptive Crystal Structures: CuAu and NiPt. *Physical Review Letters*, 90:045502–4, 2003. doi: 10.1103/PhysRevLett.90.045502.

[276] Y. Wang, Z.-K. Liu, and L.-Q. Chen. Thermodynamic properties of Al, Ni, NiAl, and Ni_3Al from first-principles calculations. *Acta Materialia*, 52(9):2665 – 2671, 2004. doi: https://doi.org/10.1016/j.actamat.2004.02.014.

[277] V. M. Es'kov, V. V. Samokhval, and A. A. Vecher. *Russian Metallurgy*, 2:118, 1974.

[278] W. Oelsen and W. Middel. *Mitt. Kaiser Wilhelm Inst. Eisenforsch. Düsseldorf*, 19:1, 1937.

[279] Hilpert K., Miller M., Gerads H., and Nickel H. Thermodynamic Study of the Liquid and Solid Alloys of the Nickel-Rich Part of the Al — Ni Phase Diagram Including the $AlNi_3$ Phase. *Berichte der Bunsengesellschaft für physikalische Chemie*, 94(1):40–47. doi: 10.1002/bbpc.19900940109.

[280] S. Kek, C. Rzyman, and F. Sommer. Determination of the Enthalpy of Formation of Ternary Ni_3Al-Based Alloys. *Anales de Fisica B*, 86:31, 1990.

[281] N. M. Rosengaard and H. L. Skriver. Ab initio study of antiphase boundaries and

stacking faults in $L1_2$ and DO_{22} compounds. *Physical Review B*, 50:4848–4858, 1994. doi: 10.1103/PhysRevB.50.4848.

[282] J. B. Liu and D. D. Johnson. First principle predictions of anomalous yield strength in $L1_2$ materials. *Materials Research Innovations*, 18(sup4):S4–1021–S4–1025, 2014. doi: 10.1179/1432891714Z.000000000872.

[283] P. Veyssiere, J. Douin, and P. Beauchamp. on the presence of super lattice intrinsic stacking faults in plastically deformed ni$_3$al.

[284] I. Baker, R. Darolia, and J. D. Whittenberger. *Materials Research Society Symposium Proceedings*. Number 288. Materials Research Society, 1993.

[285] A. T. Paxton. *Point, line and planar defects*. The Institute of Materials, 1992.

[286] G. M. Stocks, D. P. Pope, and A. F. Giame. *Materials Research Society Symposium Proceedings*. Number 186. Materials Research Society, 1991.

[287] O. N. Mryasov, Y. N. Gornostyrev, M. van Schilfgaarde, and A. J. Freeman. Superdislocation core structure in $L1_2$ Ni_3Al, Ni_3Ge and Fe_3Ge: Peierls–Nabarro analysis starting from ab-initio GSF energetics calculations. *Acta Materialia*, 50 (18):4545 – 4554, 2002. doi: https://doi.org/10.1016/S1359-6454(02)00282-3.

[288] Y. Wen, J. Sun, and J. Huang. First—principles study of stacking fault energies in Ni_3Al intermetallic alloys. *Transactions of Nonferrous Metals Society of China*, 22(3):661 – 664, 2012. doi: https://doi.org/10.1016/S1003-6326(11)61229-6.

[289] Y. Tu, Z. Mao, and D. N. Seidman. Phase-partitioning and site-substitution patterns of molybdenum in a model Ni-Al-Mo superalloy: An atom-probe tomographic and first-principles study. *Applied Physics Letters*, 101(12):121910–4, 2012. doi: 10.1063/1.4753929.

[290] A. Almazouzi, H. Numakura, M. Koiwa, K. Hono, and T. Sakurai. Site occupation preference of Fe in Ni_3Al: an atom-probe study. *Intermetallics*, 5(1):37 – 43, 1997. doi: https://doi.org/10.1016/S0966-9795(96)00064-7.

[291] A. V. Ruban, V. A. Popov, V. K. Portnoi, and V. I. Bogdanov. First-principles study of point defects in Ni_3Al. *Philosophical Magazine*, 94(1):20–34, 2014. doi: 10.1080/14786435.2013.838647.

[292] C. Jiang and B. Gleeson. Site preference of transition metal elements in Ni_3Al. *Scripta Materialia*, 55(5):433 – 436, 2006. doi: https://doi.org/10.1016/j.scriptamat.2006.05.016.

[293] A. V. Ruban and H. L. Skriver. Calculated site substitution in ternary $\gamma^{|\mathrm{IH}}$-Ni_3Al: Temperature and composition effects. *Physical Review B*, 55:856–874, 1997. doi: 10.1103/PhysRevB.55.856.

[294] O. V. Savin, N. N. Stepanova, Y. N. Akshentsev, and D. P. Rodionov. Ordering kinetics in ternary Ni_3Al–X alloys. *Scripta Materialia*, 45(8):883 – 888, 2001. doi: https://doi.org/10.1016/S1359-6462(01)01056-9.

[295] M. Morinaga, K. Sone, T. Kamimura, K. Ohtaka, and N. Yukawa. X-ray deter-

mination of static displacements of atoms in alloyed Ni_3Al. *Journal of Applied Crystallography*, 21(1):41–47, 1988. doi: 10.1107/S0021889887008975.

[296] P. V. M. Rao, K. S. Murthy, S. V. Suryanarayana, and S. V. N. Naidu. Effect of Ternary Additions on the Room Temperature Lattice Parameter of Ni_3Al. *Physica Status Solidi A*, 133(2):231–235, 1992. doi: 10.1002/pssa.2211330203.

[297] C. Schulze and M. Feller-Kniepmeier. Transmisson electron microscopy of phase composition and lattice misfit in the Re-containing nickel-base superalloy CMSX-10. *Materials Science and Engineering: A*, 281(1):204 – 212, 2000. doi: https://doi.org/10.1016/S0921-5093(99)00713-3.

[298] Y. C. Fayman. γ-γ' partitioning behaviour in Waspaloy. *Materials Science and Engineering*, 82:203 – 215, 1986. doi: https://doi.org/10.1016/0025-5416(86)90108-4.

[299] K. M. Delargy and G. D. W. Smith. Phase composition and phase stability of a high-chromium nickel-based superalloy, IN939. *Metallurgical transactions A*, 14: 1771–1783, 1983. doi: 10.1007/BF02645547.

[300] S. T. Wlodek, M. Kelly, and D. Alden. The Structure of N18. *Superalloys 1992*, pages 467–76, 1992.

[301] S. T. Wlodek, M. Kelly, and D. A. Alden. The Structure of René 88DT. *Superalloys 1996*, pages 129–36, 1996.

[302] V. Siva Kumar G. Kelekanjeri and Rosario A. Gerhardt. Etch pit and γ' precipitate evolution in controlled Waspaloy microstructures aged at

725, 800 and 875°C. *Acta Materialia*, 57(2):616 – 627, 2009. doi: https://doi.org/10.1016/j.actamat.2008.10.010.

[303] M. G. Albarrán, D. Martínez, E. D. B. Castro, J. C. Díaz-Guillén, I. Guzman, E. Saucedo, and A. Guzman. Effect of Preweld Heat Treatment on the Microstructure of Heat-Affected Zone (HAZ) and Weldability of Inconel 939 Superalloy. *Journal of Materials Engineering and Performance*, 23:1125–1130, 2014. doi: 10.1007/s11665-013-0704-y.

[304] M. Benyoucef, B. Décamps, A. Coujou, and N. Clément. Stacking-fault energy at room temperature of the matrix of the MC2 Ni-based superalloy. *Philosophical Magazine A*, 71(4):907–23, 1995. doi: 10.1080/01418619508236228.

[305] C.Y. Cui, C.G. Tian, Y. Zhou, T. Jin, and X.F. Sun. Dynamic Strain Aging in Ni Base Alloys with Different Stacking Fault Energy. *Superalloys 2012*, pages 715–22, 10 2012.